Lift Induced Particle Migration in Dilute Suspensions

by

Nilanka Indunil Kumari Ekanayake

ORCID: 0000-0003-3136-4838

A thesis submitted in total fulfillment for the degree of Doctor of Philosophy

in the
The Department of Chemical Engineering
Melbourne School of Engineering
THE UNIVERSITY OF MELBOURNE

May 2021

Abstract

Small particles moving near a wall experience particle-scale inertial lift forces in a direction normal to the wall and hence, migrate away from the wall. In addition, particles in suspensions experience hydrodynamic collision forces and migrate away from or towards the wall. These forces are critical in the biological context as they contribute to the separation between platelets and red blood cells that ensure the repair and integrity of blood vessels. These migration mechanisms have also been utilised to design and optimise micro-scale cell-sorting microfluidics for (e.g.) novel health detection systems and 'smarter' industrial shear enhanced membrane filtration devices.

Despite these important applications, a comprehensive model that can predict the lift and drag forces acting on a small particle moving near a wall is not available. Models that have previously been developed are limited to specific wall separation distances, fluid shear rates, and particle slip velocities, which do not cover practically relevant parameter ranges. Further, particle-scale lift models have not been previously employed in the context of suspension modelling to predict the averaged motion of many particles, as opposed to the motion of a single particle. Such suspension modelling is necessary to predict the performance of real biological and industrial multiphase flows. Hence, this thesis aims to develop a comprehensive model of particle lift applicable to the parameter ranges found in typical biological and industrial flows and apply this model to predict the behaviour of particle suspensions in these flows.

The work is conducted in two parts. Firstly, the hydrodynamic forces acting on a small spherical particle moving with a finite particle Reynolds numbers in single wall-bounded flows are investigated via direct numerical simulation. Based on these results, new lift and drag models are proposed for rigid spherical particles moving in quiescent and simple shear flows, valid for any wall separation distance, and shear and slip particle Reynolds numbers of order 0.1 or less. The models are used to examine the behaviour of single buoyant and neutrally-buoyant particles moving near walls, and the results are validated against existing experimental and numerical data. Secondly, a two-fluid model, which includes the developed wall-bounded forces, is implemented to predict particle migration in mono-disperse, dilute suspensions at low particle Reynolds numbers. Different implementation methods related to solid phase velocity boundary conditions, the force application phase, and secondary wall effects are discussed. Using this model, the transient solid concentration profiles in Taylor-Couette flows are examined and compared against available experimental results.

Declaration of Authorship

I, Nilanka Indunil Kumari Ekanayake, declare that this thesis titled, 'Lift Induced Particle Migration in Dilute Suspensions' and the work presented in it are my own. I confirm that:

- The thesis comprises only my original work towards the PhD except where indicated in the preface;
- due acknowledgement has been made in the text to all other material used; and
- the thesis is fewer than the maximum word limit in length, exclusive of tables, maps, bibliographies and appendices as approved by the Research Higher Degrees Committee.

Signed: *Nilanka Ekanayake*

Date: 16 October 2020

"The noblest pleasure is the joy of understanding."

-Leonardo da Vinci

Preface

This thesis presents the original work by Nilanka I. K. Ekanayake during her Ph.D candidature. The use of existing literature and work is made clear within each of those chapters. Any additional contributions of this dissertation have been suitably acknowledged and cited. One thesis chapter is published and another one is accepted to published in (submitted for publication) during the course of the Ph.D. Nilanka I. K. Ekanayake did the majority of work (substantially more than 50%) and is lead-author of all included publications.

- Published by *Journal of Fluid Mechanics* on 08 October 2020
  - Ekanayake, N. I. K., Berry, J. D., Stickland, A. D., Dunstan, D. E., Muir, I. L., Dower, S. K., & Harvie, D. J. E. (2020). Lift and drag forces acting on a particle moving with zero slip in a linear shear flow near a wall. 904, A6. (doi:10.1017/jfm.2020.662)
- Published by *Journal of Fluid Mechanics* on 24 March 2021
  - Ekanayake, N. I. K., Berry, J. D. & Harvie, D. J. E. (2021). Lift and drag forces acting on a particle moving in the presence of slip and shear near a wall. 915, A103. (doi:10.1017/jfm.2021.138)
- Published by *Australasian Fluid Mechanics Society* on December 2018
  - Ekanayake, N. I. K., Berry, J. D., Stickland, A. D., Muir, I. L., Dower, S. K., & Harvie, D. J. E. (2018). Lift and Drag forces on a particle near a wall at low Reynolds numbers. Adelaide, Australia. In 21st Australasian Fluid Mechanics Conference (ISBN 978-0-646-59784-3)

To minimise the repetition in some of background information and methodology, some chapters in this thesis include only parts of above publications. The publications used when preparing the chapters are indicated in an attempt to provide clarification for the reader.

This work was financially supported by Melbourne Research Scholarship. Also the support from the Australian Research Council (LP160100786) and CSL is gratefully acknowledged.

Acknowledgements

I wish to thank my supervisors: Dalton Harvie, for continued optimism, ideas, constructive criticism, and patience; Joe Berry for guidance and invaluable insights throughout this research. I am also indebted to Ineke Muire, Anthony Strickland, and Steven Dower for their valuable ideas and helpful discussions regarding experiments and research planning. I also wish to thank David Dunstan for the input at my yearly progress reviews.

I thank the University of Melbourne and for providing scholarships to support me and funding conference travels. I also acknowledge the support from CSL during this research project. I would like to thank the Department of Chemical Engineering team, especially Louise Baker and Michelle de Silva from the Particulate Fluids Processing Centre at the University of Melbourne, for providing resources such as seminars and travel grants.

I wish to thank Samuel Mills, Ellie Cho, and Paul McMillan from Biological Optical Microscopy Platform (BOMP) for assisting me greatly during flow experiments. I would also like to thank Jane Arthur and Alireza Sharif from CSL for the support of experiments and using the HPC clusters at CSL. Thanks to Sook Teoh, Lev Lafayette, and Sean Crosby for support with the Unimelb HPC clusters.

Thanks to all my colleagues of the Multiphysics Fluid Dynamics group: Christian, Lachlan, Malu, Raize, Mohammad, Pawan, Tom and Ivan for countless discussions and online-coffee catch-ups, especially in these insane times.

I would like to thank all my close friends and family both in Melbourne and Sri Lanka who kept me motivated and cheerful through out these years.

Words can never express how much I appreciate my parents encouragement and their endless love for me in my entire life. Last but not least, I thank my husband, Chaminga, for his love, patience, and unlimited support. This Ph.D. would not have been possible if not for the love and support given by him.

To my family; Chaminga, mum and dad

Contents

List of Figures

List of Tables

Abbreviations

1D	**1 D**imensional
2D	**2 D**imensional
3D	**3 D**imensional
CFD	**C**omputational **F**luid **D**ynamics
N-S	**N**avier - **S**tokes
SID	**S**hear **I**nduced **D**iffusion
DFM	**D**iffusion **F**lux **M**odel
SBM	**S**uspension **B**alanace **M**odel
SD	**S**tokesian **D**ynamics
FCM	**F**orce **C**oupling **M**ethod
LBM	**L**attice-**B**oltzmann **M**ethod
TCF	**T**aylor **C**ouette **F**low
CCF	**C**ircular **C**ouette **F**low
TVF	**T**aylor **V**ortex **F**low
WVF	**W**avy **V**ortex **F**low
TFM	**T**wo **F**luid **M**odel
BC	**B**oundary **C**ondition

DNS	**D**irect **N**umerical **S**imulation
LDV	**L**aser **D**oppler **V**elocimetry
LSS	**L**aser **S**heet **S**cannning
EIT	**E**lectrical **I**mpedance **T**omography
NMRI	**N**uclear **M**agnetic **R**esonance **I**maging
MRI	**M**agnetic **R**esonance **I**maging
DHM	**D**igital **H**olographic **M**icroscopy
CM	**C**onfocal **M**icroscopy
EM	**E**pifluorescence **M**icroscopy

Constants

Boltzmann's constant	k_{B}	$=$	$1.380\,6 \times 10^{-23}$ JK^{-1}
universal gas constant	R	$=$	$8.314\,462$ JK^{-1}mol^{-1}
gravitational acceleration	g	$=$	9.81 ms^{-2}
Avogadro constant	N_{A}	$=$	$6.022\,141 \times 10^{23}$ mol^{-1}
room temperature	T	$=$	298.15 K

Symbols

Normal symbols represent scalar quantities and boldface symbols represent vector and tensor quantities. Generally, boldface Latin symbols represent vector and boldface Greek symbols represent tensor quantities.

Latin

a	particle radius	m
A	surface area	m^2
AR_{min}	aspect ratio of smallest cell	
B	Couette flow gap width	m
C	single particle force coefficient	
d	particle diameter	m
$\boldsymbol{d}$	dynamic pressure force	Nm^{-3}
D	pipe diameter	m
D_{h}	equivalent hydraulic diameter	m
$\mathscr{D}_{\mathrm{sid}}$	shear induced self diffusivity	$\mathrm{m}^2\mathrm{s}^{-1}$
$\hat{\mathscr{D}}_{\mathrm{sid}}$	shear induced self diffusion coefficient	
$\mathscr{D}_{\mathrm{sid},\phi}$	concentrations gradient induced diffusivity	$\mathrm{m}^2\mathrm{s}^{-1}$

$\hat{\mathscr{D}}_{\mathrm{sid},\phi}$	concentrations gradient diffusion coefficient	
$\mathscr{D}_{\mathrm{sid},\gamma}$	shear gradient induced diffusivity	m^2
$\hat{\mathscr{D}}_{\mathrm{sid},\gamma}$	shear gradient diffusion coefficient	
$\mathbf{e}$	unit vector	
E_p	evolution profile parameter	
F	force	N
$\boldsymbol{F}$	force	N
$\hat{\boldsymbol{F}}$	phase specific force	N
$\boldsymbol{g}$	gravitational acceleration	ms^{-2}
H	channel height	m
$h(\phi_\mathrm{s})$, $H(\phi_\mathrm{s})$	hindered settling function	
I	intensity	
I^*	normalised intensity (by average)	
$\boldsymbol{I}$	identity tensor	
$\boldsymbol{j}_\mathrm{sid}$	shear induced flux	ms^{-1}
K_c	coefficient of the collision flux	
K_μ	coefficient of the viscosity gradient flux	
K_r	coefficient of the curvature induced flux	
l	particle separation distance	m
l^*	normalised wall distances (particle radius)	
$\check{l}$	normalised wall distance (channel height)	
L	length	m

L_{e}	particle development length	m
L_{d}	velocity development length	m
L_{D}	domain length	m
L_{S}	Stokes length	m
L_{G}	Saffman length	m
L_{obv}	observation plane length	m
$\boldsymbol{M}$	interphase momentum source	Nm^{-3}
n	number density	m^{-3}
n_f	number of frames in an image	
$\boldsymbol{n}$	unit normal vector	
N	number of particles	
N_{dim}	number of dimensions	
N_{p}	number of mesh points on particle	
N_{d}	number of mesh points on domain	
N_{y}	number of mesh points in y-direction	
N_{r}	number of mesh points in r-direction	
N_{θ}	number of mesh points in circumference	
N_{t}	total number of mesh points	
$\boldsymbol{N}_{\mathrm{s}}$	total solid flux	ms^{-1}
$\boldsymbol{N}_{\mathrm{c}}$	collision flux	ms^{-1}
$\boldsymbol{N}_{\mu}$	viscosity gradient flux	ms^{-1}
$\boldsymbol{N}_{\mathrm{r}}$	curvature induced flux	ms^{-1}

$\bar{p}$	perturbed dimensionless pressure	
p_{f}	fluid phase pressure	Pa
p_{s}	solid phase pressure	Pa
$p_{\mathrm{osm,s}}$	osmotic pressure	Pa
$p_{\mathrm{sid,s}}$	normal shear induced pressure	Pa
$p_{\mathrm{str,s}}$	steric pressure	Pa
$p_{\mathrm{exs,s}}$	excessive solid pressure	Pa
$\hat{p}_{\mathrm{s}}$	solid phase specific pressure	Pa
P	pressure	Pa
Pe	Peclect number	
$\boldsymbol{Q}, \boldsymbol{Z}$	Flow aligned tensor	
$\hat{\boldsymbol{Q}}$	Normalised symmetric tensor	
Δr_{min}	minimum cell height in r-direction	m
r_{in}	inner cylinder radius	m
r_{outer}	outer cylinder radius	m
Re	channel/pipe/thin-gap based Reynolds number	
Re_{p}	particle Reynolds number	
Re_{C}	channel Reynolds number	
Re_{TC}	Taylor-Couette flow Reynolds number	
Re_{γ}	shear based particle Reynolds number	
Re_{slip}	slip based particle Reynolds number	
t	time	s

$\bar{t}$	dimensionless time	
t_{ss}	steady-state time	s
Δt	time step	s
Δt_0	initial time step	s
$\boldsymbol{t}_1$, $\boldsymbol{t}_2$	unit wall tangential vector	
T	temperature	K
T_{eff}	effective temperature	K
$\boldsymbol{T}$	torque	Nm
$\boldsymbol{u}$	velocity vector	ms^{-1}
u	velocity	ms^{-1}
$\bar{\boldsymbol{u}}$	perturbed dimensionless velocity	
u_θ	azimuthal velocity	ms^{-1}
u_{p}	particle velocity	ms^{-1}
u_{f}	fluid velocity	ms^{-1}
u_{slip}	particle slip velocity	ms^{-1}
u_{avg}	average fluid velocity	ms^{-1}
u_{max}	maximum fluid velocity	ms^{-1}
u_{wall}	wall velocity	ms^{-1}
$\boldsymbol{u}_{\mathrm{s}}$	solid phase velocity vector	ms^{-1}
$\boldsymbol{u}_{\mathrm{f}}$	fluid phase velocity vector	ms^{-1}
v_{p}	particle volume	m^3
V	volume	m^3

w_{m}	migration velocity	ms^{-1}
W	channel width	m
Δy	cell height in y-direction	m
z_{eq}	equilibrium location	m
Z	compressibility	

Greek

α_1	multi-particle wall shear lift coefficient	kgm^{-2}
α_2	multi-particle wall slip-shear lift coefficient	kgm^{-3}
α_3	multi-particle wall slip lift coefficient	kgm^{-4}
α_4	multi-particle shear gradient lift coefficient	kgm
β_1	multi-particle unbounded drag coefficient	$\mathrm{Pa.sm}^{-2}$
β_2	multi-particle shear gradient drag coefficient	Pa.s
β_3,β_4	multi-particle wall-bounded slip drag coefficients	$\mathrm{Pa.sm}^{-2}$
β_5	multi-particle wall-bounded shear drag coefficient	$\mathrm{Pa.sm}^{-1}$
λ, ψ	anisotropic parameters	
χ	slip length	m
δ	percentage error	
η	ratio of inner to outer radius in Couette flow	
κ	curvature of stream line	
Γ	ratio of height to the annular gap	
γ	local shear rate	s^{-1}

γ_{g}	global shear rate for Poiseuille flow	s^{-1}
γ_{w}	wall shear rate	s^{-1}
γ'	shear rate gradient	$\mathrm{m}^{-1}\mathrm{s}^{-1}$
$\boldsymbol{\gamma}_{\mathrm{tot}}$	total deformation tensor	s^{-1}
γ_{sph}	mean spherical deformation magnitude	s^{-1}
$\boldsymbol{\gamma}_{\mathrm{sph}}$	spherical deformation tensor	s^{-1}
γ_{ipn}	magnitude of normalised strain inner product	s^{-1}
$\boldsymbol{\gamma}_{\mathrm{ipn}}$	inner product of normalised strain	s^{-1}
γ	deviatoric deformation tensor magnitude	s^{-1}
$\boldsymbol{\gamma}$	deviatoric deformation tensor	s^{-1}
$\hat{\boldsymbol{\gamma}}$	unit deviatoric deformation tensor	s^{-1}
ν	kinematic viscosity	$\mathrm{m}^2\mathrm{s}^{-1}$
μ	viscosity	Pa.s
$\hat{\mu}$	viscosity normalised by fluid viscosity	
μ_{dilute}	dilute viscosity	Pa.s
$\hat{\mu}_{\mathrm{sid1,s}}$,$\hat{\mu}_{\mathrm{sid2,s}}$	normalised SID viscosity	Pa.s
$\hat{\mu}_{\mathrm{col,s}}$	normalised collision viscosity	Pa.s
ρ	density	kgm^{-3}
ϕ	volume fraction	
ϕ_{max}	maximum packing fraction	
ϕ_{avg}	average solid fraction	
ϕ_{bulk}	bulk solid fraction	

ϕ_{peak}	peak solid fraction	
$\hat{\phi}$	normalised solid fraction by ϕ_{max}	
$\boldsymbol{\tau}$	viscous stress tensor	Pa.s
$\boldsymbol{\sigma}$	total stress tensor	Pa.s
ω	angular velocity	rads^{-1}

Superscript

b	bulk
s	solid
f	fluid
m	mixture
L	lift
D	drag
slip	slip velocity base
shear	shear rate base
slip-shear	both slip and shear rate base
shear-gradient	shear rate gradient base
x	along y-direction
y	along y-direction
z	along z-direction
θ	along θ-direction
r	along r-direction

Superscript

$*$	length quantity scaled by a particle radius (a)
$\hat{}$	length quantity scaled by a hydraulic diameter (D_{h})
ub	unbounded
wb	wall-bounded
dwb	double wall-bounded
in	inner region
outer	outer region
w	wall
w,mov	moving wall
w,sta	stationary wall
w,in	inner wall
w,out	outer wall

Chapter 1

Introduction

1.1 Particle migration

Micron-sized particles in sheared flows exhibit cross-stream migration and clustering at different equilibrium distances across channels. Hard spherical particles moving near walls generally experience particle-scale hydrodynamic inertial lift forces in a direction normal to the walls, which causes the migration away from the walls [45, 58] and hydrodynamic inertial and non-inertial drag forces in a direction parallel to the walls, which often causes finite particle slip velocities [93]. The particles in suspensions can also experience hydrodynamic interaction (collision) forces and migrate away from or towards walls, down gradients of shear and/or concentration [148, 182]. However, under extremely dilute conditions where inter-particle collisions are less significant, the transverse motion is primarily caused by hydrodynamic lift forces. While particle migration can occur in any suspension system, the present thesis focuses on hard-sphere migration primarily in shear flows under dilute conditions where lift and drag forces are most significant.

1.1.1 Applications and relevance

Principles related to particle migration are often utilised in various biological and industrial applications to separate particles in suspensions. The particle migration mechanism has been exploited in the design of micro-scale fractionation and cell sorting microfluidics [160]. Microfluidics is a laboratory-scale passive separation technology that has been utilised to isolate components of blood (e.g., red blood cells, white blood cells, platelets, bacteria, and tumor cells), or to separate diseased cells from healthy cells (e.g., malaria-infected red blood cells [112]) in biological research and health care. The separation process is based on cell characteristics such as shape, size, and deformability and operates at low and intermediate particle Reynolds numbers where inertial lift forces become important [69]. Note that deformable particles can migrate away from a wall even in non-inertial flows, allowing the cell-sorting microfluidics to operate at extremely low flow rates [140]. Optimising the design of microscale cell sorting microfluidics can enhance their throughput for clinical benefits.

In the biological fluid context, particle-scale inertial forces contribute to the separation between platelets and red blood cells and the formation of a cell-free layer (CFL) adjacent to blood vessel walls. CFL development is crucial for blood clot formation, as the platelet concentration is increased in the CFL, enhancing the hemostatic coagulation mechanisms required to repair damaged vessel walls [144]. Hence, quantifying both the near-wall platelet concentrations and the CFL thickness is necessary to predict thrombus growth. These values can be determined by the balance between wall induced lift forces and shear-induced diffusion forces acting on red blood cells and platelets. However, neither the CFL development nor the platelet distribution near the wall is well understood, and quantitative models are not available.

Targeted delivery of drugs has been explored in many cardiovascular and inflammatory diseases and is also widely studied for cancer treatment [246]. In addition to the targeting mechanism, the nano-carriers shape and size are crucial for efficient drug delivery to maximise the interactions with vascular walls [185]. In vivo and in-vitro studies have already reported smaller discoid-shaped particles to increase the margination behaviour [245]. Systematic numerical investigations on optimising the physical design parameters of carrier particles flowing in various microvessel configurations could complement and enhance our understanding of other in-vitro and in-vivo studies.

Membranes integrated with microfluidic devices are used to fractionate multi-component food suspensions and biological suspensions [70, 249]. This continuous flowing on-chip microscale filtration process is desirable when fast analysis and detection are required. The enrichment of smaller particles near walls and the diffusion of larger particles away from the walls allows the smaller particles to permeate more efficiently through the membrane. Further, shear-induced diffusion and lift forces reduce the thickness of the cake layer of particles deposited on the membrane and increase the permeate flux [4, 31, 134]. Geometric properties of the microfluidic devices (i.e., entrance length, height) and flow parameters (i.e., wall shear rate and transmembrane pressure) can be adjusted to increase the process efficiency.

A better understanding of these processes will lead to new design and optimisation of existing design leading to energy, environmental and health benefits.

1.1.2 Challenges in modelling

In the context of process applications, modelling particle margination is critical for the optimisation of device performance. Considering blood flow, it is important to quantify the cell and particle distributions in patient-specific vessels to understand the underlying health conditions and develop treatment methods.

Direct numerical simulations (DNS) of flowing suspensions can capture particle margination phenomena reasonably well. This modelling technique has been used to examine the inertial focusing of particles in microfluidic devices [44, 53, 54] and platelet distribution and CFL thickness in blood vessels [59, 60, 268, 270]. However, DNS requires very high computational memory and runtimes to resolve a broad range of temporal and spatial scales, particularly when considering many particles or cells within the simulation domain. In effect, these requirements constrain DNS to small volume and short timescale simulations. Suspension level details obtained via Eulerian-Eulerian multiphase simulations are able to model the most systems, provided there are enough particle entities present to approximate a continuum.

No clear explanations or closure models have yet been proposed for solid-liquid systems to capture the particle migration for all bulk concentrations in multiphase modelling techniques. Capturing the particle distributions in suspensions using multiphase models remains challenging due to the limitations of particle-scale hydrodynamic wall-bounded force models [253], restricted to low particle slip and shear Reynolds numbers *, and not applicable to all particle-wall separation distances. Nevertheless, individual progress has been made on related systems (e.g., concentrated suspensions under Stokes flow conditions). Even so the modelling approaches used for concentrated suspensions consider

* $Re_{\text{slip}} = |u_{\text{slip}}|a/\nu$ and $Re_\gamma = |\gamma|a^2/\nu$ where $u_{\text{slip}}, \gamma, a$ and ν and are the particle slip velocity, shear rate, particle radius and fluid kinematic viscosity.

only hydrodynamic collision forces and mostly disregard any wall-bounded lift or drag forces [182, 197]. Due to the limitations of wall-bounded force models, only a few multi-phase modelling approaches limited to linear shear and Poiseuille flows between two flat plates are reported to capture the particle migration for dilute suspensions.

Hence, despite their perceived importance, wall lift and drag forces have largely been ignored when quantitatively predicting the behaviour of suspension flows. Conversely, many studies have ascribed differences between experimental and simulation suspension particle distributions to be a result of wall lift forces, without further proof or quantification [1, 101, 102]. The work conducted within this thesis will allow these questions to be answered while also providing new opportunities to understand and simulate many critical multiphase biological and industrial problems.

1.2 Research objectives

The principle research objectives of the study described in this thesis are as follows:

- Development of improved lift and drag models for rigid spherical particles moving in quiescent (i.e., zero shear) and linear shear flows, valid for any wall separation distance (except contact), and intermediate shear and slip particle Reynolds numbers of order 0.1 and below.
- Development of a two-fluid model, which includes wall forces to predict particle migration in mono-disperse, dilute suspensions ($\phi_{\mathrm{b}} < 0.01$[†]) at low particle Reynolds numbers.

[†] Here ϕ_{b} is the bulk solid concentration.

1.3 Thesis contributions

Though existing knowledge from the fields of low Reynolds number hydrodynamics and multiphase flow simulation has been referred to throughout, some novel aspects of the present thesis include:

- While direct numerical simulations for particles translating near walls are available in the literature [141, 264, 265], a rigid particle translating with a zero slip velocity has not previously been assessed;
- The thesis computes the wall-bounded lift and drag forces for particles translating with zero slip and non-zero slip velocities up to shear and slip particle Reynolds numbers of order 0.1 or less via direct numerical simulation. Previously, DNS studies of single spheres have only been performed for relatively large slip and shear Reynolds numbers [141, 264, 265].
- The thesis identifies the limitations of existing wall-bounded lift and drag force models [45, 211], mainly due to particle-wall separation distance constraints, and proposes new lift and drag models valid for any particle-wall separation distance (except contact). The proposed models are validated against numerical and experimental data [239, 241].
- The thesis is the first to compute lift and slip velocities of neutrally buoyant particles translating near walls in linear shear flows for low but finite shear Reynolds numbers via DNS.
- The thesis contains the first use of a multiphase two-fluid model incorporating wall-bounded forces for low Reynolds number flows. The influence of wall-bounded forces on the equilibrium particle distributions can be determined with the present simulation configuration in simple shear flows (e.g., linear shear flow and cylindrical Couette flow).
- The thesis implements a new boundary condition for the solid phase velocity in the two-fluid framework based on the single-particle slip velocity analysis.
- Solid distribution profiles obtained for Taylor-Couette flows are qualitatively validated against available experimental data [157].

1.4 Chapter outline

The thesis is divided into the following four parts:

- **Part I**: This includes three literature review chapters. Chapter 2 discusses the available experimental observations for hard-sphere migrations for dilute and concentrated suspensions. The observations are used to establish the main responsible forces, as studied in the literature, and highlight the necessity of considering all the forces simultaneously to predict experimentally observed features of the particle distributions (e.g., particle concentration near walls). A review of existing single-particle hydrodynamic forces, mostly relevant for dilute suspension modelling, is presented in chapter 3. This chapter highlights the limitations associated with the existing single-particle hydrodynamic force models. The following chapter 4 provides a review of multi-particle hydrodynamic forces. Further, frameworks developed to simulate suspensions are discussed, including a summary of their limitations.

- **Part II**: This section presents direct numerical lift and drag force simulation results obtained for a single particle. Chapter 5 details the theoretical and numerical framework developed for single-particle simulations. The single-particle force measurements of a particle moving at zero slip velocity in linear shear flows near a wall are given in chapter 6. Following this, chapter 7 presents numerical results for a particle translating with a finite slip velocity in quiescent and linear shear flows near a wall. The latter two chapters suggest new wall-bounded lift and drag force models based on numerical results valid for finite slip and shear Reynolds numbers.

- **Part III**: The final part focuses on dilute suspension modelling. A two-fluid framework accounting for the wall-forces is developed in chapter 8, and the implementation methods are examined in chapter 9. Particle migration in linear shear flows and circular Couette flows at relatively low particle Reynolds numbers are examined in chapter 10.

- **Part III**: The future scope of work and conclusions are presented in chapter 11.

Part I

LITERATURE REVIEW ON PARTICLE MIGRATION

Chapter 2

Experiments

In this chapter, previous experimental studies related to particle migration are outlined. The observations of particle distributions obtained in these experiments for different suspension types and flows are critical to identify the fundamental mechanisms responsible for particle migration. The overview of existing experimental studies on hard sphere migration is provided below with experiments classified by their suspension properties;

- Type A: experiments of monodisperse, neutrally-buoyant particle suspensions.
- Type B: experiments of monodisperse, non-neutrally-buoyant particle suspensions.
- Type C: experiments of bi-disperse, neutrally-buoyant particle suspensions.
- Type D: experiments of bi-disperse, non-neutrally-buoyant particle suspensions.

In the first section (§2.1), monodisperse suspensions with neutrally-buoyant particles (Type A), mostly relevant to the present study, are extensively examined in different flow configurations for a range of volume-base bulk concentrations to understand particle equilibrium positions and clustering patterns. The effect of suspension flow speed and particle size on the particle distribution and velocity profiles are briefly discussed. The next two sections (§2.2 and §2.3) provide a brief review of hard sphere distributions for suspension Type B, and Types C and D, respectively. An overall summary of these experiments indicating the theoretical relevance is presented in table 2.1.

In the last section (§2.4), a phase map of existing experiments, particularly relevant for neutrally-buoyant hard spheres, is presented to understand the potential migration mechanisms. The dominant forces responsible for particle clustering patterns are further examined by considering different non-dimensional force ratios.

2.1 Monodisperse neutrally-buoyant suspensions

The category most relevant to the present study concerns monodisperse neutrally-buoyant suspension experiments (Type A). A significant number of experimental studies have been performed under this category, and here we will only outline the work most pertinent to this study. To provide a clear overview, Type A experiments are further categorised into two groups as 'drag flow experiments' and 'pressure-driven flow experiments'. In pressure-driven flow experiments, the suspension is sheared by an axial pressure gradient applied in a channel or pipe, whereas in drag flows, the suspension is sheared via a moving/rotating wall. All these studies span a range of particle bulk concentrations, covering single particle systems and concentrated suspension systems.

2.1.1 Pressure-driven flows

Under these flow configurations, a significant number of neutrally-buoyant particle migration studies are available for a range of bulk concentrations (ϕ_{b}) and particle Reynolds numbers (Re_{p}). Some selected studies are summarised in table 2.2 at the end of this section. For clarity, again these experiments are classified as dilute ($\phi_{\mathrm{b}} \leq 0.01$) and semi-dilute or concentrated ($\phi_{\mathrm{b}} > 0.01$) suspension studies (note, that this study is preliminary concerned with dilute suspensions, we group the we group the semi-dilute and concentrated results together in this table). Given that there are different channel/pipe based Reynolds number (Re) and particle Reynolds number (Re_{p}) definitions in the literature, the Reynolds number definitions employed in this study to characterise the suspension and particle speed are specified below.

The channel/pipe based Reynolds number (Re) is defined based on the maximum fluid velocity,

$$Re = \frac{u_{\mathrm{f,max}} D_{\mathrm{h}}}{\nu_{\mathrm{f}}} \tag{2.1}$$

where $D_{\mathrm{h}}, u_{\mathrm{f,max}}$ and ν_{f} are the hydraulic diameter, maximum fluid velocity and fluid kinematic viscosity respectively. For pipe flows, D_{h} becomes the pipe diameter (D) and

Type	Suspension	Theoretical relevance	Flow	Study
A	dilute	hydrodynamic forces, equilibrium locations, migration velocity	pipe	[51, 123, 218]
			square channel	[1, 24, 50, 69, 127, 178, 228]
			rectangular channel	[24, 111]
			cylindrical Couette	[99, 123, 157]
	semi-dilute/ concentrated	shear induced diffusion	rectangular channel	[85, 128, 153, 221]
			pipe	[36, 101, 102, 191, 231]
			cylindrical Couette	[2, 32, 52, 87, 95, 147, 194, 197, 213, 223, 224]
			parallel-plate	[41, 42, 52, 126, 173]
			cone-plate	[42]
B	dilute	hydrodynamic force, equilibrium location	quiescent	[7, 119, 123, 205, 238]
			quiescent (single wall)	[239]
			moving belt (single wall)	[241]
			horizontal pipe	[163]
	semi-dilute/ concentrated	sedimentation, hindered settling velocity, self-diffusivity	quiescent	[64, 96, 186, 187, 203]
		viscous resuspension	horizontal pipe	[5, 188]
			rectangular channel	[214]
			parallel-plate	[43, 146]
			cylindrical Couette	[3, 203, 204, 212]
C	dilute	hydrodynamic force, equilibrium location	square channel	[88, 243]
	semi-dilute/ concentrated	shear induced diffusion, normal stress partition	rectangular channel	[154, 220]
			pipe	[114]
			open rectangular chamber	[114]
			cylindrical Couette	[95, 114]
			parallel-plate	[133]
D	semi-dilute/ concentrated	sedimentation	quiescent	[25, 64]
		parallel-plate	vertical pipe	[132]
			cylindrical Couette	[247]

TABLE 2.1: A summary of existing experimental studies on hard-spheres migrations and their theoretical relevance.

for rectangular channel and square channel flows, D_{h} becomes the shortest gap width (H). Note that $u_{\mathrm{f,max}}$ is replaced by the maximum velocity of the mixture $u_{\mathrm{m,max}}$ whenever the suspended fluid velocity is not provided (i.e., in some concentrated suspension studies).

The particle based Reynolds number (Re_{p}) is used to characterise the flow speed based on the particle size and maximum wall shear rate (γ_{wall}),

$$Re_{\mathrm{p}} = \frac{a^2 \gamma_{\mathrm{wall}}}{\nu_{\mathrm{f}}} \tag{2.2}$$

where a is the particle radius. For pipes and channels with high aspect ratios (i.e., large depth:width ratios) $Re_{\mathrm{p}} = Re(d/D_{\mathrm{h}})^2$ whereas for nearly square channels $Re_{\mathrm{p}} \approx Re(d/D_{\mathrm{h}})^2$. Here $d(= 2a)$ is the particle diameter.

2.1.1.1 Dilute suspensions

The migration of neutrally-buoyant particles at dilute conditions was first observed by Segre and Silberberg [218, 219] in a vertical pipe flow experiment conducted for intermediate and large Reynolds numbers ($4 < Re < 694$). Providing the first quantitative experimental observations for macroscopic spherical particle distributions, this study reported steady-state solid (particle) distribution profiles across the pipe for several development lengths (Figure 2.1). An optical scanning device with an electronic counting circuit was used to accurately count polymethylmethacrylate spheres (PMMA). At small distances from the entrance, the particle concentration remained uniform over the entire cross-section. However, in the downstream of the pipe, the particles migrated to an equilibrium position approximately 0.6 tube radius away from the tube axis (see figure 2.2a), causing peaks in the concentration profiles. Because of the tube-like shape of the annular region to which particles migrate, this behaviour in pipe flows was termed the 'tubular pinch effect'. For relatively large flow Reynolds numbers, obtained by increasing the fluid velocity, Segre and Silberberg [218] noticed a shift of the equilibrium position towards the wall. This experiment drew a strong interest in the suspension community during the early '70s, as the theories of that time for lateral motion of particles could not explain the experimental results. In a subsequent study, Karnis et al. [124] observed a similar behaviour for a single particle in pipe flows and reported the trajectories of particles. The results also indicated that the migration velocity increased with increasing Re and particle size.

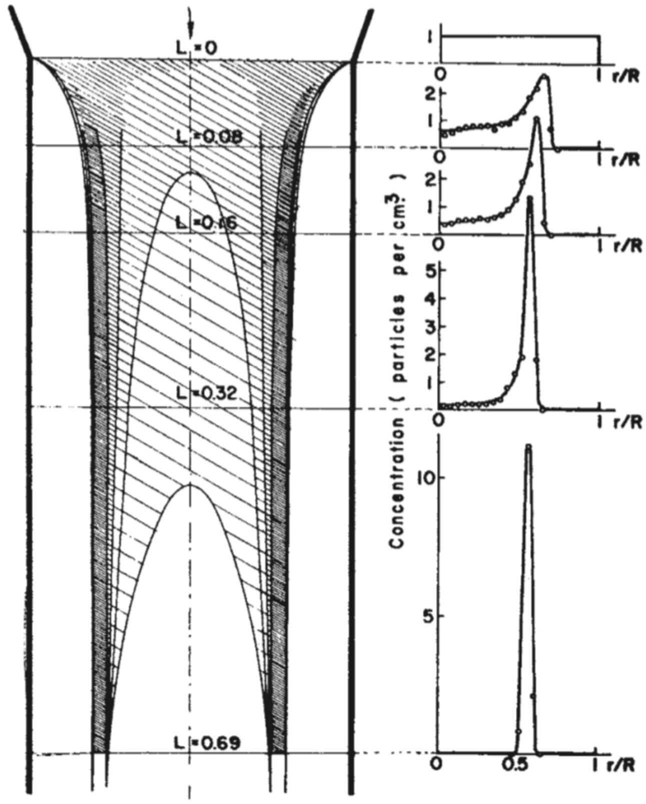

FIGURE 2.1: The 'tubular pinch' effect: Initial concentration 1 part/cm^3. Concentrations are indicated by shading; closest shading (more than 2 part/cm^3); next ($1-2$ part/cm^3); next ($0.5-1$ part/cm^3); lightest shading ($0-0.5$ part/cm^3). Adopted from Segre and Silberberg [218].

Using a similar tube diameter to particle ratio (D/d) as Segre and Silberberg [218], studies by Matas et al. [163], Morita et al. [181] and Choi and Lee [51] reported qualitatively similar patterns of particle distributions under dilute conditions. Matas et al. [163] investigated the influence of the Reynolds number and particle size on the particle distribution for neutrally-buoyant particles using a horizontal pipe flow setup. Illuminating the cross-section with a laser sheet, the measurements across the pipe were recorded via a digital video camera. Similar to Segre and Silberberg [219], Matas et al. [163] observed a shift in the equilibrium location towards the wall with increasing Reynolds numbers for $Re \geq 100$. Also, for a given channel Reynolds number, an increase of D/d resulted in a shift of the equilibrium location of the particles more towards the wall. For $Re \geq 200$, Matas et al. [163] reported a second inner annulus of clustering particles and thus named this phenomenon the 'twin tubular pinch effect'. However, in Matas et al. [163]'s study, the evolution of the concentration profile with the position was not fully investigated, as all the data had been collected at a single location close to the end of the pipe, to assure fully-developed profiles. In a recent study Morita et al. [181] reported particle migration in the pipe flows for relatively high pipe Reynolds numbers and observed a similar twin tubular pinch effect for $Re \geq 200$. However, the study reported that the observed inner annulus disappears further downstream, instead accumulating at the Segre-Silberberg annulus with a slight offset towards the wall. Hence, Morita et al. [181] suggested that this inner annulus is only an intermediate equilibrium position, and hence can be observed when the pipes are not long enough to establish truly fully-developed conditions. Choi and Lee [51] investigated the migration of neutrally-buoyant particles in a microscale pipe flow for a range of Reynolds numbers and d/D ratios. A digital holography was used to measure the 3D positions of particles in a portion of the micro-tube. Probability density distributions of the particles were then calculated to produce quantitative data of the equilibrium particle positions. Similar to Matas et al. [163], the measurements of Choi and Lee [51] were also taken at a single axial location along the length of the tube. However, in the latter study, the observation location was sufficiently downstream that the measurements were considered fully-developed. These distribution patterns observed in microscale geometries particularly with large particles relative to the tube radius at $Re \geq 1$, coincided with the macroscale results of Segre and Silberberg [219] and Matas et al. [164], and the fully-developed Segre and Silberberg [219]'s single characteristic annulus appeared even for low pipe Reynolds numbers ($Re \sim \mathcal{O}(1)$).

The more recent development of microfluidic chip technology has enabled devices operating at low Reynolds numbers to be used to uncover more information regarding the equilibrium states of particles. A study performed by Hookham [111] in microscale rectangular channels for extremely dilute conditions showed that particles migrate and cluster at two equilibrium locations near the top and bottom walls, located $\sim 0.6-0.7$ of $H/2$ distance away from the channel axis (see figure 2.2c). The large aspect ratios of the rectangular cross-section used in Hookham [111]'s experiments allowed the examination of particle migration in 2D Poiseuille flows. Both velocities and particle concentrations were obtained using a dual-beam laser Doppler anemometer system. Experiments for neutrally-buoyant particles at dilute conditions were performed for low and moderate particle Reynolds numbers ($Re_\mathrm{p} = 10^{-3} - 10^{-1}$) to assess inertial effects. Interestingly, for extremely low Re_p, only a slight increase of particle concentration near the top and bottom walls was observed, but with increasing Re_p, a clear migration was observed which developed along the channel axis. The effect of particle size on these equilibrium locations was tested in Hookham [111]'s study; however, no significant change of the

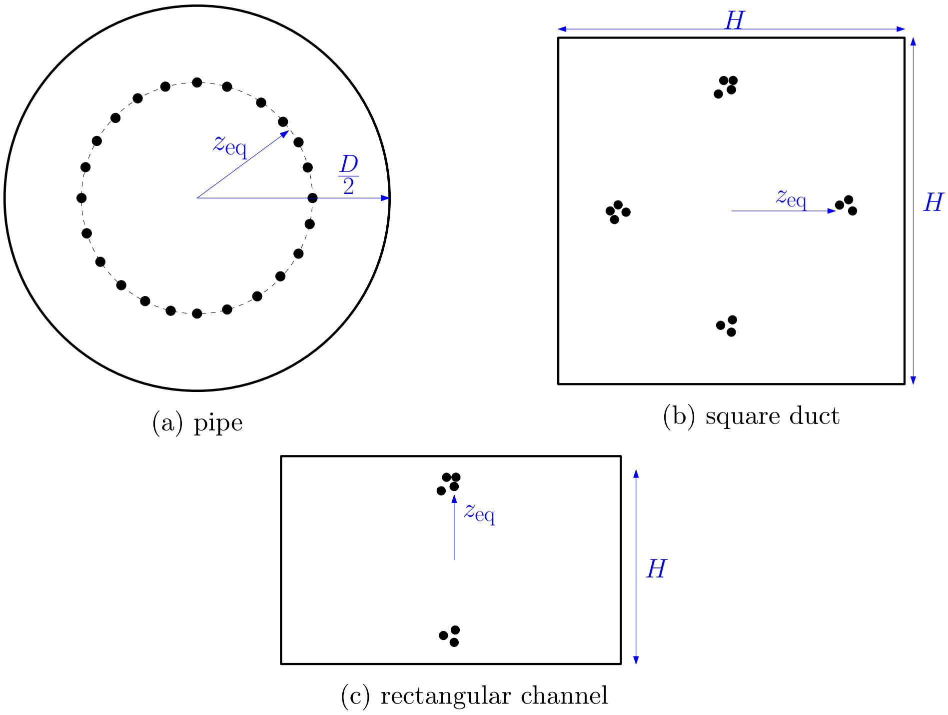

FIGURE 2.2: Schematics of fully-developed, steady-state particle distribution profiles of neutrally-buoyant particles in dilute suspensions ($\phi_b < 0.001$).

equilibrium location was found in their pipe flow study results.

Experiments in square or nearly square cross-section channels produce four peak particle concentration positions, located near and at the centre of channel faces (see Figure 2.2b) for intermediate and large channel Reynolds numbers [1, 24, 50, 69, 127, 178, 228, 254]. Kim and Yoo [127] reported particle distribution profiles for a range of channel Reynolds numbers and particle sizes in nearly square microchannels. An increase in the maximum of the probability density function of the particle distribution with increasing Re indicated a faster migration of particles towards the focusing points as inertia increased. Here, the probability density function represents the ratio between the total number of particles of four hundred images taken at a given height and the total number of particles between channel sidewalls taken at multiple heights but using the same number of images for each measurement. Comparisons with Matas et al. [163] and Choi and Lee [51], suggested that the depletion of particles in the channel centre was much faster in the rectangular geometries than tubes, even for small Reynolds numbers. However, this could be due to particle size or development length effects, rather than a geometrical factor (i.e., tube or square). Bhagat et al. [24] studied particle equilibrium positions in both low aspect rectangular channels (i.e., low depth:width) and square channels, and reported four additional intermediate equilibrium locations near corners of the square channel for $Re > 100$. Di Carlo et al. [69] reported the equilibrium locations of particles using square microchannels for finite inertial flow conditions ($20 < Re < 80$). The influence of the particle size on these equilibrium positions was tested by increasing the particle size until it approaches the channel dimensions. A shift of the equilibrium position of the particles towards the channel centre was observed as the particle size increased, in agreement with most other studies [51, 163].

Abbas et al. [1] examined a series of experiments for neutrally-buoyant particles for low channel Reynolds numbers at dilute conditions. Particle distributions in 2D planes at different heights in the microchannel were obtained using confocal microscope imaging. The results illustrated that particles migrate to the centre for low channel and extremely low particle Reynolds numbers ($Re \sim 10$ and $Re_\mathrm{p} \sim 0.0005$), as inertial effects become insignificant. The plausible explanation for this centre region migration is shear induced diffusion, which happens even under Stokes conditions due to particle interactions. However, when the channel Reynolds number was increased, the particles migrated to four equilibrium locations near the wall as in other studies. Recently, equilibrium position variation with Re was examined by Miura et al. [178] and Shichi et al. [228] for large channel Reynolds numbers. Above a critical channel Reynolds number, these studies reported four additional equilibrium positions near the channel corners similar to Bhagat et al. [24], who showed that this critical Re depends on D/d ratios.

Summarising these discussed observations, in both channel and pipe geometries, figure 2.3 illustrates the variation of dimensionless equilibrium location $z^*_\mathrm{eq}(= 2z_\mathrm{eq}/D_\mathrm{h})$ with the channel/pipe Reynolds number for dilute suspensions. Here z_eq is the distance from channel or pipe axis to the equilibrium location (see figure 2.2). The effect of channel or pipe size to particle size (D_h/d) is also indicated in the figure 2.3. Note that, $D_\mathrm{h} = D$ for pipes and $D_\mathrm{h} = H$ for channels.

Effect of Re

A general shift of peak particle concentration location towards the wall (i.e., increase in z^*_eq) with increasing Re is visible for most experiments [1, 163, 219]. Although this behaviour is apparent for $Re > 100$, some experimental results for low Re (e.g., Choi and Lee [51]'s results for $D_\mathrm{h}/d = 50, 23$ and Kim and Yoo [127]'s results for $D_\mathrm{h}/d = 14.1$) show that z^*_eq decreases with increasing Re. However, for the same low Reynolds numbers

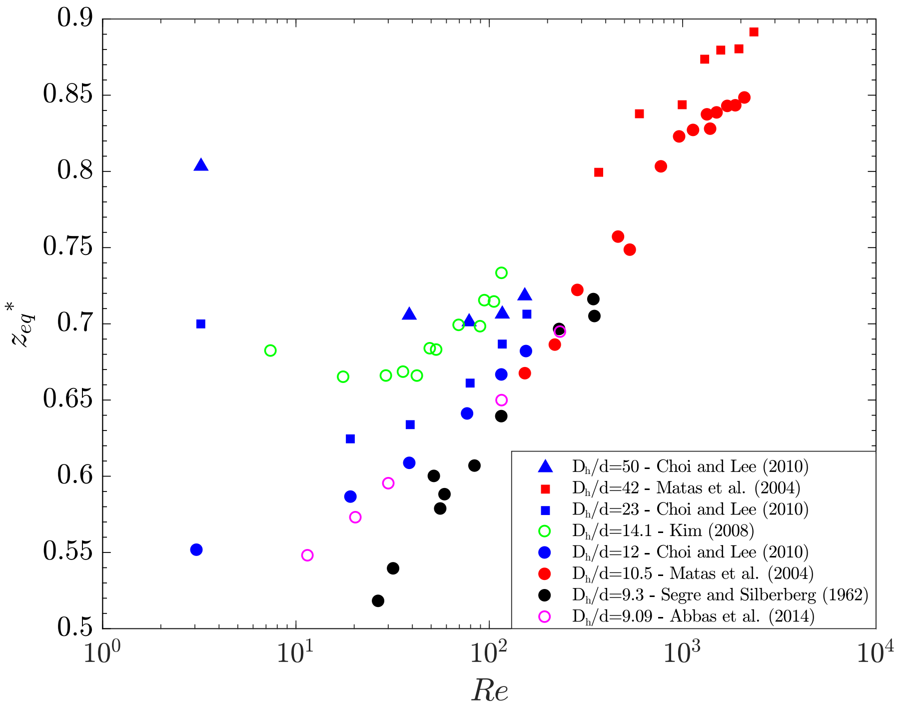

FIGURE 2.3: Variation of the equilibrium position with Re. A comparison of previous dilute suspension studies where $\phi_b < 0.001$. Solid symbols represent pipe flow experiments whereas hollow symbols represent channel flow experiments.

and for low D_h/d ratios (i.e., $9.09 < D_h/d = 12$), z^*_{eq} increases with Re similar to the high Re results.

Effect of channel/pipe to particle size ratio (D_h/d)

Figure 2.3 shows some dependence of channel height or pipe diameter to particle size ratio D_h/d on the equilibrium distance z^*_{eq}, particularly when $Re < 100$. As shown by Matas et al. [163] and Choi and Lee [51] for pipe flow experiments, a decrease of D_h/d has resulted in a shift of equilibrium position towards the axis. Interestingly, experimental work which illustrated a 'twin tubular pinch' effect at relatively high Re and larger development lengths reported that the inner annulus disappears with decreasing D_h/d ratios [181].

Particle development length

In pressure-driven flows, the particle development (entry) length (L_e) determines the minimum length required for a fully-developed solid concentration profile. Hence it is a critical parameter when monitoring particle equilibrium positions. In dilute conditions (or for a single particle), particle development length is much higher than the velocity development length (L_d), which is used to capture the axial velocity profile development. For extremely dilute suspensions, L_e has been estimated theoretically by considering the inertial lift (a force acting on a particle in the direction normal to flow) and with the viscous drag. Following the theoretical study of Asmolov [11], Matas et al. [164] suggested an expression for L_e for $Re < 100$ as,

$$\frac{L_\mathrm{e}}{h} \approx \frac{3\pi}{G_1}\left(\frac{D_\mathrm{h}}{d}\right)^3 \frac{1}{Re} \tag{2.3}$$

where $G_1 \sim 0.2 - 0.3$ for 2D Poiseuille flow [163] and $G_1 \sim 0.07 - 0.2$ for 3D Poiseuille flows [165], and h is the lateral migration distance. For a lateral displacement of half the channel height or tube diameter ($h \sim D_\mathrm{h}/2$) the entrance length can be approximated by $L_\mathrm{e} \sim (3\pi D_\mathrm{h}/2)G_1^{-1}(D_\mathrm{h}/d)^3 Re^{-1} = (3\pi D_\mathrm{h}/2)G_1^{-1}(D_\mathrm{h}/d)Re_\mathrm{p}^{-1}$. However, this estimation is only valid for $d \ll D_\mathrm{h}$. Via experimental and numerical simulations Di Carlo et al. [69] suggested a different lift force scaling for relatively large particles in confined flows, which resulted in a new L_e as,

$$\frac{L_\mathrm{e}}{h} \approx \frac{3\pi}{4G_2}\left(\frac{D_\mathrm{h}}{d}\right)^2 \frac{1}{Re} \tag{2.4}$$

where $G_2 \sim 0.02-0.05$. Similar to the previous results, a minimum particle development length can be estimated via $L_\mathrm{e} \sim (3\pi D_\mathrm{h}/8)G_2^{-1}(D_\mathrm{h}/d)^2 Re^{-1} = (3\pi D_\mathrm{h}/8)G_2^{-1}Re_\mathrm{p}^{-1}$.

Recent studies of Miura et al. [178] and Morita et al. [181] have raised concerns on the selection of the observation location based on L_e. Although many studies [1, 111, 178, 181, 219, 228] have analysed the solid profile development along the pipe/channel length, a few studies [50, 51, 127, 163] have selected a single observation location, based on asymptotic theories to present fully-developed solid distributions. Miura et al. [178] analysed the solid profile developments along a square channel for $Re > 100$ and observed that L_e estimations from Eqs. (2.3) and (2.4) are much smaller than the actual experimental observations. Hence, the authors suggested that the previous estimations

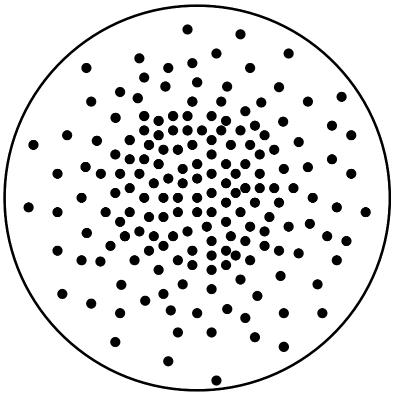

(a) Concentrated suspension ($\phi_\mathrm{b} > 0.2$)

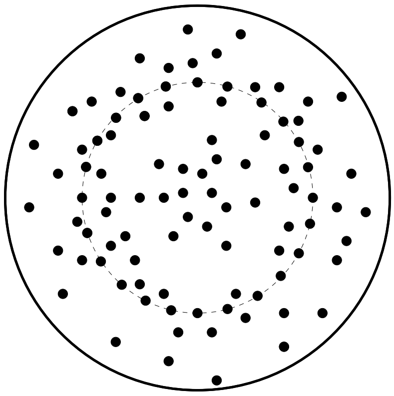

(b) Semi-dilute suspension ($0.001 < \phi_\mathrm{b} < 0.2$)

FIGURE 2.4: Schematics of fully-developed, steady-state particle pipe flow distribution profiles for neutrally-buoyant suspensions.

are only valid for $Re_\mathrm{p} < 1$ and need new correlations to explain the behaviour of particles when $Re_\mathrm{p} > 1$, given that their experiments used $2.4 < Re_\mathrm{p} < 6$. Similarly, Morita et al. [181] suggested that the asymptotic approximations for L_e do not adequately explain the fully-developed solid profiles and the intermediate 'twin tubular pinch' effect under conditions where $Re_\mathrm{p} > 1$.

2.1.1.2 Semi-dilute and concentrated suspensions

Neutrally-buoyant particle migration in semi-dilute and concentrated suspensions ($\phi_\mathrm{b} > 0.01$) has been extensively investigated experimentally for relatively low particle Reynolds numbers ($Re_\mathrm{p} \ll 1$) [85, 101, 102, 111, 123, 128, 153, 221, 231]. Non-uniform concentration distributions observed in most of the studies confirm the presence of cross stream particle migration even in the Stokes limit. In general, parameters such as initial bulk concentration (ϕ_b), particle Reynolds number (Re_p) and particle size to pipe/channel size ratio (a/D_h) were varied in these studies to determine the degree of migration. In addition to these parameters, the particle development length, a critical parameter when drawing conclusions regarding the fully-developed solid distributions, has been investigated in some studies.

Pipe flow studies have been performed for semi-dilute [102] and concentrated conditions [36, 101, 102, 124, 191, 231]. All studies that used concentrated suspensions ($\phi_\mathrm{b} \gtrsim 0.2$) reported an inward particle migration towards the pipe axis (see figure 2.4a). However, early studies of Karnis et al. [124] and Sinton and Chow [231] only showed a very weak migration of particles towards the centre in pipe flows however later, this was explained as the inadequacy of development lengths by Nott and Brady [189]. Hence, subsequent studies [36, 101, 102, 191] used relatively longer tubes in an attempt to capture the developed solid distributions. Hampton et al. [101] reported solid distributions profiles for a range of bulk concentrations, shear rates and particle to tube diameter ratios. For smaller a/D ratios, the solid profiles were sharper and more cusp-like in the centre compared to larger a/D experiments. Further, a faster migration, or otherwise a shorter particle development length, was observed as ϕ_{b} and a/D increased. Following an experimental procedure similar to that of Hampton et al. [101], Oh et al. [191] reported solid distribution profiles for concentrated suspensions with bulk solid volume fractions up to $\phi_{\mathrm{b}} \sim 0.55$ in a pipe. For very dense suspensions ($\phi_{\mathrm{b}} > 0.5$), experimental results demonstrated compaction of particles at the centre of the pipe at the maximum packing fraction of $\phi_{\mathrm{max}} \sim 0.68$. In contrast to concentrated suspension studies, Han [102] examined the particle migration in semi-dilute conditions ($\phi_{\mathrm{b}} \simeq 0.06 - 0.3$). For relatively low concentrations ($\phi_{\mathrm{b}} < 0.1$), the authors observed particle clustering at 0.6 radius away from the pipe centre similar to the 'tubular pinch' effect. However, with increasing ϕ_{b}, more inward particle migration was observed, with only small concentration peaks occurring at 0.6 radius (see figure 2.4b). The balance between inward migration and tubular pinch behaviour was shown to be affected by both ϕ_{b} and Re_{p}.

Similar to pipe flows, channel flow experiments for neutrally-buoyant particles exhibit a clear inward migration of particles, towards the channel axis [85, 111, 128, 153, 221]. By employing rectangular channels with large aspect ratios, these studies ensured a 2D planer Poiseuille flow. Hookham [111] in his thesis first reported particle concentrations for semi-dilute conditions ($\phi_{\mathrm{b}} \sim 0.1$) using rectangular channels. Similar to Han [102]'s observation in pipe flows, Hookham [111] had observed particle clustering at $\sim 0.5H - 0.6H$ away from the channel axis for semi-dilute suspensions. The studies performed for concentrated suspensions, such as Frank et al. [85], Koh et al. [128], Lyon and Leal [153] and Semwogerere et al. [221], only reported an inward migration. The degree of the migration was shown to be dependent of ϕ_{b} and a/H, given that $Re_{\mathrm{p}} < 1$ in the latter studies.

Particle development length

As previously mentioned, the particle development length (L_{e}) represents the axial length required for a solid distribution to become fully-developed. For experimental studies, this is an important parameter when obtaining fully-developed and steady-state particle distribution profiles. In concentrated suspensions with non-Brownian particles, L_e has been shown to be a function of bulk concentration and D_h/d ratio, rather than Re_p [101, 147, 189].

To calculate L_e for concentrated suspensions, two different methods have been used in the literature. The first method uses a shear induced diffusion scaling principle relevant for $Re_\mathrm{p} \ll 1$ [147, 153, 189]. Following Leighton and Acrivos [147], Nott and Brady [189] suggested an approximation for the timescale (t_ss) for a particle to reach its steady-state location (in a Lagrangian sense) by travelling an average distance similar to the order of the channel width. The time was given as $t_\mathrm{ss} \approx H^2/4\mathscr{D}_\mathrm{sid}$, where H and $\mathscr{D}_\mathrm{sid}$ are the width of a rectangular channel and the shear induced diffusivity, respectively. Here, $\mathscr{D}_\mathrm{sid}$ is equal to $\hat{\mathscr{D}}_\mathrm{sid}\gamma_\mathrm{avg}a^2$, where $\hat{\mathscr{D}}_\mathrm{sid}$ is the dimensionless diffusion coefficient and $\gamma_\mathrm{avg}(=\gamma_\mathrm{wall}/2)$ is the average shear rate. Noting that $\gamma_\mathrm{avg} = 3u_\mathrm{avg}/H$ for 2D channel flows, the particle development length was thus given as,

$$\frac{L_\mathrm{e}}{H} \approx \frac{1}{12\hat{\mathscr{D}}_\mathrm{sid}(\phi)}\left(\frac{H}{a}\right)^2 \tag{2.5}$$

For concentrated suspensions ($\phi_\mathrm{b} > 0.3$), Nott and Brady [189] suggested using $\hat{\mathscr{D}}_\mathrm{sid}(\phi) \approx 1$ to obtain approximate estimations for L_e. Owing to the fact that diffusion coefficients $\hat{\mathscr{D}}_\mathrm{sid}(\phi) \sim 0.1 - 1$, Nott and Brady [189] suggested that the effect of the concentration on L_e is fairly insignificant, and hence, suggested the following scaling,

$$\frac{L_\mathrm{e}}{D_\mathrm{h}} \sim \left(\frac{D_\mathrm{h}}{a}\right)^2 \tag{2.6}$$

where $D_\mathrm{h} = H$ for channels and $D_\mathrm{h} = D$ for pipes. Many concentrated suspension studies have used D_h/a of $\mathcal{O}(10) - \mathcal{O}(100)$ and hence require $L_\mathrm{e}/D_\mathrm{h}$ of $\mathcal{O}(10^2) - \mathcal{O}(10^4)$.

The second method of analysing the entry length uses an evolution profile parameter (E_p) to capture the local concentration development along a channel/pipe axis [101, 221]. The definition for E_p was given as [101],

$$E_\mathrm{p}(x) = \frac{1}{A}\int\left|\frac{\phi}{\phi_\mathrm{avg}} - \frac{\phi_\mathrm{ref}}{\phi_\mathrm{avg,ref}}\right| dA \tag{2.7}$$

For a given bulk concentration and D_h/a, E_p varies along the flow axis x, and asymptotes to a constant value with increasing downstream length within pipe/channel. The entrance length, L_e, is defined as the point where E_p reaches 0.95 of its asymptotic value. Based on experimental data, several studies proposed different exponent fittings for E_p as functions of x/D_h to evaluate L_e. In contrast to Eq. (2.6), Hampton et al. [101] observed that L_e depends on ϕ, and suggested that,

$$\frac{L_\mathrm{e}}{D_\mathrm{h}} \sim \left(\frac{D_\mathrm{h}}{a}\right)^{n(\phi)} \tag{2.8}$$

Based on experiments performed for $D_\mathrm{h}/a = 16$, Hampton et al. [101] suggested that the exponent $n(\phi)$ linearly increases from 0.4 to 1.8 for $\phi = 0.2$ to 0.45. For large size ratios ($D_\mathrm{h}/a = 36$) Semwogerere et al. [221] observed $n(\phi) \approx 1$ for $\phi = 0.24$ and $n(\phi) \approx 2$ for $\phi = 0.35$.

Effect of shear rate

For non-Brownian, concentrated suspensions, Hampton et al. [101] and Lyon and Leal [153] reported that the particle concentration profiles are independent of the shear rate, particularly for low particle Reynolds numbers ($Re_\mathrm{p} \ll 1$). Hence, at these conditions, the length to obtain the fully-developed concentration profile can be considered to be independent of the flow rate. However, Semwogerere et al. [221] reported that the particle development length weakly depends on the shear rate for Brownian suspensions.

Velocity profiles

Many pressure-driven flow studies have examined the development of the velocity profiles across the pipes/channels as a function of axial distance. In semi-dilute suspensions, nearly parabolic profiles for axial velocity are observed [101, 111]. However, for concentrated suspensions ($\phi_\mathrm{b} > 0.3$), a significant flattening of the velocity profile near the pipe/channel centre is observed far downstream from the inlet [85, 128, 153, 191, 221]. Authors have explained this flattening is due to the increased effective viscosity of the suspension due to the inward migration of particles.

2.1.2 Drag flows

Some suspension studies used drag flow setups to examine the particle migration. Apparatus such as sliding plates (or moving belts), Taylor-Couette devices, cone-plate devices, and parallel-plate disks devices can be categorised as drag flow setups. Experimentally,

Study	Measurement	Flow device		Suspension	Particle properties			Sus. Fluid	Flow		Obv. Loc.	Ratios	
		type	D_h (mm)	ϕ_b	material	a (μm)	ρ_p (gcm^{-3})	μ_f (mPa s)	Re	Re_γ	L_{obv} m	a/D_h	L_{obv}/D_h
Segre and Silberberg [219]	OS	pipe	11.2	0.005	PMMA	$160-855$	1.178	$17-430$	$3.7-694$	$0.003-16.03$	$0.06-1.2$	$0.0142-0.076$	$5.35-107$
Karnis et al. [123]	OS	pipe	$4-20$	$0.085-0.41$	PVA	$35-280$	1.139	2460	$1-10\times10^{-3}$	$0.1-19\times10^{-4}$	$0.5^{\ddagger}$	$0.06-20$	$1.7-20^{\ddagger}$
Hookham [111]	LDV	rectangular channel	0.8	$0.001-0.3$	polystyrene	$13.5-35$	1.052	$2-92.9$	$0.26-60.9$	$0.00036-0.47$	$0.01-0.3$	$0.014-0.043$	$12.5-370$
Sinton and Chow [231]	NMRI	pipe	$10-50.8$	$0.21-0.52$	PMMA	65.5	1.19	4800	$0.1-14\times10^{-1\dagger\dagger}$	$\sim0.5-70\times10^{-2\dagger\dagger}$	0.5	$0.013-0.04$	$10-33$
Koh et al. [128]	LDV	rectangular channel	$0.785-1.570$	$0.1-0.3$	polystyrene	$15-45.5$	1.05	124	$1.04-4.19\times10^{-1}$	$0.76-27.6\times10^{-4}$	0.127	$0.01-0.057$	$81-162$
Hampton et al. [101]	NMRI	pipe	$50.8, 25.4$	$0.1-0.5$	PMMA	$325-5187.5$	1.181	0.0021	$2.86-5.71$	$1.12-3.74\times10^{-3}$	$0-7$	$0.125-0.0512$	$0-800$
Lyon and Leal [153]	LDV	rectangular channel	$1-1.7$	$0.3-0.5$	PMMA	$350-425$	1.19	480	$2.1-6.2\times10^{-2}$	$0.87-2.1\times10^{-4}$	$0.37-0.47$	$0.021-0.043$	$220-380$
Butler and Bonnecaze [36]	EIT	pipe	20.4	$0.25-0.4$	PMMA	$125-180$	$\sim1.18^{\dagger}$	730	$6.4-133$	$\sim2-20\times10^{-3}$	$2.88-14.72$	$0.006-0.009$	$144-736$
Han [102]	NMRI	pipe	4.6	$0.06-0.4$	PMMA	275	1.188	140	$0.43-12.5$	$6.33-1.8\times10^{-3}$	3	0.06	652
Frank et al. [85]	CM	rectangular channel	0.05	$0.05-0.34$	PMMA	1.1	1.18	1.2	$0.6-40\times10^{-4}$	$1.16-7.7\times10^{-7}$	0.026	0.022	520
Matas et al. [163]	LSS	pipe	8	<0.01	polystyrene	$95-500$	$1.049-1.053$	$1.45-1.55$	$1.34-34\times10^{2}$	$0.08-47$	2.6	$0.012-0.063$	325
Semwogerere et al. [221]	CM	rectangular channel	0.05	$0.1-0.4$	PMMA	0.7	1.05	75.5	0.071	5.56×10^{-5}	0.002	0.014	40
Kim and Yoo [127]	EM	square channel	$0.875-1.41$	0.001	polystyrene	$3-5$	1.05	$1.4-1.5$	$\sim0.13-118$	$\sim6.2\times10^{-4}-0.56$	$0.035-0.06$	0.035	400
Bhagat et al. [24]	EM	sq. & rec. channel	$0.02-0.05$	0.0005	polystyrene	0.95	~0.997	0.89	$2-80$	$0.009-0.36$	$0.004-0.15$	$0.0475-0.019$	$80-7500$
Di Carlo et al. [69]	CM	sq. & rec. channel	$0.02-0.05$	$0.001-0.005$	polystyrene	$5-20$	1.05	~0.89	$20-80$	$0.8-128$	$\sim0.05^{\ddagger}$	$0.1-0.4$	$\sim1000-2500^{\ddagger}$
Choi and Lee [51]	DHM	pipe	0.35	~0.0005	polystyrene	$3.514-15.05$	1.05	0.94	$3.2-154.8$	$0.00128-0.854$	0.3	$0.01-0.041$	860
Choi et al. [50]	DHM	square channel	$0.084, 0.0943$	~0.0005	polystyrene	$7-15$	1.05	0.94	$4.7-120$	$0.00661-0.768$	$0.054-0.06$	$0.075-0.16$	640
Abbas et al. [1]	CM	square channel	0.08	$0.001-0.008$	polystyrene	$2.5-4.35$	1.05	1.5	$0.14-240$	$0.00055-2.84$	$0.01-0.288^{**}$	$0.055-0.031$	$125-3607.5^{**}$
Miura et al. [178]	LSS	square channel	6	$1.6-2.3\times10^{-4}$	polystyrene	325	$1.05-10.54$	$1.62-1.74$	$200-2400$	$2.4-6$	$0.5-4$	0.054	$84-667$
Oh et al. [191]	MRI	pipe	6.3	$0.2-0.55$	polystyrene	70	1.056	3600	$0.5-3\times10^{-7}$	$0.5-3\times10^{-7}$	$1-9$	0.01	$159-1428$
Morita et al. [181]	LSS	pipe	$5.84, 7.75$	$1.1-1.5\times10^{-4}$	polystyrene	$150-325$	1.052	$1.55-1.78$	$200-2200$	$0.54-26.6$	$0.5-4$	$0.052-0.11$	$65-516$
Shichi et al. [228]	LSS	square channel	$0.4-0.8$	$1.3-3.6\times10^{-4}$	polystyrene	$15-35$	$1.052-1.054$	$1.65-1.87$	$1-1600$	$0.012-49$	$0.02-0.6$	$0.0375-0.0875$	$50-750$
Wang et al. [254]	CM	square channel	0.08	$0.1, 0.025\times10^{-2}$	polystyrene	$5.3, 8.44$	1.050	1.5	$11.2-560$	$0.05-3.12$	0.08	$0.033-0.053$	1000

In compiling this table some assumptions have been made regarding experimental parameters † Assumed the material density, under neutrally-buoyant condition.
†† Assumed Re or Re_p are based on maximum velocity or wall shear rates. ‡ Assumed the observation location is the maximum pipe/channel length. ** Obtained corrected values via author communications.

TABLE 2.2: Monodisperse, neutrally-buoyant particle migration (Type A) experimental studies for pressure-driven flows presented in chronological order.

these devices can be more convenient than pressure-driven apparatus in handling due to their geometric simplicity and continuous operation, often requiring only a small amount of suspension. Unlike pressure-driven flows (e.g., a pipe that requires long development length), these drag flow devices can continuously operate for long periods of time to generate steady-state particle distributions.

Here again, we classify the neutrally-buoyant monodisperse experiments as dilute and semi-dilute/concentrated, similar to pressure-driven flow analysis. The suspension speed is characterised by device and particle based Reynolds numbers. The device based Reynolds number definition is provided only for the Taylor-Couette geometry, noting that the majority of experiments utilise this setup. The Taylor-Couette flow Reynolds number (Re_{TC}) is,

$$Re_{\mathrm{TC}} = \frac{(r_{\mathrm{out}} - r_{\mathrm{in}})r_{\mathrm{in}}\omega}{\nu_{\mathrm{f}}} \tag{2.9}$$

where, ω, r_{in} and r_{out} are the angular speed, inner radius and outer radius of the cylinders. For Taylor-Couette flow (TCF) the particle based Reynolds number definition is similar to Eq. (2.2), when γ_{wall} is evaluated by,

$$\gamma_{\mathrm{wall}} = \frac{2\omega r_{\mathrm{out}}^2}{r_{\mathrm{out}}^2 - r_{\mathrm{in}}^2} \tag{2.10}$$

for Couette devices with rotating inner walls and stationary outer walls. Note that for thin-gap Couette flows ($\eta = r_{\mathrm{in}}/r_{\mathrm{out}} \gtrsim 0.8$), $\gamma_{\mathrm{wall}} \approx r_{\mathrm{in}}\omega/(r_{\mathrm{out}} - r_{\mathrm{in}})$.

2.1.2.1 Dilute suspensions

Halow and Wills [99] were the first to report detailed results for the radial migration of a neutrally-buoyant single particle using a thin-gap Taylor-Couette flow system. In their study, the inner cylinder was rotated, and the outer cylinder was held fixed. Given that a thin-gap Couette system produces a nearly constant velocity gradient, theoretical inertial lift models deduced for linear shear flows can be reasonably validated against these experimental results. Halow and Wills [99] observed an equilibrium position of the particles close to the centre line between two walls, but offset slightly towards the inner moving wall (see figure 2.5a). Subsequent theoretical studies [108, 250] explained this offset as a result of the flow curvature and suggested that the midpoint between the

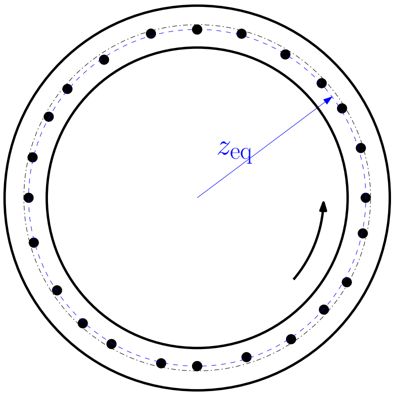

(a) Dilute suspension in thin-gap

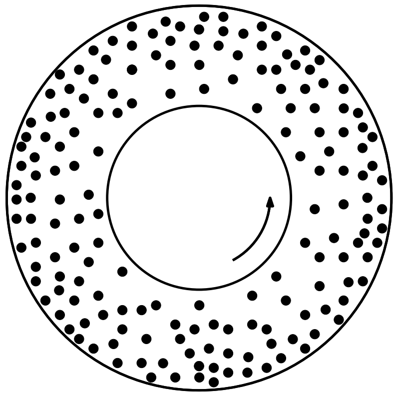

(b) Concentrated suspension in wide-gap

FIGURE 2.5: Schematics of steady-state particle distribution profiles for neutrally-buoyant suspensions in Taylor Couette flow.

two walls could be the equilibrium position for a perfect linear shear flow. From Halow and Wills [99]'s study, the migration velocity of a particle in the Couette system was understood to be a function of particle size and rotational speed of the inner cylinder.

In a recent study Majji and Morris [157] provided transient particle distributions for extremely dilute suspensions using a thin-gap Couette flow device. At low Re_{TC} values (< 80), the particles clustered close to the centre line between the two walls, with a slight offset towards the inner region similar to Halow and Wills [99]'s single particle observations. At larger Re_{TC} values, the flow produced Taylor vortices in the radial-vertical plane, and the particles clustered in circular regions in the radial-vertical plane along fluid streamlines.

2.1.2.2 Semi-dilute and concentrated suspensions

Overall, under both semi-dilute and concentrated conditions ($\phi_{\mathrm{b}} > 0.01$), measurements of the particle concentrations obtained within Taylor-Couette devices [2, 32, 52, 87, 95, 147, 194, 197, 223, 224] clearly show a radial particle migration from high shear rate regions (i.e., moving wall) to lower shear rate regions (i.e., stationary wall) (figure 2.5b).

Eckstein et al. [74] was the first to measure the radial position and development time of tracer particles in a monodisperse suspension using a Couette flow. The authors suggested particle behaviour is determined by shear induced diffusion, a mechanism which is described in §4.2. Later, Gadala-Maria and Acrivos [87] performed a series of experiments for concentrated suspensions using a wide gap Taylor-Couette device. Although direct particle distributions were not obtained via any imaging technique, the authors noted a steady decrease of the suspension effective viscosity with time, suggesting that the suspensions developed a structure based on the anisotropic nature of the suspension. In the later '80s and early '90s, experiments of Abbott et al. [2], Graham et al. [95], Leighton and Acrivos [147] and Phillips et al. [197] directly monitored the evolution of particle distributions and observed radial migration at relatively high bulk concentrations. Based on these observations, Leighton and Acrivos [147] and coworkers explained this effect using shear gradient induced migration. These authors explained that a wide-gap Taylor-Couette device creates a non-linear shear flow with high shear regions at the moving wall, and hence the particles migrate down the gradient in the shear rate and cluster in low shear regions. Abbott et al. [2] demonstrated that the shear induced diffusion migration is irreversible by switching the direction of shearing. This behaviour was again confirmed by Chow et al. [52] using a thin-gap Couette flow. In a very recent study, Sarabian et al. [213] obtained both steady-state and transient concentration profiles for a range of bulk concentrations.

Although these early studies provided particle distribution profiles that are critical to understand the shear induced diffusion, the nuclear magnetic resonance imaging (NMRI) technique does not give information about single particle behaviour. Hence, video image analysis techniques became more popular to obtain microscopic scale measurements of the dynamics of individual particles. In the context of neutrally-buoyant particle migration, Breedveld et al. [32] used a high-resolution CCD camera to obtain shear-induced self diffusion coefficients of particles in thin-gap Couette flows, whereas Shapley et al. [223] used laser Doppler velocimetry (LDV) to obtain collision velocity fluctuations in a thin-gap Couette flow.

Particle migration in very dense suspensions ($\phi_\mathrm{b} > 0.5$) was studied by Ovarlez et al. [194] using a wide-gap Couette flow device at low and intermediate shear rates. Both the velocity and concentration measurements were obtained through magnetic resonance imaging (MRI) techniques to examine particle stresses in both particle jamming and shearing zones. Using a wide-gap Couette flow but with relatively small particles, Gholami et al. [91] studied the kinetics of shear induced migration for suspensions of particles in both Newtonian and non-Newtonian suspending fluids. Gholami et al. [91] also introduced a new technique to study transient volume fraction changes using X-ray/CT-scan systems. This method allowed the authors to use high temporal and spatial resolution

Study	Measurement	Flow device		Suspension	Particle properties			Sus. fluid	Flow		Ratio
		type	B^*	ϕ_b	material	a	ρ_p	μ_f	Re_{TC}	Re_p	a/B
			mm			μm	gcm^{-3}	mPa.s			
Halow and Wills [99]	MIP	thin-gap Couette	5.93 – 18.22	SP	polystyrene	592 – 1699	$\sim$ 1.045	0.0455	1 – 1336	$2.5 - 73 \times 10^{-3}$	0.03 – 0.2
Gadala-Maria and Acrivos [87]†	Optical	wide-gap Couette	2.5	0 – 0.55	polystyrene	40 – 50	1.051	96			0.016 – 0.02
Leighton and Acrivos [147]‡	Optical	thin-gap Couette	20.1	0.05 – 0.4	polystyrene	46 – 87	1.051	107 – 120	0.02 – 104	$0.005 - 18 \times 10^{-3}$	0.012 – 0.0047
Graham et al. [95]	NMRI	wide-gap Couette	19	0.5	PMMA	300	1.185	495	0.11 – 0.24	2.15×10^{-4}	0.013 – 0.016
Abbott et al. [2]	NMRI	wide-gap Couette	17.4 – 22.3	0.39 – 0.6	PMMA	337.5 – 1567.5	1.182	1030 – 4950	0.3 – 1.5	$0.002 - 15 \times 10^{-3}$	0.003 – 0.063
Phillips et al. [197]	NMRI	wide-gap Couette	17.4	0.45 – 0.55	PMMA	50 – 337.5	1.182	4950	0.31	$6.8 - 15 \times 10^{-4}$	0.003 – 0.019
Chow et al. [52]	NMRI	thin-gap Couette	4	0.5	PMMA	90 – 416.5	1.185	4600	0.062	$5 - 64 \times 10^{-2}$	0.025 – 0.088
Breedveld et al. [32]	CCD Cam	thin-gap Couette	68.2	0.2 – 0.5	PVA	45	1.172	3400	0.011	5.44×10^{-7}	0.007
Shapley et al. [223]	LDV	thin-gap Couette	5.95	0.02 – 0.5	PMMA	98	1.183	840	80	1.40×10^{-5}	0.061
Ovarlez et al. [194]	MRI	wide-gap Couette	18.5	0.55 – 0.6	polystyrene	145	1.05	20	0.24 – 105.6	$90 - 112 \times 10^{-4}$	0.008
Majji and Morris [157]	OI	thin-gap Couette	7	0.001	polystyrene	175	1.05	17.6	80	6.07×10^{-2}	0.025
Gholami et al. [91]	X-Ray/ C-T scan	wide-gap Couette	10	0.3 – 0.7	PMMA	57.5	1.19	4.64	0.048	4.24×10^{-6}	0.02
Sarabian et al. [213]	LSS	wide-gap Couette	20	0.2 – 0.5	PMMA	0.79	1.19	4640	0.0114	3.2×10^{-5}	0.04

Here $^*B = r_{out} - r_{in}$. Some studies only provide † viscosity ‡ viscosity and diffusivity measurements.

TABLE 2.3: Monodisperse, neutrally-buoyant (Type A) particle migration experimental studies for Taylor-Couette flows in the chronological order.

to study fast-moving suspensions. Even in the absence of sedimentation, for both Newtonian and non-Newtonian suspending fluids, the concentration profiles varied in the cylinder axis direction. These results illustrated the strong impact of top and bottom boundary effects on migration, and therefore the authors highlighted the necessity of obtaining the full spatial concentration field even in Taylor-Couette geometries. As a result of the fast motion, there is a possibility of Taylor vortex developing due to flow instabilities at higher speeds, which will lead to axial variations of particle distributions.

Overall, experiments in Couette cells for concentrated suspensions, at least those performed for low Re_{TC}, have shown that the steady-state particle distributions are unaffected by the rotational speed (or alternatively the shear rate). However, the transient solid concentration profiles at a given time are different for suspensions with small and large particles, indicating that the migration velocity is a function of a. With decreasing ϕ_{b}, the steady-state particle distribution profiles across the gap width change from a concave shape to a linear shape [194, 197], highlighting the effect of bulk concentration on migration. Noting that many experiments are carried out in Couette flow devices, we summarise these experimental data in table 2.3.

Experimental measurements in the parallel-plate geometry by Chan and Powell [41], Chapman [42] and Chow et al. [52] have reported that a radial concentration gradient is absent at steady-state for both semi-dilute and concentrated suspensions in this device. However, recent studies of Merhi et al. [173] for concentrated suspensions and Kim et al. [126] for semi-dilute have reported very weak particle migration in the radial direction between two rotating parallel-plates. Merhi et al. [173]'s experimental results indicated a weak outward migration of particles in the radial direction for a $\phi_{\mathrm{b}} = 0.4$ concentrated suspension, and showed that the radial concentration gradients are less pronounced for higher bulk concentrations, becoming undetectable for $\phi_{\mathrm{b}} \sim 0.5$. For semi-dilute suspension concentrations of $\phi_{\mathrm{b}} = 0.1 - 0.2$, Kim et al. [126] reported a clear outward migration in the radial direction. [43] conducted experiments for neutrally-buoyant particle suspensions in a cone-plate geometry. The latter results also showed an outward migration of particles in the radial direction, similar to the parallel-plate flows.

Earlier theoretical models that assumed isotropic suspensions behaviour, have failed to predict the observed particle migration in cone-plate and parallel-plate flows. Based on these experimental results, new theoretical models were developed accounting for the anisotropic nature of the suspensions. More complex curvilinear flow geometries such as eccentric cylinders [195, 236] have been used to validate and understand the behaviour of neutrally-buoyant particle migration in complex geometries.

2.2 Monodisperse buoyant suspensions

Representative Type B experimental studies are designed to examine the migration of particles that lead or lag the fluid flow in the presence of the buoyancy force. At very dilute conditions, Type B experiments are commonly used to quantify the particle equilibrium locations in vertical [7, 119, 123, 205, 238], and horizontal [163] channel and pipes. Unlike the neutrally-buoyant particle results explained in §2.1.1.1, results for non-neutrally-buoyant particles in vertical flows at dilute conditions show that the equilibrium position shifts towards the pipe/channel axis when particles are lagging the flow, and towards the wall when particles are leading the flow [7, 119, 123, 205, 238]. This observation is purely due to the slip induced effects rather than the particle size or Re effect on the equilibrium location, which has been discussed for neutrally-buoyant particles (§2.1). In horizontal flows, the negatively buoyant (heavy) particles at dilute condition eventually sediment at the bottom of the pipe. The same Type B experiments, but with particles near a single flat wall are used to analyse the slip induced hydrodynamic lift and drag forces in quiescent [239] and linear shear [241] flows.

When the suspension is concentrated, Type B experiments are largely used to investigate the multi-body effects in shear flows (shear induced migration) under gravitational effects. These experiments, commonly known as viscous re-suspension studies, are used to understand different normal stress components in suspension stresses. The re-suspension experiments have been performed in horizontal pipe flows [5, 188], channel flows [214], parallel-plate flows [43, 146] and cylindrical Taylor-Couette flows [3, 203, 204, 212]. In the absence of shear, Type B experiments with non-Brownian spheres can be broadly classified as batch sedimentation experiments for semi-dilute or concentrated suspensions. Hence, these studies are widely used to obtain and validate empirical correlations for hindered settling velocity as well as the self-diffusivity of a particle falling in a monodisperse suspensions [64, 96, 186, 187, 203].

2.3 Bi-disperse suspensions

Type C and D experiments (bi-disperse suspensions) provide information on size-based segregation and the effects of the particle size on shear induced diffusion, sedimentation and hydrodynamic forces.

At dilute conditions only a few results are available for the Type C experiments with neutrally-buoyant particles. These experiments, conducted in square microchannels, showed that the particle alignments and the migration velocities of individual particles heavily depend on the particle size [88, 243]. At semi-dilute and concentrated conditions, Type C related studies reported size-based segregation in rectangular channel flows [154, 220], pipes [114] and open rectangular chamber [114]. The studies performed in closed chambers reported an enrichment of larger particles in the channel/pipe centre, a flow region with relatively low shear rate. This segregation was more apparent at low bulk concentrations. The Type C studies in wide-gap Couette flow also exhibited similar size-based separation with larger particles accumulating in the lower shear zone near the outer stationary cylinder [95, 114]. However, Type C studies in the parallel-plate geometry [133] displayed that larger tracer particles migrate towards the outer region (a high shear zone) in contrast to the previous experimental observations. In addition to the bi-dispersity, the effect of different concentrations is also analysed at semi-dilute conditions [220]. In the theoretical context, the Type C experiments provide useful information to understand the particle size effect on the shear induced diffusion mechanisms. Hence, these studies have been commonly used to validate analytical normal stress partitioning methods to obtain poly-disperse shear induced diffusion models[253].

Type D experiments with bi-disperse buoyant particles in concentrated suspensions are typically used to examine the particle size effect on viscous re-suspension. A study on bi-disperse negatively-buoyant suspensions sheared in a parallel-plate device reported that the effective diffusivity of the suspension is less than the averaged diffusivity of a monodisperse suspension containing small and large particles [132]. In addition to the size difference, the effect of density difference on re-suspension has been also studied in Couette flow devices using the same size particles [247]. In the absence of shear, Type D experiments for semi-dilute and concentrated suspensions have been used to understand the effects of particle size on the sedimentation velocities [25, 64]. Results of these experiments were used to develop a theoretical framework that describes the sedimentation of poly-disperse systems [233].

2.4 Mapping experiments

Experimental results discussed in §2.1 indicate that bulk concentration, particle size, and flow speed control the solid distributions in suspensions. To understand how these distributions originate, we have examined the forces responsible for particle migration.

Different forces can be present in a suspension. Brownian diffusion force (F_{Brownian}) [40], shear induced diffusion force (F_{sid}) [182], viscous drag force (F_{viscous}) [235] and inertial lift force (F_{inertia}) [45] can be identified as the main forces that are responsible for the migration of neutrally-buoyant, non-colloidal particles in this study. On a single particle basis, these forces scale as;

$$\begin{aligned} F_{\text{Brownian}} &\sim \frac{k_{\text{B}}T}{a} \\ F_{\text{sid}} &\sim \phi^n \mu_{\text{f}} a^2 \gamma \\ F_{\text{viscous}} &\sim \mu_{\text{f}} a^2 \gamma \\ F_{\text{inertia}} &\sim \rho_{\text{f}} a^4 \gamma^2 \end{aligned}$$

where k_{B} and T are the Boltzmann's constant and fluid temperature respectively. Brownian diffusion forces, significant for small particles, originate due to thermal fluctuations. In contrast, shear induced diffusion forces, important for both small and large particles, originate from local shear gradients and concentration gradients. Viscous forces (e.g., drag force) and inertial forces (e.g., lift forces) are mainly due to friction between the fluid layers and the momentum of the fluid, respectively. Brownian diffusion forces are inversely proportional to the particle size and independent of the flow speed (i.e., shear rate). Conversely, shear induced diffusion, viscous drag, and inertial lift forces acting on a particle scale with shear rate and particle size.

Usually to compare these forces, two non-dimensional numbers, known as the particle Reynolds number Re_{p} and Péclet number Pe are used. The particle Reynolds number;

$$\frac{F_{\text{inertia}}}{F_{\text{viscous}}} \sim \frac{\rho_{\text{f}} a^2 \gamma}{\mu_{\text{f}}} = Re_{\text{p}} \tag{2.12}$$

is defined as the ratio between inertial and viscous forces, whereas the Péclet number is the ratio between the viscous and Brownian forces;

$$\frac{F_{\text{viscous}}}{F_{\text{Brownian}}} \sim \frac{6\pi\mu_{\text{f}}a^3\gamma}{k_{\text{B}}T} = Pe \tag{2.13}$$

In suspensions, the solid volume fraction affects the shear induced diffusion forces by influencing the rate of particle collisions. When assuming $n \approx 1$ [189], the ratio between inertial lift and shear induced diffusion force is,

$$\frac{F_{\text{inertia}}}{F_{\text{sid}}} \sim \frac{\rho_{\text{f}}a^2\gamma}{\phi_{\text{b}}\mu_{\text{f}}} = \frac{Re_{\text{p}}}{\phi_{\text{b}}} \tag{2.14}$$

This parameter is a measure of inertial lift forces to shear induced diffusion for non-Brownian particles. The form of this parameter shows that inertial lift forces dominate shear induced diffusion forces, and hence determine particle distributions, when either $\phi_{\text{b}} \to 0$ or $Re_{\text{p}} \to \infty$. Conversely, shear induced diffusion forces dominate inertial lift forces when $\phi_{\text{b}} \to \phi_{\text{max}}$ or $Re_{\text{p}} \to 0$, given that the particle mobility is reducing with increasing bulk concentration (i.e., $Re_{\text{p}} \to 0$ as $\phi_{\text{b}} \to \phi_{\text{max}}$).

2.4.1 Bulk concentration vs. particle Reynolds number

A phase map based on particle Reynolds number and bulk volume fractions is constructed to summarise both pressure-driven and drag flow experimental studies (Figure 2.6). Note that $Pe \gg 1$ for all the selected cases, and hence the data is relevant for non-Brownian particles.

As shown in figure 2.6, the experiments can be qualitatively classified into two groups as well as an overlapping third group, noting that these studies have been generally designed to examine the two different particle migration mechanisms, namely lift induced migration and shear induced diffusion. The first group of experiments (yellow region) includes extremely dilute suspensions at large particle Reynolds numbers ($\phi_{\text{b}} < 10^{-2}$ and $Re_{\text{p}} \gtrsim 10^{-3}$). For these experiments, the ratio given by the Eq. 2.14 is high, and in the context of force, $F_{\text{inertia}} \gg F_{\text{sid}}$. The experiments are commonly used to provide theoretical estimations on inertia driven single particle hydrodynamics. The second group of experiments (pink region) includes concentrated suspensions at low particle Reynolds numbers ($\phi_{\text{b}} > 10^{-2}$ and $Re_{\text{p}} \lesssim 10^{-3}$), and hence $F_{\text{inertia}} \ll F_{\text{sid}}$ and the ratio of Eq. 2.14

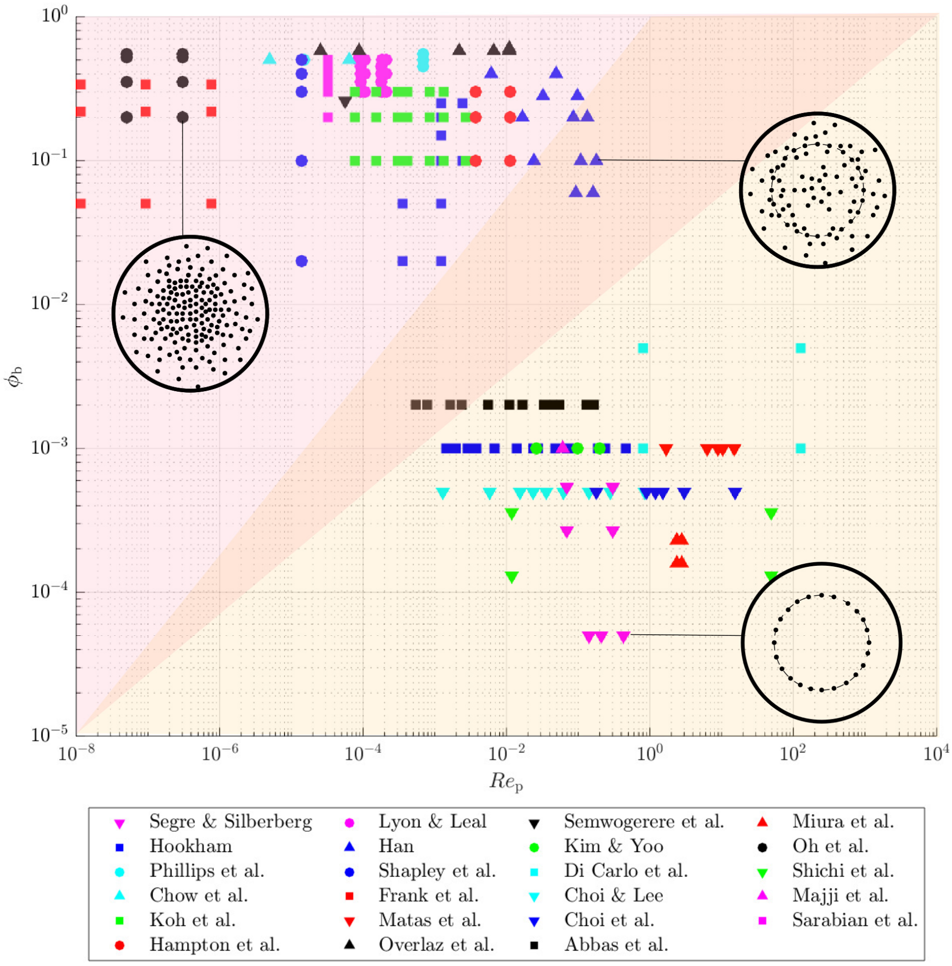

FIGURE 2.6: Phase map of neutrally-buoyant, monodisperse suspension experiments as function of Re_p and bulk concentration ϕ_b.

is low. Hence, these experiments are used to provide theoretical estimations for diffusion driven multi-particle hydrodynamics. Within the third indicated group both F_{inertia} and F_{sid} are relevant. Within each group, solid distribution profiles display common features across similar experimental apparatus. For example, in pipe flows, particles migrate to the centre of the pipe (to lower shear region) for $\phi_b \gtrsim 10^{-1}$ and $Re_p \ll 10^0$, or to a radial equilibrium location for $\phi_b \ll 10^{-3}$ and $Re_p \gtrsim 10^{-1}$ (see figure 2.6). In Couette flows, particles migrate towards the stationary outer wall (to lower shear region) for $\phi_b \gtrsim 10^{-1}$ and $Re_p \ll 1$, or to an equilibrium location between the Couette gap width for $\phi_b \ll 10^{-3}$ and $Re_p \gtrsim 10^{-1}$.

The few experiments plotted in the orange shaded (or overlapping third group) region in figure 2.6 exhibit unique solid distributions that are different from the classical solid distribution patterns observed in the dilute or concentrated regions. For example, Han [102]'s results illustrated equilibrium positions away from pipe walls and pipe centerline for semi-dilute suspensions for the highest reported Re_{p}. Also, at very dilute conditions, Abbas et al. [1]'s results indicated an inward particle migration for the lowest Re_{p} but exhibited a tubular pinch effect type solid distribution pattern with increasing Re_{p}. Since Han [102] has increased Re_{p} to $\mathcal{O}(10^{-1})$ in a relatively concentrated suspension, and Abbas et al. [1] has lowered the Re_{p} to $\mathcal{O}(10^{-4})$ in a very dilute suspension, results of these two studies can be used to explore the effect of Re_{p} on the transition behaviour of the concentration profiles as ϕ_{b} increases.

In the context of forces, as Re_{p} increases in dilute conditions, the inertial lift forces increase relative to drag forces, and particles generally move towards the single particle equilibrium locations. As ϕ_{b} increases the shear induced induced hydrodynamic forces increase, hence diminishing the importance of inertial effects. These diffusion forces act down gradients of shear and concentration and drive particles to lower shear regions (i.e., centre for pipe/channels or stationary outer cylinder in Couette flow). Hence, it is evident that a balance between these forces determines the final solid distribution profile.

2.5 Closure

Non-uniform particle distributions in sheared flows have been experimentally studied from late '60s until the present. These investigations suggest that the lateral motion of particles depends on factors such as nature of suspension (concentrated or dilute), the flow behaviour (Stokes flow or inertial), particle structure (size, rigidity, surface roughness) and properties of suspended fluid (Newtonian or viscoelastic). In this thesis we limit our study to the analyses of rigid, smooth, spherical particles suspended in Newtonian fluids.

Observed neutrally-buoyant particle studies have been broadly classified based on suspension concentration (i.e., dilute and concentrated) and flow configuration (i.e., pressure-driven flows and drag flows), in an attempt to identify the significant forces and mechanisms underpinning the particle migration. These experiments were mostly designed to address single particle hydrodynamics in inertial flows and multi-particle hydrodynamics in non-inertial flows. Different particle equilibrium locations and solid distribution patterns were noticed when increasing suspension concentration for a given particle Reynolds number.

A phase map that classifies experiments based on suspension bulk concentration and particle Reynolds number is developed to understand the migration mechanisms and significant force contributions. The phase map highlights that most experimental studies on particle migration are limited to either dilute-high particle Reynolds number or concentrated-low particle Reynolds number conditions. A few experimental studies that have used intermediate bulk concentrations and particle Reynolds numbers report anomalous solid distributions in the region where both the shear induced diffusion forces and inertial forces are significant. This observation suggests that both inertial lift and shear induced diffusion forces are equally important when quantitatively predicting the particle migration in suspensions.

Chapter 3

Single Particle Hydrodynamics - Theory and Models

The dynamics of single particles depends on the hydrodynamic forces that they experience. As highlighted in the previous chapter, a force that is crucial for clustering of particles at different equilibrium positions in channel and pipe flows is the inertial lift force. Nevertheless, the drag, a force present in both Stokes and inertial flows, is equally as important as the lift force in predicting the migration of particles, as drag can induce slip, and in the presence of wall slip alone (or slip plus shear) can induce a lift force.

In this chapter we outline the previous work related to lift and drag forces acting on rigid spherical particles, and establish the limitations to be addressed in this study. In §3.1, different analytical methods used to solve flow fields and forces are briefly discussed. In §3.2 and §3.3, existing drag and lift models are extensively reviewed. For clarity, the force models are classified as unbounded (ub), wall-bounded outer-region (wb,out) and wall-bounded inner-region (wb,in) considering the wall and particle separation distance. Wall-bounded inner-region-based models consider a particle close enough to a wall such that the viscous effects are more significant than the inertial effects. Wall-bounded outer-region-based models consider a particle located far away from a wall, where both viscous

This chapter is mainly based on the author's papers: Ekanayake, N. I., Berry, J. D., Stickland, A. D., Dunstan, D. E., Muir, I. L., Dower, S. K. & Harvie, D. J. E. (2020). Lift and drag forces acting on a particle moving with zero slip in a linear shear flow near a wall. *Journal of Fluid Mechanics*, 904, A6. and Ekanayake, N. I., Berry, J. D. & Harvie, D. J. E. (2021). Lift and drag forces acting on a particle moving in the presence of slip and shear near a wall. *Journal of Fluid Mechanics* 915, A103.

and inertial effects are significant. The corresponding notation (ub, wb,out and wb,in) will appear in the superscript of each force coefficient.

3.1 Method of solution

To obtain the hydrodynamic forces acting on a particle, first the disturbed flow field around the particle needs to be determined by solving the steady-state Navier–Stokes (N-S) equations. The disturbed flow is generally the difference between the actual flow in the presence of a particle and the undisturbed flow in the absence of any particle. The dimensionless form of the steady-state N-S equations for the disturbed flow around a particle can be written as [81]:

$$\boldsymbol{\nabla} \boldsymbol{\cdot} \bar{\boldsymbol{u}} = 0 \tag{3.1a}$$

$$Re(\boldsymbol{\nabla} \cdot \bar{\boldsymbol{u}} \boldsymbol{\cdot} \bar{\boldsymbol{u}}) = -\boldsymbol{\nabla}\bar{p} + \boldsymbol{\nabla}^2\bar{\boldsymbol{u}} \tag{3.1b}$$

where $\bar{\boldsymbol{u}}$ and $\bar{p}$ are the dimensionless perturbed (disturbed) fluid velocity and pressure due to the presence of the particle and Re is Reynolds number based on some relative characteristic velocity and length scale. In studies that attempt to derive forces via theoretical analysis, the solutions for the perturbed velocity and pressure fields in Eq. (3.1) are commonly represented as series expansions.

When solving the steady-state N-S equations for the disturbed flow field, the solution method depends on the strength of the inertial terms. For zero Reynolds numbers ($Re \to 0$), the inertial terms (the first two terms of the left-hand side of the Eq. 3.1b) disappear, and hence, the N-S equations reduce to the linear Stokes equations. The linearity of the Stokes equation implies that the particles follow the streamlines of the flow since the particle's velocity is aligned with the unperturbed flow [33]. Further, the linearity of the Stokes equation allows several flow fields to be added together (i.e., perturbed velocity and pressure fields due to translation, rotation, shear) to evaluate the net force acting on a particle. When accounting for the inertial terms, three particle Reynolds numbers, namely, the slip (Re_{slip}), shear (Re_γ) and rotational (Re_ω) Reynolds numbers which originate from the relative translation, fluid shear and relative rotation, respectively are commonly employed to solve Eq. (3.1). Here,

$$Re_{\text{slip}} = \frac{|u_{\text{slip}}|a}{\nu}, \qquad Re_{\gamma} = \frac{|\gamma|a^2}{\nu}, \qquad Re_{\omega} = \frac{\omega a^2}{\nu},$$

and u_{slip}, ω, a, ν and γ are the particle slip velocity, particle angular rotation, particle radius, fluid kinematic viscosity and fluid shear rate, respectively corresponding to the flow geometry of figure 3.1. Here, the particle slip velocity refers to the velocity of particle relative to the local undisturbed flow velocity ($u_{\text{slip}} = u_{\text{p}} - u_{\text{f}}$). The shear rate normalised by the slip velocity $\gamma^* = \gamma a/u_{\text{slip}}$, depends on both the slip velocity, and shear rate, with the direction of the lift force determined by the sign of γ^*. These Reynolds numbers can be interpreted as the ratios between the particle radius and the three characteristic lengths of the disturbed flow fields (see figure 3.1).

The characteristic lengths, associated with the disturbances due to translation, shear and rotation are the Stokes length* L_{S}, the Saffman length L_{G} and the rotational length L_{ω}, respectively. Here,

$$L_{\text{S}} = \frac{\nu}{|u_{\text{slip}}|}, \qquad L_{\text{G}} = \sqrt{\frac{\nu}{|\gamma|}}, \qquad L_{\omega} = \sqrt{\frac{\nu}{|\omega|}}$$

These lengths separate the disturbed flow field into two regions: 'inner' and 'outer' regions. The flow region within the closest characteristic length is usually defined as the inner-region ($a < r < \min(L_{\text{S}}, L_{\text{G}}, L_{\omega})$), where the viscous forces are more significant than the inertial forces. The flow domain beyond the inner-region is defined as the outer-region ($r > \min(L_{\text{S}}, L_{\text{G}}, L_{\omega})$), in which the inertial forces associated with the disturbances are greater than the viscous forces.

If the flow is bounded by a wall, the distance between the particle centre and the wall (particle-wall separation distance), l, also becomes another characteristic length of interest. For small but non-zero particle Reynolds numbers, an approximate analytical solution for the flow field is often formulated as regular or singular perturbation problems based on these length scales. In mathematics, the perturbation method finds an approximate solution using a power series of a small parameter, starting from the exact solution of a known simpler problem (i.e., starting from Stokes flow solution). In regular problems, the solution can be approximated by a single asymptotic expansion for the whole problem domain, whereas for a singular value problem, a uniform solution cannot

*In some studies, L_{S} is named as Oseen length.

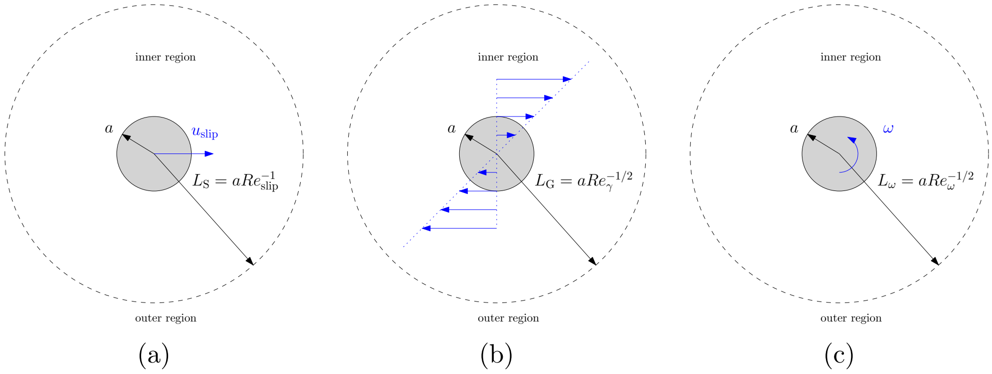

FIGURE 3.1: Schematics of different perturbed unbounded flow fields (a) perturbation due to pure relative translation in a quiescent flow (b) perturbation due to pure shear (c) perturbation due to pure relative rotation in a quiescent flow.

be found via an asymptotic expansion. If the walls are close to the particle and well within the inner-region ($a \leq l \ll \min(L_{\text{S}}, L_{\text{G}}, L_{\omega})$), the flow is considered as a 'regular' problem. Conversely, when the walls are far away from the particle and within the outer-region ($l \gg \min(L_{\text{S}}, L_{\text{G}}, L_{\omega})$), the problem is considered as a 'singular' problem (see figure 3.2). The regular problems are commonly solved using the method of reflection, the method of bipolar coordinates, or the method of tangent sphere coordinates. However, the method of reflections is applicable only when $a \ll l$ and hence fails to predict the disturbed flow when the particle is very close to the wall. Conversely, the method of bipolar coordinates allows the disturbed flow field to be solved when a particle is close to a wall (but not touching), whereas the method of tangent sphere coordinates is applicable when the particle is in contact with the wall. When the problem is singular, the method of matched asymptotic expansions is usually employed to evaluate the flow around the particle.

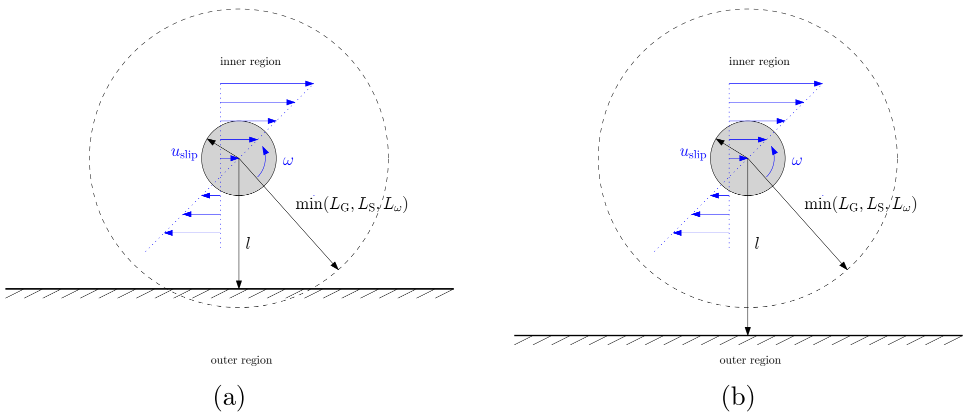

FIGURE 3.2: Schematics of wall-bounded perturbed flows (a) regular perturbation problem (b) singular perturbation problem.

All solution methods developed to solve perturbed flow fields are based on the following assumptions,

- Particles considered are rigid, solid and spherical and satisfy the no-slip boundary condition on their surface.
- All particle based Reynolds numbers are extremely low.
- Suspensions should be dilute, so that hydrodynamic interactions between particles are negligible.

Once the velocity and pressure fields surrounding the particle are determined by employing any method of solution, the forces acting on the particles can be evaluated by integrating the stress acting on the particle.

3.2 Drag force models

Hydrodynamic forces acting on a particle can be decomposed into components parallel and perpendicular to the direction of the relative motion between the particle and the fluid. The former is commonly referred to as the drag force. Given that the relative motion of a particle can be either parallel or normal to a wall, the drag force can also be parallel or normal to walls.

3.2.1 Unbounded flows

In unbounded flows the walls are assumed to be far away from a particle, such that any disturbance due to the walls reduces to zero.

3.2.1.1 Quiescent flows

The drag force acting on a non-rotating rigid sphere translating with a finite slip velocity in an unbounded quiescent flow was first examined by Stokes [235]. The study assumed that $Re_{\mathrm{slip}} \rightarrow 0$ and only considered the inner-region of the disturbed flow to solve the

Stokes equations. Under these approximations the drag force was shown as,

$$F_{\mathrm{D}} = -6\pi\mu a u_{\mathrm{slip}} \tag{3.2}$$

where μ is fluid viscosity and u_{slip} is the scalar particle velocity minus fluid velocity.

Whitehead [255] attempted to extend the Stokes' solution to non-negligible Reynolds numbers by using a regular perturbation scheme. The solutions for the dimensionless perturbed velocity and pressure field in Eq. (3.1) are represented as expansions by considering the zero and first order effects of the Reynolds numbers;

$$\bar{\boldsymbol{u}} = \bar{\boldsymbol{u}}^{(0)} + Re\bar{\boldsymbol{u}}^{(1)} + \mathcal{O}(Re^2) \tag{3.3a}$$

$$\bar{p} = \bar{p}^{(0)} + Re\bar{p}^{(1)} + \mathcal{O}(Re^2) \tag{3.3b}$$

While the zeroth order velocity field ($\bar{\boldsymbol{u}}^{(0)}$) satisfied the boundary conditions at the sphere and infinity and also reduced to the Stokes solution, a solution to the velocity field associated with the first order effects of Reynolds number ($\bar{\boldsymbol{u}}^{(1)}$) was not found. The authors pointed that the boundary conditions of the latter flow field at infinity cannot be satisfied. The inability to extend the Stokes' solution using natural expansion methods was known as *Whitehead's paradox*.

This problem was later addressed by Oseen [193], accounting for a non-rotating rigid sphere translating with a finite slip velocity in an unbounded quiescent flow. Oseen [193] illustrated that at a distance of $aRe_{\mathrm{slip}}^{-1}(= L_{\mathrm{S}})$, the inertial (convective acceleration) terms associated with u_{slip} become comparable to viscous (diffusive) terms in N-S equations and hence that the regular expansion breaks down beyond this limit. The authors also showed that the force solutions based on Stokes solution procedure is only valid for a region surrounding the sphere with a radius of L_{S} (inner-region).

To describe the far field disturbed flow ($r \gg L_{\mathrm{S}}$) which is mainly governed by the advection terms, Oseen [193] used a stretched space variable with respect to Re_{slip} to solve the N-S equations. This approximation is only valid for large distances away from sphere (outer-region). Using this approximation and accounting for the finite inertial terms in the far field of the disturbed flow, Oseen [193] proposed a first order correction for the drag force as,

$$F_{\mathrm{D}} = -6\pi\left(1 + \frac{3}{8}Re_{\mathrm{slip}}\right)\mu a u_{\mathrm{slip}} \tag{3.4}$$

The given analytical solution is only valid for $Re_{\mathrm{slip}} \ll 1$ condition, however, Maxworthy [168] experimentally verified that the Oseen correction (Eq. 3.4) is valid up to $Re_{\mathrm{slip}} = 0.45$. Later, several other studies [94, 234, 244] provided higher order inertial corrections using Re_{slip} terms for the drag force based on the Oseen approximation.

Proudman and Pearson [199] illustrated that in a region defined by the radius of $\mathcal{O}(L_{\mathrm{S}})$, both diffusion and advection are in same order of magnitude and hence neither the Stokes solution nor the Oseen's solutions alone can provide a better estimate for the drag force. Accounting for the flow field at $\mathcal{O}(L_{\mathrm{S}})$, which includes both inner and outer regions, Proudman and Pearson [199] suggested an inertial correlation as,

$$F_{\mathrm{D}} = -6\pi\left(1 + \frac{3}{8}Re_{\mathrm{slip}} + \frac{9}{40}Re_{\mathrm{slip}}^{2}\ln(Re_{\mathrm{slip}}) + \mathcal{O}(Re_{\mathrm{slip}}^{2})\right)\mu a u_{\mathrm{slip}} \tag{3.5}$$

by using a matched asymptotic expansion method valid for small $Re_{\mathrm{slip}} \ll 1$ numbers. However, when the particle slip Reynolds number is increasing, higher order terms of Re_{slip} in Eq. (3.5) become more important in accurately capturing the drag force. Chester et al. [49] extended the analysis of Proudman and Pearson [199] up to the order of $Re_{\mathrm{slip}}^{3}\log Re_{\mathrm{slip}}$, finding a modified drag model. The drag force models based on the matched asymptotic method reduce to Stokes' or Oseen's drag results, depending on the magnitude of Re_{slip}. Of note, these theoretical models are strictly limited to $Re_{\mathrm{slip}} \ll 1$ and their predictions rapidly deviate from the measured drag forces for $Re_{\mathrm{slip}} > 1$. Therefore, when $Re_{\mathrm{slip}} \gtrsim 1$, inertial corrections based on experimental and numerical data are more commonly used to capture the drag force variations the [55, 215]. Among many available models, Schiller [215] and Clift et al. [55] drag models have been extensively used in many studies to capture inertial corrections. The Schiller [215] drag model, valid for $1 < Re_{\mathrm{slip}} < 800$ is,

$$F_{\mathrm{D}} = -6\pi\left(1 + \frac{1}{6}Re_{\mathrm{slip}}^{2/3}\right)\mu a u_{\mathrm{slip}} \tag{3.6}$$

while the Clift et al. [55] drag model, valid for $0.01 < Re_{\text{slip}} < 20$, is

$$F_{\text{D}} = -6\pi\left(1 + 0.1315 Re_{\text{slip}}^{0.82-0.05\log_{10} Re_{\text{slip}}}\right)\mu a u_{\text{slip}} \tag{3.7}$$

More generally the drag force (F_{D}) acting on a spherical particle with a finite slip in an unbounded flow is usually presented as:

$$F_{\text{D}}^{*} = \frac{F_{\text{D}}\rho}{\mu^2} = -\text{sgn}(u_{\text{slip}}) Re_{\text{slip}} C_{\text{D},2}^{\text{ub}}(Re_{\text{slip}}) \tag{3.8}$$

where $C_{\text{D},2}^{\text{ub}}$ is the unbounded drag coefficient. Various theoretical and empirical correlations for $C_{\text{D},2}^{\text{ub}}$, particularly for $Re_{\text{slip}} \lesssim 10$, are listed in table 3.1.

Study	$C_{\text{D},2}^{\text{ub}}(Re_{\text{slip}})$	Limits	Eq.
Stokes [235]	6π	$Re_{\text{slip}} \to 0$	(3.9)
Oseen [193]	$6\pi(1 + 3/8 Re_{\text{slip}})$	$Re_{\text{slip}} \ll 1$	(3.10)
Proudman and Pearson [199]	$6\pi(1 + 3/8 Re_{\text{slip}} + 9/40 Re_{\text{slip}}^2 \ln(Re_{\text{slip}}))$	$Re_{\text{slip}} \ll 1$	(3.11)
Schiller [215]	$6\pi(1 + 1/6 Re_{\text{slip}}^{2/3})$	$Re_{\text{slip}} < 800$	(3.12)
Clift et al. [55]	$6\pi(1 + 0.1315 Re_{\text{slip}}^{0.82-0.05\log_{10} Re_{\text{slip}}})$	$0.01 < Re_{\text{slip}} < 20$	(3.13)

TABLE 3.1: Theoretical and empirical inertial corrections for $C_{\text{D},2}^{\text{ub}}$.

3.2.1.2 Linear shear flows

Non-uniformity of the fluid flow can alter the drag force predicted for a particle translating relative to a uniform fluid flow. Harper and Chang [105] and Miyazaki et al. [179] examined the drag force acting on a particle in an unbounded linear shear flow using the method of matched asymptotic expansions for $Re_{\text{slip}} \ll \sqrt{Re_\gamma} \ll 1$ (or equivalently $L_{\text{G}} \ll L_{\text{S}}$). Miyazaki et al. [179] presented the drag force as,

$$F_{\text{D}}^{*} = -\text{sgn}(u_{\text{slip}}) Re_{\text{slip}} C_{\text{D},2}^{\text{ub}}(Re_{\text{slip}})[1 + 0.0735\sqrt{Re_\gamma}] \tag{3.14}$$

illustrating a weak shear based dependency. For unbounded linear shear flows, numerical studies also showed that the effect of shear on the drag force is extremely weak for small slip Reynolds numbers ($Re_{\text{slip}} \lesssim 1$) [62, 139, 143]. However, for relatively large slip values ($Re_{\text{slip}} > 5$) and $Re_\gamma / Re_{\text{slip}} \sim \mathcal{O}(1)$, a noticeable effect from shear on the drag force occurs [139]. For these large slip velocities theoretical arguments predict the drag as [143]:

$$F_{\mathrm{D}}^{*} = -\mathrm{sgn}(u_{\mathrm{slip}}) Re_{\mathrm{slip}} C_{\mathrm{D},2}^{\mathrm{ub}}(Re_{\mathrm{slip}})[1 + K_0(Re_\gamma / Re_{\mathrm{slip}})^2] \tag{3.15}$$

The numerical results of Kurose and Komori [139] suggested that K_0 is of order of unity for $Re_{\mathrm{slip}} \sim \mathcal{O}(1)$ and $K_0 \simeq 0$ for $Re_{\mathrm{slip}} \ll 1$.

3.2.1.3 Non-linear shear flows

For unbounded non-inertial, non-linear shear flows (i.e., quadratic flows) Faxen [80] derived an extra drag force due to the flow curvature. This shear gradient (γ') induced drag model was presented as [103],

$$F_{\mathrm{D}} = -6\pi\mu a u_{\mathrm{slip}} + \mu\pi a^3 \gamma' \tag{3.16}$$

Here, the shear rate gradient (γ') is based on undisturbed fluid flow velocity and is evaluated at the particle centre. According to Eq. (3.16), a force free ($F_{\mathrm{D}} = 0$) particle translating in an unbounded Poiseuille flow experiences a negative slip velocity of the order $\mathcal{O}(a^2\gamma')$. Hence, this shear rate gradient induced drag force causes neutrally-buoyant particles in channel flows to lag the fluid flow, even when the particle is far away from a wall. This drag force becomes more significant for relatively large particles in flows with large shear rate gradients.

3.2.2 Single wall-bounded models

3.2.2.1 Zero-shear flow

Particle translating parallel to walls

The effect of walls on the drag force was first examined by Faxen [80] using the method of reflection for a particle translating with a finite slip velocity parallel to a wall. The study considered a non-inertial ($Re_{\mathrm{slip}} \to 0$), quiescent ($Re_\gamma = 0$) flow with the walls located in the inner-region of the disturbed flow of the particle. In Faxen's study, the unbounded Stokes drag model, Eq. (3.2) was modified to incorporate wall effects via

[103]:

$$F_{\rm D}^{*} = -{\rm sgn}(u_{\rm slip})Re_{\rm slip}\left[C_{\rm D,2}^{\rm ub}(Re_{\rm slip}) + C_{\rm D,2}^{\rm wb,in}(a/l)\right] \tag{3.17}$$

Here l is the distance between the particle centre and the wall. Thus, the net drag coefficient in a quiescent flow can be written as;

$$C_{\rm D,2} = \frac{F_{\rm D}^{*}}{-{\rm sgn}(u_{\rm slip})Re_{\rm slip}} = C_{\rm D,2}^{\rm ub} + C_{\rm D,2}^{\rm wb,in} \tag{3.18}$$

The wall-bounded drag coefficient derived by Faxen, $C_{\rm D,2}^{\rm wb,in}$ consists of higher order terms of separation distance up to $\mathcal{O}((a/l)^5)$ in the drag force expansion. The model suggested that the drag force near a wall increases as the particle gets closer to the wall.

$$\frac{C_{\rm D,2}^{\rm wb,in}}{6\pi} = \left[1 - \frac{9}{16}\left(\frac{a}{l}\right) + \frac{1}{8}\left(\frac{a}{l}\right)^3 - \frac{45}{256}\left(\frac{a}{l}\right)^4 - \frac{1}{16}\left(\frac{a}{l}\right)^5\right]^{-1} - 1 \tag{3.19}$$

This correlation is in good agreement with experimental data up to $Re_{\rm slip} = 0.1$ [6, 239].

Vasseur and Cox [251] analysed the effects of walls located in the outer-region of the flow disturbance on the drag force. The study considered a quiescent flow and used a method of matched asymptotic expansions together with the Oseen approximation. The integral expression obtained for the drag force by solving the outer-region velocity field was numerically evaluated and plotted as a function of $l/L_{\rm S}$. Two analytical models valid in the limits of $l \ll L_{\rm S}$ and $l \gg L_{\rm S}$ were also suggested in the same study. Later, Takemura [239] suggested an empirical fit for Vasseur and Cox [251]'s outer-region-based wall-bounded drag coefficient. The model was presented as a function of $l/L_{\rm S}$ and considered numerical values up to $l/L_{\rm S} < 10$:

$$C_{\rm D,2}^{\rm wb,out} = 6\pi\left(\frac{a}{l}\right)\left[\frac{9}{16 + 11.13(l/L_{\rm S}) + 0.584\,(l/L_{\rm S})^2 + 0.371(l/L_{\rm S})^3}\right] \tag{3.20}$$

The net drag coefficient under Takemura's outer-region model is obtained by replacing the $C_{\rm D,2}^{\rm wb,in}$ by $C_{\rm D,2}^{\rm wb,out}$ in Eq. (3.18) [239]. The theoretical predictions of $C_{\rm D,2}^{\rm wb,in}$ and $C_{\rm D,2}^{\rm wb,out}$, given via Eq. (3.19) and Eq. (3.20), reduce to zero with increasing separation distance, while the net drag coefficient, $C_{\rm D,2}$, reduces to the unbounded drag coefficient value $C_{\rm D,2}^{\rm ub}$. Note however that as the slip Reynolds number increases, the net drag coefficient predicted using $C_{\rm D,2}^{\rm wb,out}$ tends to reach the unbounded Stokes limit much faster than that predicted via the inner-region $C_{\mathrm{D},2}^{\mathrm{wb,in}}$ (see inset of figure 7.3).

Eqs. (3.19) and (3.20) are specific to the inner and outer-regions, respectively, and hence cannot represent the drag across all separation distances. Based on experimental results at $Re_{\mathrm{slip}} \sim 0.09 - 0.5$, Takemura [239] suggested a modification to $C_{\mathrm{D},2}^{\mathrm{wb}}$ as follows:

$$\frac{C_{\mathrm{D},2}^{\mathrm{wb}}}{6\pi} = \left[1 - \left(\frac{C_{\mathrm{D},2}^{\mathrm{wb,out}}}{6\pi}\frac{l}{a}\right)\left(\frac{a}{l}\right) + \frac{1}{8}\left(\frac{a}{l}\right)^3 - \frac{45}{256}\left(\frac{a}{l}\right)^4 - \frac{1}{16}\left(\frac{a}{l}\right)^5\right]^{-1} - 1 \tag{3.21}$$

In this modification, the 9/16 coefficient of the inner-region model represented by Eq. (3.19) was replaced by $C_{\mathrm{D},2}^{\mathrm{wb,out}}$ to capture the transition behaviour of the $C_{\mathrm{D},2}^{\mathrm{wb}}$ when a particle shifts from the inner to the outer-region.

Particle translating perpendicular to walls

The effect of walls on the drag force for a particle translating with a finite slip velocity perpendicular ($u_{\mathrm{slip},\perp}$) to a wall was examined by Happel and Brenner [103] using the method of reflection. The study considered a non-inertial ($Re_{\mathrm{slip}} \rightarrow 0$) quiescent ($Re_\gamma = 0$) flow with the walls located in the inner-region of the disturbed flow of the particle. The net drag force coefficient component normal to the wall ($C_{\mathrm{D},2,\perp}$):

$$C_{\mathrm{D},2,\perp} = \frac{F_{\mathrm{D},\perp}}{-u_{\mathrm{slip},\perp}\mu a} \tag{3.22}$$

was modified to incorporate wall effects via [103]:

$$C_{\mathrm{D},2,\perp} = C_{\mathrm{D},2,\perp}^{\mathrm{ub}} + C_{\mathrm{D},2,\perp}^{\mathrm{wb,in}} \tag{3.23}$$

where,

$$C_{\mathrm{D},2,\perp}^{\mathrm{ub}} = 6\pi$$

and

$$\frac{C_{\mathrm{D},2,\perp}^{\mathrm{wb,in}}}{6\pi} = \left[1 - \frac{9}{8}\left(\frac{a}{l}\right) + \frac{1}{2}\left(\frac{a}{l}\right)^3 - \frac{135}{256}\left(\frac{a}{l}\right)^4 + \zeta\left(\frac{a}{l}\right)^5\right]^{-1} - 1 \tag{3.24}$$

The original Happel and Brenner [103] model only consists of higher order terms of separation distance up to $\mathcal{O}((a/l)^4)$ (i.e., $\zeta = 0$ in Eq. (3.24)). Later, Fuentes et al. [86] suggested $\zeta = -1/8$, accounting for wall separation distances up to $l/a > 1.5$. This value was further validated by Becker et al. [22] numerically. However, when $\zeta = -1/8$, Eq. (3.24) breaks down for $l/a < 1.15$. Hence, accounting for the implicit solution provided by Happel and Brenner [103], Takemura [239] suggested a value of $\zeta = 39/256$. This was experimentally validated for $l/a > 1.02$ [6]. The model predicts that $C_{\mathrm{D},2,\perp}^{\mathrm{wb,in}} \to \infty$ when $l/a = 1$.

3.2.2.2 Linear shear flow

For wall-bounded linear shear flows, Magnaudet et al. [156] presented an additional contribution to the drag force due to wall-shear applicable to the inner-region of the disturbed flow when $Re_\gamma \ll 1$ and the translation of the particle is parallel to the wall. The force was given by:

$$F_{\mathrm{D}}^{*} = -\mathrm{sgn}(\gamma) Re_\gamma C_{\mathrm{D},1}^{\mathrm{wb,in}}(Re_\gamma, a/l) - \mathrm{sgn}(u_{\mathrm{slip}}) Re_{\mathrm{slip}} C_{\mathrm{D},2}(Re_{\mathrm{slip}}, a/l) \tag{3.25}$$

with the wall-shear based drag coefficient, $C_{\mathrm{D},1}^{\mathrm{wb,in}}$ given as a function of (a/l) as,

$$C_{\mathrm{D},1}^{\mathrm{wb,in}} = \frac{15\pi}{8}\left(\frac{a}{l}\right)^2\left[1 + \frac{9}{16}\left(\frac{a}{l}\right)\right] \tag{3.26}$$

This function reduces rapidly to zero moving away from the wall [156]. Note that a force-free ($F_{\mathrm{D}}^{*} = 0$) particle in a linear shear flow lags the fluid flow near the wall due to the negative slip generated by this shear based wall drag, as explained by Goldman et al. [93] under Stokes flow conditions and by Magnaudet et al. [156] for finite inertial flow conditions.

3.3 Lift force models

Hydrodynamic inertial forces that act perpendicular to the direction of the particle's relative motion are commonly referred to as lift forces. In wall-bounded flows, most studies consider the relative motion of a particle to be parallel to the wall, and hence most studied wall-bounded lift forces are directed normal to the walls.

3.3.1 Unbounded flows

Away from the wall hydrodynamic lift force is an inertia-induced force that reduces to zero for rigid particles in Stokes flow [33]. When inertia is present, a particle that either leads or lags the fluid flow can experience a lift force in unbounded linear shear flows. Accounting for this, Saffman [211] proposed an asymptotic expression for the lift force (F_{L}):

$$F_{\mathrm{L}}^* = \frac{F_{\mathrm{L}}\rho}{\mu^2} = -\mathrm{sgn}(\gamma^*) 2.255 \frac{9}{\pi} Re_\gamma{}^{\frac{1}{2}} Re_{\mathrm{slip}} + \mathrm{sgn}(\gamma^*) \frac{11}{8} Re_\gamma Re_{\mathrm{slip}} - \pi Re_\omega Re_{\mathrm{slip}} \quad (3.27)$$

valid for low slip, shear and rotational Reynolds numbers ($Re_{\mathrm{slip}}, Re_\gamma, Re_\omega \ll 1$). The shear rate normalised by the slip velocity $\gamma^* = \gamma a/u_{\mathrm{slip}}$, depends on both the slip velocity and shear rate. The direction of the lift force is determined by the sign of γ^*. Hence, in a two-dimensional Cartesian flow system, Saffman [211]'s first order lift solution (first term of Eq. (3.27)) predicts a lift force in the direction of increasing fluid velocity ($+y$ direction) for a lagging particle in a positive shear ($u_{\mathrm{slip}} < 0, \gamma > 0$) or for a leading particle in a negative shear ($u_{\mathrm{slip}} > 0, \gamma < 0$), where $\gamma = du_{\mathrm{f,x}}/dy$, and the reader is referred to figure 3.3 for coordinate directions. Hereafter for convenience, any lift force acting in the positive $+y$ direction will be defined as positive. If both the slip and shear have the same sign (i.e., $\gamma^* > 0$), the lift direction reverses and Saffman [211]'s first order lift solution predicts a negative lift force.

Saffman's model is an outer-region-based lift model, in which the boundary of the inner and outer-region is located a distance $\min(L_{\mathrm{G}}, L_{\mathrm{S}})$ from the particle. In addition to the small particle Reynolds number constraints, inertial effects due to shear must be higher than the inertial effects generated by the slip velocity ($\epsilon = \sqrt{|Re\gamma|}/Re_{\mathrm{slip}} \gg 1$ or equivalently $L_{\mathrm{G}} \ll L_{\mathrm{S}}$) for the model to be valid.

The first and second terms on the right hand side of Eq. (3.27) are both due to fluid slip-shear effects, while the third term, similar to the lift model of Rubinow and Keller [210], is due to the particle rotation. Saffman [211] illustrated that the lift force due to rotation is less than that due to the shear by an order of magnitude, unless the rotational speed of a particle is much greater than the shear rate. Since the self induced rotation of a freely-rotating particle was shown to be small compared to the slip-shear lift for the condition $Re_\gamma \ll 1$, many studies neglect the third term when considering a freely

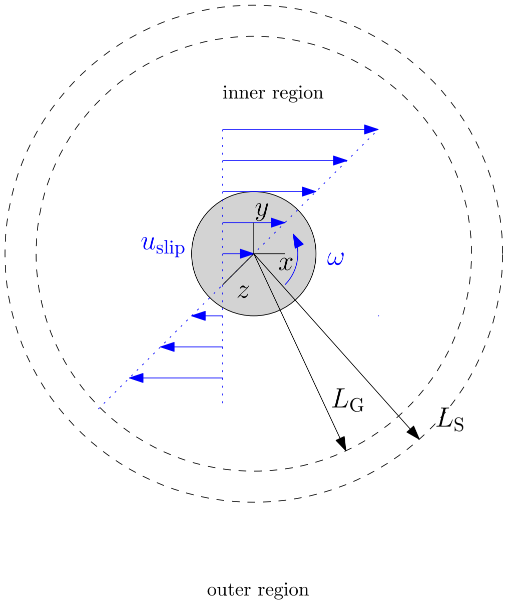

FIGURE 3.3: Schematic of perturbed unbounded flow specific to Saffman problem.

translating and rotating particle. Additionally, the second term in Eq. (3.27) is less important than the first when $\epsilon \gg 1$ [169], and as a consequence, many outer-region studies focus solely on the first term of Eq. (3.27).

Relaxing the constrains of $\epsilon \gg 1$ in Saffman's first order solution and using the Oseen approximation, McLaughlin [169] and Asmolov [10] independently proposed modified unbounded lift models in the form of,

$$F_{\text{L}}^{*} = -\text{sgn}(\gamma^{*})\frac{9}{\pi}Re_{\gamma}^{\frac{1}{2}}Re_{\text{slip}}J(\epsilon) \tag{3.28}$$

valid for non-rotating particles at $Re_{\text{slip}}, Re_{\gamma} \ll 1$. This force can be written in terms of a slip-shear lift force coefficient for unbounded flow, defined by

$$C_{\text{L},2}^{\text{ub}} = \frac{F_{\text{L}}^{*}}{-\text{sgn}(\gamma^{*})Re_{\text{slip}}^{2}} = \frac{9}{\pi}\epsilon J(\epsilon) \tag{3.29}$$

The function $J(\epsilon)$ needs to be evaluated analytically or numerically. Currently available expressions based on asymptotic solutions and empirical fitting functions for $J(\epsilon)$ are presented in table 3.2. These expressions, along with previous direct numerical simulation and experimental results, are plotted in figure 3.4. At the limit $\epsilon \to \infty$ (or equivalently at the limit $Re_{\gamma} \gg Re_{\text{slip}}$), $J(\epsilon)$ reduces to the Saffman's limit of 2.255, whereas $J(\epsilon)$ decreases rapidly as ϵ decreases.

In both the McLaughlin [169] and Asmolov [10] studies the integral expression for $J(\epsilon)$ was evaluated numerically. In addition, McLaughlin [169] also provided two analytical solutions for $J(\epsilon)$ at the limits of $\epsilon \ll 1$ and $\epsilon \gg 1$ (see figure 3.4). The values obtained from numerical evaluations suggested a positive $J(\epsilon)$ for $\epsilon > 0.23$ and a negative $J(\epsilon)$ for $\epsilon < 0.23$. Based on McLaughlin's theoretical results, specifically given for the range $0.1 < \epsilon < 20$, Mei [172] proposed a fitting function for $J(\epsilon)$. In a similar vein, the same integral expression of $J(\epsilon)$ was re-evaluated numerically by Shi and Rzehak [226] who proposed another fitting function to capture both negative and positive values accurately. Note however, these asymptotic solutions derived for $Re_\gamma, Re_{\text{slip}} \ll 1$ may not be valid for larger Reynolds numbers, specifically for the $\mathcal{O}(10^{-1})$ ranges relevant to this study.

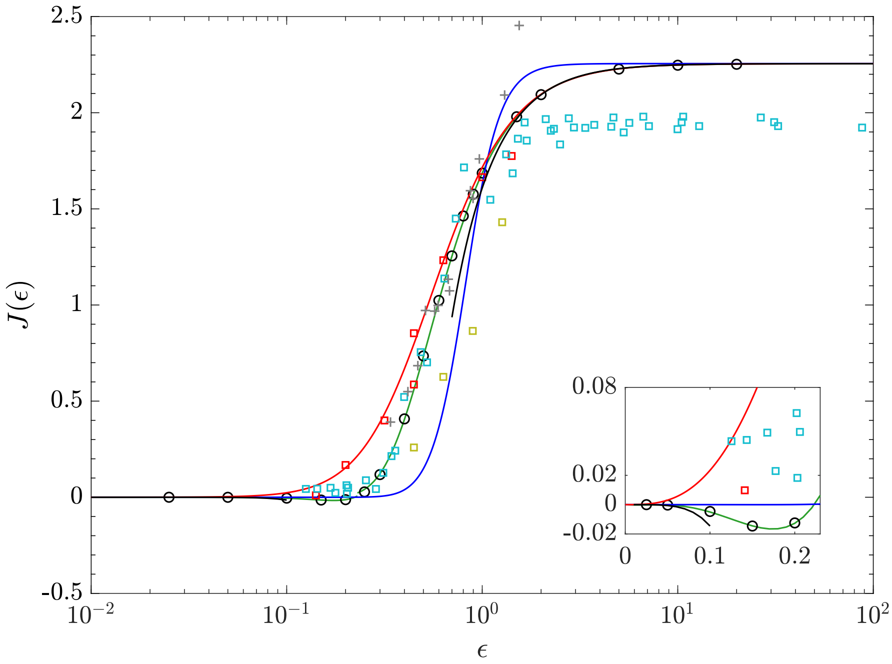

FIGURE 3.4: Comparison of $J(\epsilon)$ values from experimental and DNS data for $Re_{\text{slip}} < 1$ with empirical and theoretical correlations. Asymptotic solution (○) and Asymptotic limits (——) by McLaughlin [169]. DNS: Legendre and Magnaudet [143] (□), Cherukat et al. [48] (□), Kurose and Komori [139] (□). Experiments: Cherukat et al. [47] (+), Empirical fittings by Mei [172] (——), Shi and Rzehak [226] (——) and Legendre and Magnaudet [143] (——).

Direct numerical simulation (DNS) studies, whereby the flow around an individual particle is simulated, provide better estimations of $J(\epsilon)$ for $Re_{\text{slip}}, Re_\gamma \lesssim 1$ in unbounded-linear shear flows, as they do not rely on the Oseen approximation [48, 62, 139, 143]. Dandy and Dwyer [62] performed the first DNS study of the flow around a rigid sphere in an unbounded linear shear flow. However, the values obtained for the lift at small Reynolds numbers were later shown by subsequent DNS studies to be significantly in error due to the small domain size (25 particle radii) employed [48, 143]. Legendre and Magnaudet [143] performed simulations for a clean spherical bubble using large domain sizes (100 particle radii and 200 particle radii [226]). Note that these results for bubble simulations were used to interpret lift forces on rigid spheres by considering the $J(\epsilon)$ function which applies to both bubbles and rigid particles as shown in Legendre and Magnaudet [142]. The numerical data and theoretical estimations from McLaughlin [169] were in good agreement for $\epsilon \geq 0.5$, however, the negative $J(\epsilon)$ values for $0 < \epsilon < 0.23$ predicted by the theoretical studies were not observed. Citing reasons for this discrepancy, Legendre and Magnaudet [143], and later Takemura and Magnaudet [241], explained that the theoretical integral expression obtained for $J(\epsilon)$ is based on the Oseen approximation, which is not sufficiently accurate to evaluate the small lift forces that exists at low shear rates. They illustrated that this approximation cannot capture the higher order terms in the lift force expansion (i.e., second term in Eq. (3.27)) which is important when ϵ is very small ($Re_{\text{slip}} \gg \sqrt{Re_\gamma}$) [143, 169]. Comparing their numerical data with theoretical values, Legendre and Magnaudet [143] suggested that the lower bound of validity in the asymptotic solution is $\epsilon \approx 0.7$. In the same study an empirical fitting for $J(\epsilon)$ was suggested, based on their numerical results for $0.2 < \epsilon < 0.6$ at $Re_{\text{slip}} < 1$ and McLaughlin [169]'s theoretical results for $\epsilon > 0.8$. The resulting correlation predicts a positive lift force for all ϵ values. Both Kurose and Komori [139] and Cherukat et al. [48] performed DNS simulations specifically for a rigid sphere translating in unbounded linear shear flows. Cherukat et al. [48] used large domains (75 and 105 particle radii) and tested for low slip and shear Reynolds number combinations ($0.01 < Re_{\text{slip}} < 1$, $0.01 < Re_\gamma < 0.025$). The computed $J(\epsilon)$ values were positive for all ϵ at $Re_{\text{slip}}, Re_\gamma < 1$ as illustrated in the figure 3.4. However, the results for $\epsilon \geq 2$ deviated from other asymptotic predictions. The discrepancy has been explained as a domain truncation error [48]. Kurose and Komori [139] performed simulations for relatively large slip Reynolds numbers $0.25 < Re_{\text{slip}} < 250$, using relatively small domain sizes (10, 20 particle radii), and founded that the computed $J(\epsilon)$ values agreed well with other numerical studies.

Experimentally, Cherukat et al. [47] investigated the variation of $J(\epsilon)$ at small Re_γ and Re_{slip} numbers in unbounded flows. The migration velocities of a small negatively buoyant particle sedimenting in a linear shear flow were measured. To allow comparison with theory, these migration velocities have been converted to $J(\epsilon)$ values using Eq.(3.28) and Stokes Law, and the results plotted in figure 3.4. As illustrated in the figure, the

Study	$J(\epsilon)$	Limits	Eq.
McLaughlin [169]	$-32\pi^2\epsilon^5 ln(1/\epsilon^2)$	$\epsilon \ll 1$	(3.30)
	$2.255 - 0.6463\epsilon^{-2}$	$\epsilon \gg 1$	
Mei [172]	$0.6765\{1 + \tanh[2.5(lg\epsilon + 0.191)]\}\{0.667 + \tanh[6(\epsilon - 0.32]\}$	$0.2 < \epsilon < 20$	(3.31)
Legendre and Magnaudet [143]	$2.255(1 + 0.20\epsilon^{-2})^{-3/2}$	$0 < \epsilon < 10$	(3.32)
Shi and Rzehak [226]	$-0.04\epsilon + 2.05\epsilon^2 - 32.2\epsilon^3 + 106.8\epsilon^4$	$\epsilon \leq 0.23$	
	$2.255(1 + 0.02304\epsilon^{-2})^{-12.77}$	$\epsilon > 0.23$	(3.33)

TABLE 3.2: Correlations for $J(\epsilon)$.

experimental values for $J(\epsilon)$ closely follow the asymptotic theories up to $\epsilon \sim 1$, but beyond this there is a difference between the two results. Cherukat et al. [47] explained that the inconsistencies between experimental and theoretical values in this region could be due to experimental errors in the measurements of low migration velocities at low Re_{slip}. Consistent with the DNS results, negative $J(\epsilon)$ values were not observed in any of these experiments, specifically for $\epsilon < 0.23$. This again suggests that any analytical solution or empirical correlation based on the Oseen's approximation are not accurate for low ϵ.

For relatively large slip Reynolds numbers with weak shear ($Re_{\text{slip}} \gg Re_\gamma$), a significant change in the lift coefficient and the direction were observed numerically beyond a specific value of Re_{slip} ($Re_{\text{slip}} > 50$) [14, 139]. Accounting for these numerical results, Loth [151] and recently Shi and Rzehak [226] proposed correlations for lift force coefficient, $C_{\text{L},2}^{\text{ub}}$, valid for $Re_{\text{slip}} > 50$. Also, for the inviscid limit ($Re_{\text{slip}} \to \infty$) and weak shear ($Re_{\text{slip}} \gg Re_\gamma$), Auton [13] suggested a theoretical estimation for a rigid spherical particle's lift coefficient.

3.3.2 Single wall-bounded models

3.3.2.1 Outer region

In bounded flows (i.e., near a wall), particles moving at a finite slip velocity experience an additional lift force even in the absence of shear. This wall-slip lift is greatest near the wall and reduces rapidly to zero away from the wall. Note that while a particle slip velocity can be in any direction relative to a wall, in this study we only consider slip-lift due to slip velocity in the direction parallel to a wall.

The wall-slip lift for a spherical particle sedimenting in a quiescent fluid ($Re_\gamma = 0$) with a single wall located in the outer-region ($l > L_\mathrm{S}$) was first investigated by Vasseur and Cox [251]. Singular perturbation techniques were used to determine the migration velocity and the equivalent lift force was then calculated using Stokes law. The deduced lift force valid for $Re_\mathrm{slip} \ll 1$ was given as:

$$F_\mathrm{L}^* = C_{\mathrm{L},3}^{\mathrm{wb,out}}(l/L_\mathrm{S})Re_\mathrm{slip}^2 \tag{3.34}$$

The integral expression for $C_{\mathrm{L},3}^{\mathrm{wb,out}}$ was evaluated numerically as a function of separation distance normalized by Stokes length l/L_S. In the same study, the asymptotic behaviour at small and large values of L_S was obtained analytically considering the inner and outer boundary limits of the outer-region ($l/L_\mathrm{S} \ll 1$ and $l/L_\mathrm{S} \gg 1$ respectively). Although a rotating sphere was originally considered, Vasseur and Cox [251] illustrated that the calculated lift force is independent of rotation as long as the angular velocity is less than $\mathcal{O}(Re_\mathrm{slip})$ in the outer-region. Hence Eq. (3.34) is applicable for a non-rotating sphere as well. Several studies have developed empirical fitting correlations for $C_{\mathrm{L},3}^{\mathrm{wb,out}}$ by solving the integral expression for $C_{\mathrm{L},3}^{\mathrm{wb,out}}$ numerically [227, 239, 240]. These expressions are listed in table 3.3, in addition to the analytical solutions obtained for the asymptotic limits, and the predictions of these correlations show that a leading or lagging particle in quiescent flows always moves away from the wall. Hence the deduced lift coefficient $C_{\mathrm{L},3}^{\mathrm{wb,out}}$ is positive irrespective of the slip velocity direction, but reduces to zero as $l/L_\mathrm{S} \to \infty$.

Vasseur and Cox [251] and later Takemura [239] conducted experiments to measure the migration velocity of a rigid particle sedimenting in a quiescent flow. While the first study obtained migration velocities of a particle falling relatively far away from the wall, the latter study focused mainly on obtaining experimental results for the inner-region. The experimental measurements of Vasseur and Cox [251] obtained mainly for $l/L_\mathrm{S} > 1$ agreed well with the outer-region-based $C_{\mathrm{L},3}^{\mathrm{wb,out}}$ correlations.

The presence of a wall also affects the slip-shear lift force acting on a particle in a linear shear flow. A non-rotating sphere in a single wall-bounded linear shear flow with the wall lying in the outer-region was first investigated by Drew [73], and later by Asmolov [9] and McLaughlin [170]. The latter two studies used the method of matched asymptotic expansions, and considered a leading and a lagging particle in a positive shear field.

Study	$C_{\mathrm{L},3}^{\mathrm{wb,out}}$	Limits	Eq.
Vasseur and Cox [251]	$(9\pi/16)\left[1-11/32(l/L_{\mathrm{S}})\right]$	$l/L_{\mathrm{S}} \ll 1$	(3.35)
	$(9\pi/4)\left[(l/L_{\mathrm{S}})^{-2}+2.21901(l/L_{\mathrm{S}})^{-5/2}\right]$	$l/L_{\mathrm{S}} \gg 1$	
Takemura and Magnaudet [240]	$\left[9\pi/16+2.89\pi\times10^{-6}(l/L_{\mathrm{S}})^{4.58}\right]e^{-0.292(l/L_{\mathrm{S}})}$	$0 < l/L_{\mathrm{S}} < 10$	(3.36)
	$4.47\pi(l/L_{\mathrm{S}})^{-2.09}$	$10 \leq l/L_{\mathrm{S}} < 100$	
Takemura [239]	$18\pi\left[32+2(l/L_{\mathrm{S}})+3.8(l/L_{\mathrm{S}})^2+0.049(l/L_{\mathrm{S}})^3\right]^{-1}$	$0 < l/L_{\mathrm{S}} < 10$	(3.37)
Shi and Rzehak [227]	$(9\pi/16)\left[1+0.13(l/L_{\mathrm{S}})\left((l/L_{\mathrm{S}})+0.53\right)\right]^{-1}$	$0 < l/L_{\mathrm{S}} < 10$	(3.38)
	$4.47\pi(l/L_{\mathrm{S}})^{-2.09}$	$10 \leq l/L_{\mathrm{S}} < 100$	

TABLE 3.3: Numerical correlations for outer-region-based wall-slip lift coefficient $C_{\mathrm{L},3}^{\mathrm{wb,out}}$.

These cases correspond to $\gamma^* > 0$ and $\gamma^* < 0$ respectively. In the outer-region, the effect of rotation was shown to be less significant, and hence the developed models are applicable for both freely-rotating or non-rotating particles. Drew [73] considered the problem in the limit of $\epsilon \gg 1$ while McLaughlin [170] and Asmolov [9] considered a range of ϵ values. Based on the Oseen approximation, an analytical solution for $l \gg L_{\mathrm{G}}$ and $\epsilon \gg 1$ (but not necessarily $Re_{\mathrm{slip}} = 0$) was also provided in the McLaughlin [170] study.

For $Re_\gamma, Re_{\mathrm{slip}} \ll 1$ and $l \gg \min(L_{\mathrm{G}}, L_{\mathrm{S}})$, (i.e., in the outer-region), the wall-bounded slip-lift force can be presented as,

$$F_{\mathrm{L}}^* = -\mathrm{sgn}(\gamma^*)C_{\mathrm{L},2}^{\mathrm{wb,out}}Re_{\mathrm{slip}}^2 \tag{3.39}$$

The numerical values obtained for $C_{\mathrm{L},2}^{\mathrm{wb,out}}$ by solving Airy functions indicated that the unbounded slip-shear lift varies as l/L_{G} changes [9, 170]. For $\epsilon \gg 1$, $C_{\mathrm{L},2}^{\mathrm{wb,out}}$ monotonically reduced from the unbounded values to near zero values for small enough l/L_{G}, irrespective of the sign of γ^*. McLaughlin [170] showed that these near zero values are similar to the outer boundary values of the inner-region solutions of Cox and Hsu [58] when $l/L_{\mathrm{G}} < 1$ and $\epsilon > 1$. Based on the numerical data tabulated in McLaughlin [170], for both $\gamma^* > 0$ and $\gamma^* < 0$, and considering the asymptotic inner-region solution of Cox and Hsu [58] valid for $l^* < L_{\mathrm{G}}^*$, both Takemura et al. [242] and Shi and Rzehak [227] both proposed semi-empirical fits for $C_{\mathrm{L},2}^{\mathrm{wb,out}}$ for $\epsilon > 1$ in the form of:

$$C_{\mathrm{L},2}^{\mathrm{wb,out}} = f(\epsilon, l/L_{\mathrm{G}})C_{\mathrm{L},2}^{\mathrm{ub}} \tag{3.40}$$

Table 3.4 summarises the available theoretical and empirical correlations for $f(\epsilon, l/L_{\mathrm{G}})$.

Study	$f(\epsilon, l/L_{\mathrm{G}})$	Limits	Eq.
McLaughlin [170]	$1 - 1.8778(l/L_{\mathrm{G}})^{-5/3}/J(\epsilon)$	$l/L_{\mathrm{G}} \gg 1, \epsilon \gg 1$	(3.41)
Cox and Hsu [58]	$11/96\pi^2(l/L_{\mathrm{G}})/J(\epsilon)$	$l/L_{\mathrm{G}} \ll 1$	(3.42)
Takemura et al. [242]	$1 - \exp\Big[-\dfrac{11}{96}\pi^2(l/L_{\mathrm{G}})/J(\epsilon)\Big]$	$l/L_{\mathrm{G}} > 1, \epsilon > 1$	(3.43)
Shi and Rzehak [227]	$1 - \exp\Big[-\dfrac{11}{96}\pi^2\dfrac{70}{70+(l/L_{\mathrm{G}})^{1.378}}(l/L_{\mathrm{G}})/\lvert J(\epsilon)\rvert\Big]$	$l/L_{\mathrm{G}} < 15, \epsilon > 1$	(3.44)
	$1 - 1.8778L_{\mathrm{G}}^{-5/3}/\lvert J(\epsilon)\rvert$	$l/L_{\mathrm{G}} \geq 15, \epsilon > 1$	

TABLE 3.4: Numerical correlations for $f(\epsilon, L_{\mathrm{G}})$.

Noting that when shear is negligibly small ($\epsilon \to 0$, or $Re_\gamma \to 0$) the lift contribution should be entirely due to the disturbance produced by the wall and slip effects, several studies attempted to combine Eq. (3.39) and Eq. (3.34), such that $\mathrm{sgn}(\gamma^*)C_{\mathrm{L},2}^{\mathrm{wb,out}}$ tends towards to $C_{\mathrm{L},3}^{\mathrm{wb,out}}$ in the limit of $\epsilon \to 0$. Using Eqs.(3.37) and (3.43) for $C_{\mathrm{L},3}^{\mathrm{wb,out}}$ and $C_{\mathrm{L},2}^{\mathrm{wb,out}}$ respectively, Takemura et al. [242] combined these two coefficients using a fitting function ($f_2(\epsilon, l/L_{\mathrm{S}})$) as below:

$$F_{\mathrm{L}}^* = \Big(-\mathrm{sgn}(\gamma^*)C_{\mathrm{L},2}^{\mathrm{wb,out}} + f_2(\epsilon, l/L_{\mathrm{S}})C_{\mathrm{L},3}^{\mathrm{wb,out}}\Big)Re_{\mathrm{slip}}^2 \tag{3.45a}$$

where

$$f_2(\epsilon, l/L_{\mathrm{S}}) = \exp(-0.22\epsilon^{3.3}(l/L_{\mathrm{S}})^{2.5}) \tag{3.45b}$$

Eq. 3.45a can be expressed as a force coefficient,

$$C_{\mathrm{L},23}^{\mathrm{wb,out}} = \frac{F_{\mathrm{L}}^*}{Re_{\mathrm{slip}}^2} = -\mathrm{sgn}(\gamma^*)C_{\mathrm{L},2}^{\mathrm{wb,out}} + f_2(\epsilon, l/L_{\mathrm{S}})C_{\mathrm{L},3}^{\mathrm{wb,out}} \tag{3.45c}$$

with the lift normalised by the slip Reynolds number. The outer-region-based lift model given by Eq. (3.45) performs well for small and intermediate $\epsilon \gtrsim 1$ [227, 242], however, it is worth noting that this model predicts a zero lift force in the absence of slip which is not the case for non-zero shear rates.

The lift force acting on a spherical particle translating with zero-slip velocity ($Re_{\mathrm{slip}} = 0$ or equivalently $\epsilon = \infty$) in the outer-region of a positive shear flow has also been studied theoretically. Asymptotic studies for $Re_\gamma \ll 1$ [11] find a lift force that decays rapidly to zero with increasing separation distance. This force can be written in the form:

$$F_{\mathrm{L}}^{*} = C_{\mathrm{L},1}^{\mathrm{wb,out}}(l/L_{\mathrm{G}})Re_{\gamma}^{2} \tag{3.46}$$

with results indicating that $C_{\mathrm{L},1}^{\mathrm{wb,out}}$ approaches zero as l/L_{G} increases. Similar to the slip based lift coefficient ($C_{\mathrm{L},3}^{\mathrm{wb,out}}$), the shear based lift coefficient $C_{\mathrm{L},1}^{\mathrm{wb,out}}$ remains positive for both negative and positive shear rates, promoting in particle migration away from the wall.

3.3.2.2 Inner region

Inner-region-based models require a particle to be located close to the wall such that $l \ll \min(L_{\mathrm{G}}, L_{\mathrm{S}})$ and $Re_{\mathrm{slip}}, Re_{\gamma} \ll 1$ [57]. In these models the lift force on both freely-rotating and non-rotating particles is obtained by coupling the two flow disturbances that originate from particle slip and fluid shear in a non-linear manner. These inner-region-based lift models present the lift as [45, 156]:

$$F_{\mathrm{L}}^{*} = C_{\mathrm{L},1}^{\mathrm{wb,in}}Re_{\gamma}^{2} + \mathrm{sgn}(\gamma^{*})C_{\mathrm{L},2}^{\mathrm{wb,in}}Re_{\gamma}Re_{\mathrm{slip}} + C_{\mathrm{L},3}^{\mathrm{wb,in}}Re_{\mathrm{slip}}^{2} \tag{3.47}$$

where the three lift coefficients, $C_{\mathrm{L},1}^{\mathrm{wb,in}}, C_{\mathrm{L},2}^{\mathrm{wb,in}}$ and $C_{\mathrm{L},3}^{\mathrm{wb,in}}$ are functions of separation distance. The first and last terms on the right hand side of Eq. (3.47) originate from the disturbance induced by the presence of the wall in a shear flow field and by the presence of the wall in quiescent flow, respectively. The corresponding lift coefficients $C_{\mathrm{L},1}^{\mathrm{wb,in}}$ and $C_{\mathrm{L},3}^{\mathrm{wb,in}}$ are therefore associated with a force in the absence of slip ($Re_{\mathrm{slip}} = 0$) and a force in the absence of shear ($Re_{\gamma} = 0$), respectively. The second term depends on both the slip velocity and shear rate, and the corresponding coefficient $C_{\mathrm{L},2}^{\mathrm{wb,in}}$ is associated with a force when both the slip and shear are of the same order of magnitude. The first and last terms in Eq. (3.47) produce forces directed away from the wall, promoting positive lift, whereas the lift force due to the second term depends on both slip and shear rate directions, with the direction of this force captured by the sign of (γ^{*}). The available correlations for $C_{\mathrm{L},1}^{\mathrm{wb,in}}$, $C_{\mathrm{L},2}^{\mathrm{wb,in}}$ and $C_{\mathrm{L},3}^{\mathrm{wb,in}}$ are summarised in tables 3.5 - 3.7.

In the theoretical context, Cox and Brenner [57] were the first to obtain an implicit expression for the lift forces in the inner-region by using point force approximations at $l/a \gg 1$. Later Cox and Hsu [58] simplified this analysis and presented closure

Study	$C_{\mathrm{L},1}^{\mathrm{wb,in}}$	Comments	Eq.
Cox and Hsu [58]	$\dfrac{366\pi}{576}$	Non-rotating, $l/a \gg 1$	(3.48)
	$\dfrac{330\pi}{576}$	Freely-rotating, $l/a \gg 1$	(3.49)
Cherukat and McLaughlin [45]	$2.0069 + 1.0575\left(\dfrac{a}{l}\right) - 2.4007\left(\dfrac{a}{l}\right)^2 + 1.3174\left(\dfrac{a}{l}\right)^3$	Non-rotating, $l/a \gtrsim 1$	(3.50)
Cherukat and McLaughlin [46]	$1.8065 + 0.89934\left(\dfrac{a}{l}\right) - 1.961\left(\dfrac{a}{l}\right)^2 + 1.02161\left(\dfrac{a}{l}\right)^3$	Freely-rotating, $l/a \gtrsim 1$	(3.51)
Krishnan and Leighton [131]	1.9680	Non-rotating, $l/a = 1$	(3.52)
	1.6988	Freely-rotating, $l/a = 1$	(3.53)
Magnaudet et al. [156]	$\dfrac{55\pi}{96}\left[1 + \dfrac{9}{16}\left(\dfrac{a}{l}\right)\right]$	Freely-rotating, $l/a \gtrsim 1$	(3.54)

TABLE 3.5: Wall-shear lift coefficients ($C_{\mathrm{L},1}^{\mathrm{wb,in}}$) of inner-region studies.

Study	$C_{\mathrm{L},2}^{\mathrm{wb,in}}$	Comments	Eq.
Cox and Hsu [58][††]	$-\dfrac{66\pi}{64}\left[\left(\dfrac{l}{a}\right) + \dfrac{374\pi}{1056}\right]$	Non-rotating, $l/a \gg 1$	(3.55)
	$-\dfrac{66\pi}{64}\left[\left(\dfrac{l}{a}\right) + \dfrac{443\pi}{528}\right]$	Freely-rotating, $l/a \gg 1$	(3.56)
Cherukat and McLaughlin [45]	$-3.2397\left(\dfrac{l}{a}\right) - 1.1450 - 2.0840\left(\dfrac{a}{l}\right) + 0.9059\left(\dfrac{a}{l}\right)^2$	Non-rotating, $l/a \gtrsim 1$	(3.57)
Cherukat and McLaughlin [46]	$-3.2415\left(\dfrac{l}{a}\right) - 2.6729 - 0.8373\left(\dfrac{a}{l}\right) + 0.4683\left(\dfrac{a}{l}\right)^2$	Freely-rotating, $l/a \gtrsim 1$	(3.58)
Krishnan and Leighton [131]	-5.534	Non-rotating, $l/a = 1$	(3.59)
	-2.091	Freely-rotating, $l/a = 1$	(3.60)
Magnaudet et al. [156]	$\dfrac{-66\pi}{64}\left[\left(\dfrac{l}{a}\right) + \dfrac{443}{528} + \dfrac{52}{55}\left(\dfrac{a}{l}\right)\right]$	Freely-rotating, $l/a \gtrsim 1$	(3.61)

TABLE 3.6: Wall-slip-shear lift coefficients ($C_{\mathrm{L},2}^{\mathrm{wb,in}}$) of inner-region studies.

expressions for lift coefficients with the leading order term proportional to l/a. This model is valid only when the separation distance is large compared to the sphere radius ($l/a \gg 1$). Accounting for the finite size of the particle, several other inner-region studies considered higher order contributions to the flow disturbances, and proposed lift correlations that are valid for a particle almost in contact with the wall ($l/a \gtrsim 1$)

Study	$C_{L,3}^{wb,in}$	Comments	Eq.
Cox and Hsu [58][†]	$\frac{18\pi}{32}$	Non-rotating, $l/a \gg 1$	(3.62)
	$\frac{18\pi}{32}$	Freely-rotating, $l/a \gg 1$	(3.63)
Cherukat and McLaughlin [45]	$1.7716 + 0.2160\left(\frac{a}{l}\right) - 0.7292\left(\frac{a}{l}\right)^2 + 0.4854\left(\frac{a}{l}\right)^3$	Non-rotating, $l/a \gtrsim 1$	(3.64)
Cherukat and McLaughlin [46]	$1.7669 + 0.2885\left(\frac{a}{l}\right) - 0.9025\left(\frac{a}{l}\right)^2 + 0.5076\left(\frac{a}{l}\right)^3$	Freely-rotating, $l/a \gtrsim 1$	(3.65)
Krishnan and Leighton [131]	1.755	Non-rotating, $l/a = 1$	(3.66)
	0.236	Freely-rotating, $l/a = 1$	(3.67)
Magnaudet et al. [156]	$\frac{18\pi}{32}\left[1 + 0.1875\left(\frac{a}{l}\right) - 0.168\left(\frac{a}{l}\right)^2\right]$	Freely-rotating, $l/a \gtrsim 1$	(3.68)

TABLE 3.7: Wall-slip lift coefficients ($C_{L,3}^{wb,in}$) of inner-region studies.

[45, 131, 145, 156]. Unlike for the outer-region models, the rotation has a significant effect on lift coefficients within the inner-region, particularly when the particle is close to the wall. Overall, as the inner-region models require a particle to be close to a wall, these models cannot be used to predict unbounded results as l/a becomes large.

3.3.3 Double wall-bounded models

3.3.3.1 Inner region

The effect of a secondary wall on the lift force, mainly when both walls are located in the inner-region, is discussed in this section. Various double-wall-bounded lift models developed for quiescent flows, 2D linear shear flows, and 2D Poiseuille flows are discussed in this section.

Quiescent flow

A sphere sedimenting in a quiescent flow or a slowly moving uniform flow bounded by two flat walls was first investigated by Vasseur and Cox [250] for small slip Reynolds numbers ($Re_{\mathrm{slip}} \ll 1$). In this study it was assumed that both walls are located well within the inner-region of the disturbed flow field, that is $H \ll L_S$, where, H is the

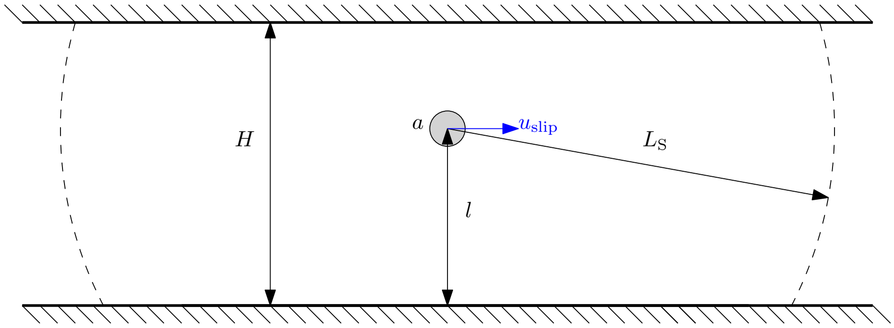

FIGURE 3.5: Schematic representation of a spherical particle translating in a quiescent fluid bounded by two flat walls (both walls are within the inner-region of the disturbed flow).

distance between two flat walls (see figure 3.5). This approximation allowed the authors to utilise Cox and Brenner's method of solution, which solves the inner-region flow using a Stokes expansion. Vasseur and Cox [250] also assumed that the particle is relatively small ($a \ll H$), similar to Cox and Hsu's point force approximation. The migration velocities obtained by solving the flow field using a regular expansion method were plotted as a function of particle separation distance normalised by the channel height ($\check{l} = l/H$). The corresponding lift force coefficient ($C_{\text{L},3}^{\text{dwb,in}} = F_{\text{L}}^{*}/Re_{\text{slip}}^{2}$) obtained via Stokes law ($F_{\text{L}} = 6\pi\mu a u_{\text{mig}}$) can be presented as [81],

$$C_{\text{L},3}^{\text{dwb,in}} = \frac{F_{\text{L}}^{*}}{Re_{\gamma}^{2}} = 6\pi f_{\text{L},3}^{\text{dwb,in}}(\check{l}) \tag{3.69a}$$

Recently, Feuillebois [81] suggested an empirical fitting for $f_{\text{L},3}^{\text{dwb,in}}$ as,

$$f_{\text{L},3}^{\text{dwb,in}}(\check{l}) = -0.312\check{l} - 0.0996\check{l}^{3} + 14.3\check{l}^{5} - 116.3\check{l}^{7} + 403.7\check{l}^{9} - 518.0\check{l}^{11} \tag{3.69b}$$

Due to the secondary wall effect and the symmetry, the lift obtained for double wall-bounded flows rapidly reduce to zero as the particle moves to the centre-line between the two-flat walls (figure 3.8a). This causes particles to migrate away from the walls to an equilibrium position at the channel centre ($\check{l} = 0.5$). Also, the migration is independent of the direction of particle motion. Similar behaviour was experimentally observed for particles sedimenting in quiescent bounded flows (i.e., circular tubes [124, 192]). In addition, these analytical results predict that the migration velocity at walls asymptotes to the single wall-bounded model predictions of Cox and Hsu [58], also deduced under the same $a \ll l$ approximation.

Linear shear flow

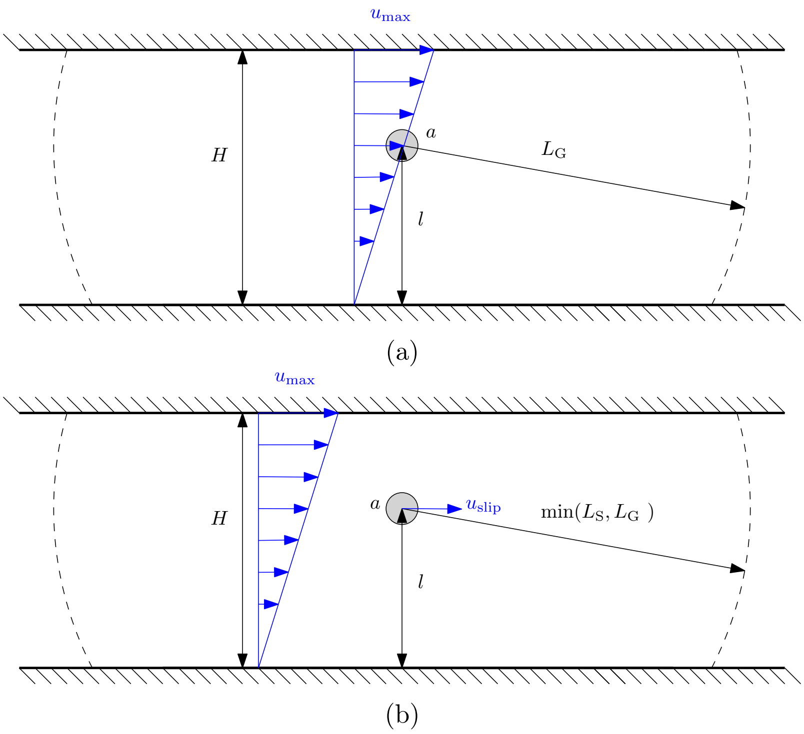

FIGURE 3.6: Schematic representation of a (a) zero-slip (b) finite-slip (buoyant) spherical particle translating in a linear shear fluid bounded by two flat walls where walls are within the inner-region of the disturbed flow.

Vasseur and Cox [250] and Ho and Leal [108] calculated the migration of velocities of neutrally-buoyant (figure 3.6a) and buoyant (figure 3.6b) spheres in linear shear flows for low slip and shear Reynolds numbers ($Re_{\text{slip}}, Re_\gamma \ll 1$). The models were based on the assumption that both walls are located well within the inner-region of the disturbed flow field ($H \ll \min(L_S, L_G)$), in addition to the $a \ll l$ condition. The method of solution is similar to that used for the quiescent flows, in which the the flow equations are solved using regular expansion methods (i.e., method of reflection).

These studies use the term 'neutrally-buoyant' to refer to particles moving with zero-slip, and 'buoyant' to refer to particles moving with a finite slip. However, in reality neutrally-buoyant particles in a linear shear flow experience a finite slip very close to a wall ($l/a \sim 1$), caused by the wall-shear induced drag acting on the particle (a subject of the present study). Hence, the terms 'neutrally-buoyant' and 'zero-slip' (or 'buoyant' and 'finite slip') are not strictly equivalent. Nevertheless, for the conditions considered in these studies, the slip decays rapidly to zero as the distance between the particle and the wall increases [93]. Given that these early models are deduced for the condition $a \ll l$, their interchangeable use of the terms 'zero-slip' and 'neutrally-buoyant' is justified. More generally however, a neutrally-buoyant particle is not necessarily moving at precisely the fluid velocity, and the terms 'zero-slip' and 'neutrally-buoyant' are not equivalent. In the remainder of this thesis we avoid using the terms 'neutrally-buoyant' and 'buoyant' to describe particle slip.

For bounded linear shear flows, the Vasseur and Cox [250] and Ho and Leal [108] studies predict that zero-slip particles migrate towards the channel centre due to a wall-shear lift force that is greatest near the walls but zero at the channel centre. The calculated migration velocities of Vasseur and Cox [250] for zero-slip, freely-rotating particles agreed well with the results of Ho and Leal [108] in the channel centre, but deviated significantly in the vicinity of the wall. As explained by Vasseur and Cox [250], this deviation is due to poor convergence of the numerical computation in the Ho and Leal [108] solution, particularly when the sphere is close to a wall. The same model predictions of Vasseur and Cox [250] agreed well with the asymptotic behaviour suggested by the single wall Cox and Hsu [58] model when the particle is near one of the walls. The corresponding lift force coefficient ($C_{\mathrm{L},1}^{\mathrm{dwb,in}} = F_{\mathrm{L}}^{*}/Re_{\gamma}^{2}$) is,

$$C_{\mathrm{L},1}^{\mathrm{dwb,in}} = \frac{F_{\mathrm{L}}^{*}}{Re_{\gamma}^{2}} = 6\pi f_{\mathrm{L},1}^{\mathrm{dwb,in}}(\check{l}) \tag{3.70a}$$

with an empirical fitting for $f_{\mathrm{L},3}^{\mathrm{dwb,in}}$ based on Feuillebois [81] can be given as,

$$f_{\mathrm{L},1}^{\mathrm{dwb,in}}(\check{l}) = -0.2845\check{l} + 0.4104\check{l}^{3} + 0.4165\check{l}^{5} - 2.3364\check{l}^{7} \tag{3.70b}$$

The predicted zero-slip particle migration in Couette flow agrees substantially with the neutrally-buoyant particle experimental observations of Halow and Wills [99].

Vasseur and Cox [250] also calculated the migration velocity of leading and lagging particles in linear shear flows satisfying $a/H \ll Re_{\mathrm{slip}}/Re_{\gamma} \ll H/a$. The results indicated that the direction of the migration velocity depends on both the slip velocity and shear rate direction. When the particle slip velocity direction is the same as the fluid flow direction, the particle migrates towards the stationary wall, and conversely if the particle slip velocity is opposite to the fluid flow direction, the particle migrates towards the moving wall. In contrast to zero-slip case, these results are independent of particle rotation. The corresponding lift force coefficient ($C_{\mathrm{L},2}^{\mathrm{dwb,in}} = F_{\mathrm{L}}^{*}/Re_{\gamma}Re_{\mathrm{slip}}$) is presented as,

$$C_{\mathrm{L},2}^{\mathrm{dwb,in}} = \frac{F_{\mathrm{L}}^*}{Re_{\mathrm{slip}} Re_{\gamma}} = \mathrm{sgn}(\gamma^*) 6\pi f_{\mathrm{L},2}^{\mathrm{dwb,in}}(\check{l}) \tag{3.71a}$$

with an empirical fitting for $f_{\mathrm{L},2}^{\mathrm{dwb,in}}$ based on Feuillebois [81] can be given as,

$$f_{\mathrm{L},2}^{\mathrm{dwb,in}}(\check{l}) = -0.0353 + 0.0973\check{l}^2 + 0.2898\check{l}^4 - 0.4363\check{l}^6 \tag{3.71b}$$

2D Poiseuille flow

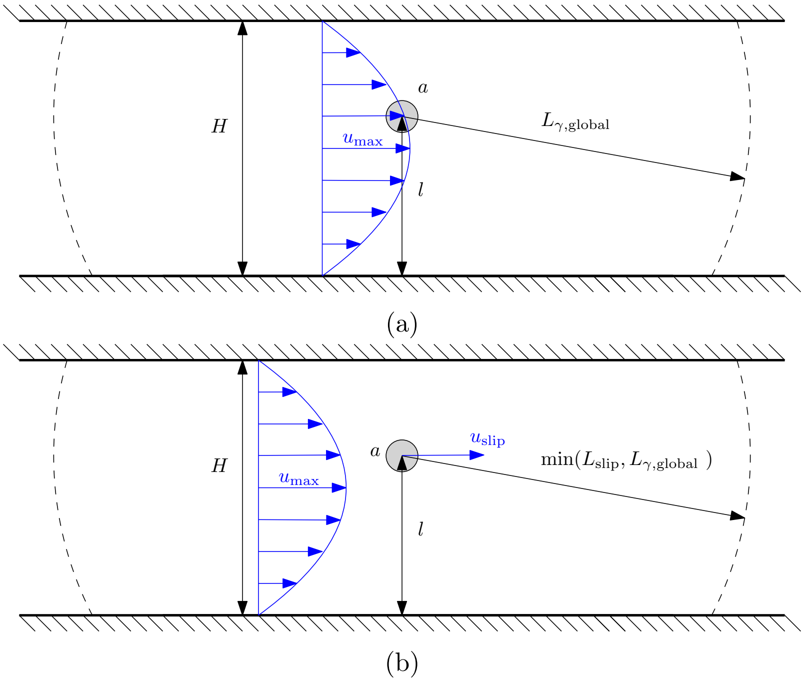

FIGURE 3.7: Schematic representation of a (a) zero-slip (b) finite-slip spherical particle translating in a two-dimensional Poiseuille bounded by two flat walls (both walls are within the inner-region of the disturbed flow).

Ho and Leal [108] and Vasseur and Cox [250] also predicted migration velocities for particles with zero-slip and finite-slip velocities in 2D Poiseuille flows when both walls are in the inner-region. Both studies used regular expansion methods to solve the disturbed flow fields under the $a \ll l$ condition. Unlike in linear shear flows, the local shear rate (γ) in Poiseuille flows varies across the channel. Hence models developed for 2D Poiseuille flows [11, 108, 109, 217, 250] characterise the flow via a global shear rate $\gamma_{\mathrm{g}}(= u_{\mathrm{max}}/H)$

based on the maximum velocity, to define the particle shear Reynolds number:

$$Re_{\gamma,\mathrm{global}} = \frac{\gamma_{\mathrm{g}} a^2}{\nu} = \frac{\gamma_{\mathrm{w}} a^2}{4\nu} = \frac{1}{4} Re_{\gamma|\mathrm{wall}} \tag{3.72}$$

Here, γ_{w} is the wall shear rate. Based on this global shear rate, a new inertial length is defined for parabolic flows as,

$$L_{\gamma,\mathrm{global}} = \frac{a}{|Re^{1/2}_{\gamma,\mathrm{global}}|} = \frac{H}{|Re_{\mathrm{c}}|} \tag{3.73}$$

to determine the inner-region of the flow. Both the Vasseur and Cox [250] and Ho and Leal [108] studies assumed that the particle based slip and channel based Reynolds numbers ($Re_{\mathrm{c}} = (a/H)^2 Re_{\gamma,\mathrm{global}}$) are less than unity ($Re_{\mathrm{slip}}, Re_{\mathrm{c}} \ll 1$) and $H \ll \min(L_{\mathrm{S}}, L_{\gamma,\mathrm{global}})$ when developing force correlations. The corresponding lift force coefficient ($C^{\mathrm{dwb,in}}_{\mathrm{L},1} = F^*_{\mathrm{L}}/Re^2_{\gamma|\mathrm{wall}}$) can be defined as,

$$C^{\mathrm{dwb,in}}_{\mathrm{L},1} = \frac{F^*_{\mathrm{L}}}{Re^2_{\gamma|\mathrm{wall}}} = \frac{6\pi}{16} f^{\mathrm{dwb,in}}_{\mathrm{L},1}(\check{l}) \tag{3.74a}$$

with an empirical fitting for $f^{\mathrm{dwb,in}}_{\mathrm{L},1}$ based on Feuillebois [81] can be given as,

$$f^{\mathrm{dwb,in}}_{\mathrm{L},1}(\check{l}) = (19.85\check{l}(0.31 - \check{l})(0.31 + \check{l})) \tag{3.74b}$$

For zero-slip particles (figure 3.7a), the predicted migration values [108, 250] indicate that a particle always migrates away from walls and also away from the centre plane towards a stable equilibrium position located a distance $0.62(H/2)$ away from the centre of the channel. The migration is known as the 'tubular-pinch' effect, and observed in experimental studies for neutrally-buoyant particles at low Reynolds numbers [111, 219].

Similar to linear shear flows, the calculated migration velocities of Vasseur and Cox [250] deviated significantly from Ho and Leal [108] results in the vicinity of the wall, but agreed well with the results of Ho and Leal [108] in the channel centre (figure 3.8d). Nevertheless, the model predictions of Vasseur and Cox [250] agreed well with the asymptotic behaviour suggested by the single wall Cox and Hsu [58] model when the particle is near one of the walls.

Vasseur and Cox [250] calculated migration velocities for leading and lagging particles in 2D Poiseuille flows. Interestingly, for leading particles translating in the same direction as the flow (figure 3.7b), Vasseur and Cox [250] predicted migration towards the walls. Conversely, for lagging particles, the same model predicted migration towards to the channel centre. The corresponding lift force coefficient, $C_{\mathrm{L},2}^{\mathrm{dwb,in}}$, can be defined as,

$$C_{\mathrm{L},2}^{\mathrm{dwb,in}} = \frac{F_{\mathrm{L}}^{*}}{Re_{\mathrm{slip}} Re_{\gamma|\mathrm{wall}} (H/a)} = \frac{6\pi}{4} \frac{H}{a} f_{\mathrm{L},2}^{\mathrm{dwb,in}}(\check{l}) \tag{3.75a}$$

with an empirical fitting for $f_{\mathrm{L},2}^{\mathrm{dwb,in}}$ based on Feuillebois [81] can be given as,

$$f_{\mathrm{L},2}^{\mathrm{dwb,in}}(\check{l}) = (1.15\check{l}(0.5+\check{l})(0.5-\check{l})(1-1.1681(0.5+\check{l})(0.5-\check{l}))) \tag{3.75b}$$

Qualitative agreement of theoretical predictions with experimental data has been shown for both channel [205] and tube flows [119].

A schematic showing the stable equilibrium positions of spherical particles translating in double wall-bounded flows is given in figure 3.9, adapted from the work of Feuillebois [81].

3.3.3.2 Outer region

The effect of a secondary wall on the lift force, when one wall is located in the outer-region, has rarely been studied. Vasseur and Cox [251] calculated the migration velocity of a particle sedimenting in a quiescent fluid when the second wall is a large distance from the particle so that the wall lies within the outer-region of expansion. The study used the method of matched asymptotic expansions to solve the flow field. Similar to the inner-region models, this outer-region based model predicted that particles migrate away from the walls until it reaches an equilibrium position in the centre plane.

The migration within channel flows for Reynolds number Re_{c} less than 100 was investigated by Schonberg and Hinch [217] for zero-slip and by Hogg [109] for finite-slip particles when $Re_{\mathrm{slip}}, Re_{\gamma,\mathrm{global}} \ll 1$. These studies considered both inner and outer-region expansions and used the method of matched asymptotic expansions to include inertial effects. Both studies showed that the Vasseur and Cox [250] model is valid up to $Re_{\mathrm{c}} \sim 30$ for small particle Reynolds numbers. Later, Asmolov [11] extended these results up to $Re_{\mathrm{c}} = 1000$ and observed a shift in the 'tubular pinch' equilibrium position towards the wall for 2D Poiseuille flow. In these analytical studies all particle based Reynolds

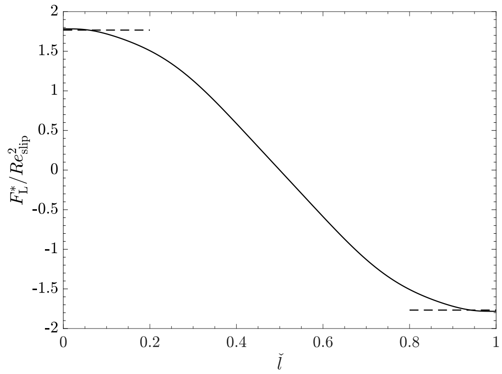

(a) particle sedimenting in a quiescent flow

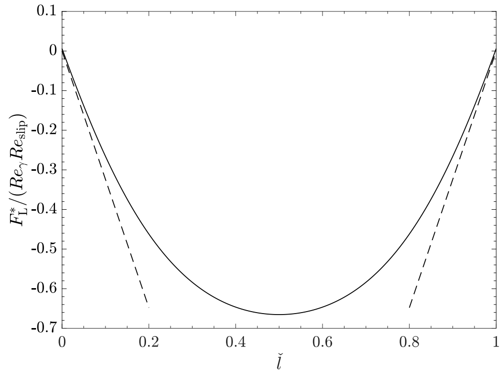

(b) zero-slip particle in linear shear flow

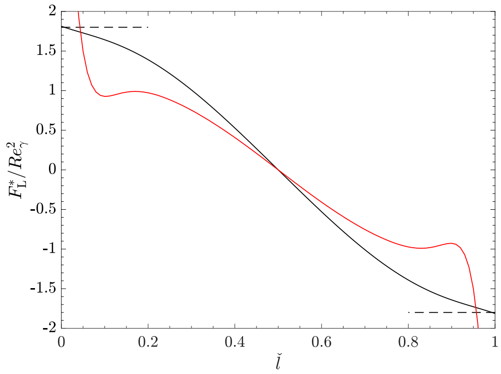

(c) finite-slip particle in linear shear flow

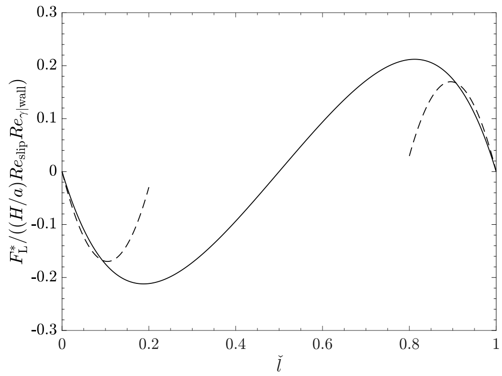

(d) zero-slip particle in 2D Poiseuille flow

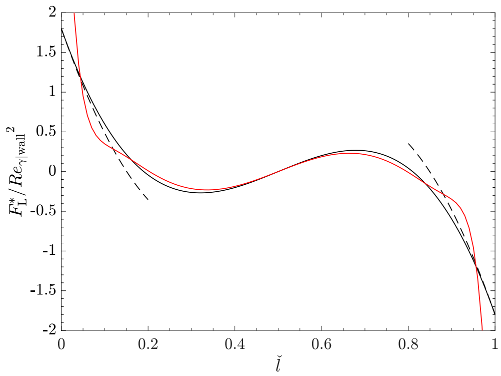

(e) finite-slip particle in 2D Poiseuille flow

FIGURE 3.8: Inner-region based lift coefficients as a function of normalised wall separation distance for particles bounded by two flat walls. Particle velocity and particle slip velocity is in the same direction as flow Vasseur and Cox [250] (——), Ho and Leal [108] (——) and asymptotic values of Cox and Hsu [58] (- - -).

numbers are considered as less than unity. Further, direct numerical studies on planar Poiseuille performed for neutrally-buoyant particles when $Re_{\gamma,\text{global}} \sim \mathcal{O}(10^{-1})$ [12, 110] and experimental studies for $Re_{\gamma,\text{global}} \sim \mathcal{O}(10^1) - \mathcal{O}(10^2)$ [163, 178] have confirmed these theoretical results.

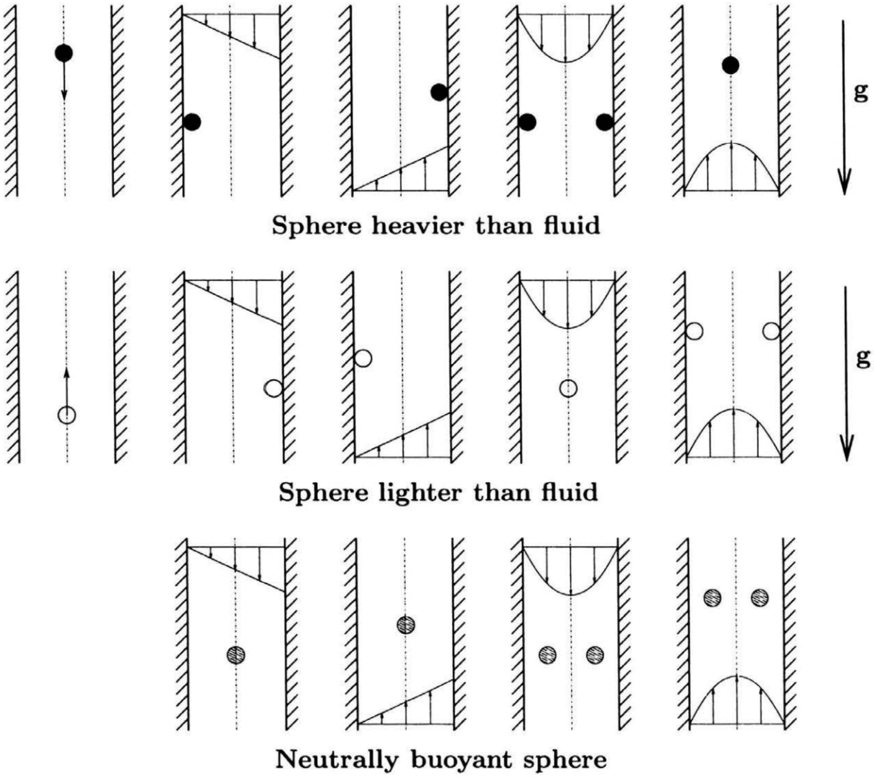

FIGURE 3.9: Schematic representation of the stable equilibrium positions of spherical particle in quiescent flow, linear shear flow and Poiseuille flows predicted by the inner-region models. Adopted from Feuillebois [81]).

3.4 Closure

Different solution methods and theoretical hydrodynamic force models relevant to the migration of single particles are discussed in this chapter. These studies have examined the importance of the particle slip and fluid shear when predicting lift and drag forces. However, most theoretical hydrodynamic force models are limited to low particle slip and shear Reynolds numbers ($Re_\gamma, Re_{\text{slip}} \ll 1$).

Practically relevant applications (i.e., biological flows, microfluidics and shear-enhanced membrane) have small but finite slip and shear Reynolds numbers ($Re_\gamma, Re_{\text{slip}} < 0.1$). Hence, inaccuracies resulting from the assumptions, limitations, and simplifications considered in the theoretical studies could be significant for many applications. For example, as indicated in figure 3.10, there is no analytical model that can be applied predicting the lift force on a rigid particle across both the inner and outer regions of the flow. Further, most models that are valid when the wall resides in the outer-region fail to predict any lift in the absence of a particle slip. Also, given that all listed analytical models are valid only for low shear and slip Reynolds numbers ($Re_\gamma, Re_{\text{slip}} \ll 1$) the models do not capture the finite inertial effects accurately, particularly within the inner region.

To account correctly for inertial effects at any separation distances between the particle and wall, a new lift model will be developed in the subsequent chapters in Part II of this thesis that:

- captures the transition behaviour of lift force coefficients when a particle shifts from the inner to the outer region and is therefore valid for any wall-particle separation distances.
- is applicable for any slip and shear based particle Reynolds number ranging from $0 < Re_\gamma, Re_{\text{slip}} \leq \mathcal{O}(10^{-1})$.

The new model will be shown to overcome the shortcomings of the existing single wall-bounded theoretical models identified above.

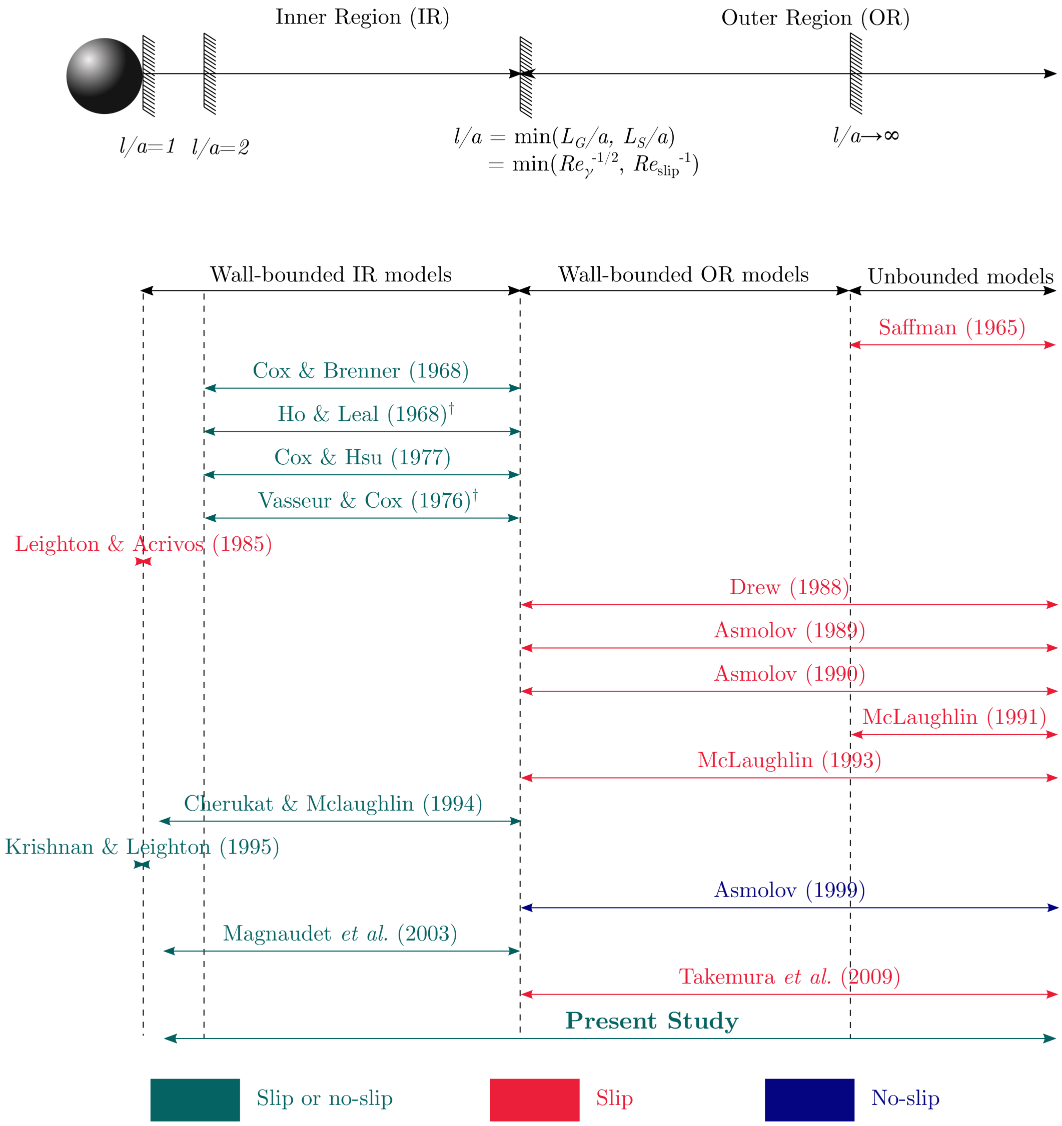

FIGURE 3.10: Analytical lift force models available for linear shear flows illustrating the range of applicability based on dimensionless wall distance (l/a) and on 'slip' and 'no-slip' conditions. The lift coefficient of 'slip' models depends upon both Re_{slip} and Re_γ whereas the lift coefficient of 'no-slip' models depends only on Re_γ. †Models bounded by two walls.

Chapter 4

Multi-particle Hydrodynamics - Theory and Modelling

This chapter contains an overview of the available literature on particle migration due to multi-particle effects, mainly related to semi-dilute and concentrated suspensions. In the first section (§4.1), theoretical concepts associated with multi-body interactions are briefly discussed. This is followed by a section (§4.2) on the mechanisms established to model particle migration. Analytical models, based on the proposed mechanisms, are critically reviewed in §4.3. The governing equations, assumptions, limitations, and various applications are discussed for each model. Finally, a brief discussion of the existing numerical techniques available for suspension modelling is provided in §4.4.

4.1 Particle interactions

In a multi-particle system, particles interact through hydrodynamic forces, Brownian diffusion forces, and inter-particle forces. Batchelor [18] was the first to study the macroscopic behaviour of suspensions accounting for the bulk stress [21] and pairwise particle interactions [20] in a linear shear flow using a Stokes flow assumption. Theoretically, under these conditions an interaction between two approaching smooth rigid spherical particles is reversible with each particle returning to its original streamline after the interaction [16, 17, 33, 158]. However, experimentally, even at very low Reynolds numbers, non-Brownian smooth rigid particles in sheared suspensions exhibit a diffusion like motion. This permanent particle migration is often explained as a result of three-body (or multi-body) particle interactions (broadly discussed in §4.2), or binary-interactions of non-smooth or non-spherical particles.

The small-scale surface roughness of a particle can keep other particles at a distance greater than a minimum separation distance ($\lesssim 10^{-4}$ of particle radii [61]) and lead to an irreversible collision even under Stokes flow [8, 61]. The experimental study of Smart and Leighton [232] with non-dimensional particle roughness $(0.01 - 0.1)$ reported that particles do not come closer than the asperity lengths. Further, the theoretical work of Da Cunha and Hinch [61] showed that both the self-induced and gradient induced diffusivities (explained in the §4.2) increase with surface roughness.

In this context most multi-body hydrodynamic interactions have been studied under the Stokes flow assumption. Hence, the role of finite inertia on the motion of the suspended particles has not been understood clearly. At dilute conditions (non-interacting particles), streamlines around single particles can also get altered by finite inertial effects and cause a lift force on particles that acts perpendicular to the stream-wise direction. The particle and fluid inertia add extra stress in the bulk suspension due to the acceleration of particles and the fluid velocity fluctuations. Accounting for finite inertia at $Re_\mathrm{p} \ll 1$, Lin et al. [150] theoretically showed an increase of the particle contribution to the suspension viscosity and non-isotropic normal stress. A few numerical studies have examined the pairwise interactions and normal stress distributions in bulk suspensions by considering dense suspensions at $Re_\mathrm{p} \sim \mathcal{O}(1)$ [98, 136–138] and explained the importance of accounting for inertia in these multi-particle systems.

4.2 Shear induced diffusion

Particle migration in a sheared suspension primarily due to hydrodynamic interactions is broadly termed 'Shear Induced Diffusion' (SID) [148]. In the theoretical context, SID has been studied at the microscopic level to analyse the self-diffusion of individual particles [74] and at the macroscopic level to understand the gradient diffusion and net migration of particles. Self diffusion (or molecular diffusion) refers to the mixing of spheres in a suspension under uniform concentration and uniform shear, whereas the gradient diffusion refers to particle fluxes down a concentration or shear gradient.

Nevertheless, the self diffusion is strongly related to the collective gradient diffusion particularly at dilute conditions [32].

Computationally, shear induced diffusion has been extensively studied for non-inertial particles using Stokesian dynamics simulations [29, 30, 83, 198]. The measurements relevant to self-induced diffusion coefficients, gradient induced diffusion coefficients, and particle stress contributions to the bulk suspension have been obtained from these simulations to develop analytical models. Further to this, extra particle pressure due to Brownian motion acting on the hydrodynamic shear induced diffusion migration has been examined using these Stokesian dynamics simulations.

4.2.1 Self-induced diffusivity

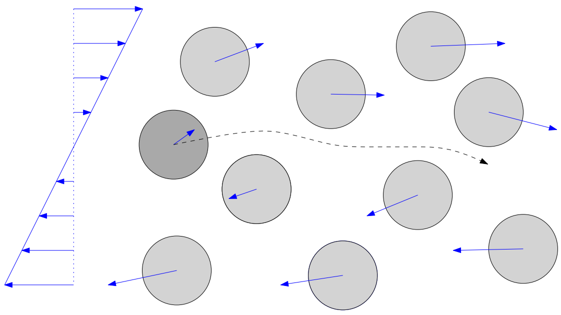

FIGURE 4.1: Schematic of the movement of a particle in a homogeneous concentrated suspension under a linear shear flow.

The self-diffusion of an individual particle occurs when that particle is prevented from moving along the streamline by the neighbouring particles. As a result, the particle exhibits a fluctuating motion, and eventually, this behaviour is propagated to the adjacent particles (random walk). The displacement of individual particles due to these fluctuating velocities is diffusive in nature. However, the net movement of all particles exhibit zero mean displacement, indicating a zero bulk motion.

The self-induced diffusivity of a particle has been measured experimentally [32, 74, 148, 262], numerically [27, 83, 198, 230], and theoretically [30] in linear shear flows. Using simple scaling arguments, Eckstein et al. [74] showed that the shear induced diffusivity ($\mathscr{D}_{\mathrm{sid}}$) in a homogeneous suspension scales with the rate of interactions which is proportional to γ and particle displacement length ($\sim a$).

$$\mathscr{D}_{\mathrm{sid}} = \hat{\mathscr{D}}_{\mathrm{sid}} \gamma a^2 \tag{4.1}$$

The non-dimensional shear induced diffusion coefficient, $\hat{\mathscr{D}}_{\mathrm{sid}}$, is a dimensionless parameter that varies with the volume fraction ϕ_{s}. In the dilute limit ($\phi_{\mathrm{s}} < 0.2$), Eckstein et al. [74] found that the non-dimensional shear induced diffusion coefficient, $\hat{\mathscr{D}}_{\mathrm{sid}}$, is proportional to suspension concentration ϕ_{s}, and suggested that $\mathscr{D}_{\mathrm{sid}} \approx 0.025\phi_{\mathrm{s}}\gamma a^2$. In relatively concentrated limits ($0.05 < \phi_{\mathrm{s}} < 0.4$) Leighton and Acrivos [148] reported a rapid increase of $\hat{\mathscr{D}}_{\mathrm{sid}}$ with ϕ_{s} and approximated the self diffusivity variation as $\mathscr{D}_{\mathrm{sid}} \approx 0.5\phi_{\mathrm{s}}^2\gamma a^2$.

In dilute suspensions, a particle interacting with another particle under the Stokes condition will exhibit a permanent displacement from the original streamline only if asymmetry is introduced to the system. Roughness or interaction with a third particle can generate such asymmetry and result in self-induced diffusion [61, 202]. In the dilute limit, the diffusivity scales linearly with the concentration ϕ_{s} mainly due to the roughness. However, the same parameter scales with ϕ_{s}^2 for a three-body hydrodynamic interaction [262]. With increasing solid volume fraction, the probability of multi-body interactions increases, and hence the diffusivity tends to scales with ϕ_{s}^2 rather than ϕ_{s} for concentrated suspensions, consistent with Leighton and Acrivos's diffusivity values in the concentrated limits.

During pure shear, diffusion can occur in either the shear or vorticity directions. Hence $\hat{\mathscr{D}}_{\mathrm{sid}}$ can be defined as a tensor that includes diffusion coefficients along the flow ($\hat{\mathscr{D}}_{\mathrm{sid},11}$), shear ($\hat{\mathscr{D}}_{\mathrm{sid},22}$) and the vorticity axis ($\hat{\mathscr{D}}_{\mathrm{sid},33}$) as;

$$\hat{\boldsymbol{\mathscr{D}}}_{\mathrm{sid}} = \gamma a^2 \begin{bmatrix} \hat{\mathscr{D}}_{\mathrm{sid},11} & 0 & 0 \\ 0 & \hat{\mathscr{D}}_{\mathrm{sid},22} & 0 \\ 0 & 0 & \hat{\mathscr{D}}_{\mathrm{sid},33} \end{bmatrix} \tag{4.2}$$

where here the three coordinate directions are aligned with velocity, velocity gradient and vorticity directions, respectively. Brady and Morris [30] extrapolated the scaling laws to predict the diffusivity values for concentrated suspensions and showed a monotonic growth of $\hat{\mathscr{D}}_{\mathrm{sid},22}$ and $\hat{\mathscr{D}}_{\mathrm{sid},33}$ with increasing ϕ_{s}. However, experimental studies [32] showed that the diffusivity values asymptote to a constant when ϕ_{s} is increased up to 0.5. Later the experimentally observed plateau at high volume fraction was confirmed in a numerical study by Foss and Brady [84]. However, the plateau was only found for $\hat{\mathscr{D}}_{\mathrm{sid},22}$ and not for $\hat{\mathscr{D}}_{\mathrm{sid},33}$. Further, under dilute conditions, the ratio of the two diffusion coefficients ($\hat{\mathscr{D}}_{\mathrm{sid},22}/\hat{\mathscr{D}}_{\mathrm{sid},33}$) was estimated as $\mathcal{O}(10)$. As for concentrated suspensions, the ratio was estimated as 2. These values suggest the anisotropy decreases with increasing ϕ_{s} [32].

4.2.2 Gradient induced diffusivity

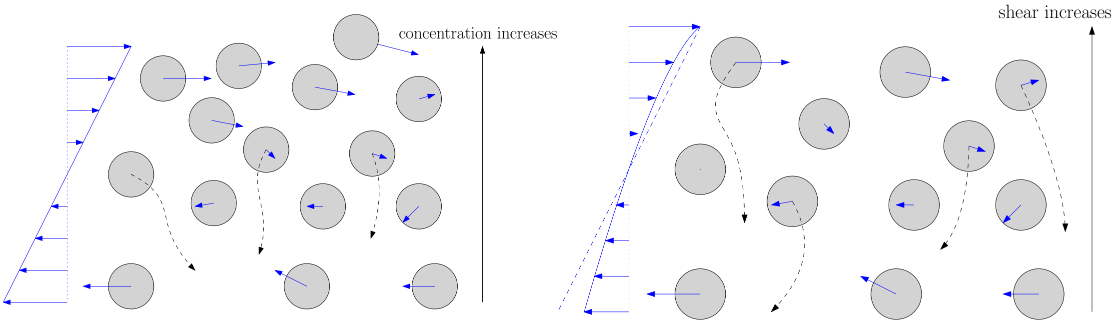

(a) Concentration gradient diffusion

(b) Shear gradient diffusion

FIGURE 4.2: Schematic of the collective movement of particles in the presence of (a) concentration gradient (b) shear gradient.

Collective particle migration can happen in the presence of concentration gradients or shear gradients, resulting in particle flux ($\boldsymbol{j}_{\mathrm{sid}}$) down the gradients of concentration or shear. This macroscopic behaviour has been theoretically explained using the spatially varying 'interaction frequency' that scales as $\phi_{\mathrm{s}}\gamma$ [147, 197]. For a 2D flow the total flux can be expressed in terms of diffusivities as [252];

$$\boldsymbol{j}_{\mathrm{sid}} = \mathscr{D}_{\mathrm{sid},\phi}\boldsymbol{\nabla}\phi_{\mathrm{s}} + \mathscr{D}_{\mathrm{sid},\gamma}\boldsymbol{\nabla}\gamma \tag{4.3}$$

The concentration gradient induced diffusivity $\mathscr{D}_{\mathrm{sid},\phi}$ scales with γa^2 similar to the self-induced diffusivity and causes a bulk particle motion from high to low concentration regions. Note that $\mathscr{D}_{\mathrm{sid},\phi}$ is a macroscopic parameter defined in the presence of a concentration gradient, whereas self-induced diffusivity $\mathscr{D}_{\mathrm{sid}}$ is a microscopic parameter defined based on individual particle movement. Hence, a zero net flux due to a zero concentration gradient does not necessarily mean that individual particles do not move across streamlines. Such motions are only microscopic in nature, and hence do not affect bulk flux. Most of the diffusivity values measured in experiments describe the random walk of a particle. To obtain the gradient induced diffusivity, one needs to determine the actual flux of the particles arising from non-uniform concentrations, which requires the

Study	$\hat{\mathscr{D}}_{\mathrm{sid},\phi}/(\frac{2}{9})$
Leighton and Acrivos [147]	$0.5\phi_s^2(1+0.09e^{7\phi_s})$
Davis and Leighton [65]†	$0.33\phi_s^2(1+0.5e^{8.8\phi_s})$
Zydney et al. [271]‡	$0.03\phi_s^2$
Phillips et al. [197]	$0.091\phi_s+0.26\phi_s^2(1-\hat{\phi}_s)^{-1}$
Morris and Boulay [182]	$(1-\phi_s)^4 1.5\hat{\phi}_s/\phi_{s,\max}(1+\hat{\phi}_s(1-\hat{\phi}_s)^{-1})$
Vollebregt [252]	$(1-\phi_s)^2 1.5\hat{\phi}_s/\phi_{s,\max}(1+\hat{\phi}_s(1-\hat{\phi}_s)^{-1})$

† Proposed for experimental data of Leighton and Acrivos [148]
‡ Proposed for experimental data valid for $\phi_s > 0.2$ of Eckstein et al. [74]

TABLE 4.1: Closure relations for bulk concentration diffusion coefficient $\hat{\mathscr{D}}_{\mathrm{sid},\phi}$.

Study	$\hat{\mathscr{D}}_{\mathrm{sid},\gamma}/(\frac{2}{9})$
Phillips et al. [197]	$0.091\phi_s^2$
Morris and Boulay [182]	$0.75(1-\phi_s)^4\hat{\phi}_s^2$
Vollebregt [252]	$0.75(1-\phi_s)^2\hat{\phi}_s^2$

TABLE 4.2: Closure relations for bulk shear diffusion coefficient $\hat{\mathscr{D}}_{\mathrm{sid},\gamma}$.

macroscopic experimental measurements (i.e., bulk motion) to be fitted to the flux correlations.

By examining different analytical models, Vollebregt [252] has reformulated the particle flux as,

$$\boldsymbol{j}_{\mathrm{sid}} = \hat{\mathscr{D}}_{\mathrm{sid},\phi}\gamma a^2 \boldsymbol{\nabla}\phi_s + \hat{\mathscr{D}}_{\mathrm{sid},\gamma} a^2 \boldsymbol{\nabla}\gamma \tag{4.4}$$

and presented correlations for diffusion coefficients, $\hat{\mathscr{D}}_{\mathrm{sid},\phi}$ and $\hat{\mathscr{D}}_{\mathrm{sid},\gamma}$. These correlations as well as a few other experimental based correlations are listed in tables 4.1 and 4.2. Here, $\hat{\phi}_s(=\phi_s/\phi_{\max})$ is the reduced solid volume fraction and $\phi_{\max}$ is the the maximum solid packing fraction.

4.3 Analytical models

In the theoretical context, multi-particle hydrodynamics in sheared suspensions are most commonly analysed for non-Brownian suspension under the Stokes condition ($Pe \gg 1$ and $Re_p \ll 1$). As mentioned previously, under these conditions hydrodynamic forces due to inertial forces and Brownian diffusion forces become less dominant. Hence, particle migration in such suspension is modelled using the concepts of 'Shear Induced Diffusion' which accounts for the influence of neighbouring particles have on a reference particle. SID based analytical models often employ the framework of the mixture model derived from the two-fluid model. The suspension balance model (SBM), a subclass of the mixture model which was initially developed by Brady and co-workers [189] and later modified by Morris and co-workers [182], is so far the best available model describing the phenomena of shear induced migration.

Two basic multiphase flow approaches used to model particle migration are the mixture models and two-fluid models. Mixture model equations were initially derived from the two-fluid model deduced for dilute suspensions [155]. In this section, the two-fluid model will be first introduced before discussing the mixture model in detail. However, note that the two-fluid framework was not originally designed to capture the shear induced migration. Hence, there remain limitations and assumptions associated with the mixture model that originated from the two-fluid model, which needs to be accounted for when applying the mixture model.

4.3.1 Two-fluid model

The two-fluid model describes the solid and liquid phases as two continuum, interpenetrating phases and solves equations governing the conservation of mass and momentum for each phase. Different types of averaging techniques such as ensemble-averaging [267] and volume averaging [117] have been utilised to derive the macroscopic field equations from the microscopic particle scale level equations. Commonly used field equations for a monodispersed suspension proposed by Jackson [117] can be presented as;

Fluid Continuity Equation

$$\frac{\partial \phi_{\mathrm{f}}\rho_{\mathrm{f}}}{\partial t} + \boldsymbol{\nabla}\cdot\phi_{\mathrm{f}}\rho_{\mathrm{f}}\boldsymbol{u}_{\mathrm{f}} = 0 \tag{4.5a}$$

Fluid Linear Momentum Equation

$$\frac{\partial \phi_{\mathrm{f}}\rho_{\mathrm{f}}\boldsymbol{u}_{\mathrm{f}}}{\partial t} + \boldsymbol{\nabla}\cdot\phi_{\mathrm{f}}\rho_{\mathrm{f}}\boldsymbol{u}_{\mathrm{f}}\boldsymbol{u}_{\mathrm{f}} = \boldsymbol{\nabla}\cdot\boldsymbol{\sigma}_{\mathrm{f}} - \boldsymbol{M} + \phi_{\mathrm{f}}\rho_{\mathrm{f}}\boldsymbol{g} \tag{4.5b}$$

Solid Continuity Equation

$$\frac{\partial \phi_{\mathrm{s}}\rho_{\mathrm{s}}}{\partial t} + \boldsymbol{\nabla}\cdot\phi_{\mathrm{s}}\rho_{\mathrm{s}}\boldsymbol{u}_{\mathrm{s}} = 0 \tag{4.5c}$$

Solid Linear Momentum Equation

$$\frac{\partial \phi_{\mathrm{s}}\rho_{\mathrm{s}}\boldsymbol{u}_{\mathrm{s}}}{\partial t} + \boldsymbol{\nabla}\cdot\phi_{\mathrm{s}}\rho_{\mathrm{s}}\boldsymbol{u}_{\mathrm{s}}\boldsymbol{u}_{\mathrm{s}} = \boldsymbol{\nabla}\cdot\boldsymbol{\sigma}_{\mathrm{s}} + \boldsymbol{M} + \phi_{\mathrm{s}}\rho_{\mathrm{s}}\boldsymbol{g} \tag{4.5d}$$

Here ρ_i, $\boldsymbol{u}_i$ and $\boldsymbol{\sigma}_i$ are the density, volume-averaged velocity and the stress tensor of phase i, respectively. $\boldsymbol{M}$ is the interphase momentum term that couples the fluid and solid momentum balance equations. In the absence of fluid and solid inertia, $\boldsymbol{M}$ consists of only the drag related forces (i.e., Stokes drag and Faxen drag). Existing theoretical closure expressions for the stress tensor in each phase $\boldsymbol{\sigma}_i$ have subtle differences mainly due to the averaged techniques applied [117, 149, 267], and are reviewed in Harvie [107].

The TFM is often used in the field of gas-fluidised beds, but rarely used in the area of viscous suspension flows to analyse shear induced particle migration. Instead of incorporating particle stress due to hydrodynamic interactions, Lhuillier [149] used an extra particle phase force in the two-fluid framework. This force accounts for the 'shear-induced' and 'stress-induced' migration, partly due to the Faxen force on a particle that arises from gradients in the velocity field. Based on Lhuillier [149]'s work, Nott et al. [190] pointed out that there cannot be an averaged hydrodynamic contribution to the particle stress. Instead, Nott et al. [190] showed that the extra particle phase force could be presented as a sum of the interphase drag force and divergence of a particle phase stress due to hydrodynamic interactions. However, as mentioned in the Vollebregt [252] and Nott et al. [190] review papers, unclear areas such as particle phase stress and interphase particle forces need to be addressed further to obtain accurate shear-induced migration using the TFM framework.

4.3.2 Mixture model

The mixture model has been widely used to describe particle migration in semi-dilute and concentrated suspensions. The mixture model is derived from the two-fluid model by adding the solid and fluid phase momentum and continuity equations to form mass and momentum equations for the mixture phase. The transport of solid species within the system is solved using algebraic slip equations derived from the solid and fluid momentum equations and solid phase continuity equation. A general form for the volume-averaged mixture phase equations can be presented as [155], *Mixture Continuity Equation*

$$\frac{\partial \rho_{\mathrm{m}}}{\partial t} + \boldsymbol{\nabla} \cdot \rho_{\mathrm{m}} \boldsymbol{u}_{\mathrm{m}} = 0 \tag{4.6a}$$

Mixture Linear Momentum Equation

$$\frac{\partial \rho_{\mathrm{m}} \boldsymbol{u}_{\mathrm{m}}}{\partial t} + \boldsymbol{\nabla} \cdot \rho_{\mathrm{m}} \boldsymbol{u}_{\mathrm{m}} \boldsymbol{u}_{\mathrm{m}} = \boldsymbol{\nabla} \cdot \boldsymbol{\sigma}_{\mathrm{m}} + \rho_{\mathrm{m}} \boldsymbol{g} \tag{4.6b}$$

where ρ_{m} and $\boldsymbol{u}_{\mathrm{m}}$ are the mixture density and volume averaged suspension velocity, respectively as:

$$\boldsymbol{u}_{\mathrm{m}} = \phi_{\mathrm{s}} \boldsymbol{u}_{\mathrm{s}} + \phi_{\mathrm{f}} \boldsymbol{u}_{\mathrm{f}}$$

$$\rho_{\mathrm{m}} = \phi_{\mathrm{s}} \rho_{\mathrm{s}} + \phi_{\mathrm{f}} \rho_{\mathrm{f}}$$

The closure expression for the total suspension stress, $\boldsymbol{\sigma}_{\mathrm{m}}$, can be formulated by considering the mixture as a single continuum phase;

$$\boldsymbol{\sigma}_{\mathrm{m}} = -p_{\mathrm{m}} \boldsymbol{I} + \boldsymbol{\tau}_{\mathrm{m}} \tag{4.7}$$

where p_{m}, $\boldsymbol{\tau}_{\mathrm{m}}$ and $\boldsymbol{I}$ are the mixture phase pressure, viscous stress tensor and identity tensor, respectively. For suspensions with non-Brownian particles, the mixture phase pressure is often approximated as the fluid pressure $p_{\mathrm{m}} \approx p_{\mathrm{f}}$ [72]. Ideally, the mixture stress has contributions from both the fluid and solid phases ($\boldsymbol{\tau}_{\mathrm{m}} = \phi_{\mathrm{s}} \boldsymbol{\tau}_{\mathrm{s}} + \phi_{\mathrm{f}} \boldsymbol{\tau}_{\mathrm{f}}$) [120], however, often the mixture stress $\boldsymbol{\tau}_{\mathrm{m}}$ is expressed in a Newtonian form, based on mixture average strain rates, with a varying mixture viscosity (μ_{m}) as;

$$\boldsymbol{\tau}_{\mathrm{m}} = \mu_{\mathrm{m}} \boldsymbol{\gamma}_{\mathrm{m}} \tag{4.8}$$

Generally the mixture phase deformation strain rate tensor, $\boldsymbol{\gamma}_{\mathrm{m}} (= \boldsymbol{\nabla} \boldsymbol{u}_{\mathrm{m}} + (\boldsymbol{\nabla} \boldsymbol{u}_{\mathrm{m}})^{\mathrm{T}})$, is assumed to be similar to the fluid and solid phases strain rate tensors under dilute conditions ($\boldsymbol{\gamma}_{\mathrm{m}} = \boldsymbol{\gamma}_{\mathrm{s}} = \boldsymbol{\gamma}_{\mathrm{f}}$).

Suspension viscosity

Following Eq. (4.8), the mixture viscosity is a key parameter within the mixture model. The mixture viscosity for a very dilute mono-disperse suspension ($0 < \phi_s < 0.02$) was first suggested by Einstein [75] as;

$$\mu_m = \mu_f(1 + 2.5\phi_s) \tag{4.9}$$

At high bulk concentrations, the mixture viscosity of a suspension increases due to the hydrodynamic interactions between particles. By extending the dilute limit to intermediate solid fractions ($\phi_s \lesssim 0.15$), Batchelor [19] proposed an expression for the mixture viscosity accounting for the hydrodynamic interactions as below;

$$\mu_m = \mu_f(1 + 2.5\phi_s + K\phi_s^2 + \mathcal{O}(\phi_s^3)) \tag{4.10}$$

The coefficient K, associated with ϕ_s^2, depends on the suspension type. Batchelor [19] suggested $K = 6.2$ for Brownian suspensions and $K = 7.2$ for weak Brownian suspensions in a linear flow. For concentrated solid suspensions, most theoretical and experimental studies extend Einstein's (dilute) mixture viscosity model via a term dependent on a reduced solid volume fraction, $\hat{\phi}_s(= \phi_s/\phi_{max})$. These models ensure that at a maximum solid packing fraction, the mixture suspension viscosity approaches infinity. Note that ϕ_{max} is an empirical parameter which depends strongly on particle shape and associated interactions. The measured values for this parameter generally vary between $0.58 - 0.72$ for monodisperse hard spheres [66]. Frequently used correlations for the suspension mixture viscosity are presented in table 4.3 and the corresponding behaviour of the non-dimensional mixture viscosities $\hat{\mu}_m(= \mu_m/\mu_f)$ are illustrated in figure 4.3.

In addition to these two mixture equations, a separate mass conservation equation for the solid phase is also employed in the mixture model framework to capture the particle distribution development within the suspension. The solid phase continuity equation is given by,

Solid Continuity Equation

$$\frac{\partial \phi_s}{\partial t} + \boldsymbol{\nabla} \cdot \phi_s \boldsymbol{u}_s = 0 \tag{4.11}$$

Study	Correlation
Roscoe [209]	$\mu_\mathrm{f}(1-\hat{\phi}_\mathrm{s})^{-2.5}$
Maron and Pierce [159]	$\mu_\mathrm{f}(1-\hat{\phi}_\mathrm{s})^{-2}$
Krieger and Dougherty [130]	$\mu_\mathrm{f}(1-\hat{\phi}_\mathrm{s})^{-2.5\phi_\mathrm{s,max}}$
Krieger [129]	$\mu_\mathrm{f}(1-\hat{\phi}_\mathrm{s})^{-1.8}$
Batchelor [19]	$\mu_\mathrm{f}(1+2.5\phi_\mathrm{s}+K\phi_\mathrm{s}^2)$
Leighton and Acrivos [146]	$\mu_\mathrm{f}[1+1.5\phi_\mathrm{s}(1-\hat{\phi}_\mathrm{s})^{-1}]^2$
Morris and Boulay [182]†	$\mu_\mathrm{f}[(1+2.5\phi_\mathrm{s}(1-\hat{\phi}_\mathrm{s})^{-1}+\hat{\mu}_\mathrm{col,s}\hat{\phi}_\mathrm{s}^2(1-\hat{\phi}_\mathrm{s})^{-2}]$
Boyer et al. [28]‡	$\mu_\mathrm{f}[(1+2.5\phi_\mathrm{s}(1-\hat{\phi}_\mathrm{s})^{-1}+\hat{\mu}_\mathrm{col,s}(\hat{\phi}_\mathrm{s})\hat{\phi}_\mathrm{s}^2(1-\hat{\phi}_\mathrm{s})^{-2}]$

† $\hat{\mu}_\mathrm{col,s}=0.1$

‡ $\hat{\mu}_\mathrm{col,s}=\hat{\mu}_1+\frac{(\hat{\mu}_2-\hat{\mu}_1)}{1+I_0\hat{\phi}_\mathrm{s}^2(1-\hat{\phi}_\mathrm{s})^{-2}}$ where $\hat{\mu}_1=0.32$, $\hat{\mu}_2=0.7$ and $I_0=0.005$ values based on experimental data.

TABLE 4.3: Closure relations for the mixture viscosity μ_m for mono-disperse hard sphere suspensions.

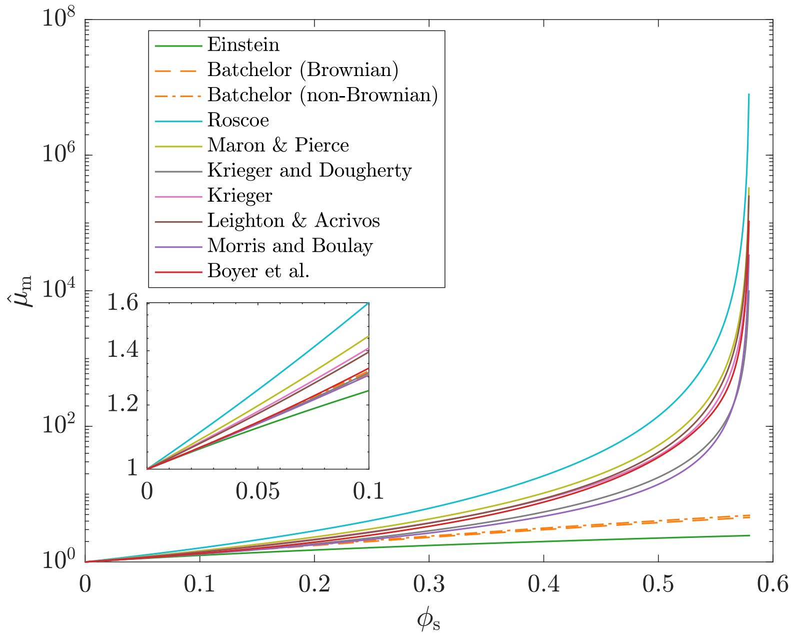

FIGURE 4.3: Non-dimensional mixture viscosity $\hat{\mu}_\mathrm{m}$ for mono-disperse hard sphere suspensions. Here $\phi_\mathrm{s,max}$ is taken as 0.58.

An algebraic phase slip velocity $(\boldsymbol{u}_\mathrm{s}-\boldsymbol{u}_\mathrm{f})$, determined using individual phase momentum equations, is used to solve Eqs. (4.6a), (4.6b), and (4.11). When deriving the algebraic slip equations, specific momentum terms are often neglected under a low-inertia assumption. Here, extra stresses, such as turbulent and inertial diffusion stresses, which originate from the solid phase slip velocities (parallel to the flow), and inertial lift forces, which originates from shear and slip, are usually neglected in the mixture model [155].

Neglecting the slip based particle movement in the flow direction is a reasonable assumption if the solid and fluid velocities come to a local equilibrium quickly. However, in dilute suspensions, the diffusive behaviour (motion perpendicular to flow direction) originating from shear induced diffusion forces and lift forces are relatively slow, and hence the neglect of the particle-scale inertial forces may not be a valid assumption.

Different mixture models available in literature to capture the slow diffusive type motion are discussed below.

4.3.2.1 Diffusive flux model - DFM

The diffusive flux model, originally proposed by Phillips et al. [197], is a simplified form of the mixture model, using a few assumptions for the mixture continuity and momentum equations. In general, DFM considers incompressible, neutrally-buoyant suspensions moving at low particle Reynolds numbers. Hence the continuity and momentum equations of the mixture phase (Eqs. 4.6a and 4.6b) and continuity equation of solid phase (Eq. 4.11) simplify to;

Mixture Continuity Equation

$$\boldsymbol{\nabla} \cdot \boldsymbol{u}_\mathrm{m} = 0 \tag{4.12a}$$

Mixture Linear Momentum Equation

$$\boldsymbol{\nabla} \cdot \boldsymbol{\sigma}_\mathrm{m} = 0 \tag{4.12b}$$

Solid Continuity Equation

$$\frac{\partial \rho_\mathrm{s}\phi_\mathrm{s}}{\partial t} + \boldsymbol{\nabla} \cdot \rho_\mathrm{s}\phi_\mathrm{s}\boldsymbol{u}_\mathrm{s} = 0 \tag{4.12c}$$

The suspension stress tensor $\boldsymbol{\sigma}_\mathrm{m}$ in DFM is obtained from Eq. (4.7).

In DFM, the mass conservation equation for the solid particle given by Eq.(4.12c) is formulated in the Lagrangian frame [197] as;

$$\frac{\partial \phi_\mathrm{s}}{\partial t} + \boldsymbol{u}_\mathrm{m}\boldsymbol{\nabla} \cdot \phi_\mathrm{s} = -\boldsymbol{\nabla} \cdot \boldsymbol{N}_\mathrm{s} \tag{4.13}$$

where $\boldsymbol{N}_\mathrm{s} = \phi_\mathrm{s}(\boldsymbol{u}_\mathrm{p} - \boldsymbol{u}_\mathrm{m})$ is the particle flux relative to the suspension average velocity.

Using the scaling principles of Leighton and Acrivos [148], Phillips et al. [197] suggested an expression for the diffusive particle flux ($\boldsymbol{N}_\mathrm{s} = \phi(\boldsymbol{u}_\mathrm{p} - \boldsymbol{u}_\mathrm{m})$) at steady-state in terms of gradients in collision and viscosity. Macroscopic experimental results suggested that particles drift to regions of lower interaction frequency ($\phi_\mathrm{s}\gamma$) and towards the lower effective viscosity regions.

Assuming the variation in the frequency over a distance of particle radius is proportional to $a\boldsymbol{\nabla}(\gamma\phi)$, the flux due to gradients in collision frequency, $\boldsymbol{N}_\mathrm{c}$ is given as [197];

$$\boldsymbol{N}_\mathrm{c} = -K_\mathrm{c} a^2 \phi \boldsymbol{\nabla}(\phi\gamma) \tag{4.14}$$

Phillips et al. [197] also proposed a correlation for the particle flux due to gradients in viscosity ($\boldsymbol{N}_\mu$), assuming that a particle drift velocity is proportional to the viscosity change over the distance of particle radius relative to the overall viscosity change ($a/\mu_\mathrm{m}\boldsymbol{\nabla}(\mu_\mathrm{m})$) and the collision frequency ($\gamma\phi$);

$$\begin{aligned} \boldsymbol{N}_\mu &= -K_\mu \frac{a^2\gamma\phi^2}{\mu_\mathrm{m}} \boldsymbol{\nabla}\mu_\mathrm{m} \\ &= -K_\mu \frac{a^2\gamma\phi^2}{\mu_\mathrm{m}} \frac{d\mu_\mathrm{m}}{d\phi} \boldsymbol{\nabla}\phi \end{aligned} \tag{4.15}$$

Here the effective mixture viscosity μ_m depends only on the local particle concentration.

The total particle flux $\boldsymbol{N}_\mathrm{s}$ is obtained by the sum of the two fluxes ($\boldsymbol{N}_\mathrm{s} = \boldsymbol{N}_\mathrm{c} + \boldsymbol{N}_\mu$). Parameters K_c and K_μ were determined in Phillips et al. [197] to match the experimental data [2, 197] at relatively high bulk concentrations. The obtained values are $\mathcal{O}(1)$ with $K_\mathrm{c} = 0.41$ and $K_\mu = 0.63$.

Although a good agreement was found between DFM predictions and experiments for wide gap Couette flows [197], the model failed to capture the migration in cone-plate and parallel-plate flows. The DFM predictions suggested a zero migration for cone-plate devices and an inward migration towards the axis of rotation in parallel-plate flow devices. In contrast, the experimental observations showed a clear outward migration in cone-plate devices and a very weak outward particle migration in parallel-plate devices. To address this limitation in DFM, Krishnan et al. [133] suggested an additional particle flux due to curved streamlines ($\boldsymbol{N}_\mathrm{r}$) considering the parallel-plate flow geometries.

$$\boldsymbol{N}_\mathrm{r} = -K_\mathrm{r}\kappa a^2\phi\boldsymbol{n} \tag{4.16}$$

where $\boldsymbol{n}$ is the unit normal vector in the radially outward direction in curved-streamline shear flow, and κ is the curvature of the streamline. The curvature induced diffusion coefficient, K_r, is assumed to be similar to K_c. This modifies the total flux to $\boldsymbol{N}_\mathrm{s} = \boldsymbol{N}_\mathrm{c} + \boldsymbol{N}_\mu + \boldsymbol{N}_\mathrm{r}$. The modified DFM model has been widely used in many numerical studies to examine the particle migration in simple geometries [95, 195, 196, 225].

Fang et al. [79] showed that Krishnan et al.'s modification for curvature induced flux is not frame invariant such that it could be extended for general flows. Following the work of Nott and Brady [189] and Morris and Boulay [182] and accounting for the inter-particle interactions in different flow directions, Fang et al. [79] proposed modifications for the particle fluxes provided in the original DFM;

$$\boldsymbol{N}_\mathrm{c} = -K_\mathrm{c}a^2\phi\boldsymbol{\nabla}\cdot(\phi\gamma\boldsymbol{Z}) \tag{4.17a}$$

$$\boldsymbol{N}_\mu = -K_\mu a^2\phi(\gamma\phi)\boldsymbol{Z}\cdot\boldsymbol{\nabla}\ln\mu_\mathrm{m} \tag{4.17b}$$

The flow aligned tensor, $\boldsymbol{Z}$, is:

$$\boldsymbol{Z} = \begin{bmatrix} \psi_1 = 1 & 0 & 0 \\ 0 & \psi_2 & 0 \\ 0 & 0 & \psi_3 \end{bmatrix} \tag{4.18}$$

The corresponding unit vectors of this tensor, $\boldsymbol{e}_1, \boldsymbol{e}_2$ and $\boldsymbol{e}_3$ represent the principal directions of the shear flow plane. For simple flows, $\boldsymbol{e}_1$ coincides with the direction of velocity streamlines, $\boldsymbol{e}_2$ is the direction of the velocity gradient (shear) and $\boldsymbol{e}_3$ is the vorticity direction. Fang et al. used different values in the plane of shear ($\psi_2 \neq 1$) and in the direction normal to it ($\psi_3 \neq 1$). This non-isotropic nature in the modified DFM was successful in predicting the solid distributions in many general flow configurations (i.e., flow between eccentric cylinders) as the modified DFM was frame invariant. Fang et al. [79] showed that the original Phillips et al. model could be recovered by using an identity tensor for $\boldsymbol{Z}$.

For Poiseuille flows, DFM predicts a cusp in the solid distribution profile at the centre-line where $\gamma = 0$, and increases the concentration to the maximum packing limit. Although pipe and channel flow experiments exhibit an increase of particles, a cusp like peak was not observed, mainly when the particle size is significant compared to the dimensions of the flow geometry [101]. Note that any finite-sized particle at the centre-line does not necessarily experience a shear rate and that the inward migration strongly depends on the ratio of particle to pipe radius/channel height. Ingber et al. [115] and Kauzlaric et al. [125] proposed modifications for the DFM using a local averaged shear rate over the particle size and channel/tube size. This modification resolved the cusp behaviour predicted by the original DFM model.

Apart from these two main modifications, Shauly et al. [225] extended the DFM for poly-disperse systems, and [122] attempted to include an additional particle flux resulting from the Brownian diffusion in DFM. Accounting for these modifications, DFM has been widely used for suspension flow modelling in complex geometries such as bifurcation channels [261] and eccentric journal bearing geometries [79, 236].

4.3.2.2 Suspension balance model - SBM

The suspension balance model (SBM) was originally developed by Nott and Brady [189] and later modified by Morris and Brady [183] to account for the buoyancy effects and by Morris and Boulay [182] to deal with the curvilinear flows. The model is often applied for mono-disperse suspensions with rigid spherical particles in a Newtonian fluid under the Stokes condition. Unlike DFM, SBM relates the rheology of suspension to the particle flux through the particle phase mass conservation equation. However, by recovering the DFM model from the SBM equations, Nott and Brady [189] showed that the underlying physics is same for both models.

SBM considers an extra particle phase pressure and assumes that inhomogeneity in the particle phase normal stress drives the particles within the suspension. Hence, the particle drift flux, which is orthogonal to the suspension velocity, is described by the divergence of the particle phase stress. The early SBM of Nott and Brady [189] and Morris and Brady [183] used a parameter called the ‘granular temperature’ to define the particle pressure. Generally the kinetic energy balance of the particle phase quantifies this parameter. Buyevich [38] used a shear rate scaling instead of a granular temperature scaling to interpret the additional particle phase normal stress that appears in the SBM. Mills and Snabre [177] defined an isotropic particle stress tensor, accounting for the lubrication force, which resulted in a particle normal stress that is a function of shear and solid volume fraction. Morris and Boulay [182] and co-workers [174, 175] suggested an anisotropic particle stress tensor, accounting for the normal stress differences to generalise the SBM for curvilinear flows. In the Morris and and co-workers work [174, 175, 182], the particle normal stress tensor is defined as a linear function of the shear rate and as a non-linear function of the solid volume fraction.

Governing equations

In the SBM, the three main governing equations are the mixture continuity and momentum balance equations and the particle phase continuity equation. However, to solve the particle phase continuity, the relative particle flux is related to the particle phase momentum equation.

Thus the simplified mixture phase and solid phase governing equations can be presented as,

Mixture Continuity Equation

$$\boldsymbol{\nabla} \cdot \boldsymbol{u}_{\mathrm{m}} = 0 \tag{4.19a}$$

Mixture Linear Momentum Equation

$$\frac{\partial \rho_{\mathrm{m}} \boldsymbol{u}_{\mathrm{m}}}{\partial t} = \boldsymbol{\nabla} \cdot \boldsymbol{\sigma}_{\mathrm{m}} + \phi_{\mathrm{s}} \rho_{\mathrm{s}} \boldsymbol{g} \tag{4.19b}$$

Solid Continuity Equation

$$\frac{\partial \phi_{\mathrm{s}}}{\partial t} + \boldsymbol{u}_{\mathrm{m}} \boldsymbol{\nabla} \cdot \phi_{\mathrm{s}} = -\boldsymbol{\nabla} \cdot \boldsymbol{j}_{\mathrm{s},\perp}, \tag{4.19c}$$

Solid Linear Momentum Equation

$$\frac{\partial \rho_{\mathrm{s}} \phi_{\mathrm{s}} \boldsymbol{u}_{\mathrm{s}}}{\partial t} + \boldsymbol{\nabla} \cdot \rho_{\mathrm{s}} \phi_{\mathrm{s}} \boldsymbol{u}_{\mathrm{s}} \boldsymbol{u}_{\mathrm{s}} = \boldsymbol{\nabla} \cdot \boldsymbol{\sigma}_{\mathrm{s}} + \boldsymbol{M}_{\mathrm{H}} + \phi_{\mathrm{s}} \rho_{\mathrm{s}} \boldsymbol{g} \tag{4.19d}$$

The relative particle flux of the suspension, $\boldsymbol{j}_{\mathrm{s},\perp} (= \phi_{\mathrm{s}}(\boldsymbol{u}_{\mathrm{s}} - \boldsymbol{u}_{\mathrm{m}}))$, which appears in the solid phase continuity equation (Eq. 4.19c), is related to the particle phase averaged hydrodynamic force $\boldsymbol{M}_{\mathrm{H}}$ that arises due to interphase momentum transfer. Note that the left-hand side of Eq. (4.19d) reduces to zero under the quasi-steady-state assumption in the Stokes limit, and Eq. (4.19d) simplifies to,

$$\boldsymbol{M}_{\mathrm{D}} + \boldsymbol{\nabla} \cdot \boldsymbol{\sigma}_{\mathrm{s}} + \phi_{\mathrm{s}} \rho_{\mathrm{s}} \boldsymbol{g} = 0 \tag{4.20}$$

when $\boldsymbol{M}_{\mathrm{H}} \approx \boldsymbol{M}_{\mathrm{D}}$. Here $\boldsymbol{\sigma}_{\mathrm{s}}$ is the total particle phase stress tensor and $\boldsymbol{M}_{\mathrm{D}}$ is the particle phase averaged interphase drag force. The drag in SBM is modelled as [175];

$$\boldsymbol{M}_{\mathrm{D}} = -\frac{9\mu_{\mathrm{f}}\phi_{\mathrm{s}}}{2a^2}\frac{1}{h(\phi_{\mathrm{s}})}(\boldsymbol{u}_{\mathrm{s}} - \boldsymbol{u}_{\mathrm{m}}) \tag{4.21}$$

with $h(\phi_{\mathrm{s}})$ being the hindered settling function which modifies the particle velocities accounting for the other particles in the suspension.

When Eqs. (4.20) and (4.21) are combined, one can obtain an expression for the particle flux as,

$$\boldsymbol{j}_{\mathrm{s},\perp} = \phi_{\mathrm{s}}(\boldsymbol{u}_{\mathrm{s}} - \boldsymbol{u}_{\mathrm{m}}) = \frac{2a^2}{9\mu_{\mathrm{f}}\phi_{\mathrm{s}}} h(\phi_{\mathrm{s}})(\boldsymbol{\nabla} \cdot \boldsymbol{\sigma}_{\mathrm{s}} + \phi_{\mathrm{s}} \Delta\rho \boldsymbol{g}) \tag{4.22}$$

Particle stress tensor

The particle phase stress ($\boldsymbol{\sigma}_{\mathrm{s}}$) is a critical component in SBM, and is obtained by decomposing the total mixture stress tensor ($\boldsymbol{\sigma}_{\mathrm{m}}$) into a fluid phase stress ($\boldsymbol{\sigma}_{\mathrm{f}}$) and a particle phase stress,such that, $\boldsymbol{\sigma}_{\mathrm{m}} = \boldsymbol{\sigma}_{\mathrm{f}} + \boldsymbol{\sigma}_{\mathrm{s}}$. Assuming strain rates are equal in all phases ($\boldsymbol{\gamma}_{\mathrm{m}} \approx \boldsymbol{\gamma}_{\mathrm{f}} \approx \boldsymbol{\gamma}_{\mathrm{s}}$), the fluid phase stress tensor is defined as;

$$\begin{aligned} \boldsymbol{\sigma}_{\mathrm{f}} &= -p_{\mathrm{f}}\boldsymbol{I} + \boldsymbol{\tau}_{\mathrm{f}} && (4.23) \\ &= -p_{\mathrm{f}}\boldsymbol{I} + \mu_{\mathrm{f}}\boldsymbol{\gamma}_{\mathrm{m}} && (4.24) \end{aligned}$$

Accounting for the anisotropic normal stresses and the collision induced viscous stresses in the particle phase, Morris and Boulay [182] proposed the following closure expression for the total particle stress tensor;

$$\begin{aligned} \boldsymbol{\sigma}_{\mathrm{s}} &= -\boldsymbol{\sigma}_{\mathrm{s,nn}} + \boldsymbol{\tau}_{\mathrm{s}} \\ &= -\mu_{\mathrm{f}}\hat{\mu}_{\mathrm{n}}\gamma_{\mathrm{s}}\boldsymbol{Q} + \mu_{\mathrm{f}}\hat{\mu}_{\mathrm{s}}\boldsymbol{\gamma}_{\mathrm{m}} && (4.25) \end{aligned}$$

Here $\boldsymbol{\sigma}_{\mathrm{s,nn}}$ is the particle phase normal stress tensor (a diagonal tensor) and $\boldsymbol{\tau}_{\mathrm{s}}$ is the collision induced particle phase viscous shear tensor. The particle phase normal stress tensor, $\boldsymbol{\sigma}_{\mathrm{s,nn}}$, is defined using a 'normal stress viscosity' function ($\mu_{\mathrm{f}}\hat{\mu}_{\mathrm{n}}$), the local mixture shear rate magnitude (γ_{m}) and lastly using a non-dimensional parametric tensor ($\boldsymbol{Q}$) which describes the anisotropy of the normal stresses. Here $\boldsymbol{Q}$ is a flow-aligned tensor defined as,

$$\boldsymbol{Q} = \begin{bmatrix} \lambda_1 = 1 & 0 & 0 \\ 0 & \lambda_2 & 0 \\ 0 & 0 & \lambda_3 \end{bmatrix} \tag{4.26}$$

where λ_1, λ_2 and λ_2 are the anisotropic parameters which are defined to be positive. The principal directions of $\boldsymbol{Q}$ denoted by 1,2 and 3, are the flow, velocity gradient, and vorticity directions, respectively. The particle phase viscous stress is defined accounting for the particle contribution to the shear viscosity $\hat{\mu}_{\mathrm{s}}(= \hat{\mu}_{\mathrm{m}} - 1)$ and the mixture strain rates. In SBM applications, the mixture viscosity $\hat{\mu}_{\mathrm{m}}$ is often calculated using the last two correlations given in the table 4.3 [66, 174].

By substituting the closure expressions, the aligned mixture phase total stress tensor can be explicitly written as;

$$\boldsymbol{\sigma}_{\mathrm{m}} = \begin{bmatrix} \mu_{\mathrm{f}}\hat{\mu}_{\mathrm{n}}\gamma + p_{\mathrm{f}} + \mu_{\mathrm{f}}\hat{\mu}_{\mathrm{m}}\gamma_{\mathrm{m},11} & \mu_{\mathrm{f}}\hat{\mu}_{\mathrm{m}}\gamma_{\mathrm{m},12} & \mu_{\mathrm{f}}\hat{\mu}_{\mathrm{m}}\gamma_{\mathrm{m},13} \\ \mu_{\mathrm{f}}\hat{\mu}_{\mathrm{m}}\gamma_{\mathrm{m},21} & \mu_{\mathrm{f}}\hat{\mu}_{\mathrm{n}}\gamma\lambda_2 + p_{\mathrm{f}} + \mu_{\mathrm{f}}\hat{\mu}_{\mathrm{m}}\gamma_{\mathrm{m},22} & \mu_{\mathrm{f}}\hat{\mu}_{\mathrm{m}}\gamma_{\mathrm{m},23} \\ \mu_{\mathrm{f}}\hat{\mu}_{\mathrm{m}}\gamma_{\mathrm{m},31} & \mu_{\mathrm{f}}\hat{\mu}_{\mathrm{m}}\gamma_{\mathrm{m},32} & \mu_{\mathrm{f}}\hat{\mu}_{\mathrm{n}}\gamma\lambda_3 + p_{\mathrm{f}} + \mu_{\mathrm{f}}\hat{\mu}_{\mathrm{m}}\gamma_{\mathrm{m},33} \end{bmatrix} \tag{4.27}$$

Note that the diagonal components of the symmetric strain rate tensor are equal in magnitudes ($\gamma_{\mathrm{m},11} = \gamma_{\mathrm{m},22} = \gamma_{\mathrm{m},22}$).

The first and the second normal stress differences, N_1 and N_2, which describe the anisotropic behaviour of suspension are given as [182];

$$N_1 = \sigma_{\mathrm{m},11} - \sigma_{\mathrm{m},22} = \sigma_{\mathrm{s},11} - \sigma_{\mathrm{s},22} = \mu_{\mathrm{f}}\hat{\mu}_{\mathrm{n}}\gamma(\lambda_1 - \lambda_2) \tag{4.28a}$$

$$N_2 = \sigma_{\mathrm{m},22} - \sigma_{\mathrm{m},33} = \sigma_{\mathrm{s},22} - \sigma_{\mathrm{s},33} = \mu_{\mathrm{f}}\hat{\mu}_{\mathrm{n}}\gamma(\lambda_2 - \lambda_3) \tag{4.28b}$$

whereas the non-Brownian particle pressure which arises from the normal contacts of particles in a shear flow is defined as [182],

$$p_{\mathrm{sid,s}} = -\frac{1}{3}tr(\boldsymbol{\sigma}_{\mathrm{s}}) = -\sigma_{\mathrm{s},11}\frac{\lambda_1 + \lambda_2 + \lambda_3}{3} \tag{4.29}$$

Given that $\gamma_{\mathrm{m},11} = \gamma_{\mathrm{m},22} = \gamma_{\mathrm{m},33} = 0$ for many types of shear flows, Eq. (4.29) can be further simplified as [182];

$$p_{\mathrm{sid,s}} = -\mu_{\mathrm{f}}\hat{\mu}_{\mathrm{n}}\gamma\frac{\lambda_1 + \lambda_2 + \lambda_3}{3} \tag{4.30}$$

with

$$\lambda_2 = \frac{\sigma_{\mathrm{s},22}}{\sigma_{\mathrm{s},11}} \tag{4.31}$$

$$\lambda_3 = \frac{\sigma_{\mathrm{s},33}}{\sigma_{\mathrm{s},11}} \tag{4.32}$$

Hence to evaluate the shear induced diffusion pressure in the SBM, parameters such as $\hat{\mu}_{\mathrm{n}}$, λ_1 and λ_2 must be determined empirically. Morris and Boulay proposed a correlation for the non-dimensional normal stress viscosity as,

$$\hat{\mu}_{\mathrm{n}} = K_{\mathrm{n}}\hat{\phi}^2(1-\hat{\phi})^{-2} \tag{4.33}$$

with $K_{\mathrm{n}} = 0.75$. For a linear shear flow, the theoretical study of Brady and Morris [30] suggested that N_1 is zero and N_2 is negative, considering $\lambda_1+\lambda_2+\lambda_3 = 3$, results in $\lambda_1 = \lambda_2 = 2\lambda_3$. Measurements from Stokesian dynamics simulations[83, 198] and experiments [263] in different flow configurations for the first and second normal stress differences have also provided indirect measurements for λ_1, λ_2 and λ_3. The measurements have confirmed that $N_2 < 0$, but showed that N_1 is not necessarily zero. Morris and Boulay [182] used $\lambda_2 \approx 0.6 - 0.8$ to fit the solid distribution observed in Phillips et al.'s study, which resulted in a small negative N_1 and $\lambda_3 \approx 0.5$. This choice of parameters in SBM successfully predicted the results of a weak migration in torsional flow (between parallel plates) and outward migration in cone-and-plate flows [79, 182]. Recent direct experimental measurements provide values and correlations for $\sigma_{\mathrm{s},33}$ and $\sigma_{\mathrm{s},22}$ in addition to N_1 and N_2 [28, 56, 67, 68]. Dbouk et al. [67] suggested $K_{\mathrm{n}} = 1.08$ and λ_2, λ_3 as functions of solid volume fraction.

Applications of SBM

SBM with an anisotropic particle stress tensor has been extensively used in macroscopic particle migration modelling [66, 174, 175, 201]. Miller and Morris [174] and Miller et al. [175] examined pressure driven flows in pipes and non-uniform geometries (i.e., contraction flows and cavity flows) using the SBM under semi-dilute and concentrated condition ($0.2 < \phi_\mathrm{s} < 0.5$). Miller and Morris [174] addressed the issue of peak solid concentration build-up at the centerline of the channel or pipe, where the shear rate approaches zero. The study introduced a non-local contribution to the local shear rate accounting for the finite size of the spheres. The estimations of solid distribution showed a significant dependence on particle size to pipe diameter ratios. Frank et al. [85] extended the SBM to model Brownian suspensions by making the normal stress differences and the normal suspension viscosity a function of the Péclet number. The study used the modified SBM to investigate the solid distributions when $0.05 < \phi_\mathrm{s} < 0.34$ and $70 < Pe < 4400$. Kulkarni [136] investigated the effect of small particle Reynolds number on suspension behaviour via SBM, and successfully predicted the semi-dilute and concentrated particle distributions ($0.05 < \phi_\mathrm{s} < 0.4$) in pipe flows at intermediate particle Reynolds number ($0.01 < Re_\mathrm{p} < 5$). Based on a suspension property study for finite particle Reynolds number in linear shear flows [137], Kulkarni [136] modified the normal stress differences, $N_1/\mu_\mathrm{f}\gamma$ and $N_2/\mu_\mathrm{f}\gamma$, to be functions of Re_p. Further, Kulkarni [136] states the importance of accounting for the shear rate dependence on the suspension shear viscosity (i.e., shear-thinning suspension) at finite particle Reynolds numbers. Noting that the original SBM only considers momentum exchange via the drag and buoyancy forces, Kulkarni also included a double wall-bounded lift force as an additional momentum exchange term to account for finite inertial effects.

Overall, SBM models have succeeded in predicting qualitative features of the migration process in different flow situations as well as quantitative steady-state velocity and concentration profiles under semi-dilute and concentrated suspensions. However, the SBM has not been used to investigate the solid distribution in dilute suspensions at finite particle Reynolds numbers. Under dilute conditions, the pair distributions can be significantly affected by the particle roughness compared to the long-range particle interactions. Hence more experimental and numerical investigations on normal stress differences in the dilute-range, even under Stokes condition, would be more beneficial. It will be more useful to include a generalised wall-bounded (i.e., slip and shear based single wall-bounded) lift model to increase SBM applicability at finite inertial Reynolds number and to capture the near-wall particle distributions.

4.4 Direct numerical simulation

Direct numerical simulations solve for the details of flow at the scale of the particles numerically. With the advances in numerical simulations, different numerical models have been developed to examine the dynamic behaviour of particles in dilute and concentrated suspensions for a range of particle Reynolds numbers. In addition to macroscopic data on solid distributions, the numerical models also provide microscopic information on particle dynamics that is not easily measured via experiments. In a recent study Maxey [166] provides an excellent review of various numerical approaches available for suspension modelling. In this section, we briefly discuss a few selected numerical models that have been extensively used to describe multi-particle hydrodynamics.

4.4.1 Stokesian dynamics

Brady and Bossis [29] introduced the 'Stokesian Dynamics' (SD) simulation technique to study dilute and concentrated suspension behaviours at the limit of vanishing particle Reynolds numbers. This discrete particle simulation method neglects the fluid inertia and solves the flow around each particle using linear Stokes equations. When particles are close to contact, SD simulations use lubrication force corrections, and short-range repulsive forces to prevent particle overlap and direct particle-particle contact [71]. These extra forces are justified in terms of particle roughness and fluctuations due to Brownian motions.

The Stokesian dynamics technique has been extensively used to simulate the motion of non-Brownian [229, 230, 237], and Brownian particles [83, 84, 184, 198], being those that are mainly governed by shear induced diffusion and Brownian diffusion, respectively. The microscopic level properties, such as self-induced diffusivity values and normal stresses, and macroscopic level rheological properties such as suspension viscosity, are quantified using these simulations.

4.4.2 Lattice-Boltzmann method

The Lattice-Boltzmann method (LBM) is a mesoscopic simulation method that solves the Navier-Stokes equations for the fluid and Newton's equation of motion for the particles. Unlike SD, LBM can solve particulate suspensions at finite Reynolds numbers and systems bounded by container walls. LBM can also use to analyse poly-disperse and non-spherical particle behaviour.

LBM has been used to study the microscopic aspects related to shear induced migration such as pair-wise distribution functions, self diffusivity and particle trajectories at finite Reynolds numbers [135, 258]. LBM based studies have examined the behaviour of dense suspension and rheological properties even at finite Reynolds numbers [98, 136, 137, 200, 222]. These studies reported an increased particle migration for dilute and semi-dilute suspensions ($0.05 < \phi_{\mathrm{s}} < 0.3$) at $0 < Re_{\mathrm{p}} < 10$ due to increased normal stress differences.

4.4.3 Force coupling method - FCM

The force coupling method (FCM) is used to capture the dynamics of Stokes and low Reynolds number suspensions in both open and wall-bounded flows. Under this method, particles are represented by low-order multipoles, and the interactions of particles are captured by the lubrication forces and multi-body hydrodynamic interaction forces [166]. These forces are coupled with the Stokes fluid flow field to predict the particle distribution. Although FCM based simulations are computationally faster than both SD and LBM simulations, FCM is limited to low Reynolds number [259] since the flow is solved in the Stokes limit.

In the particle migration context, FCM has been used by Yeo and Maxey [260] to examine the non-Brownian particle migration in Couette flows for $0.2 < \phi_{\mathrm{s}} < 0.4$ with relatively large particle to domain size ratios. Recently, Howard et al. [113] employed the FCM to analyse the sedimentation rheology of bi-disperse suspension systems.

4.5 Closure

This chapter provides an overview of the modelling efforts of multi-particle hydrodynamics. Most analytical and numerical models are limited to Stokes flow suspensions and explain migration phenomena occurring in concentrated suspensions.

Shear induced diffusion forces are commonly used to model multi-body particle effects and particle distributions under Stokes condition. A few analytical models, namely, the Diffusive Flux Model and the Suspension Balance Model, employ SID based forces to predict the particle migration observed in concentrated suspensions. While these models provide reasonable predictions of solid distributions for concentrated suspension in simple flow configurations (i.e., Couette flows, pipe flows), some unique particle distribution patterns, observed in semi-dilute suspensions [102] and dilute suspensions [1, 157] (i.e., peak particle concentrations away from pipe/Couette gap centre-line and walls), and near-wall concentrations in both dilute and concentrated suspensions are not captured by these analytical models.

Many applications related to particle migration which involve non-Brownian particles have finite particle Reynolds numbers $Re_{\mathrm{p}} > \mathcal{O}(10^{-3})$. Hence particle-scale inertial forces, such as lift forces and other multi-particle scale inertial forces, become more significant. Interestingly, only very few suspension models have been developed that account for these inertial terms. The main obstacle to including particle-scale inertial lift forces is the lack of simple closure relations that could be easily adapted to a multi-fluid environment. Hence, it is more important to employ a framework that can include multi-particle and single-particle hydrodynamics together with other notable wall-forces that are significant for finite inertial conditions.

Direct numerical simulations can also be used to explore the dynamics of suspensions of rigid particles that cover a spectrum of zero to moderate Reynolds numbers and different particle shapes. These simulations can provide details not readily available from experiments. However, the choice of the modelling technique depends on factors such as the suspension system, flow configuration, and computation capacity.

Part II

SINGLE PARTICLE STUDY

Chapter 5

Model Development

.

The main objective of the first part of the thesis is to address the limitations of single wall-bounded lift and drag force models detailed in chapter 3 (i.e., a single particle interacting with a single wall). This includes:

(a) Developing single wall-bounded force models valid for any particle-wall separation distance (except contact).

(b) Extending the existing slip-shear-wall based theoretical results given for Re_{slip}, $Re_\gamma \ll 1$ to larger particle Reynolds numbers (up to $\mathcal{O}(10^{-1})$) and for any combination of Re_{slip} and Re_γ within this range, as directly relevant to particulate flows within small channels (e.g., particle migration in microfluidic devices).

For this, we first quantify the lift and drag forces acting on a rigid spherical particle moving tangential to a flat wall in quiescent and linear shear flows in the range of $10^{-3} \leq Re_{\text{slip}}, Re_\gamma \leq 10^{-1}$ and $1.2 \leq l/a \leq 9.5$ using well resolved numerical simulations. We then express the computed lift and drag results as new force models valid under the above conditions.

In this chapter we present the frame work used for the single particle simulations and the forms of force models used to present lift and drag forces. In the subsequent chapters,

This chapter is mainly based on the author's papers: Ekanayake, N. I., Berry, J. D., Stickland, A. D., Dunstan, D. E., Muir, I. L., Dower, S. K. & Harvie, D. J. E. (2020). Lift and drag forces acting on a particle moving with zero slip in a linear shear flow near a wall. *Journal of Fluid Mechanics*, 904, A6 [77]. and Ekanayake, N. I., Berry, J. D. & Harvie, D. J. E. (2021). Lift and drag forces acting on a particle moving in the presence of slip and shear near a wall. *Journal of Fluid Mechanics* 915, A103 [78] chapters 6 and 7, we examine the lift and drag results for a particle moving in the absence of slip in linear shear flows and a particle moving with a finite slip in quiescent and linear shear flows, respectively.

5.1 Background

Despite many numerical studies available in the literature, most studies that calculate the forces acting on a wall-bounded particle are for intermediate Reynolds numbers $Re_\gamma, Re_{\text{slip}} \sim 0.5 - 3 \times 10^2$. Among these, simulations performed on particles translating performed in quiescent flows are used to evaluate the effect of separation distance on both slip based lift and drag correlations [264]. Several other direct numerical studies examining hydrodynamic forces acting on a particle in a linear shear flow and with non-zero slip closer to the wall propose inertial corrections that are functions of both shear rate and slip velocity [141, 265].

To perform simulations satisfying $Re_\gamma, Re_{\text{slip}} < 1$ conditions, one must employ large computational domains with high mesh refinement near the particle surface in order to capture the small inertial forces. These simulations require high computational power. To our knowledge no numerical results have been presented for small but non-zero inertial conditions Re_γ or $Re_{\text{slip}} \leq \mathcal{O}(1)$ [227], possibly due to these computational limitations, particularly for wall-bounded flows under zero-slip conditions. This will be the first DNS study to present data for this intermediate range of particle Reynolds numbers for arbitrary combinations of both slip and shear Reynolds numbers.

5.2 New lift and drag model definitions

We define the lift force on a particle experiencing both slip and shear within a linear shear flow as:

$$F_{\text{L}}^* = C_{\text{L},1} Re_\gamma^2 + \text{sgn}(\gamma^*) C_{\text{L},2} Re_\gamma Re_{\text{slip}} + C_{\text{L},3} Re_{\text{slip}}^2 \tag{5.1a}$$

which may also be written in the alternative form:

$$F_{\mathrm{L}}^{*} = F_{\mathrm{L},1}^{*} + F_{\mathrm{L},2}^{*} + F_{\mathrm{L},3}^{*} \tag{5.1b}$$

The form chosen for our model is the same as used in previously discussed inner region studies [45, 58], but we now apply this model over the entire inner, outer and unbounded regions. Further, we provide unambiguous definitions for the three coefficients that allow Eq. (5.1) to be a valid representation of the lift force at any separation distance. Namely, the force term $F_{\mathrm{L},1}^{*} = C_{\mathrm{L},1} Re_{\gamma}^{2}$ is defined by the force in a linear shear flow in the absence of slip. The corresponding force coefficient $C_{\mathrm{L},1}$ (the main focus of chapter 6) depends only on shear rate and wall distance. The last term $F_{\mathrm{L},3}^{*} = C_{\mathrm{L},3} Re_{\mathrm{slip}}^{2}$ provides the lift in a quiescent flow in the absence of shear, and the force coefficient $C_{\mathrm{L},3}$ is only a function of slip velocity and wall distance (chapter 7). The remaining term $F_{\mathrm{L},2}^{*} = \mathrm{sgn}(\gamma^{*}) C_{\mathrm{L},2} Re_{\gamma} Re_{\mathrm{slip}}$ captures the remaining lift contributions in the presence of both slip and shear. Hence, the corresponding force coefficient, $C_{\mathrm{L},2}$ depends upon slip, shear and wall distance (chapter 7).

In the same spirit, the net drag acting on a particle with a finite slip in a linear shear flow, is defined as

$$F_{\mathrm{D}}^{*} = -\mathrm{sgn}(\gamma) C_{\mathrm{D},1} Re_{\gamma} - \mathrm{sgn}(u_{\mathrm{slip}}) C_{\mathrm{D},2} Re_{\mathrm{slip}} \tag{5.2a}$$

which may also be written in the alternative form:

$$F_{\mathrm{D}}^{*} = F_{\mathrm{D},1}^{*} + F_{\mathrm{D},2}^{*} \tag{5.2b}$$

Again, while the form of this equation comes from previous work [156], our definition of the coefficients ensures that it provides an accurate expression for the drag force across all separation distances. Specifically, the force term $F_{\mathrm{D},1}^{*} = -\mathrm{sgn}(\gamma) C_{\mathrm{L},1} Re_{\gamma}$ in Eq. (5.2) is defined as the drag force in a linear shear flow in the absence of slip. The corresponding force coefficient $C_{\mathrm{D},1}$, valid for all separation distances, is only a function of shear and wall distance. The term $F_{\mathrm{D},2}^{*} = -\mathrm{sgn}(u_{\mathrm{slip}}) C_{\mathrm{D},2} Re_{\mathrm{slip}}$ in Eq. (5.2) captures the remaining drag contributions in the presence of both the slip and shear. The force coefficient $C_{\mathrm{D},2}$, is a function of slip, shear and wall distance (chapters 6 and 7).

5.3 Problem specification

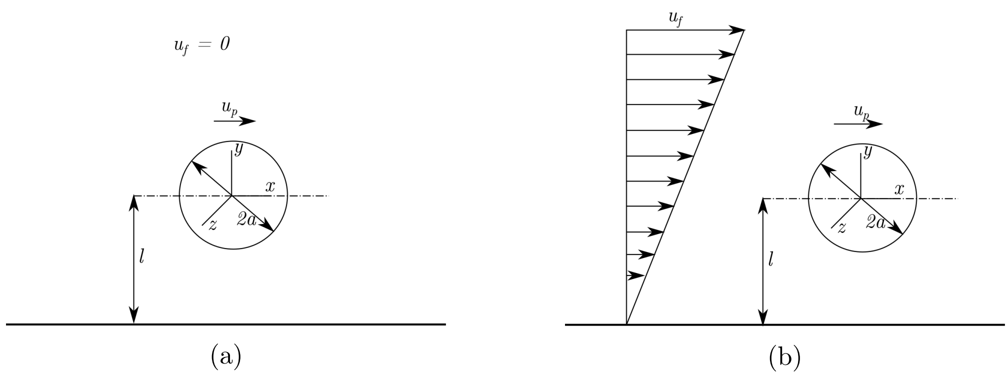

FIGURE 5.1: Schematic of a translating sphere of radius a moving at velocity u_p in a wall-bounded (a) quiescent flow (b) linear shear flow.

A rigid, smooth sphere of radius a is suspended in a linear shear flow with the origin of the Cartesian coordinate system located at the centre of the sphere. Both quiescent and linear shear fluid flows are considered (figure 5.1). The coordinate unit vectors are $\boldsymbol{e}_\mathrm{x}$, $\boldsymbol{e}_\mathrm{y}$ and $\boldsymbol{e}_\mathrm{z}$. A no-slip wall is placed at distance $(0, -l, 0)$ away from sphere centre. Outer boundaries are located at large distances $L(\gg l)$ away from the sphere centre to minimise any secondary boundary effects. For this study l/a is varied from 1.2 - 9.5 to obtain the lift and drag force variation as a function of particle distance from the wall.

To obtain the forces generated due to wall and shear effects in the absence of relative motion between the particle and the fluid, the particle slip velocity $\boldsymbol{u}_\mathrm{slip}$ is explicitly set to zero:

$$\boldsymbol{u}_\mathrm{slip} = \boldsymbol{u}_\mathrm{p} - \boldsymbol{u}_\mathrm{f}(y = 0) = \mathbf{0}$$

For other cases the particle slip velocity is explicitly set to a known value:

$$\boldsymbol{u}_\mathrm{slip} = \boldsymbol{u}_\mathrm{p} - \boldsymbol{u}_\mathrm{f}(y = 0) = u_\mathrm{slip}\boldsymbol{e}_\mathrm{x}$$

Here $\boldsymbol{u}_\mathrm{p} = u_\mathrm{p}\boldsymbol{e}_\mathrm{x}$ is the particle velocity and $\boldsymbol{u}_\mathrm{f}$ is the undisturbed fluid velocity defined as,

$$\boldsymbol{u}_\mathrm{f} = \gamma(y + l)\boldsymbol{e}_\mathrm{x}$$

For the quiescent flow cases, γ is set to zero. Note that under this formulation the particle is constrained to translate only in the x direction with particle velocity u_p (for zero-slip case $u_\mathrm{p} = \gamma l$).

To determine the forces acting on the particle, we solve the steady-state Navier Stokes (N-S) equations in a frame of reference that moves with the particle [17]. Specifically, we solve

$$\boldsymbol{\nabla} \cdot \rho \boldsymbol{u'} = 0 \tag{5.3a}$$

$$\boldsymbol{\nabla} \cdot (\rho \boldsymbol{u'} \boldsymbol{u'} + \boldsymbol{\sigma}) = 0 \tag{5.3b}$$

where $\boldsymbol{u'} = \boldsymbol{u} - \boldsymbol{u}_\mathrm{p}$ and $\boldsymbol{u}$ is the local fluid velocity. The boundary conditions used in the moving frame of reference are:

$$\boldsymbol{u'} = \begin{cases} [\gamma(y+l) - u_\mathrm{p}]\boldsymbol{e}_\mathrm{x} & y = +\infty; y = -l; x, z = \pm\infty \\ \boldsymbol{\omega} \times \boldsymbol{r} & |\boldsymbol{r}| = a \end{cases} \tag{5.4}$$

where $\boldsymbol{r}$ is a radial displacement vector pointing from the sphere centre to the particle surface and $\boldsymbol{\omega}$ is the angular rotation of the particle.

The fluid is assumed to be Newtonian with a dynamic viscosity μ and density ρ, and the 'no-slip' boundary condition is applied on the particle surface. The total stress tensor ($\boldsymbol{\sigma} = p\boldsymbol{I} + \boldsymbol{\tau}$) (Bird et al. [26] sign convention), is computed using the fluid pressure, p and viscous stress tensor, $\boldsymbol{\tau} = -\mu(\boldsymbol{\nabla u'} + \boldsymbol{\nabla u'}^\mathrm{T})$. The forces acting on the particle are evaluated by integrating the total stress contributions around the particle surface S:

$$\boldsymbol{F}_\mathrm{p} = -\int_S \boldsymbol{n} \cdot \boldsymbol{\sigma} dS \tag{5.5}$$

Here $\boldsymbol{n}(= \hat{\boldsymbol{r}})$ is a unit normal vector directed out of the particle. The drag ($F_\mathrm{D} = \boldsymbol{F}_\mathrm{p} \cdot \boldsymbol{e}_\mathrm{x}$) and lift ($F_\mathrm{L} = \boldsymbol{F}_\mathrm{p} \cdot \boldsymbol{e}_\mathrm{y}$) are defined as the fluid forces acting on the sphere in $+x$ and $+y$ directions, respectively. Similarly the net torque $\boldsymbol{T}_\mathrm{p}$ acting on the particle is evaluated using:

$$\boldsymbol{T}_\mathrm{p} = -\int_S \boldsymbol{r} \times \boldsymbol{\sigma} \cdot \boldsymbol{n} dS \tag{5.6}$$

In this single particle study, two cases are considered: in the first, the particle is constrained from rotating, whereas, in the second, the particle is allowed to freely-rotate about the z axis, at an angular velocity ω_p. For the non-rotating (first) case all components of the rotation $\boldsymbol{\omega}$ are explicitly set to zero, whereas for the (second) freely-rotating case the z component of the net torque $\boldsymbol{T}_\mathrm{p}$ is explicitly set to zero and the z component of $\boldsymbol{\omega}$ ($\boldsymbol{\omega} \cdot \boldsymbol{e}_\mathrm{z} = \omega_\mathrm{p}$) is solved for as an unknown (with other components of $\boldsymbol{\omega}$ set to zero).

Most of the results in the remainder of this thesis are presented in non-dimensional form (indicated by an asterisk) using length scale a and force scale μ^2/ρ. Depending whether its a non-zero slip particle in a zero-shear flow or a zero-slip particle in a non-zero shear flow, two different velocity and time scales, u_slip, a/u_slip and γa, $1/\gamma$ are used, respectively. Unless stated otherwise, for a non-zero slip particle in a non-zero shear flow, γa and a/u_slip are used for velocity and time scaling.

5.4 Numerical approach

The system of equations is solved using the finite volume package *arb* [106] over a non-uniform body-fitted structured mesh that is generated with *gmsh* [90] (Figure 5.2a). The sphere surface is resolved with N_p mesh points on each curved side length of a cubed-sphere. This results in $6(N_\mathrm{p}-1)^2$ cells on the sphere surface. $(N_\mathrm{p}-1)$ number of inflation layers with an α geometric progression ratio around the sphere are used to capture gradients in velocity occurring near the particle wall. Outer boundaries, except the bottom wall located at $y^* = -l^*$, are placed at a distance L^* from the sphere centre in all directions. To resolve the far field of the domain (excluding the inflation layers), N_d points are used with a geometric progression β expanding towards the domain boundaries. For larger separation distances, $l^* > 1.2$, $(N_\mathrm{w}-1)$ layers are introduced in the gap between the bounding box and the bottom wall, with a non-uniform progression (i.e., geometric progression) of β producing more refinement near the sphere and the bottom wall. The total cell count in the mesh is N_t.

The non-dimensional lift force magnitudes measured in this study are significantly low, $|F^*_\mathrm{L}| \sim 10^{-6} - 10^{-1}$, and hence require a high resolution mesh around the sphere to accurately determine the lift coefficient. Further, the lift force is highly sensitive to the cell distribution around the particle, requiring perfect symmetry of the mesh in the y direction to ensure that the lift reduces to zero as inertial effects are reduced. For this reason the symmetry of the sphere surface mesh and its surrounding cells in

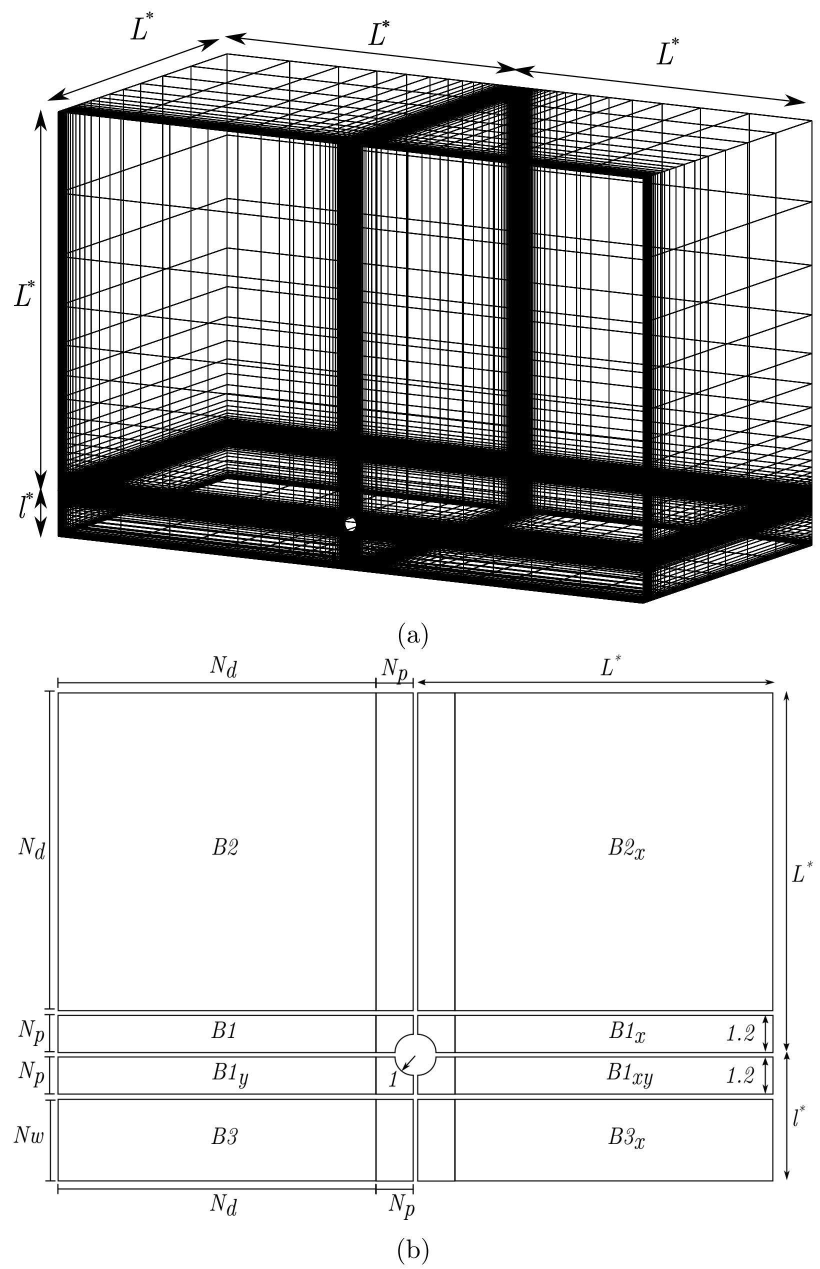

FIGURE 5.2: Mesh construction (a) The domain mesh for a particle located at $l/a = 4$. (b) A detailed 2D frame at $z = 0$ of 'lego' mesh showing how individual blocks are duplicated to form the complete mesh. $N_{\mathrm{d}}, N_{\mathrm{p}}$ and N_{w} indicate number of points, while L^*, l^* are dimensionless domain sizes.

the bounding box are enforced by employing a 'lego' type construction (Figure 5.2b) whereby groups of mesh 'blocks' are copied, translated, rotated and joined to construct the full computational domain. For example, a single block mesh ($B1$) is copied and then rotated about the $x = 0$ and $y = 0$ axes to create identically discretised blocks that surround the sphere ($B1_{\mathrm{x}}, B1_{\mathrm{y}}$ and $B1_{\mathrm{xy}}$). Similarly, the upper and lower mesh domain blocks are built using two separate block mesh entities, $B2$ and $B3$ as illustrated in figure 5.2b, which are later rotated about $x = 0$ axis. For an example, this mesh configuration ensures that we compute the zero lift force on a slip free particle to high numerical accuracy ($F_{\mathrm{L}}^* \sim 10^{-15}$) under Stokes conditions. The shear and slip Reynolds numbers considered in this study are sufficiently small to assume flow symmetry about the $z = 0$ plane. Hence a final domain size of $x \in [-L, L]$, $y \in [-l, L]$ and $z \in [0, L]$ is used for simulations.

Note that we tried several meshing software in an attempt to enforce the symmetry of the mesh (not detailed here); however, none were able to produce a perfectly symmetric mesh. Hence, we presented the concept of the 'lego' mesh, which used identical mesh blocks around the particle to strictly enforce symmetry, with individual blocks constructed using the open-source software *gmsh* [90].

5.4.1 Domain size dependency

The domain size is first tested to determine a suitable choice of L^* such that the lift and drag forces are negligibly affected by this parameter. For the zero-slip case, we perform a series of simulations where L^* is increased from 20 to 100. Simulations are performed for seven selected shear Reynolds numbers; $Re_\gamma = (1, 2, 4, 6, 8) \times 10^{-3}, 10^{-2}$ and 10^{-1}; and five selected wall distances; $l^* = 1.2, 2, 4, 6$ and 9.5; at $Re_{\mathrm{slip}} = 0$. For quiescent flow (zero-shear) condition, simulations are performed for three selected slip Reynolds numbers; $Re_{\mathrm{slip}} = 10^{-3}, 10^{-2}$ and 10^{-1} and for seven wall distances; $l^* = 1.2, 2, 3, 4, 6, 8$ and 9.5; at $Re_\gamma = 0$. In both cases, the number of mesh points in the domain (N_{d}) is systematically increased with L^* while maintaining a constant progression ratio (β) and a constant minimum cell thickness in the outer domain.

The lift and drag coefficients corresponding to zero-slip and zero-shear flows and the percentage differences (δ) for these coefficients relative to the corresponding values obtained using the maximum domain size (L^*) are examined. We use δ as an indicator of the coefficient accuracy, noting the limitations of this measure as we approach the maximum domain size. For example, a decrease in δ as L^* increases will only indicate the reduction in error relative to the largest domain.

l^*	Re_γ	Domain		Non-rotating				Freely-rotating			
				Lift		Drag		Lift		Drag	
		L^*	N_t	$C_{L,1}$	$\delta\%$	$-C_{D,1}$	$\delta\%$	$C_{L,1}$	$\delta\%$	$-C_{D,1}$	$\delta\%$
		20	124672	1.8644	6.46	-8.4178	0.54	1.7101	4.33	-7.9135	0.35
		40	149710	1.9597	1.68	-8.4576	0.07	1.7674	1.12	-7.9373	0.05
	0.001	50	158976	1.9740	0.96	-8.4608	0.04	1.7759	0.64	-7.9392	0.02
		80	178960	1.9901	0.16	-8.4634	0.00	1.7866	0.11	-7.9407	0.00
		100	189702	1.9933	-	-8.4638	-	1.7874	-	-7.9409	-
		20	124672	1.8565	3.84	-8.4162	0.49	1.7049	2.54	-7.9124	0.31
1.2		40	149710	1.9258	0.25	-8.4534	0.05	1.7465	0.16	-7.9346	0.03
	0.01	50	158976	1.9296	0.06	-8.4558	0.02	1.7487	0.04	-7.9360	0.01
		80	178960	1.9307	0.00	-8.4576	0.00	1.7493	0.00	-7.9371	0.00
		100	189702	1.9307	-	-8.4578	-	1.7493	-	-7.9372	-
		20	124672	1.6215	0.23	-8.3313	0.36	1.5453	0.16	-7.8553	0.22
		40	149710	1.6188	0.06	-8.3570	0.05	1.5435	0.04	-7.8703	0.03
	0.1	50	158976	1.6183	0.04	-8.3591	0.03	1.5432	0.02	-7.8715	0.02
		80	178960	1.6179	0.01	-8.3610	0.00	1.5429	0.00	-7.8726	0.00
		100	189702	1.6178	-	-8.3614	-	1.5429	-	-7.8728	-
		20	186112	0.8483	55.99	-0.0223	66.42	0.8752	50.86	-0.0396	41.27
		40	223210	1.5593	19.12	-0.0513	22.74	1.5107	15.18	-0.0580	14.02
	0.001	50	236736	1.6964	12.00	-0.0577	13.15	1.6180	9.15	-0.0620	8.08
		80	265600	1.8814	2.41	-0.0649	2.27	1.7503	1.73	-0.0665	1.39
		90	265600	1.9091	0.97	-0.0658	0.94	1.7690	0.68	-0.0670	0.60
		100	280962	1.9278	-	-0.0664	-	1.7810	-	-0.0674	-
9.5		20	186112	0.8203	41.60	-0.0212	62.32	0.8487	38.20	-0.0387	35.83
		40	223210	1.3488	3.98	-0.0459	18.28	1.3288	3.23	-0.0540	10.42
	0.01	50	236736	1.3882	1.17	-0.0505	10.07	1.3607	0.91	-0.0569	5.74
		80	265600	1.4042	0.03	-0.0552	1.70	1.3729	0.02	-0.0597	0.97
		90	265600	1.4047	0.00	-0.0558	0.72	1.3734	0.01	-0.0601	0.44
		100	280962	1.4047	-	-0.0562	-	1.3732	-	-0.0603	-
		20	186112	0.2091	18.88	0.0159	42.33	0.2600	14.79	-0.0101	21.84
		40	223210	0.2542	1.39	0.0154	37.30	0.3026	0.83	-0.0107	17.35
	0.1	50	236736	0.2569	0.33	0.0139	24.06	0.3045	0.20	-0.0114	11.56
		80	265600	0.2579	0.05	0.0118	4.97	0.3052	0.03	-0.0126	2.50
		90	265600	0.2578	0.02	0.0115	2.25	0.3053	0.05	-0.0128	1.28
		100	280962	0.2578	-	0.0112	-	0.3051	-	-0.0129	-

TABLE 5.1: Effect of domain size on drag and lift coefficients for maximum and minimum separation distances ($l^* = 1.2$ and 9.5) and shear Reynolds number ($Re_\gamma = 10^{-3}$ and 10^{-1}) at $Re_{\text{slip}} = 0$. δ is the percentage error in coefficient, relative to results calculated using the largest domain size ($L^* = 100$).

5.4.1.1 Zero-slip flow

Results for the lift and drag coefficients, $C_{\mathrm{L},1}$ and $C_{\mathrm{D},1}$ respectively, for the minimum and maximum separation distances ($l^* = 1.2$ and 9.5, respectively) and minimum and maximum shear Reynolds numbers ($Re_\gamma = 10^{-3}$ and 10^{-1}) are shown in table 5.1. Also shown are the percentage differences (δ).

For $Re_\gamma \geq 10^{-2}$, a domain size of $L^* = 50$ is sufficient to capture all the inertial effects responsible for the lift forces, with δ less than 1% for all separation distances ($1.2 \leq l^* \leq 9.5$) under both non-rotating and freely-rotating conditions. In contrast, for low shear Reynolds numbers, for example the conditions of $Re_\gamma = 10^{-3}$, non-rotating (freely-rotating) particles and a domain size of $L^* = 50$, an increase of δ from $\sim 0.96\%$ (0.64%) to $\sim 12\%$ (9.15%) is observed as the separation distance increases from $l^* = 1.2$ to 9.5. For smaller separation distances (i.e. $l^* = 1.2$), even at low Re_γ, smaller values for δ are expected as wall effects dominate outer boundary effects in this near-to-wall regime [76]. However, when the distance to the wall is large and Re_γ low, the lift force is quite sensitive to the location of the outer boundary. Noting that the boundary layer thickness around a translating sphere in an unbounded environment is inversely proportional to $Re_{\mathrm{slip}}^{1/2}$ [62], it follows that larger domain sizes are required to minimise outer boundary effects when Re_γ is small [62]. Therefore, for the simulations where $Re_\gamma < 10^{-2}$, a larger domain size of $L^* = 100$ is used in this study, compared to the domain size of $L^* = 50$ used for the higher Re_γ situations. Using this strategy we believe the accuracy of all presented lift coefficients to be better than 1%, with the possible exception of values calculated using the combination of the lowest Re_γ and highest l^* values considered.

For drag, the accuracy of the drag coefficient calculation is largely a function of wall separation distance. With the selected domain size of $L^* = 50$ that is used for the $Re_\gamma \geq 10^{-2}$ results, $\delta < 1\%$ only for $l^* \leq 4$. Further away from the wall, a notable dependency on domain size is found, with a δ variation of $\sim 5\%$ (2%) to 24% (12%) for non-rotating (freely-rotating) conditions as l^* increases from 6 to 9.5 for $Re_\gamma = 10^{-1}$. Results for $Re_\gamma = 10^{-3}$ are similar. Also at these larger separation distances, specifically at $l^* = 8$ and 9.5, small negative drag coefficients are observed for $C_{\mathrm{D},1}$ when $Re_\gamma = 10^{-1}$ (noting that results for $l^* = 4, 6, 8$ are not presented in the table). The small negative values for $C_{\mathrm{D},1}$ and larger δ values found at large separation distances are caused by small errors in $F^*_{\mathrm{D},1}$ which are amplified when expressed as a relative drag coefficient error, because as the separation distance increases, both the coefficients and the force approach zero. Note however that while the drag coefficient errors are higher at the largest separation distances, an 11% change in domain size from $L^* = 90$ to 100 results in less than a 1% change in drag coefficient (for $Re_\gamma = 10^{-3}$), suggesting that the results are close to independent of domain size. In summary, while the errors in the calculated drag coefficients are larger than for lift, the largest errors occur under conditions in which the drag force is low. Under conditions in which the drag force is appreciable, the error in the drag force coefficient is similar to that reported for the lift force coefficient.

5.4.1.2 Quiescent flow

The lift and drag coefficients, $C_{\mathrm{L},3}$ and $C_{\mathrm{D},2}$ respectively are shown in table 5.2 for the minimum and maximum separation distances ($l^* = 1.2$ and 9.5) and minimum and maximum slip Reynolds numbers ($Re_{\mathrm{slip}} = 10^{-3}$ and 10^{-1}). The percentage difference of each force coefficient relative to the values obtained using the maximum domain size ($L^* = 120$), δ, is used an indicator of the coefficient accuracy.

For all non-rotating and freely-rotating cases, a domain size of $L^* = 100$ is sufficient to capture the inertial effects responsible for lift results, since $|\delta| \ll 1\%$, with the exception of lift results at $l^* = 9.5$ and $Re_{\mathrm{slip}} = 10^{-3}$. However, even for these conditions, increasing the domain size by 20% (from $L^* = 100$ to $L^* = 120$) only results in a change in $C_{\mathrm{L},3}$ of less than 1%. For smaller separation distances (i.e., $l^* = 1.2$), the reported δ values are very small as the near-wall effects dominate outer boundary effects [76]. The δ values calculated for drag force coefficients are again much less than 1% for the selected domain size of $L^* = 100$ for all separation distances. Hence, a domain size of $L^* = 100$ is used for all simulations in this study.

5.4.2 Mesh dependency

The effect of mesh resolution within the boundary layers surrounding the sphere is first examined in this section. The number of inflation layers around the sphere and the number of cells on the sphere surface were adjusted by varying N_p while maintaining the same progression rate α in the bounding box. Concurrently, N_d was also changed, maintaining $N_\mathrm{d} = N_\mathrm{p}$ for all cases.

l^*	Re_{slip}	Domain		Non-rotating				Freely-rotating			
				Lift		Drag		Lift		Drag	
		L^*	N_{t}	$C_{\text{L},3}$	$\|\delta\%\|$	$-C_{\text{D},2}$	$\|\delta\%\|$	$C_{\text{L},3}$	$\|\delta\%\|$	$-C_{\text{D},2}$	$\|\delta\%\|$
1.2	0.001	50	158976	1.7828	1.6284	-36.831	0.1792	1.7121	1.8196	-36.786	0.1858
		100	189702	1.7545	0.0138	-36.766	0.0026	1.6818	0.0165	-36.719	0.0027
		120	200960	1.7542	-	-36.765	-	1.6815	-	-36.718	-
	0.1	50	158976	1.7653	1.2595	-36.849	0.1410	1.6947	1.4308	-36.804	0.1464
		100	189702	1.7434	0.0149	-36.798	0.0019	1.6711	0.0175	-36.751	0.0020
		120	200960	1.7431	-	-36.797	-	1.6708	-	-36.751	-
9.5	0.001	50	236736	1.7086	5.6979	-20.222	0.7455	1.7096	5.6488	-20.222	0.7454
		100	280962	1.8037	0.4493	-20.084	0.0563	1.8039	0.4444	-20.084	0.0562
		120	296960	1.8118	-	-20.072	-	1.8120	-	-20.072	-
	0.1	50	236736	1.5206	2.5743	-20.362	0.5574	1.5215	2.5324	-20.362	0.5574
		100	280962	1.5597	0.0723	-20.256	0.0348	1.5600	0.0685	-20.256	0.0348
		120	296960	1.5608	-	-20.249	-	1.5611	-	-20.249	-

TABLE 5.2: Effect of domain size on drag and lift coefficients for maximum and minimum separation distances ($l^* = 1.2$ and 9.5) and slip Reynolds number ($Re_{\text{slip}} = 10^{-3}$ and 10^{-1}) at $Re_\gamma = 0$. δ is the percentage error in coefficient, relative to results calculated using the largest domain size ($L^* = 120$).

5.4.2.1 Zero-slip flow

Figure 5.4 shows the resulting lift coefficients and non-dimensionalised lift forces for four mesh refinement levels around the sphere and for the conditions of $l^* = 1.2$, a domain size of $L^* = 50$, and a range of shear Reynolds numbers. As $F^*_{\text{L},1}$ reduces to zero, $C_{\text{L},1}$ asymptotes to different finite values as Re_γ approaches zero. A considerable variation of $C_{\text{L},1}$ with mesh refinement is observed, particularly at low Re_γ, however the relative change in $C_{\text{L},1}$ decreases as N_{p} and N_{d} increase. Indeed, increasing N_{p} and N_{d} from 25 to 30 only changes $C_{\text{L},1}$ by a small amount, but concurrently increases the total cell count N_{t} from 158,976 to 310,500, significantly increasing computational memory requirements ($\sim$ 1.2 TB of RAM). Noting that for low Re_γ the force will be negligible anyway, and that across the entire Re_γ range the difference between the $N_{\text{p}}, N_{\text{d}} = 25$ and $N_{\text{p}}, N_{\text{d}} = 30$ results is small anyway, we employed the mesh with $N_{\text{p}}, N_{\text{d}} = 25$ for the remainder of the study.

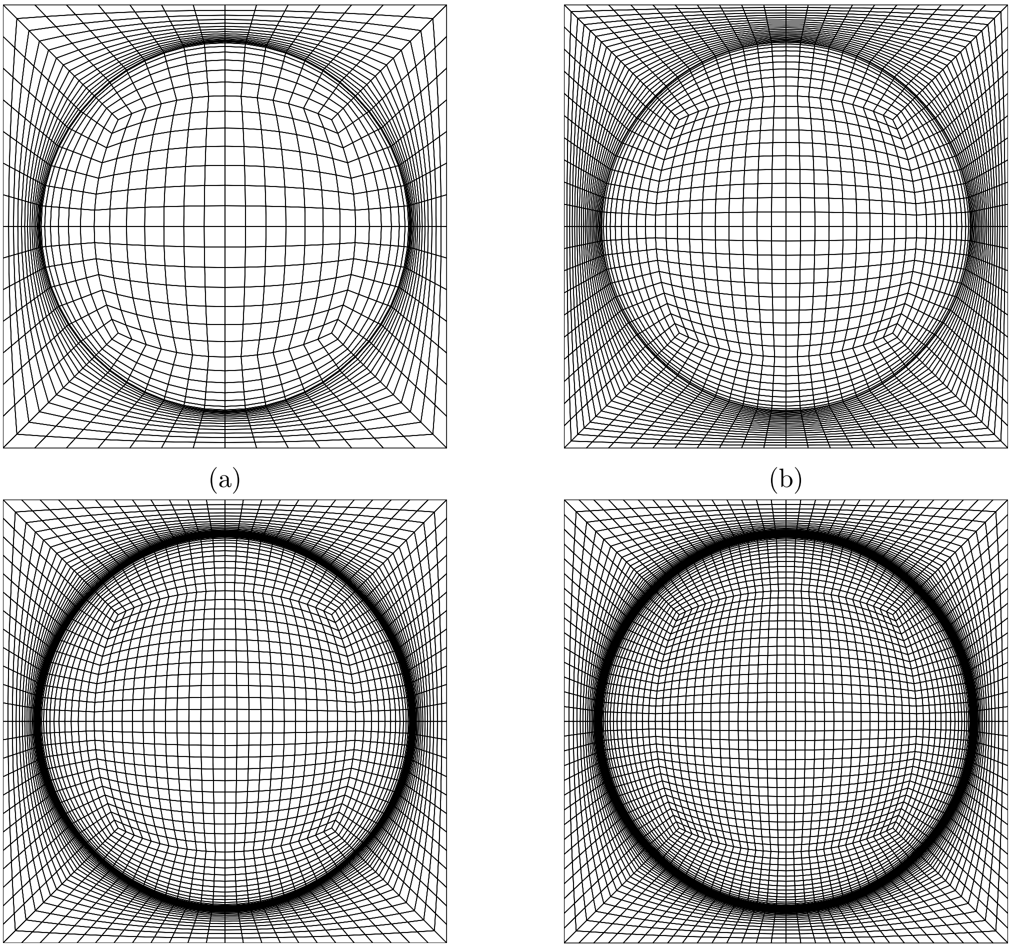

(a) (b) (c) (d)

FIGURE 5.3: Mesh resolution around the sphere when $N_{\mathrm{p}}, N_{\mathrm{d}}$ = (a) 15, (b) 20, (c) 25 and (d) 30

5.4.2.2 Quiescent flow

Figure 5.5 shows the variation of lift coefficients and non-dimensionalised lift forces as a function of Re_{slip} for four mesh refinement levels. The simulations are performed for the smallest separation distance $l^* = 1.2$ with a domain size of $L^* = 100$. As Re_{slip} approaches zero, F_{L}^* reduces to zero while $C_{\mathrm{L},3}$ asymptotes to different finite values. While results for F_{L}^* appear to be independent of mesh refinement, $C_{\mathrm{L},3}$ exhibits considerable variation with mesh refinement, particularly for low Re_{slip} values. This relative difference in $C_{\mathrm{L},3}$ decreases as N_{p} increases. For example, at the lowest Re_{slip} value, $C_{\mathrm{L},3}$ changed by 3.77% as N_{p} is increased from 15 to 25, but changes by only 0.37% as N_{p} is increased from 25 to 30. Noting the significant increase of the total cell count N_{t} from 158,976 to 310,500 with increasing N_{p} from 25 to 30 and by considering the computational memory requirements, we employed the mesh with $N_{\mathrm{p}} = 25$ for the remainder of the study.

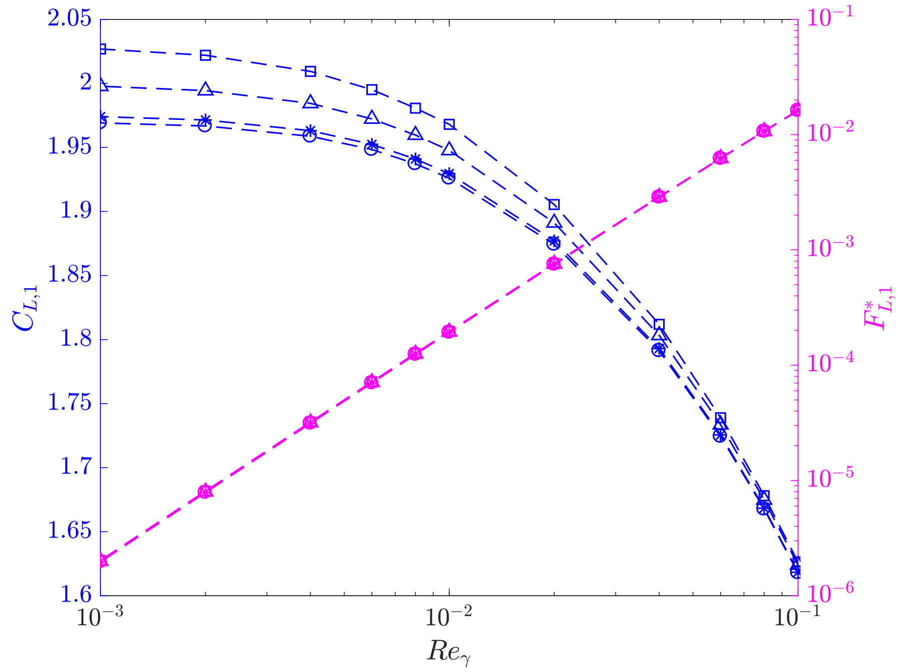

FIGURE 5.4: Effect of mesh resolution around the sphere on $C_{\mathrm{L},1}$ for a non-rotating particle at $l^* = 1.2$. $N_\mathrm{p}, N_\mathrm{d} = 15$ (—□—); 20 (—△—); 25 (—∗—); 30 (—○—).

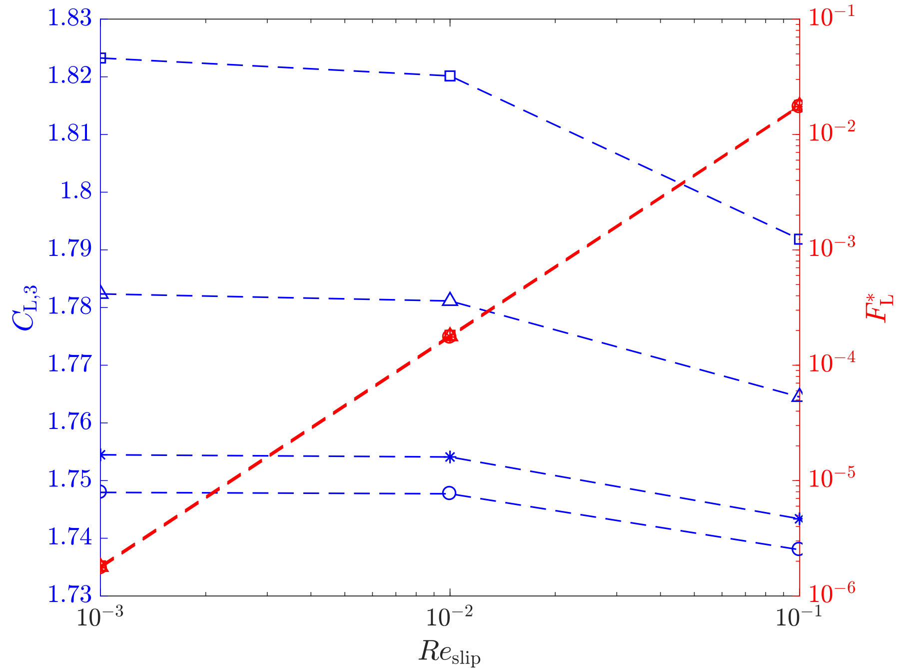

FIGURE 5.5: Effect of mesh resolution around the sphere on $C_{\mathrm{L},3}$ for a non-rotating particle at $l^* = 1.2$. $N_\mathrm{p} = 15$ (—□—); 20 (—△—); 25 (—∗—); 30 (—○—).

The effect of mesh resolution between the the sphere and bottom wall is also examined for a non-rotating particle. The number of cells of the bottom blocks ($B3$ and $B3_\mathrm{x}$) were adjusted by varying the double progression rate β while matching the bottom (maximum) inflation layer thickness of the bounding box for the selected $N_\mathrm{p} = 25$ case. As a result,

Domain			Lift		Drag	
β	$N_{\rm w}$	$N_{\rm t}$	$C_{\rm L,1}$	$\delta\%$	$-C_{\rm D,1}$	$\delta\%$
1.28	24	216000	2.0289	0.018	-0.4095	0.263
1.15	32	236736	2.0290	0.012	-0.4089	0.111
1.025	64	319680	2.0292	0.002	-0.4087	0.072
1	92	392256	2.0293	-	-0.4086	-

TABLE 5.3: Effect of mesh resolution around the sphere on $C_{\rm L,1}$ and $C_{\rm D,1}$ for a non-rotating particle at $l^* = 4$ and $Re_\gamma = 10^{-3}$. δ is the percentage error in coefficient, relative to results calculated using the lowest progression ratio ($\beta = 1$).

$N_{\rm w}$ and $N_{\rm d}$ were also changed for all cases. Results for the lift and drag coefficients, $C_{\rm L,1}$ and $C_{\rm D,1}$ respectively, for the separation distance $l^* = 4$ and minimum shear Reynolds number ($Re_\gamma = 10^{-3}$ are shown in table 5.3. Also shown are the percentage differences (δ).

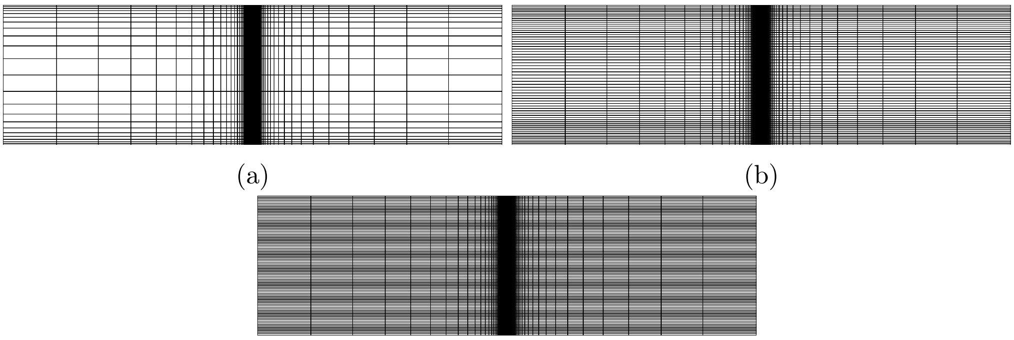

(a) (b) (c)

FIGURE 5.6: Mesh resolution between the sphere and the wall when $\beta =$ (a) 1.28, (b) 1.025 and (c) 1 for $l^* = 4$

A small variation of $C_{\rm L,1}$ and $C_{\rm D,1}$ with mesh refinement is observed, indicating the relative change in $C_{\rm L,1}$ decreases as β and decreases. Indeed, decreasing β from 1.28 to 1 only changes $C_{\rm L,1}$ and $C_{\rm D,1}$ by a small amount, but concurrently increases the total cell count $N_{\rm t}$ from 216000 to 236736, significantly increasing computational memory requirements. Noting that the difference between the $\beta = 1.28$ and $\beta = 1$ results is small, we employed meshes with $\beta = 1.28$ for the remainder of the study.

5.5 Closure

The numerical setup developed for the direct particle simulations is discussed in this chapter. Both domain size effects and mesh resolution were tested to select meshes such that lift and drag forces are negligibly affected by those parameters.

Sensitivity analyses show that large computational flow domains, combined with careful mesh construction, are required to accurately predict these forces at these low shear rates and wall separations.

Chapter 6

Particle Moving with Zero-Slip in a Linear Shear Flow Near a Wall

6.1 Introduction

The primary aim of the present chapter is to investigate the forces acting on a particle under zero-slip conditions ($Re_{\mathrm{slip}} = 0$). In §6.2 and 6.3, we express our numerical results as new zero-slip lift and drag coefficient ($C_{\mathrm{L},1}$ and $C_{\mathrm{D},1}$, respectively) correlations, expressed as per Eq. (5.1) and Eq. (5.2) respectively, now defined across the inner, outer and unbounded regions. In §6.4, we apply the new zero-slip drag and lift correlations together with existing slip-based drag and lift correlations to analyse the motion of force-free (zero drag) and freely-rotating (zero torque) particles near a wall in a linear shear flow. Note that in this chapter we do use the full form of Eqs. (5.1) and (5.2) when applying our new correlations to analyse the movement of force-free particles translating near wall, using existing literature expression for the remaining force coefficients.

A rigid spherical particle moving at the same velocity as the fluid ($u_{\mathrm{slip}} = 0$) in a linear shear flow tangential to a flat wall is considered. We study non-rotating as well as freely-rotating spheres, for shear Reynolds numbers (Re_γ) in the range of 10^{-3} to 10^{-1}.

This chapter is mainly based on the author's paper: Ekanayake, N. I., Berry, J. D., Stickland, A. D., Dunstan, D. E., Muir, I. L., Dower, S. K. & Harvie, D. J. E. (2020). Lift and drag forces acting on a particle moving with zero slip in a linear shear flow near a wall. *Journal of Fluid Mechanics*, 904, A6.

6.2 Lift force

In figure 6.1, the lift coefficient $C_{\mathrm{L},1}$, computed for both non-rotating and a freely-rotating particles, is plotted as a function of separation distance ($l^* = l/a$). The numerical results are compared with the available inner region correlations listed in table 3.5 that are valid for $Re_\gamma \ll 1$ and $Re_{\mathrm{slip}} = 0$. For $Re_\gamma < 10^{-2}$, the numerically computed lift forces in the region close to the wall ($l^* < 2$) agree reasonably well with the asymptotic values predicted by the analytical solutions derived for low Reynolds numbers [45, 131]. Specifically, the lowest shear Reynolds number simulation conducted at the smallest distance to the wall ($l^* = 1.2$) gives a $C_{\mathrm{L},1}$ of 1.993 (1.787) for a non-rotating (freely-rotating) particle, which is only $\sim 1.3\%$ (5.2%) higher than the asymptotic value of 1.9680 (1.6988) predicted for a non-rotating (freely-rotating) particle at $l^* = 1$ [131]. The computed lift coefficients also agree very well with the low Reynolds number theoretical values of 1.9834 (1.7854) for non-rotating (freely-rotating) particles at $l^* = 1.2$, as predicted by Cherukat and McLaughlin [45]. However, as illustrated in figure 6.1b, for a freely-rotating particle the Magnaudet et al. [156] lift correlation predicts a larger coefficient of 2.81 at $l^* = 1$ which is inconsistent with the numerical data and the available theories in this region. As explained in Shi and Rzehak [227], this over-prediction of the lift coefficient near the wall is due to the neglect of the higher order separation distance terms ($\mathcal{O}(1/l^*) > 2$) that are significant when representing lift in the vicinity of the wall. At large l^* the Magnaudet et al. [156] lift correlation gives $C_{\mathrm{L},1} = 1.8$, a result that is consistent with the large l^* value from the Cox and Hsu [58] lift correlation. However, like all inner region based models, this large separation limit only has practical relevance for very small Reynolds numbers.

As Re_γ increases and inertial effects become more significant, the computed lift coefficients deviate significantly from the available theoretical values. Even when the wall is far away from the particle but still within the inner region (eg. results for $Re_\gamma < 10^{-2}$), the computed lift force coefficient decreases with shear rate, in contrast to the available inner region models which give coefficients that are independent of Re_γ. For example, the Cherukat and McLaughlin [45] model gives a $C_{\mathrm{L},1}$ of 2.0069 (1.8065) for a non-rotating (freely-rotating) particle as $l^* \to \infty$. Eventually, with increasing shear rate and increasing separation distance, the walls move to the outer region ($l^*/{L_\mathrm{G}}^* > 1$) and unsurprisingly, the inner region based models do not capture the lift coefficient variation

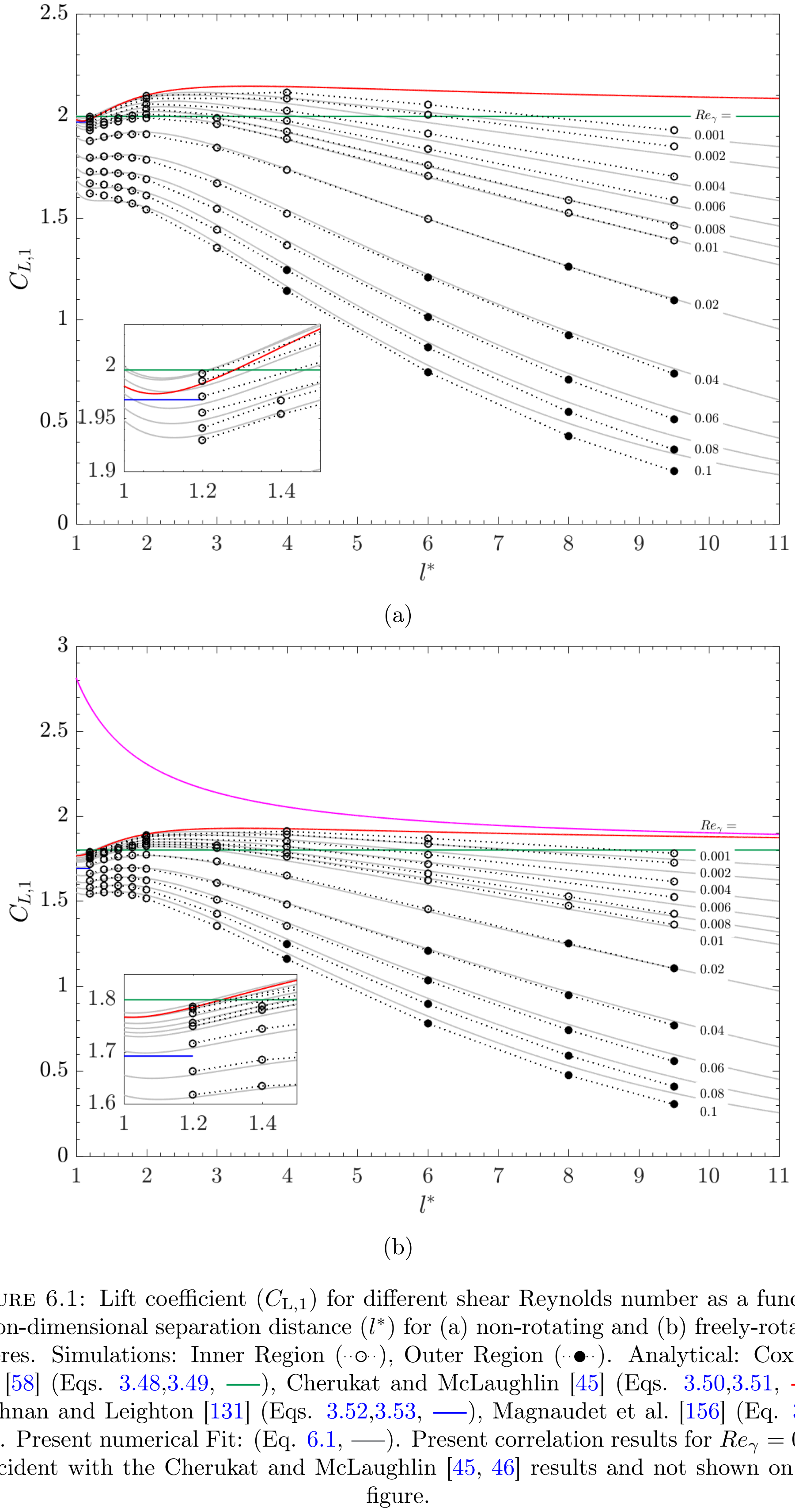

FIGURE 6.1: Lift coefficient ($C_{\mathrm{L},1}$) for different shear Reynolds number as a function of non-dimensional separation distance (l^*) for (a) non-rotating and (b) freely-rotating spheres. Simulations: Inner Region (··○··), Outer Region (··●··). Analytical: Cox and Hsu [58] (Eqs. 3.48,3.49, ——), Cherukat and McLaughlin [45] (Eqs. 3.50,3.51, ——), Krishnan and Leighton [131] (Eqs. 3.52,3.53, ——), Magnaudet et al. [156] (Eq. 3.54, ——). Present numerical Fit: (Eq. 6.1, ——). Present correlation results for $Re_\gamma = 0$ are coincident with the Cherukat and McLaughlin [45, 46] results and not shown on this figure.

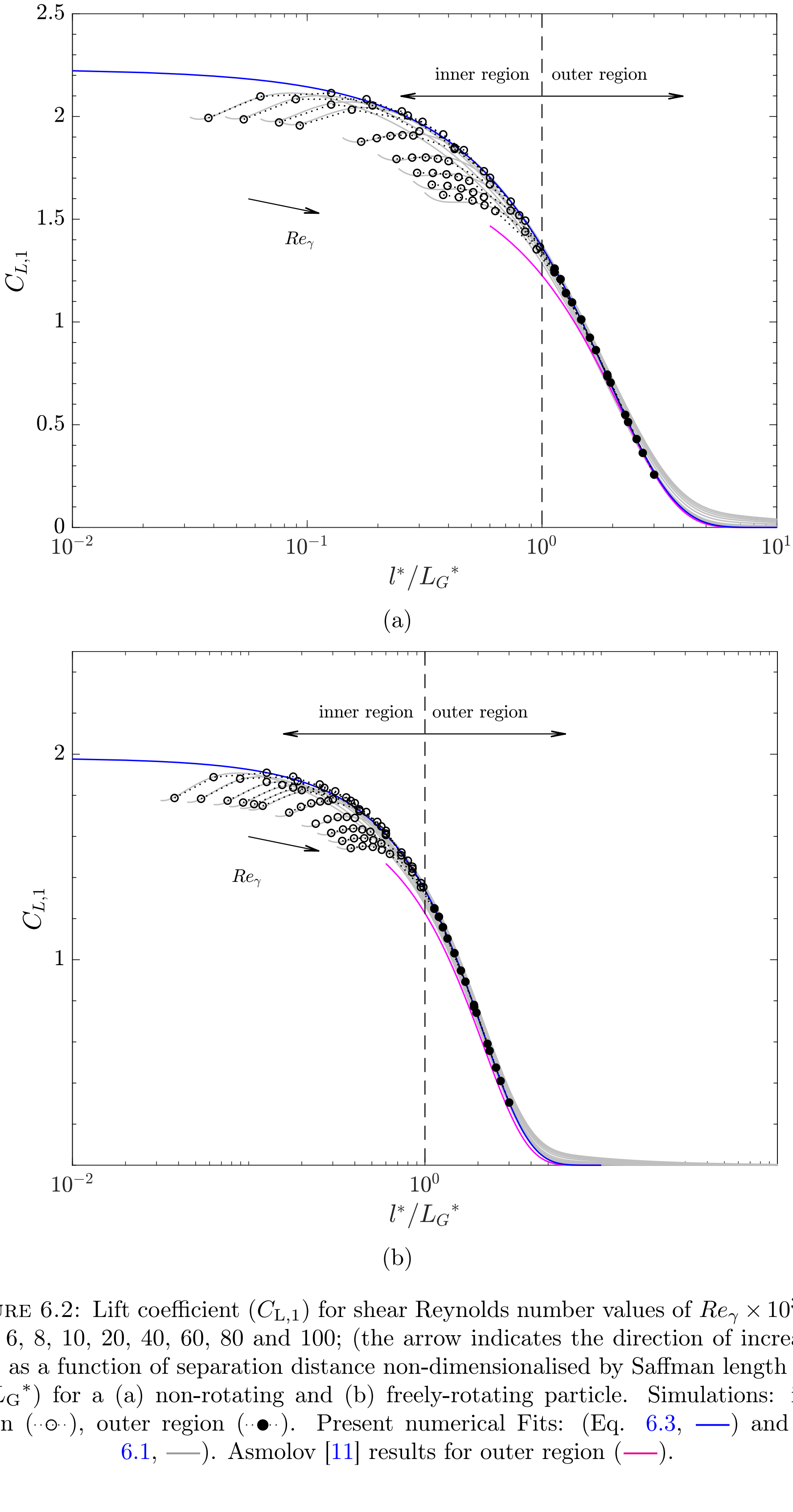

FIGURE 6.2: Lift coefficient ($C_{\mathrm{L},1}$) for shear Reynolds number values of $Re_\gamma \times 10^3 = 1$, 2, 4, 6, 8, 10, 20, 40, 60, 80 and 100; (the arrow indicates the direction of increasing Re_γ) as a function of separation distance non-dimensionalised by Saffman length scale ($l^*/L_{\mathrm{G}}{}^*$) for a (a) non-rotating and (b) freely-rotating particle. Simulations: inner region (··○·), outer region (··●·). Present numerical Fits: (Eq. 6.3, ——) and (Eq. 6.1, ——). Asmolov [11] results for outer region (——).

well at all. Hence the available inner region based theoretical lift models overestimate the lift coefficient for all but the lowest shear Reynolds numbers, for particles both near

Coefficient	Non-rotating	Freely-rotating
λ_1	0.9300	0.9250
λ_2	-0.8800	-0.3500
λ_3	-0.0300	-0.0135
λ_4	-1000	-7000
λ_5	2.231	1.982
λ_6	-0.1054	-0.1150
λ_7	-0.3859	-0.2771
$\lambda_8{}^\dagger$	1.0575	0.89934
$\lambda_9{}^\dagger$	-2.4007	-1.9610
$\lambda_{10}{}^\dagger$	1.3174	1.0216

Table 6.1: Coefficients for Eq. (6.1) for a non-rotating and freely-rotating particle. †coefficients from Cherukat and McLaughlin [45] & Cherukat and McLaughlin [46].

and (especially) further away from the wall.

The discrepancy between simulation and theory arises for the inner region based models because they use a first-order expansion for the disturbance velocity that cannot satisfy the boundary conditions at infinity [45]. For many applications relevant to cell sorting in microfluidics, or to understand mechanical phenomena like particle deposition and fouling at $Re_\gamma \lesssim \mathcal{O}(1)$, this is problematic, and a single equation for the wall-induced lift force valid across both the inner and outer regions would be beneficial. Therefore, as well as providing a shear-based inertial correction for the analytical inner region model of Cherukat and McLaughlin [45], we here propose a model that simultaneously captures the outer and inner region behaviour.

In this vein, we first plot the computed lift force coefficients against the separation distance, now normalised using Saffman's length scale (L^*_{G}). Recall that this length scale defines the boundary between the inner and outer regions in this problem. These results, shown in figure 6.2, indicate that the outer region data ($l^*/L^*_{\mathrm{G}} > 1$) collapses to a single curve for the selected range of shear Reynolds numbers, similar to the results given for a freely-rotating particle at $Re_\gamma \ll 1$ presented by Asmolov [11]. The difference between a non-rotating and freely-rotating lift coefficient value is less significant in the outer region, particularly at $l^*/L^*_{\mathrm{G}} \gg 1$. Utilising this outer region behaviour, together with the existing low Re_γ inner region Cherukat and McLaughlin [45] results, the following lift correlation is proposed for particles moving near a wall under zero-slip conditions:

$$C_{\mathrm{L},1} = f_1(Re_\gamma)C_{\mathrm{L},1}^{\mathrm{wb,out}}(l^*/L_{\mathrm{G}}{}^*) + f_2(Re_\gamma)C_{\mathrm{L},1}^{\mathrm{wb,in}'}(1/l^*) \tag{6.1}$$

where

$$f_1(Re_\gamma) = \lambda_1 \exp(\lambda_2 Re_\gamma) + \lambda_3 \exp(\lambda_4 Re_\gamma); \tag{6.2}$$

$$C_{\mathrm{L},1}^{\mathrm{wb,out}}(l^*/L_{\mathrm{G}}^*) = \lambda_5 \exp\left[\lambda_6\big(l^*/L_{\mathrm{G}}^*\big)^2 + \lambda_7\big(l^*/L_{\mathrm{G}}^*\big)\right]; \tag{6.3}$$

$$f_2(Re_\gamma) = 1 + \sqrt{Re_\gamma}; \tag{6.4}$$

$$C_{\mathrm{L},1}^{\mathrm{wb,in}'}(1/l^*) = \lambda_8(1/l^*) + \lambda_9(1/l^*)^2 + \lambda_{10}(1/l^*)^3. \tag{6.5}$$

Coefficients for the above functions are listed in table 6.1 for both non-rotating and freely-rotating particles.

The functions used in equation (6.1) represent different limits. Within the inner region, the first term of equation (6.1) rapidly reduces to a constant as both $Re_\gamma \to 0$ and $l^* \to 1$. At $l^* = 1$ and $Re_\gamma = 0$, the product of $f_1(Re_\gamma)C_{\mathrm{L},1}^{\mathrm{wb,out}}$ reduces to the constant value of 2.0079 (1.8065), consistent with the Cherukat and McLaughlin [45] result for a non-rotating (freely-rotating) particle. The function $C_{\mathrm{L},1}^{\mathrm{wb,in}'}$ consists of the non-zero degree polynomial terms of the Cherukat and McLaughlin [45] model. Here $f_2(Re_\gamma)$, which is independent of wall distance, captures inertial effects when the particle is close to the wall. With increasing shear rate ($Re_\gamma \to 0.1$) and wall distance, the first term of the Eq. (6.1) becomes dominant and captures the outer region variation. This term gives zero $C_{\mathrm{L},1}$ as $l^* \to \infty$.

Figure 6.1 shows that the proposed model captures the simulated lift coefficients accurately over most of the Re_γ range and separation distances considered in this study. For low shear rates ($Re_\gamma \sim 10^{-3}$), the model performs well, slightly underestimating the simulated results with a maximum deviation of 1.6% (3.2%) for a non-rotating (freely-rotating) particle at distances far from the wall. For high shear rates ($Re_\gamma \sim 10^{-1}$), the model generally overestimates the simulated results, with a maximum deviation of 41% (21%) for a non-rotating particle (freely-rotating particle) occurring when the particle is furthest from the wall, that is at $l^* = 9.5$. This deviation rapidly reduces down to 4.5% (5.6%) for a non-rotating (freely-rotating) particle when the separation distance decreases to $l^* = 6$, showing that even for the relatively high $Re_\gamma = 10^{-1}$, the proposed model still accurately captures the lift force variation provided that the particle is within a few diameters of the wall. Note that as discussed in §5.4.1, we expect the numerical data to have the highest errors under the same high Re_γ and l^* conditions that generate the largest deviations between correlation and simulation - conditions that also result in low lift forces. Hence, the proposed model captures the variation of lift coefficient with Re_γ and separation distance reasonably well across all conditions considered, but is most accurate when the resulting lift force is most significant.

6.3 Drag force

The drag force on a spherical particle moving parallel to a wall and in the absence of slip is considered in this section. Under these conditions the presence of the wall (combined with the positive shear rate) produces a force on the particle that is in the opposite direction to the flow, and which rapidly decays as the separation distance between the sphere and wall increases. Note that this wall-shear drag causes force-free particles to lag the flow when moving in close proximity to a wall.

Figure 6.3 shows the variation in drag coefficient $C_{\mathrm{D},1}$ for shear Reynolds numbers in the range $Re_\gamma = 10^{-3} - 10^{-1}$ as a function of wall separation distance. Results for both non-rotating and freely-rotating conditions are shown.

Figure 6.3a is specific to non-rotating particles. The highest drag coefficient magnitudes are observed close to the wall, with a rapid decrease occurring with increasing wall distance or increasing Re_γ. For the largest separation considered ($l^* = 9.5$), small negative $C_{\mathrm{D},1}$ values of $\mathcal{O}(10^{-3})$ - $\mathcal{O}(10^{-2})$ are reported for $Re_\gamma = 10^{-1}, 8 \times 10^{-2}$ as illustrated in the inset of figure 6.3a. As discussed in §5.4.1, these small negative drag coefficients are more likely to be due to the limited domain size employed in the simulations (numerical accuracy), rather than being physically meaningful.

Figure 6.3b shows the drag coefficient for a freely-rotating particle as a function of wall distance. The highest positive values for $C_{\mathrm{D},1}$ are obtained when the particle is close to the wall, reducing to zero with increasing wall distance, in a manner similar to that observed for a non-rotating particle. The highest reported $C_{\mathrm{D},1}$ values are $\sim 6\%$ less than the values reported for a non-rotating particle. The simulated drag coefficient results are also compared with the inner region analytical drag correlation of Magnaudet et al. [156]

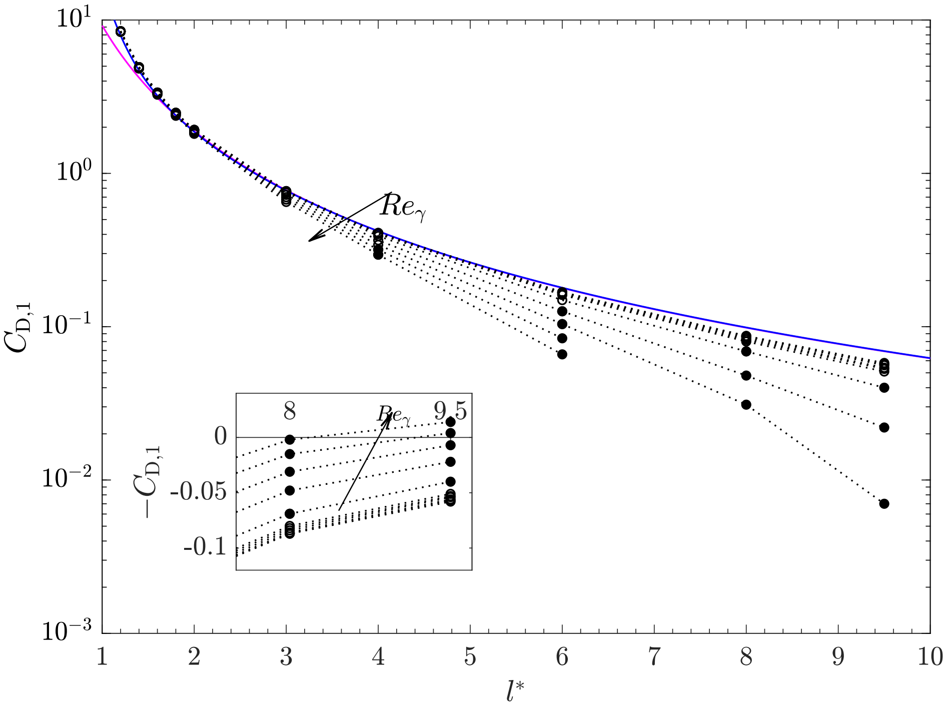

(a)

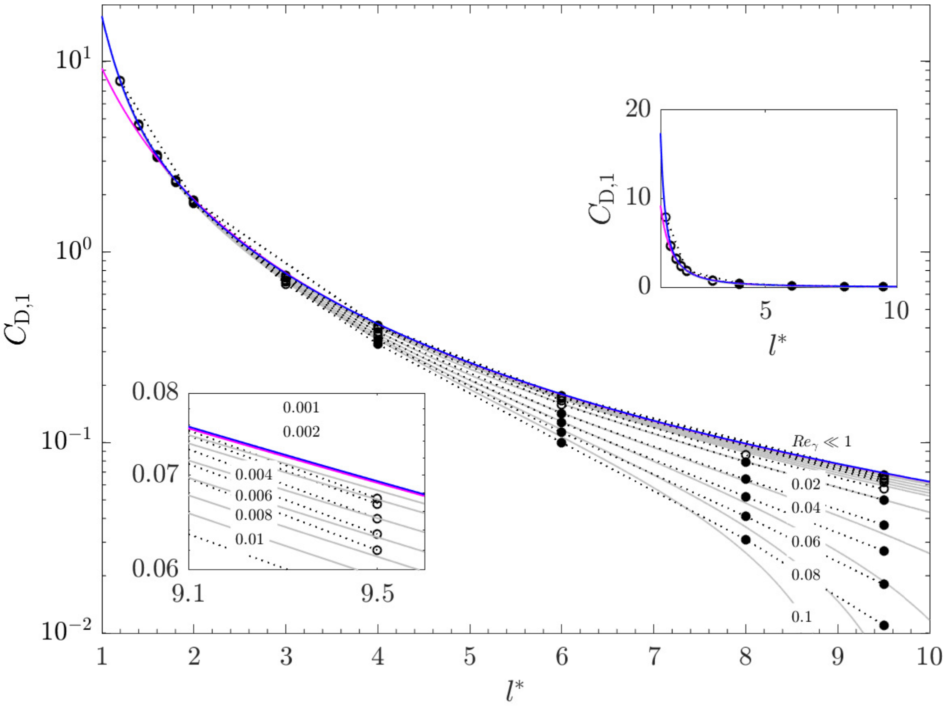

(b)

FIGURE 6.3: Magnitude of drag force coefficient in the absence of slip ($C_{\mathrm{D},1}$) (a) for a non-rotating (b) freely-rotating particle. The arrow indicates the direction of increasing Re_γ. Simulations: Inner Region (··○··), Outer Region (··●··). Analytical prediction of Magnaudet et al. [156] (Eq. (3.26,——). Present numerical fits for $Re_\gamma \ll 1$: Eq. (6.6, ——) and finite Re_γ Eq. (6.7,——).

for a freely-rotating particle at low $Re_\gamma \ll 1$. The computed drag coefficients are in good agreement with the correlation values for Reynolds numbers $Re_\gamma < 10^{-2}$ and for wall distances $l^* > 1.6$. However, as the separation distance decreases ($l^* \to 1$), the theoretical predictions of Eq. (3.26) underestimate the drag, resulting in a difference of $\sim 32\%$ at $l^* = 1.2$. This could again be due to the neglect of higher order terms in the analytical solution, Eq. (3.26). In support of this, in the same study by Magnaudet et al. [156], but for zero-shear flows ($Re_\gamma = 0$), the effect of higher-order l^* terms on $C_{\mathrm{D},2}$ was examined in the context of small separation distances ($l^* < 3$), and it was found that a $\sim 60\%$ difference in this drag coefficient occurred when using $\mathcal{O}((1/l^*)^3)$ over $\mathcal{O}((1/l^*)^5)$ terms in their analysis, for $l^* \to 1$. Similar higher order terms for the $C_{\mathrm{D},1}$ drag coefficient examined in our study are not available in the literature, however.

The freely-rotating drag coefficients shown in Figure 6.3b also display a dependence on shear rate, as well as separation distance. Generally studies of force-free particles and fixed particles give inertial corrections for $C_{\mathrm{D},1}$ and $C_{\mathrm{D},2}$ in terms of the slip velocity (Re_{slip}) [139, 156]. However, in the present zero-slip context these inertial corrections are not relevant, and instead an inertial correction based on Re_γ is required.

Hence, to accurately predict the variation of $C_{\mathrm{D},1}$ in Eq. (5.2) over the shear rates and separation distances considered in this study, we propose a new correlation that is partially based on existing inner region results [156], but includes two modifications.

Firstly, to capture the drag force variation close to the wall at $Re_\gamma \ll 1$, Eq. (3.26) is modified as:

$$C'_{\mathrm{D},1} = \frac{15\pi}{8}\left(\frac{1}{l^*}\right)^2\left[1 + \frac{9}{16}\left(\frac{1}{l^*}\right) + 0.5801\left(\frac{1}{l^*}\right)^2 - 3.34\left(\frac{1}{l^*}\right)^3 + 4.15\left(\frac{1}{l^*}\right)^4\right] \tag{6.6}$$

where $C'_{\mathrm{D},1}$ consists of the terms given by Magnaudet et al. [156] in Eq. (3.26), combined with three new higher-order terms in separation distance derived through a numerical fitting to our simulation results for $Re_\gamma \ll 1$. The proposed correlation accurately captures the computed drag coefficient down to a minimum separation distance of $l^* = 1.2$. When the particle is in contact with the wall ($l^* = 1$), the current model predicts a finite drag coefficient $C_{\mathrm{D},1}$ of 17.392 (compared to a value of 9.204 from Eq. (3.26)). Whilst the proposed model performs better than the Magnaudet et al. [156] correlation at $l^* = 1.2$, for the limiting case of $l^* = 1$ there is no asymptotic value available for $C_{\mathrm{D},1}$ upon which to validate the new expression.

Secondly, we present an inertial correction to the proposed low Re_γ equation (Eq. 6.7), based on fits to our data, that predicts the variation of $C_{\mathrm{D},1}$ with finite Re_γ. Note that this correction is independent of l^*. The final wall-shear drag correlation can be written:

$$C_{\mathrm{D},1} = C'_{\mathrm{D},1} + (3.001 Re_\gamma^2 - 1.025 Re_\gamma) \tag{6.7}$$

where $C'_{\mathrm{D},1}$ is given via equation (6.6). Although the new inertial correction captures the shear dependence of $C_{\mathrm{D},1}$ across all considered separations at low Re_γ, far away from the wall ($l^* > 8$) the coefficient is underestimated for $Re_\gamma > 6 \times 10^{-2}$. Note however that these are the same conditions that result in small $F^*_{\mathrm{D},1}$ contributions to the total F^*_{D}, and the poorest accuracy of the computed $C_{\mathrm{D},1}$, as previously discussed.

6.4 Application of force correlations

In this section, we analyse the movement of a force-free particle in a linear shear flow using the proposed force correlations. This is accomplished in two parts. First, we use the new drag correlation to find the slip velocity of a particle moving near a wall. Second, this slip velocity is combined with the new lift correlation to find the lift force acting on the particle and migration velocity of the particle, accounting for both shear and slip effects.

In order to validate these analytical predictions, a small number of additional simulations were performed for force-free (zero-drag) and torque-free particles. For these simulations the net drag acting on the particle in the flow direction $\boldsymbol{F}_\mathrm{p} \cdot \boldsymbol{e}_\mathrm{x}$ was explicitly set to zero and the slip velocity $\boldsymbol{u}_\mathrm{slip} \cdot \boldsymbol{e}_\mathrm{x}$ in the flow direction was solved for as an unknown.

6.4.1 Slip velocity

The slip velocity of a force-free particle is first calculated by setting the net drag force ($F_\mathrm{D}{}^*$) in Eq. (5.2) to zero. The resulting non-dimensional velocity $u^*_\mathrm{slip}(= Re_\mathrm{slip}/Re_\gamma)$ is:

$$u^*_\mathrm{slip} = -\frac{C_{\mathrm{D},1}}{C_{\mathrm{D},2}} \tag{6.8}$$

The present numerical drag correlation for $C_{\mathrm{D},1}$ provided by Eq. (6.7) is used to evaluate the slip velocity for three finite shear Reynolds numbers ($Re_\gamma = 10^{-1}$, 10^{-2}, 10^{-3}) as well as $Re_\gamma = 0$. In these calculations the Faxen drag correlation given by Happel and Brenner [103] (with higher order terms up to $\mathcal{O}((1/l^*)^5)$) is used to evaluate $C_{\mathrm{D},2}$. Note that this correlation has been derived for the inner region of quiescent flows ($Re_\gamma = 0$) at low slip Reynolds numbers ($Re_{\mathrm{slip}} \ll 1$), and yet we are applying it in this section for finite slip Reynolds number in the presence of shear, and across all three regions (inner, outer and unbounded regions). However, although this Faxen drag model is derived for $Re_{\mathrm{slip}} \ll 1$, Ambari et al. [6] and Takemura [239] experimentally showed that this correlation is valid for $Re_{\mathrm{slip}} \leq 0.1$ in quiescent flows, partly justifying the use of this correlation for the slip Reynolds numbers considered here. Further, in unbounded linear shear flows, Kurose and Komori [139] showed that $C_{\mathrm{D},2}$ is nearly independent of shear rate for $Re_{\mathrm{slip}} < 5$ and $\mathcal{O}(Re_\gamma/Re_{\mathrm{slip}}) < 1$.

It is also worth mentioning that in quiescent flows, L_{S} has been used to define the boundary of the inner and outer regions. However, for non-zero shear flows (as in this case), the inner and outer region boundary is defined based on the $\min(L_{\mathrm{S}}, L_{\mathrm{G}})$ condition. For this specific force-free and torque-free particle case, L_{S} increases rapidly with separation distance since $L_{\mathrm{S}} = Re_{\mathrm{slip}}^{-1} = \nu/u_{\mathrm{slip}}a$ and $u_{\mathrm{slip}} \to 0$ as $l^* \to \infty$ (see figure 6.4). This results in $L_{\mathrm{S}} \gg L_{\mathrm{G}}$ for all the separation distances and all Re_γ values considered in this study. Hence, L_{G} is chosen to define the inner and outer regions. However, with respect to L_{S} (as defined for quiescent flows), the walls are well within the inner region, which may again partly justify the use of $C_{\mathrm{D},2}$ when $L_{\mathrm{G}} < l < L_{\mathrm{S}}$. Hence, while we are applying this $C_{\mathrm{D},2}$ correlation outside its range of validity (i.e., across all three regions and for $Re_\gamma \neq 0$ and $Re_{\mathrm{slip}} \neq 0$), evidence suggests that the associated error should not be large.[a]

The calculated u^*_{slip} values are plotted as a function of separation distance in figure 6.4. The velocities are compared with: i) our numerical predictions, ii) numerical predictions by Fischer and Rosenberger [82] based on a Boundary Element Method (BEM) that included small inertial effects ($Re_\gamma \ll 1$); iii) theoretical/numerical predictions by Goldman et al. [93] applicable to Stokes flow; iv) slip velocities again calculated using Eq. (6.8), but with $C_{\mathrm{D},1}$ evaluated using the Magnaudet et al. [156] correlation of Eq. (3.26).

Consistent with earlier studies [93, 241], the negative slip velocities obtained confirm that a force-free particle translating in a linear shear flow lags the fluid when in close proximity

[a] see chapter 7 for validation of $C_{\mathrm{D},2}$ applicability beyond inner region.

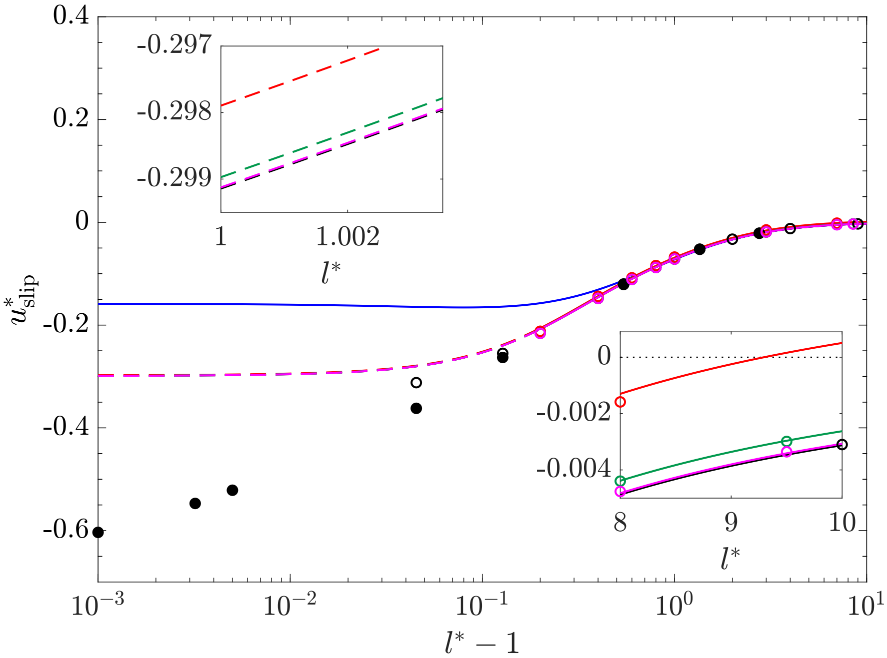

FIGURE 6.4: Non-dimensional slip velocity when $C_{\rm D,1}$ is evaluated using the present numerical correlation, Eq. (6.7) for $Re_\gamma = 0$ (——), $Re_\gamma = 10^{-3}$ (——), $Re_\gamma = 10^{-2}$ (——), $Re_\gamma = 10^{-1}$ (——). Dashed lines indicate results evaluated outside the strict range in which the new correlation has been validated. Slip velocity when $C_{\rm D,1}$ is evaluated using the Magnaudet et al. [156] correlation, Eq. (3.26) for $Re_\gamma = 0$ (——); Fischer and Rosenberger [82] numerical results for $Re_\gamma \ll 1$ (○); Goldman et al. [93] numerical results for Stokes flow (●); present force-free numerical results (coloured hollow circles).

to a wall. The present correlation, Eq. (6.7), used for evaluating $C_{\rm D,1}$ predicts a slip velocity that is consistent with the all available numerical results down to reasonably small separation distances ($l^* \sim 1.1$). In comparison the results obtained using the Magnaudet et al. [156] correlation (Eq. (3.26)) diverge from the numerical results at $l^* \sim 1.5$. At small separation distances ($l^* \lesssim 1.1$) the two numerical results diverge. The predicted Stokes flow velocities from Goldman et al. [93] exhibit large negative values when the particle is almost in contact with the wall ($l^* \sim 1$), whereas the few results of Fischer and Rosenberger [82] in this region, that are valid for small but finite inertial effects, show smaller slip velocities. The difference between Fischer and Rosenberger [82] and Goldman et al. [93] may be due to insufficient numerical accuracy of a Gauss-Legendre product formula used by Fischer and Rosenberger [82], as suggested by Shi and Rzehak [227]. We make no further comment on this difference, but note that the extrapolation of our correlation (indicted by the dashed lines in figure 6.4) appears to be more consistent with the Fischer and Rosenberger [82] results at $l^* = 1.05$ than those of Goldman et al. [93].

Slip velocity curves for the selected range of Reynolds numbers suggest that the shear rate has only a small effect ($\sim \mathcal{O}(10^{-3})$) on u^*_{slip} for all separation distances. As expected, predicted slip velocities reduce to small values with increasing separation distance for the low $Re_\gamma = 10^{-3}, 10^{-2}$ cases. However, for $Re_\gamma = 10^{-1}$ the effect of inertia is relatively more important and the slip velocity further reduces, becoming approximately zero. In fact, small positive slip velocities are predicted under the conditions $Re_\gamma = 10^{-1}$ and $l^* > 9.2$. However, as mentioned in §6.3, numerical inaccuracy of the fitted correlation, Eq. (6.7), at large separation distances for high Re_γ, is more likely to be the main reason that such positive slip velocities are obtained, rather than being physically meaningful. Significantly, the slip velocities are very small in this high separation distance region for all Re_γ considered.

6.4.2 Lift force and migration velocity

By using the slip velocity calculated via Eq. (6.8) and the lift formulation given in Eq. (5.1), the lift force on a force-free particle experiencing both slip and shear within a linear shear flow can be written:

$$\frac{F^*_{\text{L}}}{Re^2_\gamma} = C_{\text{L},1} + C_{\text{L},2} u^*_{\text{slip}} + C_{\text{L},3} {u^*_{\text{slip}}}^2 \tag{6.9}$$

which may also be written in the alternative form:

$$F'_{\text{L,tot}} = F'_{\text{L},1} + F'_{\text{L},2} + F'_{\text{L},3} \tag{6.10}$$

Again note that the form of Eq. (6.10) is valid for all three regions (inner, outer, unbounded), provided that the lift coefficients used are valid in all three regions. Here however, lift force coefficients for $C_{\text{L},2}$ and $C_{\text{L},3}$ are evaluated using the Cherukat and McLaughlin [46] inner region based correlations as there are no correlations available for these coefficients which span all three regions (note: next chapter provides correlations for $C_{\text{L},2}$ and $C_{\text{L},3}$). $C_{\text{L},1}$ is evaluated using our freely-rotating particle correlation, as given by Eq. (6.1), which is valid across all three regions. Here $F'_{\text{L,tot}}(= F^*_{\text{L}}/Re^2_\gamma)$ is the net lift force non-dimensionalised by shear Reynolds number.

The lift contributions, as well as the net lift force, are plotted in figure 6.5 for $Re_\gamma \ll 1$ and $Re_\gamma = 10^{-3}, 10^{-2}, 10^{-1}$. The numerical lift results obtained from our force-free and

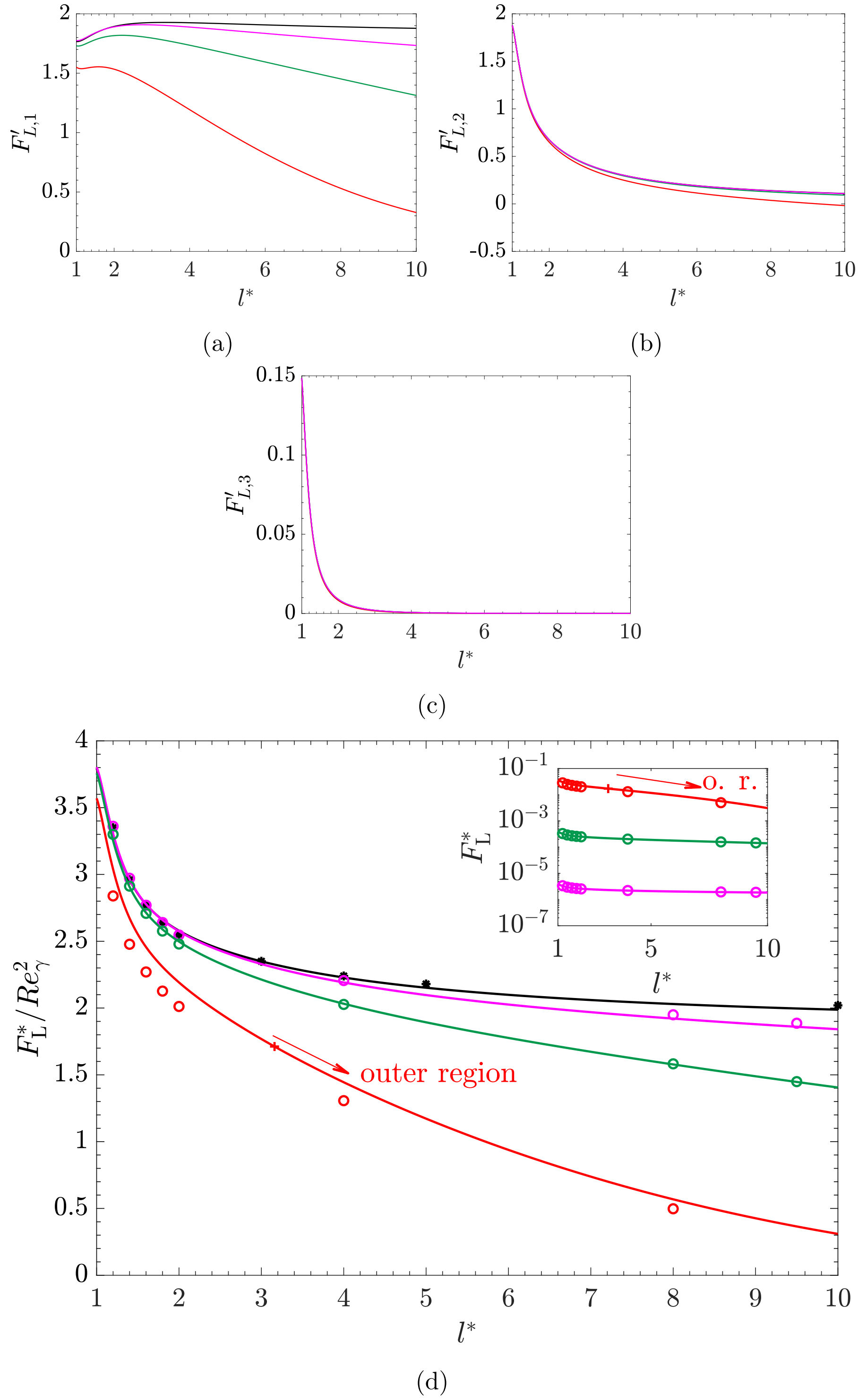

FIGURE 6.5: Analysis of a force-free particle translating in a linear shear flow near a wall. (a-c) Different contributions to the net lift force acting on the particle, $F'_{\mathrm{L},1}, F'_{\mathrm{L},2}$ and $F'_{\mathrm{L},3}$ representing shear, slip-shear and slip effects, respectively. (d) Net lift force non-dimensionalised by shear Reynolds number when $F'_{\mathrm{L,tot}}$ is evaluated using Eq. (6.10) for $Re_\gamma = 0$ (——), $Re_\gamma = 10^{-3}$ (——), $Re_\gamma = 10^{-2}$ (——), $Re_\gamma = 10^{-1}$ (——); Fischer and Rosenberger [82] numerical results for $Re_\gamma \ll 1$ ($\ast$); present force-free numerical results (coloured hollow circles).

torque-free particles simulations are also given in figure 6.5d. For separation distances $l^* \gtrsim 2$, the force contributions illustrate that $F'_{\mathrm{L},1} > F'_{\mathrm{L},2} \gg F'_{\mathrm{L},3}$ for a force-free particle. This indicates that the wall-shear lift contribution, $C_{\mathrm{L},1}$, either dominates or is similar to the other forces in this high force region, with the consequence that an accurate inertial correction for $C_{\mathrm{L},1}$ is required to accurately predict the net lift force acting on a force-free particle. Figure 6.5d also shows that the estimated $F'_{\mathrm{L,tot}}$ using our correlations agrees well with the low Re_γ results of Fischer and Rosenberger [82] (using $Re_\gamma = 0$ in our correlation), but deviates significantly from these results as the shear Reynolds number and separation distance increase. Most of our numerical results agree reasonably well with Eq. (6.10) predictions for the selected separation distances and shear Reynolds number ranges. The present numerical results clearly exhibit the inertial dependence predicted by new lift model, and thus reinforces the importance of the Reynolds number correction to $C_{\mathrm{L},1}$.

Interestingly, the inset of figure 6.5d illustrates that the net lift force, F^*_{L}, while increasing with shear rate, is relatively independent of separation distance, except at the highest Re_γ considered. When Re_γ is low, the net lift (and the lift coefficient) does not reduce to zero until well into the outer region, which for low Re_γ is a large distance from the wall: For $Re_\gamma = 10^{-2}$ and 10^{-3}, the transition from the inner to the outer region (L^*_{G}), occurs at $l^* = 10$ and 31.62 respectively. Therefore, a clear lift dependence on the separation distance is not visible in figure 6.5d as the maximum l^* indicated is 10. Nevertheless, a strong lift dependence on the separation distance is visible for the largest particle shear Reynolds number ($Re_\gamma = 10^{-1}$) as the transition from the inner to outer region occurs at $l^* = 3.16$, well within the region of analysis.

The minor deviations between numerical and correlation results observed in the predicted lift force for the highest Re_γ could be a result of two factors. Firstly, as discussed in §6.2, at high Re_γ our freely-rotating $C_{\mathrm{L},1}$ correlation slightly overestimates the lift force, particularly far from the wall. Secondly, there are errors in using the inner region based correlations for $C_{\mathrm{L},2}$ and $C_{\mathrm{L},3}$ in our analysis. The main draw back is the overestimation of the slip based lift forces when the particle is far from the wall. This happens as a result of $C_{\mathrm{L},2}$ and $C_{\mathrm{L},3}$ reducing to the outer boundary values of the inner region, instead of reducing to the unbounded values as $l^* \to \infty$. Additionally, the inertial dependence of $F'_{\mathrm{L},2}$ and $F'_{\mathrm{L},3}$ is weakly captured with the current coupling, as the inner region models for $C_{\mathrm{L},2}$ and $C_{\mathrm{L},3}$ are derived for $Re_\gamma, Re_{\mathrm{slip}} \ll 1$ and $Re_{\mathrm{slip}} \ll 1$ conditions, respectively.

However for the present case of a force-free particle, these two limitations are not that significant because u^*_{slip} rapidly reduces with increasing l^* (figure 6.4). Therefore the slip based lift forces, $F'_{\text{L},2}$ and $F'_{\text{L},3}$ contribute only a small amount to the overall lift force for $l^* > 2$. Whenever slip becomes significant for the case of a force-free particle, the walls are well within the inner region ($l^* < 2$), and therefore the net lift correlation reduces to the original Cherukat and McLaughlin [46] inner region correlation. However for relatively large slip velocities (e.g., buoyant particles near walls), where $F'_{\text{L},2}$ and $F'_{\text{L},3}$ are more significant, predictions of Eq. (6.10) with inner region based slip lift coefficients will be not necessarily be accurate. This is a limitation which will be addressed in the next chapter in order to completely generalise the net lift model given by Eq. (5.1).

Dimensionless migration velocities $u^*_{\text{mig}} (= u_{\text{mig}}/\gamma a)$ obtained by balancing the lift force and the wall normal drag force,

$$u^*_{\text{mig}} = \frac{F^*_{\text{L}}}{6\pi Re_\gamma (1 + C^{\text{wb,in}}_{\text{D},2,\perp})} \tag{6.11}$$

are presented in figure 6.6a for the same set of shear Reynolds numbers. Here $C^{\text{wb,in}}_{\text{D},2,\perp}$,

$$\frac{C^{\text{wb,in}}_{\text{D},2,\perp}}{6\pi} = \left[1 - \frac{9}{8}\left(\frac{a}{l}\right) + \frac{1}{2}\left(\frac{a}{l}\right)^3 - \frac{135}{256}\left(\frac{a}{l}\right)^4 + \frac{39}{256}\left(\frac{a}{l}\right)^5\right]^{-1} - 1, \tag{6.12}$$

the wall bounded drag coefficient of a particle translating normal to a wall, is evaluated via the analytical inner region correlation of Faxen [80] [103]. The migration velocities obtained by balancing the lift with Stokes unbounded drag ($C^{\text{wb,in}}_{\text{D},2,\perp} = 0$ in Eq. (6.11)) are also shown in the same figure using dashed lines. It is evident that the wall normal correction to the Stokes drag greatly decreases the migration velocity close to the wall. Noting that $C^{\text{wb,in}}_{\text{D},2,\perp}$ is an inner region model which rapidly decays to zero we assume that $C^{\text{wb,in}}_{\text{D},2,\perp}$ can be used for all the separation distances to predict the migration velocity of a particle. Based on the migration velocity normal to the wall and the particle velocity parallel to the wall, we can calculate the lateral displacement in the wall normal direction, h, and longitudinal displacement in the flow direction, d, per unit time t as illustrated in figure 6.6a. Here,

$$h = u_{\text{mig}} t; \qquad d = u_{\text{p}} t$$

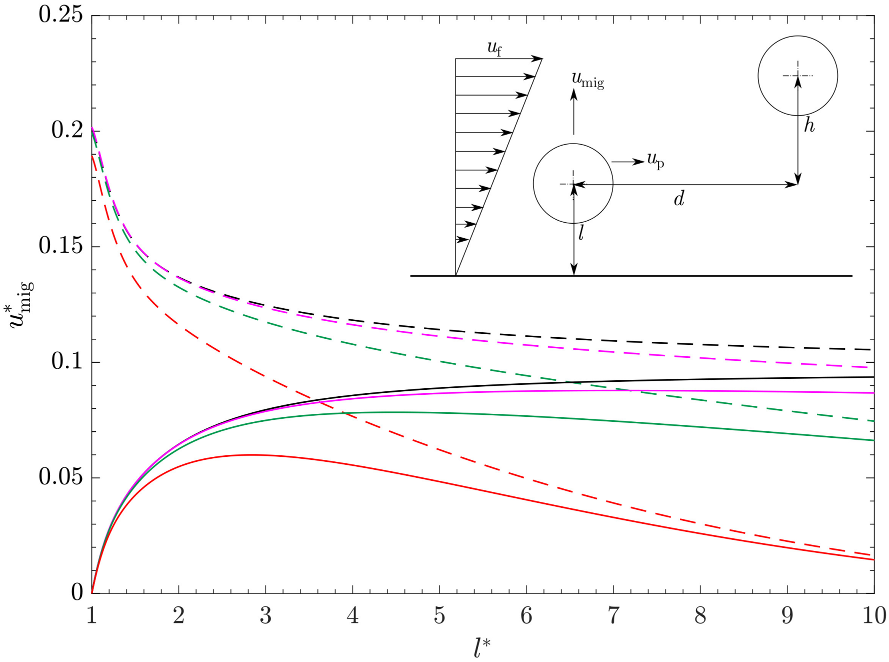

(a)

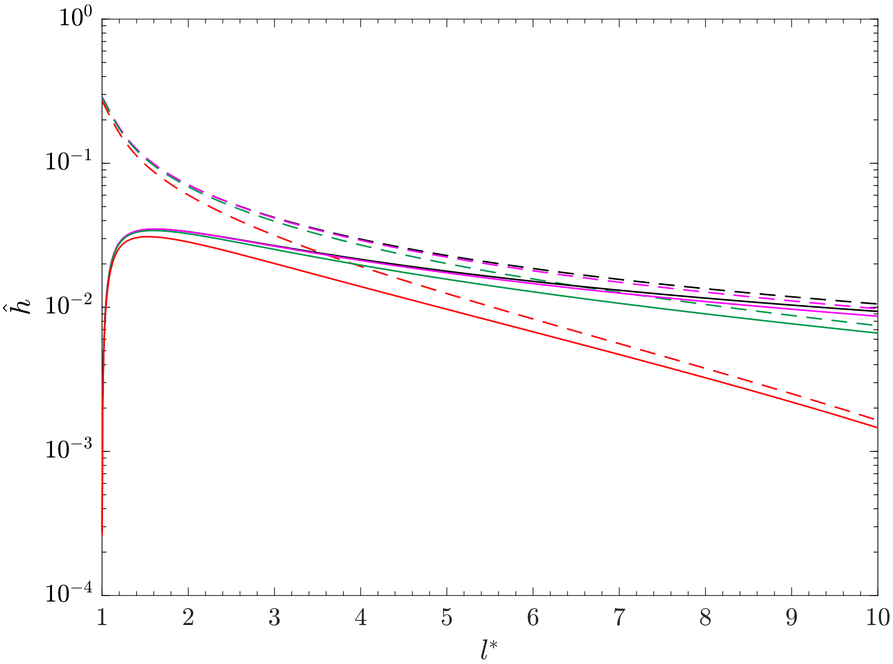

(b)

FIGURE 6.6: (a) Dimensionless migration velocity and (b) Lateral displacement per unit movement in the flow direction of a force-free particle for $Re_\gamma \ll 1$ (——), $Re_\gamma = 10^{-3}$ (——), $Re_\gamma = 10^{-2}$ (——) and $Re_\gamma = 10^{-1}$ (——). Dashed lines show the values obtained when $C_{\mathrm{D}\perp} = 0$ in Eq. (6.11). Here $\hat{h} = h/d$, $l^* = l/a$ and $u^*_{\mathrm{mig}} = u_{\mathrm{mig}}/\gamma a$.

Given that $u_{\mathrm{p}} = u_{\mathrm{slip}} + \gamma l$, the lateral displacement per unit longitudinal displacement $\hat{h}(= h/d)$

$$\hat{h} = \frac{u_{\mathrm{mig}}/\gamma a}{(u_{\mathrm{slip}} + \gamma l)/\gamma a} = \frac{u^*_{\mathrm{mig}}}{u^*_{\mathrm{slip}} + l^*} \tag{6.13}$$

The calculated lateral displacement per unit longitudinal displacement $\hat{h}(= h/d)$ of a particle located at l^* is also given in figure 6.6b. For all shear Reynolds numbers the lateral displacement of a force-free particle closer to the wall is much higher than that of a particle travelling further away from the wall. The maximum lateral displacement $\hat{h} \sim 0.035$ that occurs when the particle is closer to the wall ($l^* \sim 1.5$) would quite quickly push a free particle away from the wall. The lateral displacement also displays a weak dependence on the shear rate close to the wall ($l^* \sim 1$), however when a particle is away from the wall $\hat{h}$ decreases significantly as the shear Reynolds number increases.

Although the present study focuses on linear shear flows, it is interesting to briefly discuss the behaviour of lift coefficients of force-free particles in Poiseuille flows at $Re_\gamma < 1$. Direct numerical studies on planar Poiseuille flows have shown that the net lift coefficient ($F'_{\mathrm{L,tot}}$) of force-free particles is relatively independent of Re_γ even when $Re_\gamma \sim \mathcal{O}(10^{-1})$ [12, 110]. This discrepancy is possibly due to the weak inertial dependency of the double-wall-bounded shear gradient lift force [11, 217] which is not relevant for linear flows. However, as shown in the present linear shear flow study which has a uniform local Re_γ throughout the separation distance, the net lift is clearly dependent on Re_γ, particularly away from the wall.

6.5 Closure

The lift and drag forces acting on a spherical particle in a single wall-bounded linear shear flow field are examined via numerical computation. Forces are obtained under a zero-slip condition, by setting the particle to translate at the same velocity as the fluid. The Navier-Stokes equations are solved using a finite-volume solver to find the fluid flow around the particle. The effect of shear rate and wall presence are investigated by varying the shear Reynolds number over the range $Re_\gamma = 10^{-3} - 10^{-1}$, and the wall separation distance over $l^* = 1.2 - 9.5$. Computed lift and drag coefficients at $Re_\gamma \sim \mathcal{O}(1)$ are compared against theoretical values, predicted by asymptotic models mainly derived for $Re_\gamma \ll 1$. Accounting for the variations, slip independent inertial corrections are suggested for both the lift and drag force coefficients.

The computed lift force coefficients at the lowest Reynolds numbers are in good agreement with the previous theoretical results when the particle is close to the wall [45, 58, 131]. With increasing shear rate, a significant decrease of the computed lift coefficient is observed for both non-rotating and freely-rotating particles. This decrease of lift coefficient is further enhanced when the wall is away from the particle and is located in the outer region. Numerical lift correlations for non-rotating and freely-rotating conditions are presented, accounting for both the inner and outer region behaviour in the limit of finite Re_γ. These expressions reduce to theoretical values predicted in the three limits of $Re_\gamma \to 0, l^* \to 1$ and $l^* \to \infty$.

Drag force coefficients computed for the freely-rotating sphere agree reasonably well with low Re_γ results from a previous analytical study over most of the wall separation range [156], however considerable deviation is seen when the particle is within one radius of the wall. Consequently a drag coefficient model is proposed that includes higher order terms in separation distance (up to $\mathcal{O}((1/l^*)^6)$) that more accurately captures this near-wall drag behaviour. A shear based inertial correction, independent of slip velocity, is also provided for the modified drag coefficient.

The behaviour of a force-free particle suspended in a linear shear flow is analysed using the new drag and lift correlations. Slip velocities calculated within the range of validity of our correlations compare favourably with previously presented results that are valid for low Re_γ. The negative slip velocities indicate that force-free particles lag the fluid near walls for low Re_γ. Noting the limitations associated with existing slip based lift coefficients, the lift force on a force-free particle at finite Re_γ, accounting for both shear induced slip and slip induced lift, is also analysed. A rapid decrease of the lift force is observed as both the shear Reynolds number and separation distance increase. This behaviour is not captured via existing analytical lift correlations that are limited to $Re_\gamma \ll 1$. Interestingly, a maximum lateral displacement per distance travelled of ~ 0.035 occurs when the particle is separated from the wall by approximately half its radius.

Overall, the suggested zero-slip correlations will aid in providing accurate constitutive equations for interphase forces to predict the behaviour of particles moving near walls.

Chapter 7

Finite Slip Effect on Wall Bounded Lift and Drag Forces

In this chapter, we are particularly interested in the lift forces acting on rigid spherical particles that are moving with finite slip velocities and low particle Reynolds numbers, as opposed to the zero slip case examined in chapter 6. In dilute systems, particle slip velocities can originate from a variety of forces, including fluid drag or buoyancy. These forces are often much higher in magnitude than the lift forces. For example, freely translating neutrally-buoyant particles experience a non-zero but relatively small slip velocity due to the wall-shear fluid drag force [77]. In contrast, buoyant particles sedimenting in vertical flows can experience much larger slip velocities due to strong buoyancy forces, which are further affected by wall-bounded fluid drag forces when particles are moving in close proximity to a wall. In both cases, the lift force acting on a particle strongly depends on the slip velocity, fluid shear rate and distance to the wall. A significant amount of theoretical work has examined lift forces for rigid particles at finite slip, however, a generalised wall-bounded correlation applicable for all particle-wall separation distances is not available.

The main objective of this chapter is to extend the existing slip-shear-wall based theoretical results given for $Re_{\text{slip}}, Re_{\gamma} \ll 1$ to larger particle Reynolds numbers up to $\mathcal{O}(10^{-1})$, directly relevant to particulate flows within small channels (i.e., particle migration in

This chapter is mainly based on the author's paper: Ekanayake, N. I. K., Berry, J. D. & Harvie, D. J. E. (2021). Lift and drag forces acting on a particle moving in the presence of slip and shear near a wall. 915, A103.

microfluidic devices). We use well resolved numerical simulations to define a general lift model for a particle experiencing slip in a shear flow for arbitrary particle-wall separation distances. For this, rigid spherical particles moving with finite slip tangential to a flat wall in quiescent and linear shear flows are considered for slip and shear Reynolds numbers in the range of 10^{-3} to 10^{-1}. We consider both non-rotating and freely-rotating particles.

In §7.1 and §7.2, we express our numerical results, for both quiescent and linear shear flows, as new lift correlations valid for arbitrary wall-particle separation distance. In §7.3, we compare the results of these new lift correlations together with selected drag correlations against previous near wall experimental results for buoyant particles in quiescent and linear shear flows, as well as previous numerical results for force-free particles in linear shear flows.

7.1 Particle translating in a quiescent flow

7.1.1 Lift force

In figure 7.1, the lift coefficients $C_{\mathrm{L},3}$ computed for both non-rotating and a freely-rotating particles in a quiescent flow are plotted as a function of non-dimensional separation distance (l^*). The numerical results are compared against the available inner-region correlations listed in table 3.7 that are valid for $Re_{\mathrm{slip}} \ll 1$. In general, the lift coefficient values predicted via most of the analytical solutions slightly underestimate the numerically computed lift forces, particularly for $Re_{\mathrm{slip}} < 10^{-2}$ near the wall. For example, the lowest slip Reynolds number ($Re_{\mathrm{slip}} = 10^{-3}$) simulation conducted at the smallest distance to the wall ($l^* = 1.2$) gives a $C_{\mathrm{L},3}$ of 1.755 (1.682) for a non-rotating (freely-rotating) particle, which is $\sim$ 1.68% (0.48%) higher than the asymptotic value of 1.726 (1.674) predicted for a non-rotating (freely-rotating) particle at $l^* = 1.2$ [45]. The Cox and Hsu [58] first order lift expression, which does not account for the finite particle size, produces a lift coefficient (independent of l^*) for both non-rotating and freely-rotating particles. The value agrees to a certain extent with the present numerical and other theoretical predictions, but is not particularly accurate near the wall. When a particle is almost in contact with the wall ($l^* = 1$), the Krishnan and Leighton [131] study gives a $C_{\mathrm{L},3}$ of 1.755 for a non-rotating particle, which is reasonably consistent

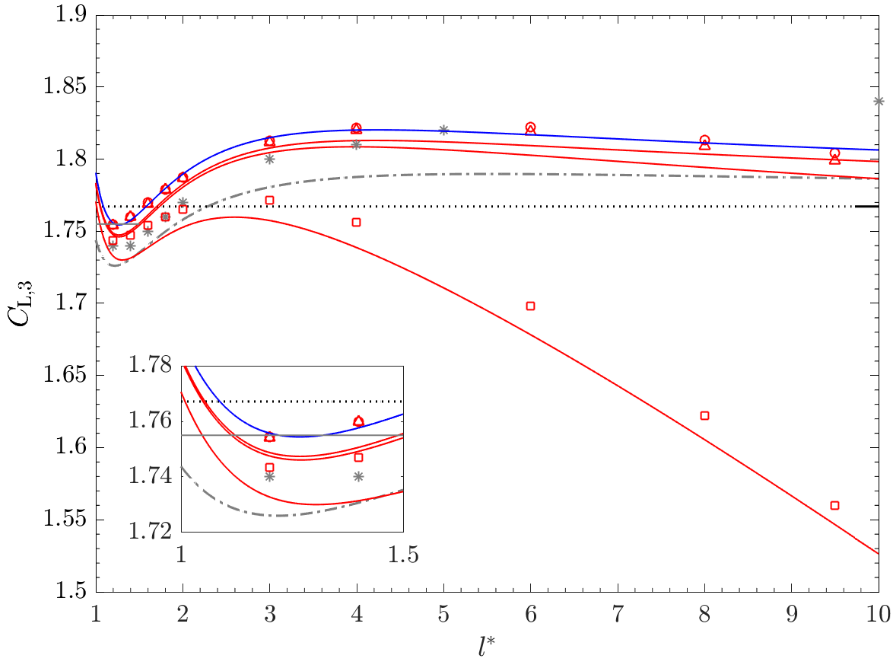

(a) non-rotating

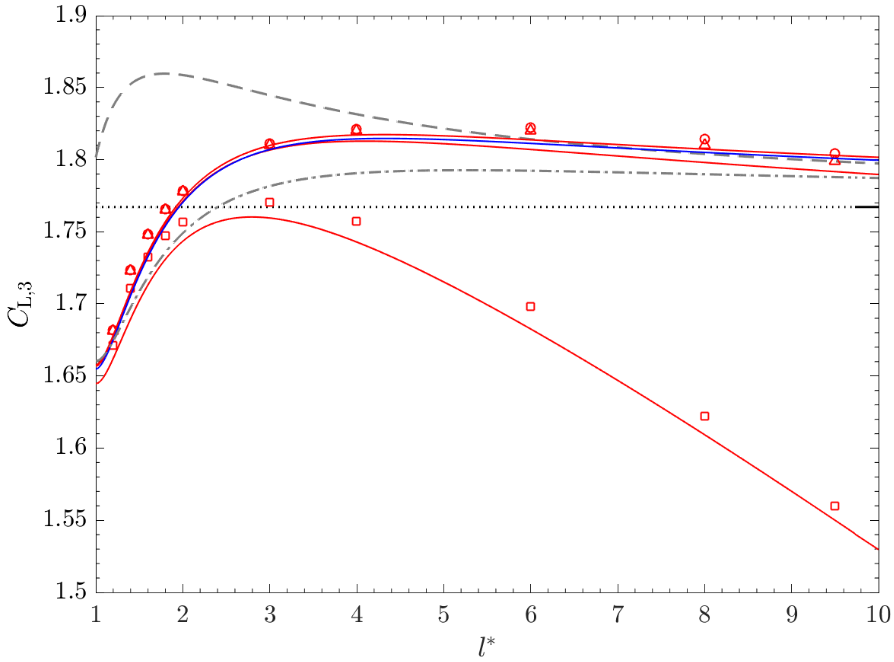

(b) freely-rotating

FIGURE 7.1: Lift coefficient ($C_{L,3}$) for different shear Reynolds number as a function of non-dimensional separation distance (l^*) for (a) non-rotating and (b) freely-rotating spheres. Simulations: $Re_{slip} = 10^{-3}$ (○), 10^{-2} (△) and 10^{-1} (□). Numerical predictions by Fischer and Rosenberger [82] that included small inertial effects at $Re_\gamma \ll 1$ ($*$). Analytical predictions of Cox and Hsu [58] (······, Eqs. 3.62,3.63), Cherukat and McLaughlin [45] (-·-·, Eqs. 3.64, 3.65), Krishnan and Leighton [131] (——, Eqs. 3.66) and Magnaudet et al. [156] (- - -, Eq. 3.68) . Present numerical fit for inner-region (——, Eqs. 7.1a, 7.1b). Present numerical fit for all regions (——, Eqs. 7.2a,7.2b)

with the present numerical results obtained at $l^* = 1.2$. For a freely-rotating particle at $l^* = 1$, Krishnan and Leighton [131] also predict a value of $C_{\mathrm{L},3} = 0.236$, which is nearly an order of magnitude less than the non-rotating $C_{\mathrm{L},3}$ value, and is far from ours and the other inner-region model predictions in this region. Although the rotation of the sphere acts to decrease this lift for a particle near the wall, the reason for the significant deviation between these two theoretical analyses is not clear. For a freely-rotating particle the Magnaudet et al. [156] lift correlation predicts a lift coefficient which is larger than the available asymptotic inner-region theories for $Re_{\mathrm{slip}} \ll 1$ (Figure 7.1b). A similar over-prediction is observed for $C_{\mathrm{L},1}$ near the wall (see Ekanayake et al. [77] and chapter 6) which may be caused by the neglect of higher order separation distance terms ($\mathcal{O}(1/l^*) > 2$) that are significant when in the vicinity of the wall.

For the non-rotating case (figure 7.1a), the lift results are also compared with numerical predictions based on a Boundary Element Method (BEM) which included small inertial effects ($Re_\gamma \ll 1$) [82]. The computed lift coefficient values for the lowest slip Reynolds number ($Re_{\mathrm{slip}} = 10^{-3}$) are consistent with the BEM results for small separation distances (figure 7.1a). However, a considerable difference between the present results and BEM predictions is apparent at larger separation distances ($l^* \sim 10$). This could be possibly due to insufficient numerical accuracy of a Gauss-Legendre product formula used by Fischer and Rosenberger [82], as suggested by Shi and Rzehak [227]. However, to our knowledge there is no numerical data available for a freely-rotating particle at these low slip Reynolds numbers for additional verification. We also note from our domain dependence study that the errors in our numerical simulations are also highest at these large l^* and small Re_{slip} values.

As Re_{slip} increases, the computed lift coefficients deviate significantly from the asymptotic inner-region correlations as inertial effects become significant, in both the non-rotating and freely-rotating cases. Although most of our numerical data are well within the inner-region, the computed lift force coefficient decreases with Re_{slip} number in contrast to the inner-region models which predict lift coefficients that are independent of Re_{slip}. The discrepancy between simulation and theory arises as the force expansion used in the inner-region models does not satisfy the boundary conditions at large distances from the wall. With increasing slip velocity and separation distance, the walls move to the outer-region, and the inner-region-based theoretical lift models then fail to capture the lift coefficient variation.

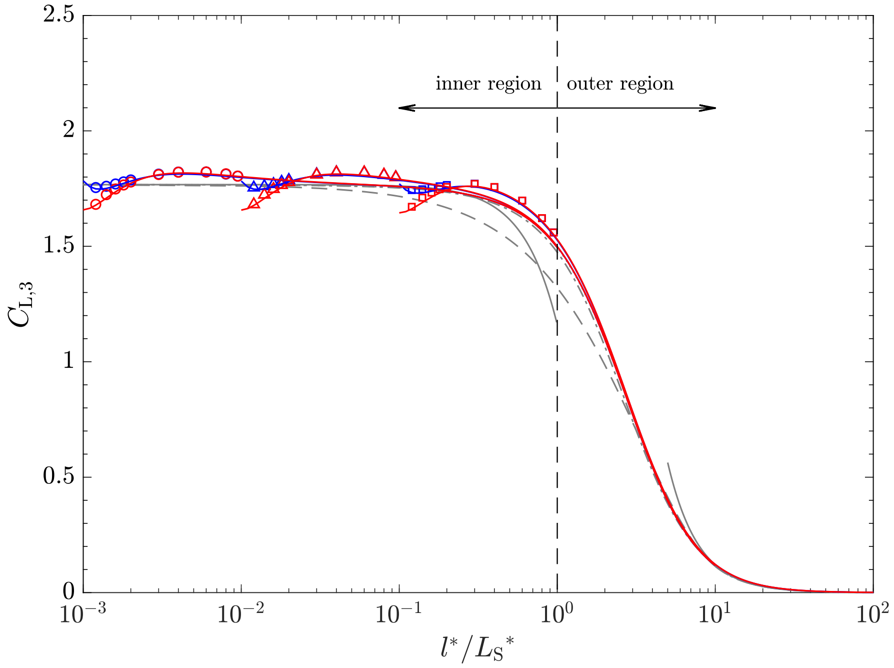

FIGURE 7.2: Lift coefficient ($C_{L,3}$) for slip Reynolds number values of $Re_{\mathrm{slip}} = 10^{-3}$ (○), 10^{-2} (△) and 10^{-1} (□) as a function of separation distance non-dimensionalised by Stokes length scale ($l^*/L_S{}^*$). Red and blue symbols are for freely-rotating and non-rotating particles, respectively. Asymptotic models for $Re_{\mathrm{slip}} \ll 1$ by Vasseur and Cox [251] (——, Eq. 3.35), Takemura and Magnaudet [240] (- - -, Eq. 3.36), Takemura [239] (⋯⋯, Eq. 3.37) and Shi and Rzehak [227] (-·-·, Eq. 3.38). Present numerical fit for non-rotating particles (——, Eq. 7.2a) and freely rotating particles (——, Eq. 7.2b)

The numerical lift coefficient values and the outer-region asymptotic predictions valid for $Re_{\mathrm{slip}} \ll 1$ are plotted in figure 7.2 as a function of $l^*/L_S{}^*$. Although all the computed results are in inner-region, the coefficients closer to the outer boundary ($l^*/L_S{}^* \sim 1$), particularly at $Re_{\mathrm{slip}} = 10^{-1}$, trend towards the outer-region theoretical predictions. In this boundary limit, the difference between a non-rotating and freely-rotating lift coefficient value is less significant and the lift results are consistent with outer-region theory [251]. Since the outer-region asymptotic models are strictly valid for $l^*/L_S{}^* \gg 1$, variations in the lift correlation observed to occur in the inner-region are thus not captured. This further highlights the need for a model capable of capturing both inner and outer-region slip-lift behaviours simultaneously.

Following Cherukat and McLaughlin [45]'s correlations, we first propose a numerical fit for the wall-slip lift force in the inner-region as a function of separation distance (l^*) accounting for the smallest Re_{slip} results, because of the under prediction of existing inner-region correlations. The proposed correlations are given by:

$$C_{\mathrm{L},3}^{\mathrm{wb,in}} = 1.774 + 0.4353\left(\frac{1}{l^*}\right) - 1.198\left(\frac{1}{l^*}\right)^2 + 0.7792\left(\frac{1}{l^*}\right)^3 \quad (7.1a)$$

for a non-rotating particle and

$$C_{\mathrm{L},3}^{\mathrm{wb,in}} = 1.764 + 0.4757\left(\frac{1}{l^*}\right) - 1.268\left(\frac{1}{l^*}\right)^2 + 0.683\left(\frac{1}{l^*}\right)^3 \quad (7.1b)$$

for a freely-rotating particle. Figure 7.1 indicates that there is no significant variation of the numerical results for $C_{\mathrm{L},3}$ when the slip Reynolds number increases from $Re_{\mathrm{slip}} = 10^{-3}$ to 10^{-2}. This behaviour suggests that the proposed inner-region-based correlations, shown in figure 7.1, can be used for very small slip Reynolds numbers ($Re_{\mathrm{slip}} \ll 1$) as the numerical lift results are almost independent of slip for $Re_{\mathrm{slip}} < 10^{-2}$.

Next, by replacing the constant in the proposed inner-region lift model (Eq. 7.1) with Takemura [239]'s outer-region model (Eq. 3.37), the following correlation is proposed to account for the inertial dependency over all wall separation distances as:

$$C_{\mathrm{L},3} = C_{\mathrm{L},3}^{\mathrm{wb,out}} + 0.4353\left(\frac{1}{l^*}\right) - 1.198\left(\frac{1}{l^*}\right)^2 + 0.7792\left(\frac{1}{l^*}\right)^3 \quad (7.2a)$$

for a non-rotating particle and

$$C_{\mathrm{L},3} = C_{\mathrm{L},3}^{\mathrm{wb,out}} + 0.4757\left(\frac{1}{l^*}\right) - 1.268\left(\frac{1}{l^*}\right)^2 + 0.683\left(\frac{1}{l^*}\right)^3 \quad (7.2b)$$

for a freely-rotating particle. Here, Takemura [239]'s outer-region model (Eq. 3.37) gives a definition for $C_{\mathrm{L},3}^{\mathrm{wb,out}}$ as

$$C_{\mathrm{L},3}^{\mathrm{wb,out}} = \frac{18\pi}{32 + 2\left(\frac{l^*}{L_{\mathrm{S}}^*}\right) + 3.8\left(\frac{l^*}{L_{\mathrm{S}}^*}\right)^2 + 0.049\left(\frac{l^*}{L_{\mathrm{S}}*}\right)^3}$$

These correlations are also plotted in figures 7.1 and 7.2, demonstrating that inertial effects are accurately predicted as a particle moves from the inner to outer-region, and the correct limit of $C_{\mathrm{L},3} \to 0$ for $l^*/L_{\mathrm{S}}^* \to \infty$ and $l^* \to \infty$ is achieved. When a particle is very close to the wall for the smallest Reynolds number, i.e., $l^*/L_{\mathrm{S}}^* \to 0$ and $l^* = 1$, Eq. 7.2a (Eq. 7.2b) calculates the lift coefficient as 1.784 (1.659) for a non-rotating (freely-rotating) particle, a value that is just 2.3%(0.1%) higher (lower) than the asymptotic

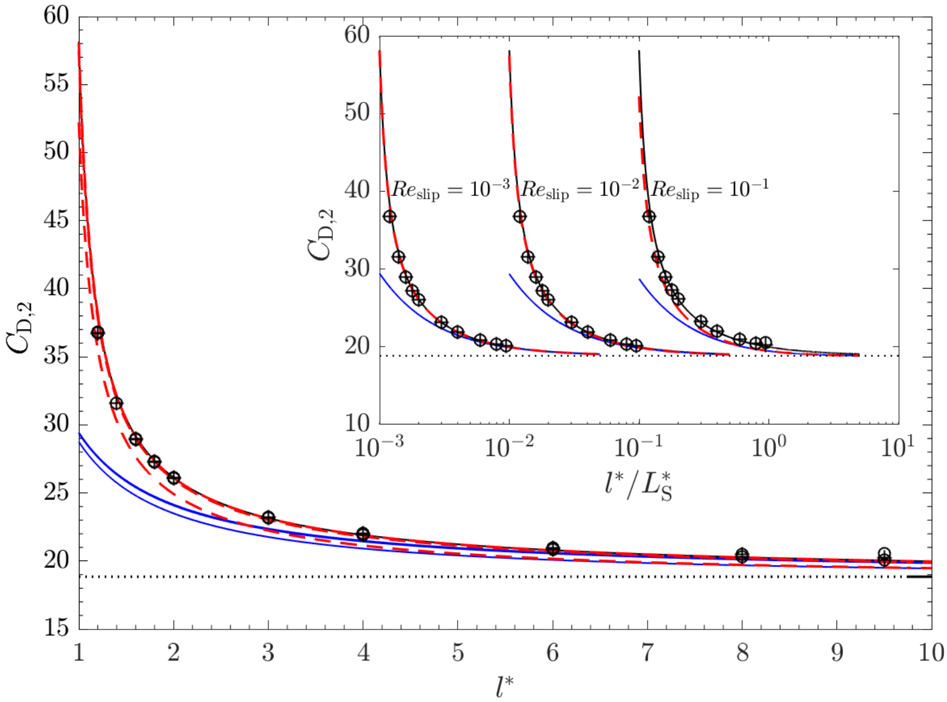

FIGURE 7.3: Drag force coefficient of a spherical particle in the absence of shear ($C_{D,2}$). Simulations: Non-rotating (○), freely-rotating (+). Analytical prediction: Faxen inner-region correlation [103] (—, Eq.3.19), Takemura [239] outer-region correlation (—, Eq. 3.20) and Takemura [239] inner-outer-region correlation (- - -, Eq. 3.21). Unbounded Stokes drag (⋯⋯, Eq. 3.9)

inner-region result of Cherukat and McLaughlin [45] (Cherukat and McLaughlin [46]).

7.1.2 Drag force

In this section we validate existing drag models using the numerical data obtained for quiescent flows. Under these conditions there is no shear and hence $C_{D,1} = 0$. Figure 7.3 shows the variation in net drag coefficient, $C_{D,2}$, as a function of dimensionless separation distance (l^*) for both non-rotating and freely-rotating particles. The inset in the figure shows the variation as a function of separation distance normalised by Stokes length scale (l^*/L_S^*). The results are compared against the wall-bounded inner-region analytical correlation of Faxen [103] (Eq. 3.19) and the outer-region empirical drag model of Takemura [239] (Eq. 3.20). The predictions of the Takemura [239] inner-outer based theoretical model given by Eq. 3.21 for low slip Reynolds numbers are also shown.

For each of the slip Reynolds numbers, the highest numerical value for $C_{D,2}$ is reported when the particle is close to the wall, and with increasing wall distance, these coefficients asymptote to the unbounded Stokes limit ($C_{D,2} = 6\pi$) for both non-rotating and freely-rotating particles. The effect of rotation on the drag force is hardly discernible for all separation distances. As indicated in figure 7.3, no inertial dependency is observed in the computed drag coefficients for all tested Re_{slip} values. The numerical drag results are in good agreement with the analytical inner-region correlation, Eq. (3.19), noting that all the numerical results are inside the inner region $l^*/L_S^* < 1$ (inset of figure 7.3). However, even in the outer boundary limit (when $l^*/L_S^* \sim 1$), the results given for $Re_{slip} = 10^{-1}$ do not significantly deviate from the inner-region predictions (Eq. 3.19) or follow the transition behaviour predicted by Takemura [239] in Eq. (3.20). Note that Eq. (3.20) was originally validated for relatively large slip Reynolds numbers ($0.09 \leq Re_{slip} \leq 0.5$), compared to our simulated slip range. Hence, we conclude that the correlation given by Eq. (3.19) is valid up to $Re_{slip} = 10^{-1}$ for both rotating and freely-rotating particles without requiring any further correction for inertial effects.

7.2 Particle translating with a finite slip in a shear flow

In this section, we build on the previous results by analysing the lift and drag force acting on a spherical particle moving parallel to a wall with a finite slip in a linear shear field. We again use the force correlations given in §5.2 to express the results in terms of lift and drag coefficients. Both Re_{slip} and Re_γ are varied systematically covering a range from 10^{-3} to 10^{-1} (corresponding to $0.32 < \epsilon < 326$ and $10^{-2} < |\gamma^*| < 10^2$). Both positive and negative slip velocities are considered.

7.2.1 Lift force

Figure 7.4 shows the variation in dimensionless lift force (F_L^*) for a freely-rotating particle as a function of l^* for different combinations of slip and shear Reynolds numbers. Figure 7.4a and figure 7.4b present results for a leading ($u_{slip} > 0$) and a lagging particle ($u_{slip} < 0$) respectively, in a positive shear field ($\gamma > 0$). The numerical results are compared against the available inner and outer-region lift models that are valid for $Re_\gamma, Re_{slip} \ll 1$. Here the inner-region model of Cherukat and McLaughlin [46] given by Eq. (3.47), and the outer-region model of Takemura et al. [242] given by Eq. (3.45) are included for comparison.

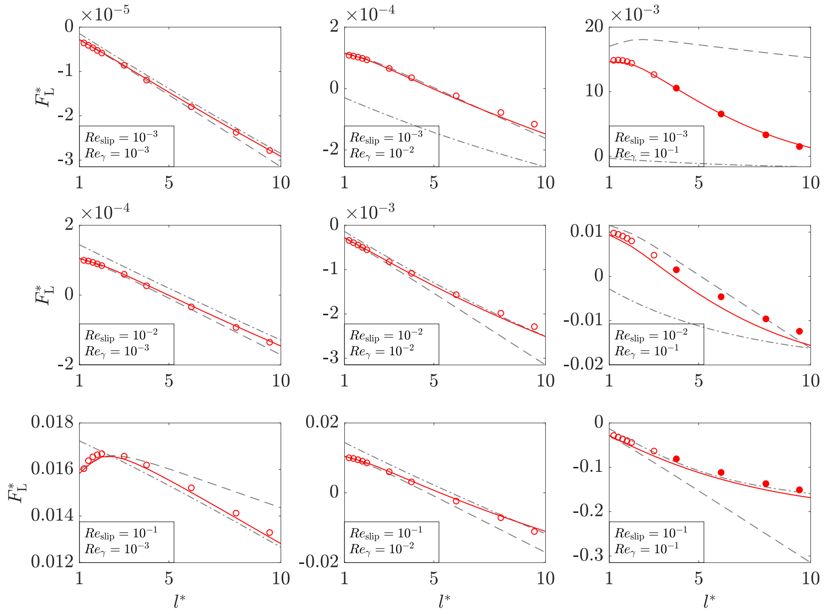

(a) Leading particle in a positive shear field ($\gamma^* > 0$)

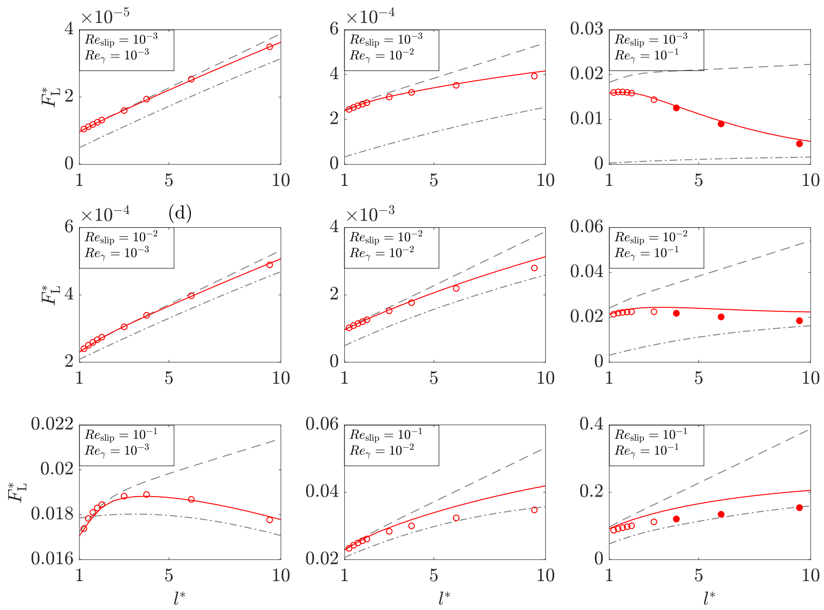

(b) Lagging particle in a positive shear field ($\gamma^* < 0$)

FIGURE 7.4: Non-dimensional lift force (F^*_L) of a freely-rotating particle. Re_γ and Re_{slip} increase in the order of $10^{-3}, 10^{-2}, 10^{-1}$ from left to right and top to bottom respectively. Simulations: inner-region (○) and outer-region (●) for each subplot. Analytical predictions: inner-region model of Cherukat and McLaughlin [46] (- - -, Eq. 3.47), outer-region model of Takemura et al. [242] (-·-·, Eq. 3.45). Present model prediction (——, Eq. 7.4)

For $Re_{\text{slip}}, Re_\gamma < 10^{-2}$, the numerically computed lift forces in the region close to the wall ($l^* < 5$) agree reasonably well with the asymptotic values predicted by the inner-region model [46] for both positive and negative slip velocities. As Re_{slip} and Re_γ increase and inertial effects become more significant, the computed lift coefficients deviate significantly from the inner-region theoretical values. With increasing slip, shear and separation distance, the walls move to the outer-region ($l^* > \min({L_\text{G}}^*, {L_\text{S}}^*)$) and unsurprisingly, the inner-region-based models fail to capture the lift coefficient variations accurately. At Re_{slip} and $Re_\gamma > 10^{-2}$ and $l^* \gtrsim 5$, the computed results coincide reasonably well with values predicted by the Takemura et al. [242] outer-region correlation. However, for the largest shear Reynolds numbers and smallest slip Reynolds numbers (i.e., results for $Re_\gamma > 10^{-2}, Re_{\text{slip}} < 10^{-1}$), the existing outer-region model significantly underestimates the simulated lift results.

In order to better understand the outer-region behaviour, in figure 7.5 we plot the computed lift force coefficients against the separation distance normalised using Saffman's length scale (l^*/L_G^*). The numerical results are compared against two existing outer-region-based correlations, namely $C_{\text{L},23}^{\text{wb,out}}$ given via Eq. (3.45) and $C_{\text{L},2}^{\text{wb,out}}$ given via Eq. (3.40). While $C_{\text{L},23}^{\text{wb,out}}$ is valid for both small and large ϵ values, $C_{\text{L},2}^{\text{wb,out}}$ is only valid when shear dominates ($\epsilon > 1$). In both cases $J(\epsilon)$ is evaluated using Legendre and Magnaudet [143]'s correlation (Eq. 3.32) and $f(\epsilon, l/L_\text{G})$ is evaluated using Takemura et al. [242]'s correlation, Eq. (3.43). Eq. (3.37) is used to evaluate $C_{\text{L},3}^{\text{wb,out}}$, present in the expression for $C_{\text{L},23}^{\text{wb,out}}$. As ($l^*/L_\text{G}^*$) increases, the theoretical lift force results for positive and negative $\gamma^*(= \gamma/u_{\text{slip}})$, obtained by varying only the slip direction, asymptote to the negative and positive unbounded lift forces, respectively. Although the theoretical model given by Eq. (3.45) fails to capture the numerical lift variation in the transition region ($l^* \sim L_\text{G}^*$) when $|\gamma^*| \geq 10$, the same model predicts the numerical data reasonably well when $|\gamma^*| \leq 1$. On the other hand, the predictions of Eq. (3.40) coincide with the numerical data only when $|\gamma^*| \sim 1$ ($Re_\gamma \sim Re_{\text{slip}}$) (see figure 7.5a).

No existing models capture the force variation in both the inner and outer-regions successfully for all of the Reynolds numbers considered here. Recalling our definition for the net lift force given by Eq. (5.1), since the coefficients $C_{\text{L},1}$ and $C_{\text{L},3}$ capture the lift contributions due to finite shear and finite slip conditions in the limits of $\gamma^* \to \infty$ and $\gamma^* = 0$, respectively, the remaining coefficient $C_{\text{L},2}$ is found by subtracting the force contributions due to $C_{\text{L},1}$ and $C_{\text{L},3}$, from the present numerical results (see figure 7.6).

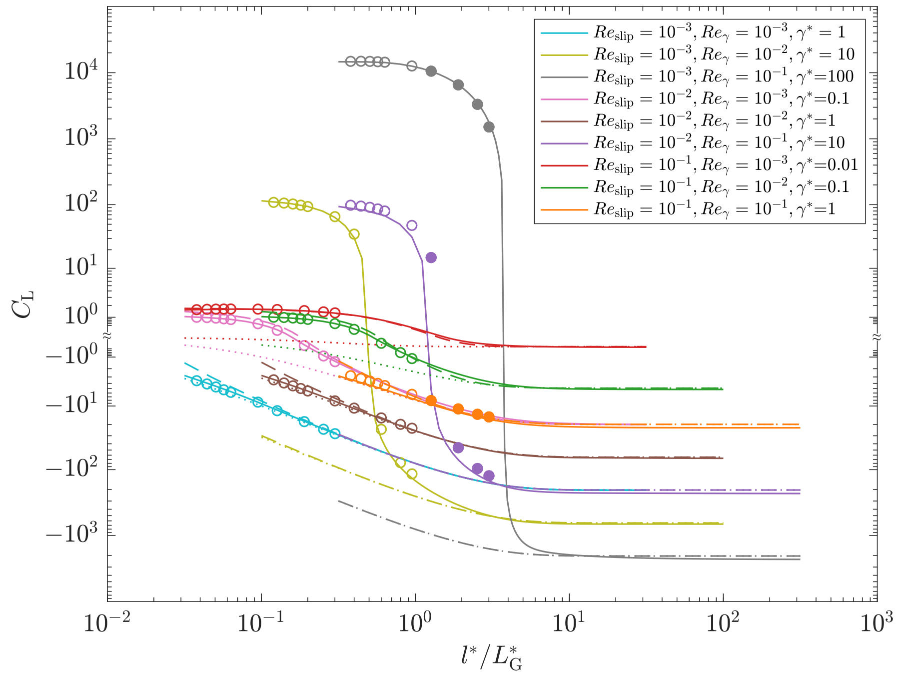

(a) Leading particle in a positive shear field ($\gamma^* > 0$)

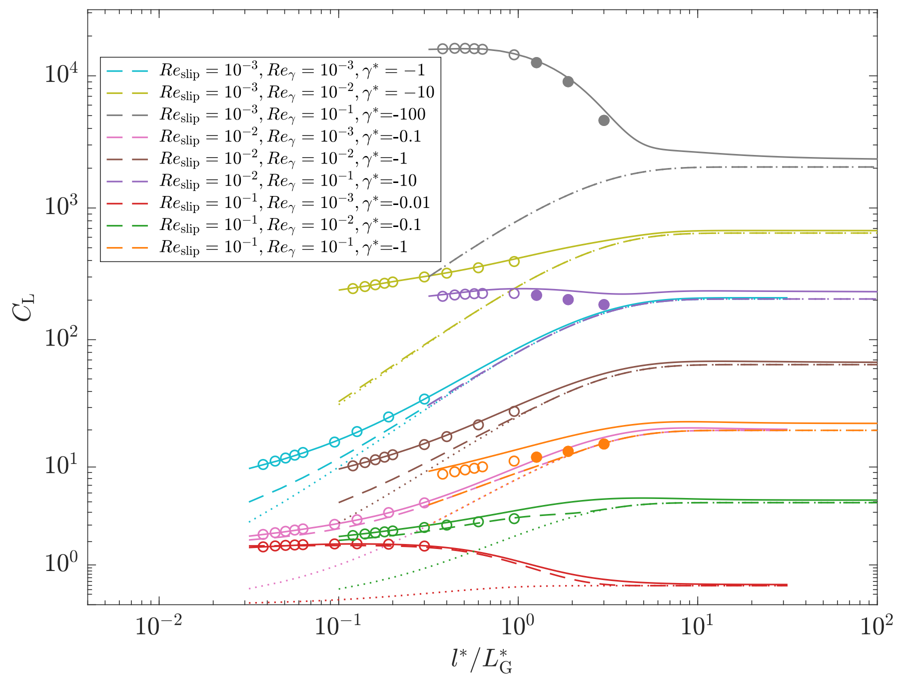

(b) Lagging particle in a positive shear field ($\gamma^* < 0$)

FIGURE 7.5: Lift force coefficient ($C_L = F_L^*/Re_{\text{slip}}^2$) of a freely-rotating particle as a function of separation distance non-dimensionalised by Saffman length scale ($l^*/L_G{}^*$). Simulations: inner-region (○) and outer-region (●). Analytical outer-region correlation of Takemura et al. [242] (- - -, Eq. 3.45) and (⋯⋯, Eq. 3.40) . Present model predictions (—, Eq. 7.4).

Here, $C_{\mathrm{L},1}$ and $C_{\mathrm{L},3}$ are evaluated using Eq. (6.1) in chapter 6 and Eq. (7.2) in the present chapter respectively.

We define a new correlation for $C_{\mathrm{L},2}$ in the following manner. To capture the variation of the remaining force contributions and the inner and outer-region transition behaviour, the outer-region-based, wall-bounded lift coefficient $C_{\mathrm{L},2}^{\mathrm{wb,out}}$ given by Eq. (3.40) is substituted into the lowest order term of the Cherukat and McLaughlin [46]'s inner-region slip-shear lift $C_{\mathrm{L},2}^{\mathrm{wb,in}}$ correlation given by Eq. (3.57) for a non-rotating particle and Eq. (3.58) for a freely-rotating particle. Noting that $C_{\mathrm{L},2}^{\mathrm{wb,out}}$ in Eq. (3.40) scales with Re_{slip}^2, the outer-region coefficient is divided by $|\gamma^*|$ to match the inner-region lift correlation scaling. The resulting slip-shear based net lift coefficient $C_{\mathrm{L},2}$, which is valid for all three regions (i.e., inner, outer and unbounded) is,

$$C_{\mathrm{L},2} = -C_{\mathrm{L},2}^{\mathrm{wb,out}} \frac{1}{|\gamma^*|} - 1.1450 - 2.0840\left(\frac{1}{l^*}\right) + 0.9059\left(\frac{1}{l^*}\right)^2 \tag{7.3a}$$

for a non-rotating particle and

$$C_{\mathrm{L},2} = -C_{\mathrm{L},2}^{\mathrm{wb,out}} \frac{1}{|\gamma^*|} - 2.6729 - 0.8373\left(\frac{1}{l^*}\right) + 0.4683\left(\frac{1}{l^*}\right)^2 \tag{7.3b}$$

for a freely-rotating particle. The new $C_{\mathrm{L},2}$ correlation proposed for the freely rotating particle is plotted as a function of l^* in figure 7.6 and as a function of normalised Saffman's length l^*/L_{G}^* in figure 7.7. Given that the new correlation for $C_{\mathrm{L},2}$ (Eq. 7.3) captures the variation of the remaining lift force contributions reasonably well for most of the slip and shear Reynolds numbers considered, we substitute this force model into the main net lift force correlation. The performance of the net lift correlation (Eq. 5.1) is then examined for a freely-rotating particle by plotting the force (F_{L}^*) predictions in figure 7.4. The overall lift coefficient (C_{L}), obtained by normalising the net lift force by the slip Reynolds number,

$$C_{\mathrm{L}} = \frac{F_{\mathrm{L}}^*}{Re_{\mathrm{slip}}^2} = {\gamma^*}^2 C_{\mathrm{L},1} + \gamma^* C_{\mathrm{L},2} + C_{\mathrm{L},3} \tag{7.4}$$

is shown in figure 7.5. Here again, the lift coefficients, $C_{\mathrm{L},1}$ and $C_{\mathrm{L},3}$ are evaluated using Eq. (6.1) from our previous chapter 6 and (Eq. 7.2b) from §7.1. For reference a summary of all the lift correlations used in the net lift force calculations are provided in Appendix B.

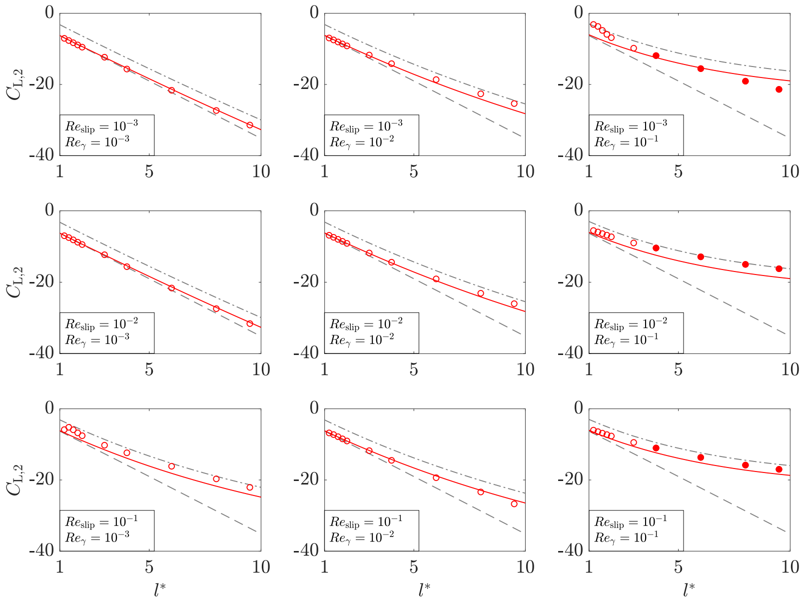

(a) Leading particle in a positive shear field ($\gamma^* > 0$)

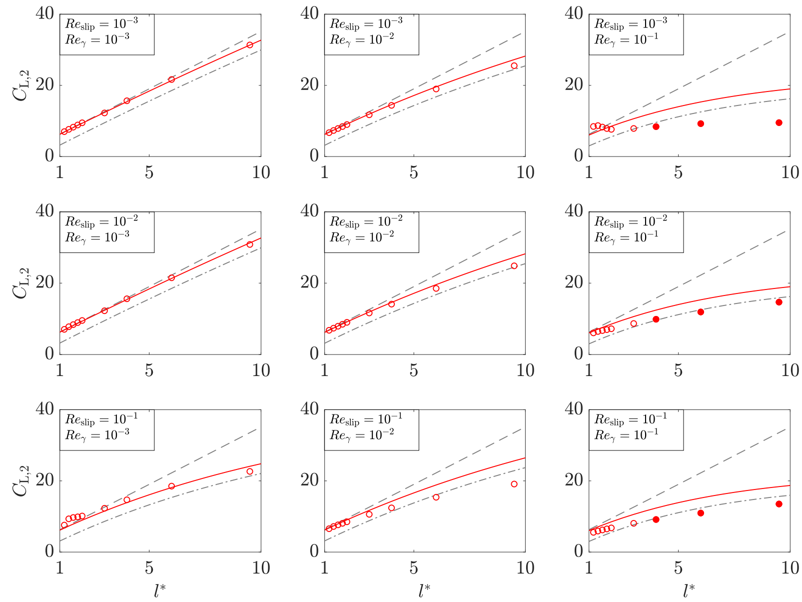

(b) Lagging particle in a positive shear field ($\gamma^* < 0$)

FIGURE 7.6: Lift force coefficient $C_{L,2}$ of a freely-rotating particle. Re_γ and Re_{slip} increase in the order of $10^{-3}, 10^{-2}, 10^{-1}$ from left to right and top to bottom respectively. Simulations: inner-region (○) and outer-region (●) for each subplot. Analytical predictions: inner-region $C_{L,2}$ model of Cherukat and McLaughlin [46] (- - -, Eq. 3.58), outer-region model of Takemura et al. [242] (-·-·, Eq. 3.40). Present model prediction (——, Eq. 7.3b)

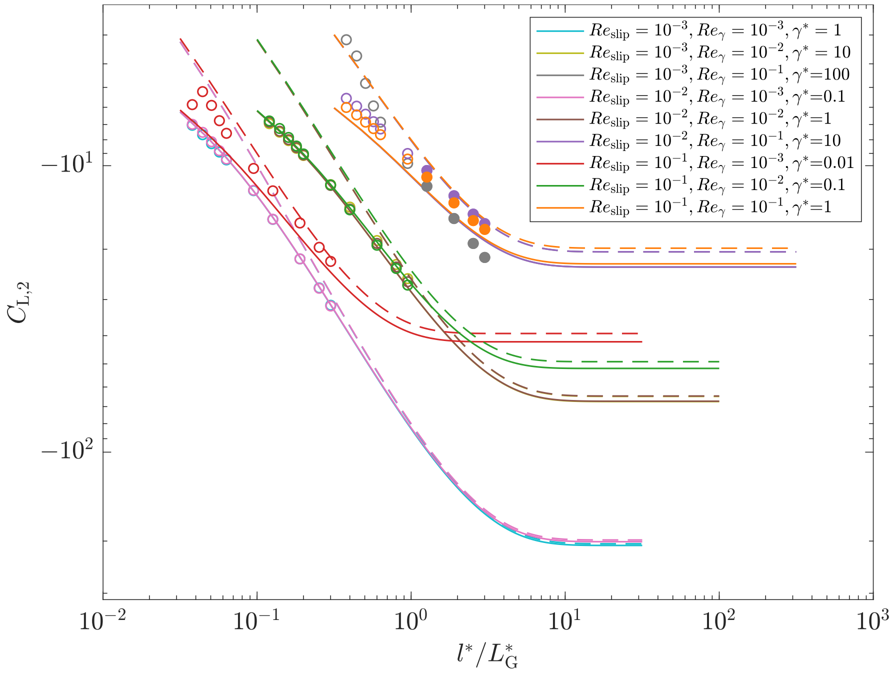

(a) Leading particle in a positive shear field ($\gamma^* > 0$)

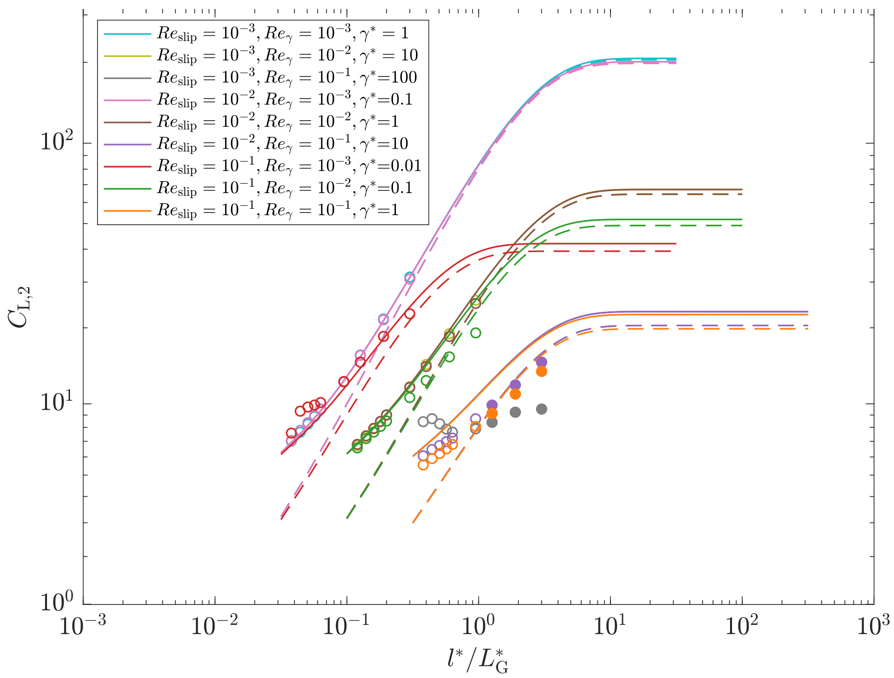

(b) Lagging particle in a positive shear field ($\gamma^* < 0$)

FIGURE 7.7: Lift force coefficient $C_{L,2}$ of a freely-rotating particle as a function of separation distance non-dimensionalised by Saffman length scale ($l^*/L_G{}^*$). Simulations: inner-region (○) and outer-region (●). Analytical outer-region correlation of Takemura et al. [242] (- - -, Eq. 3.40). Present model predictions (——, Eq. 7.3).

As shown in both figures 7.4 and 7.5, the new model captures the inner-outer transition behaviour of the computed lift results well. Referring to figure 7.4, for low slip and shear values (Re_γ and $Re_{\text{slip}} \lesssim 10^{-2}$), the model performs well for both positive and negative γ^*. For large slip values and for small shear rates (i.e., $Re_{\text{slip}} = 10^{-1}$ and $Re_\gamma = 10^{-3}$), the model slightly overestimates (underestimates) the simulated results with a maximum deviation of 4.96% (3.67%) for $\gamma^* > 0$ ($\gamma^* < 0$) when the particle is furthest from the wall. With increasing shear rate (i.e., $Re_\gamma \sim 10^{-1}$) for the same large slip values, this deviation rapidly reduces for $\gamma^* > 0$, but increases to 24.03% for $\gamma^* < 0$.

As well as the force magnitudes, the change of the lift force direction is more accurately predicted (i.e., $Re_\gamma = 10^{-1}$) using the new correlation than any other available model. Note that a positive lift ($F^*_{\text{L}} > 0$) and a negative lift ($F^*_{\text{L}} < 0$) represent a force directed away from and towards the wall, respectively. In figure 7.4a, the lift forces computed for $\gamma^* > 0$ indicate a change in lift force direction and a decrease in the force with increasing separation distance. However, for the same Re_γ and Re_{slip} values, the numerical data given in figure 7.4b for $\gamma^* < 0$, only indicate positive lift forces for the selected range of separation distances, and generally an increase in the lift force with increasing separation distance.

The force variations shown in figures 7.4 and 7.5 can be explained by examining the behaviour of the three theoretical lift coefficients ($C_{\text{L},1}, C_{\text{L},2}$ and $C_{\text{L},3}$) separately. The coefficients $C_{\text{L},1}$ and $C_{\text{L},3}$, responsible for the lift due to pure shear and pure slip respectively, always remain positive irrespective of the direction of both slip and shear. Thus, the lift forces due to these two coefficients always act to push a particle away from the wall. However, with increasing separation distance, the values of these two lift coefficients rapidly reduce to zero [77, 251]. Therefore $C_{\text{L},1}$ and $C_{\text{L},3}$ are only important close to the wall. The remaining slip-shear lift coefficient, $C_{\text{L},2}$, behaves differently. Unlike the other two coefficients, $C_{\text{L},2}$ is sensitive to the direction of slip and shear (determined by $\text{sgn}(\gamma^*)$), and also has a finite negative or positive value in the unbounded limit. Hence, at large separation distances, the net lift force mainly depends on the $C_{\text{L},2}$ coefficient and its corresponding sign. However near a wall, the net lift force magnitude and the direction strongly depend upon the inner-region contributions of all three coefficients.

Including all lift contributions covering the inner and outer-regions means that the present lift model predicts the correct lift coefficient variation with $Re_\gamma, Re_{\text{slip}}$ and l^*, over the wide range of parameters considered in this study (Figs 7.4 & 7.5).

7.2.2 Drag force

The drag force on a freely-rotating spherical particle moving parallel to a wall in a linear shear flow is analysed in this section. Here, the drag force normalised by the slip Reynolds number,

$$C_{\mathrm{D}} = \frac{F_{\mathrm{D}}^*}{Re_{\mathrm{slip}}} = -\gamma^* C_{\mathrm{D},1} - C_{\mathrm{D},2} \tag{7.5}$$

is used to define the net drag coefficients. Results are presented for positive and negative slip velocities in a positive shear field, noting that results for a negative shear field are identical to the presented positive shear field results with the sign of the slip velocity swapped. Figure 7.8 shows the variation in the net drag coefficient C_{D} for slip and shear Reynolds numbers in the range $10^{-3} - 10^{-1}$ as a function of wall separation distance normalised by Saffman's length. A positive slip in the presence of the wall produces a force on a leading particle that is in the opposite direction to the flow (Figure 7.8a). The largest negative values for C_{D} are obtained when the particle is close to the wall, reducing to the unbounded Stokes drag result with increasing wall distance. Both positive and negative values for C_{D} are reported for a lagging particle close to the wall (Figure 7.8b), with the direction of the force depending on both the $C_{\mathrm{D},1}$ and $C_{\mathrm{D},2}$ magnitudes. Although a lagging particle results in a positive slip-drag force contribution, the positive shear produces a force in the opposite direction to the flow. As a result negative net drag forces are obtained near the wall at high γ^*.

The simulated drag coefficient results are also compared against the inner-region and outer-region-based theoretical drag correlations at low $Re_\gamma \ll 1$. Two correlations, Eqs. (6.7 & 3.26) for $C_{\mathrm{D},1}$ are first tested while using an inner-region-based Faxen drag coefficient for $C_{\mathrm{D},2}$ (Eq. 3.19). As shown in figure 7.8, Eq. (6.7) for $C_{\mathrm{D},1}$ performs better than Eq. (3.26) when predicting the lift results for high γ^*. However, no significant difference between these two models is observed for small γ^*. The outer-region-based drag model of Takemura [239] (Eq. 3.20) is also tested for $C_{\mathrm{D},2}$ in combination with Eq. (6.7) for $C_{\mathrm{D},1}$. Unsurprisingly, this model fails to capture the inner-region behaviour in either slip direction, particularly closer to the wall, although the model predictions agree reasonably well with other theoretical models for large $l^*/{L_{\mathrm{G}}}^*$ values. In summary, for

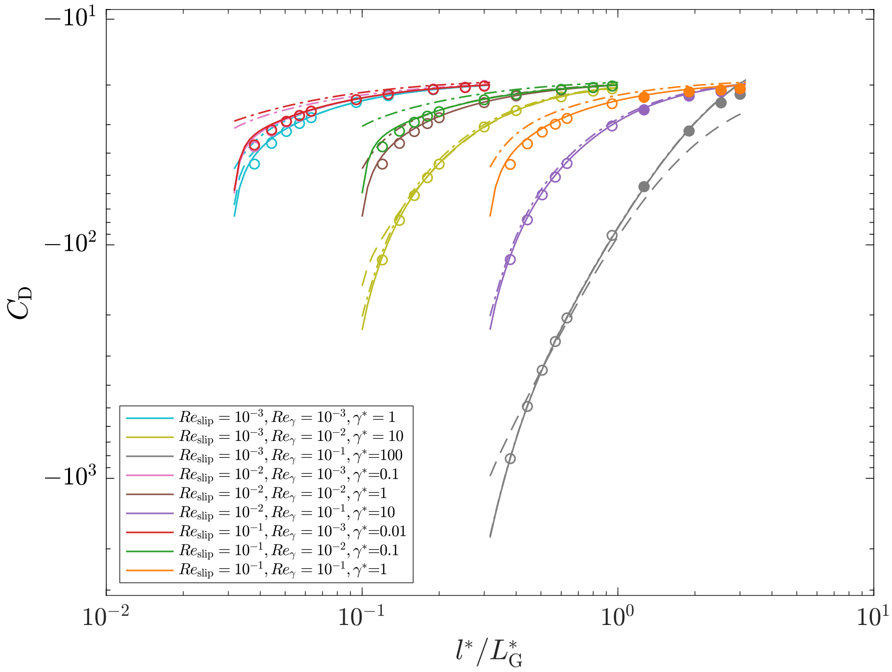

(a) Leading particle in a positive shear field ($\gamma^* > 0$)

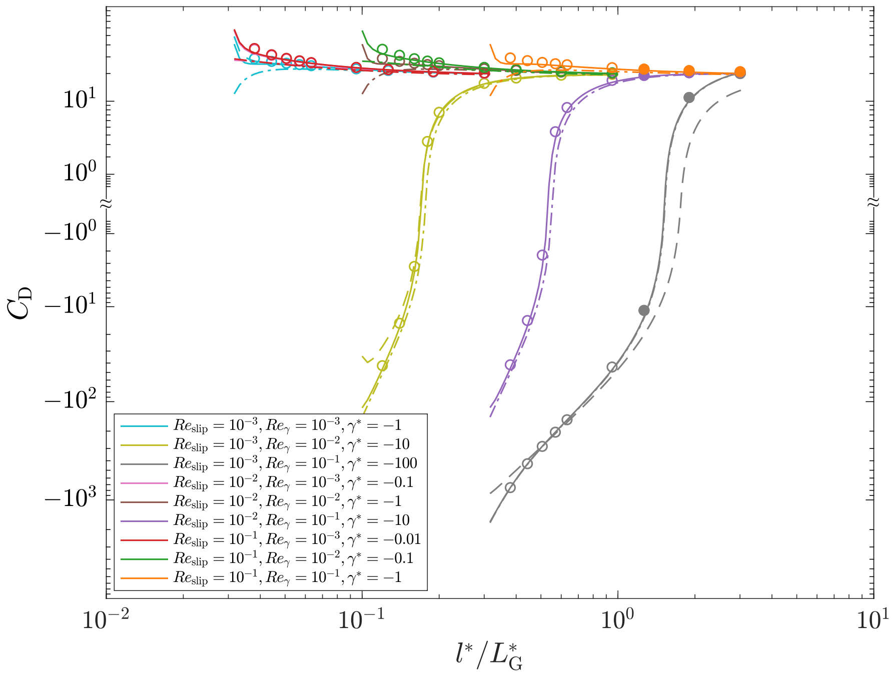

(b) Lagging particle in a positive shear field ($\gamma^* < 0$)

FIGURE 7.8: Drag force coefficient ($C_{\rm D}$) of a freely-rotating particle as a function of separation distance non-dimensionalised by Saffman length scale ($l^*/L_{\rm G}{}^*$). Simulations: inner-region ($\circ$) and outer-region ($\bullet$). inner-region analytical predictions when $C_{\rm D,1}$ is evaluated by Eq. (6.7) (——) and by Eq. (3.26) (- - -). For both cases $C_{\rm D,2}$ is evaluated by Eq. (3.19). Outer-region analytical prediction when $C_{\rm D,2}$ and $C_{\rm D,1}$ are evaluated by Eq. (3.20) and Eq. (6.7) respectively (-·-·).

the considered range of slip and shear Reynolds numbers, the most accurate drag predictions are obtained using the chapter 6 model (Eq. 6.7) for $C_{\mathrm{D},1}$ and the Faxen [80] model (Eq. 3.19) for $C_{\mathrm{D},2}$, respectively.

7.3 Application of the combined model: Neutrally-buoyant and negatively-buoyant particles

In this section, we examine the movement of both force-free (neutrally-buoyant) and negatively-buoyant particles in a linear shear flow using the new correlations. We also examine the movement of negatively-buoyant particles in a quiescent flow. To validate the force-free results, we compare against the numerical results presented in §6.4. To validate the negatively-buoyant results we use results of two previous experimental studies conducted by Takemura [239] and Takemura and Magnaudet [241] for rigid spherical particles at low but finite slip Reynolds numbers ($0.05 < Re_{\mathrm{slip}} < 2.5$). Given the scope of the current study, we only use the experimental data relevant to $Re_{\mathrm{slip}} < 1$.

7.3.1 Force-free particle in a linear shear flow

In this section, we re-examine the movement of the force-free particle as previously discussed in §6.4, but now employ the proposed $C_{\mathrm{L},2}$ and $C_{\mathrm{L},3}$ coefficients in Eq. (5.1). These coefficients span across all three regions. In this section, the net lift force coefficient obtained by normalising the net lift force (Eq. 5.1) using the shear Reynolds number,

$$C_{\mathrm{L}} = \frac{F_{\mathrm{L}}^*}{Re_\gamma^2} = C_{\mathrm{L},1} + \frac{1}{\gamma^*} C_{\mathrm{L},2} + \frac{1}{\gamma^{*2}} C_{\mathrm{L},3} \tag{7.6}$$

is used to present the lift results. The procedure followed to calculate the slip velocity of the force-free particle is same as in §6.4. Note that the $C_{\mathrm{D},2}$ correlation, specific for quiescent flows used in the slip velocity calculation, has now been validated for linear shear flows in the present study (see §7.2), allowing us to use the coefficient in linear flows more confidently. The calculated slip velocities are applied to Eq. (7.6) together with the new $C_{\mathrm{L},2}$ and $C_{\mathrm{L},3}$ lift coefficients. The lift results are plotted in figure 7.9, and compared against the direct numerical results. The previous estimations which used the inner-region-based correlations for $C_{\mathrm{L},2}$ and $C_{\mathrm{L},3}$ are also plotted in the same figure.

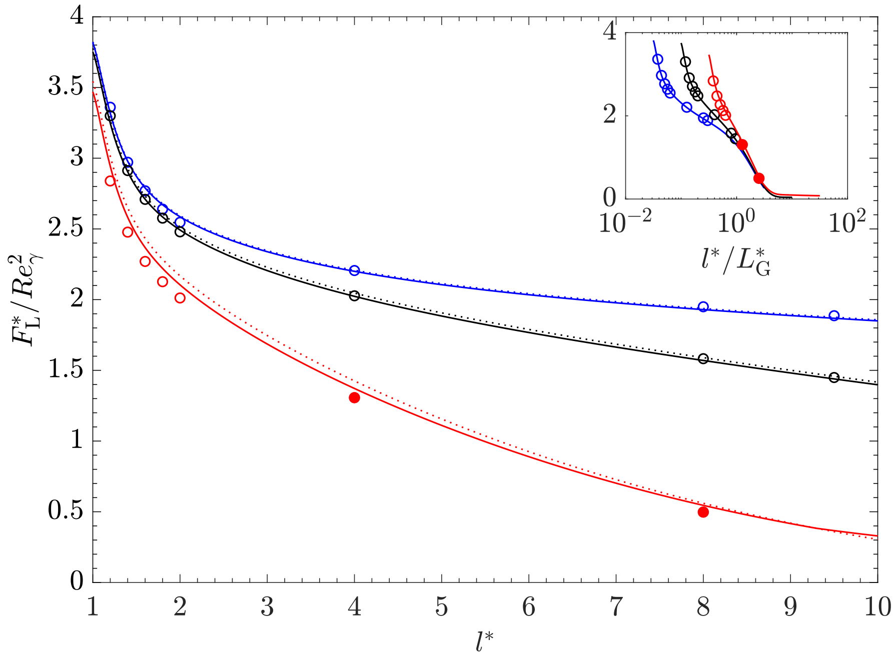

FIGURE 7.9: Lift force of a force-free particle translating in a linear shear flow near a wall when $F'_{\mathrm{L,tot}}$ is evaluated using Eq. (7.6) for $Re_\gamma = 10^{-3}$ (——), $Re_\gamma = 10^{-2}$ (——), $Re_\gamma = 10^{-1}$ (——); Numerical results [77] (coloured hollow circles). $C_{\mathrm{L},2}$ and $C_{\mathrm{L},3}$ in Eq. (7.6) are evaluated using inner-region-based Cherukat and McLaughlin [46]'s models (dotted lines).

The predictions from Eq. (7.6) as well as the previous estimations which used the inner-region-based correlations agree reasonably well with the numerical results. Near the wall ($l^* < 2$), the present lift model predictions are more accurate than the previous estimations, particularly for the highest shear Reynolds number. Given that the significance of $C_{\mathrm{L},2}$ and $C_{\mathrm{L},3}$ reduces with rapidly decreasing slip velocity under increasing separation distance, the differences between the present and previous correlations at large distances are very small regardless. Also, the inset of the figure illustrates that the net lift of a force-free particle reduces to zero as the separation distance increases.

7.3.2 Negatively-buoyant particle in a quiescent fluid

The migration of a small particle falling near a wall in a quiescent flow is analysed using the lift correlations proposed in §7.1. For this, the slip velocity of the sedimenting particle is first calculated by balancing the excess gravitational force due to the difference between the weight and buoyancy forces, $F_{\mathrm{G}} = 4/3\pi a^3(\rho_{\mathrm{s}} - \rho_{\mathrm{f}})g$ with the wall-bounded

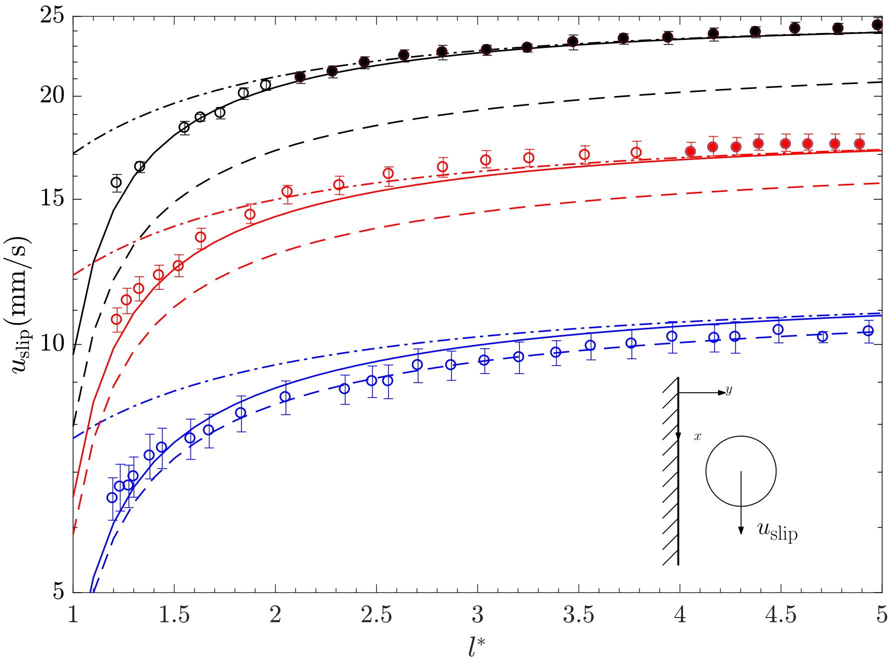

(a) Slip velocity when $C_{\mathrm{D},2}^{\mathrm{wb}}$ is evaluated using, Eq. (3.19) (dashed line), Eq. (3.20) (dashed and dotted line) and Eq. (3.21) (solid line) and $C_{\mathrm{D},2}^{\mathrm{ub}}$ is evaluated by Eq. (3.13).

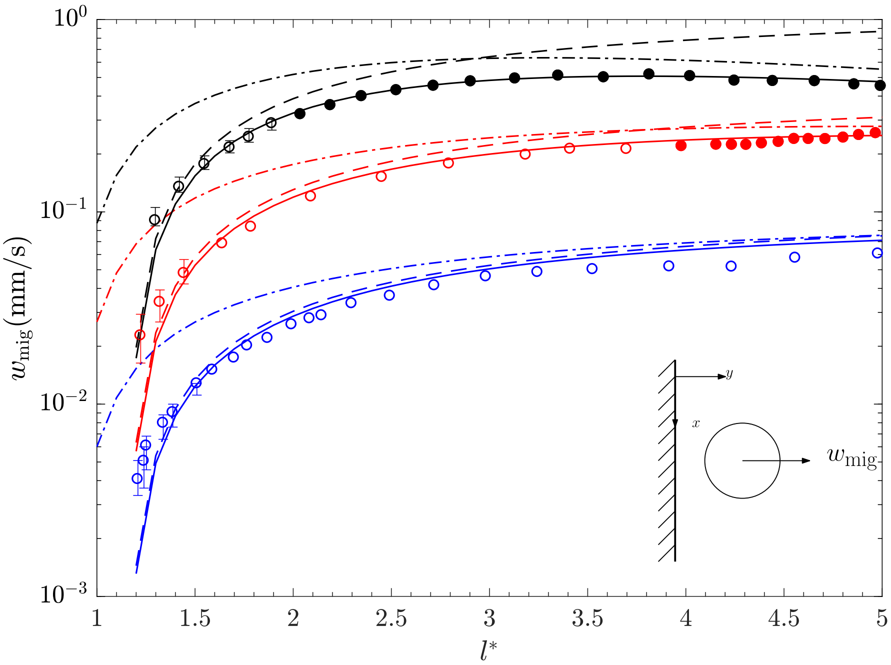

(b) Migration velocity when $C_{\mathrm{L},3}$ is evaluated by present model Eq. (7.2b) solid line) and by using inner-region correlation Eq. (3.68) (dashed line) and outer-region correlation Eq. (3.37) (dashed and dotted line) as given in Takemura [239].

FIGURE 7.10: Analysis of a sedimenting particle in a quiescent single wall-bounded flow. Experiments: $Re_{\text{slip},\infty} = 0.1005$ (○), $Re_{\text{slip},\infty} = 0.255$ (○), $Re_{\text{slip},\infty} = 0.5$ (○). Outer-region data are indicated using solid circles, and inner-region data by hollow circles.

fluid drag force, $F_{\mathrm{D}} = C_{\mathrm{D}}\mu_{\mathrm{f}} a u_{\mathrm{slip}}$ [239].

$$\begin{aligned} F_{\mathrm{G}} &= F_{\mathrm{D}} \\ \frac{4}{3}\pi a^3 g(\rho_{\mathrm{s}} - \rho_{\mathrm{f}}) &= C_{\mathrm{D}}\mu a u_{\mathrm{slip}} \end{aligned}$$

Here ρ_{s} and ρ_{f} are the solid and fluid densities respectively and g and C_{D} are the gravitational constant and wall bounded drag coefficient. In the original experimental study, results were reported using the unbounded slip Reynolds numbers, $Re_{\mathrm{slip},\infty}(= au_{\mathrm{slip},\infty}/\nu)$. Here, Re_{slip} was calculated by balancing F_{G} with the unbounded fluid drag force, $F_{\mathrm{D},\infty}(= 6\pi\mu a u_{\mathrm{slip},\infty})$ as,

$$\begin{aligned} F_{\mathrm{G}} &= F_{\mathrm{D},\infty} \\ \frac{4}{3}\pi a^3 g(\rho_{\mathrm{s}} - \rho_{\mathrm{f}}) &= 6\pi\mu a u_{\mathrm{slip},\infty} \\ &= \mu^2/\rho_{\mathrm{f}} 6\pi Re_{\mathrm{slip},\infty} \end{aligned}$$

Noting that the excess gravitational force is the same for both unbounded and bounded flows, the local slip velocity that varies with the separation distance can hence can be written in terms of this unbounded slip velocity as:

$$u_{\mathrm{slip}} = -6\pi\frac{\nu}{a}\left(\frac{Re_{\mathrm{slip},\infty}}{C_{\mathrm{D}}}\right) \tag{7.7}$$

Figure 7.10a shows the calculated and measured slip values [239] as a function of l^* for three different values of $Re_{\mathrm{slip},\infty}$. For quiescent flows, the net drag coefficient, C_{D} given in Eq. (7.7) reduces to $-C_{\mathrm{D},2}$ according to Eq. (7.5). For comparison, three correlations are used to evaluate the wall-bounded drag coefficient, $C^{\mathrm{wb}}_{\mathrm{D},2}$, that capture the inner-region, outer-region and inner-outer-region transition behaviours. The inertial correction for $C^{\mathrm{ub}}_{\mathrm{D},2}$ is evaluated by Eq. (3.13). Note that when plotting these figures, for the lowest slip Reynolds number, the $Re_{\mathrm{slip},\infty} = 0.09$ value quoted in Takemura [239] had to be adjusted to $Re_{\mathrm{slip},\infty} = 0.1005$ to get the correspondence on the kinetic viscosity and density values combinations given in the original paper (refer to Appendix A for more detail). The reason for this discrepancy is unclear.

The overall combined inner-outer correlation predicts C_{D} well over all parameter ranges considered. However, the results for the $Re_{\mathrm{slip},\infty} = 0.1005$ in figure 7.10a indicate that

Faxen's inner-region drag correlation given by Eq. (3.19) does a better job at predicting the slip velocity, noting the modification we used on the reported $Re_{\mathrm{slip},\infty}$. For the two larger $Re_{\mathrm{slip},\infty}$, Eq. (3.21) captures both inner-region and outer-region data points reasonably well, while for these particular cases Eqs. (3.19) and (3.20), deviate significantly from one another.

The derived slip velocities from Eq. (7.7) are then combined with the new lift correlation given for a freely-rotating particle in a quiescent flow (Eq. 7.4). Since the measured quantity was actually the dimensional transverse migration velocity of the particle relative to the wall (w_{mig}), a force balance normal to the wall is performed [239]. The forces considered here are the fluid drag force normal to the wall ($F_{\mathrm{D}\perp} = \mu a w_{\mathrm{mig}} C_{\mathrm{D}\perp}$) and the particle lift force (F_{L}).

$$w_{\mathrm{mig}} = u_{\mathrm{slip}} Re_{\mathrm{slip}} \frac{C_{\mathrm{L}}}{C_{\mathrm{D}\perp}} \tag{7.8}$$

Here $C_{\mathrm{D}\perp}$ is the wall-bounded drag coefficient of a particle translating normal to a wall. Similar to $C_{\mathrm{D},2}$, Faxen [103] provided an analytical inner-region correlation for $C_{\mathrm{D}\perp}$ while Takemura [239] provided an empirical fit to the outer-region correlations for $Re_{\mathrm{slip}} \ll 1$. Since the reported w_{mig} are small compared to u_{slip}, the inner-region correlation proposed by Faxen [103] is used to calculate $C_{\mathrm{D}\perp}$ in Eq. (7.8):

$$C_{\mathrm{D}\perp} = \frac{6\pi}{1 - \frac{9}{8}\left(\frac{1}{l^*}\right) + \frac{1}{2}\left(\frac{1}{l^*}\right)^3 - \frac{135}{256}\left(\frac{1}{l^*}\right)^4 - \frac{1}{8}\left(\frac{1}{l^*}\right)^5} \tag{7.9}$$

Note that the lift coefficient C_{L} in Eq. (7.8) reduces to $C_{\mathrm{L},3}$ due to the quiescent flow condition and the corresponding coefficients are evaluated using the new correlation Eq. (7.2b).

The calculated migration velocity values are shown for different $Re_{\mathrm{slip},\infty}$ in figure 7.10b and compared against the previous inner and outer-region lift models suggested in the original paper [239]. The theoretical and experimental migration velocity values show a strong dependence on both $Re_{\mathrm{slip},\infty}$ and l^*. The analytical predictions using the new inner-outer based lift correlation (Eq. 7.2b) agree reasonably well with the experimental results for all three $Re_{\mathrm{slip},\infty}$ numbers. Although the pure inner-region-based predictions are fairly accurate for low slip Reynolds number (i.e, $Re_{\mathrm{slip},\infty} = 0.1005$), the predictions for larger $Re_{\text{slip},\infty}$ values deviate from the experimental results at larger separation distances. The outer-region-based migration velocity predictions are less accurate for all the examined cases. Interestingly, with increasing l^*, the experimental migration velocity results obtained for $Re_{\text{slip},\infty} = 0.5$ reach a maximum around $l^* \sim 2 - 2.5$. For this particular slip Reynolds number, the transition from inner to outer-region also happens at $l^* \sim 2$, and the predictions based on the new lift correlation capture this transition behaviour more accurately than the other available models. Experimental values very close to the wall ($l^* \sim 1.2$) are slightly higher than the theoretical prediction. Nevertheless, notable measurement deviations were also reported closer to the wall, suggesting one potential cause for the discrepancies between experimental and theoretical values here.

7.3.3 Negatively-buoyant particle in a linear shear flow

In this section a small spherical particle falling in a linear shear flow near a wall is examined using the lift and drag correlations from §7.2. Both positive and negative shear flows are considered.

First, the net drag coefficient for positive and negative shear rates of the same magnitude are analysed at small slip ($Re_{\text{slip}} = 0.029$). The variations are compared against experimentally measured drag coefficient values [241]. Unlike the quiescent situation, here C_D is a function of both $C_{\text{D},1}$ and $C_{\text{D},2}$. We compare two different correlations for $C_{\text{D},1}$ (Eqs. 3.26 and 6.7) and use the inner-region-based Faxen drag correlation (Eq. 3.19) for $C_{\text{D},2}$.

As expected, the net drag coefficient of a sedimenting particle increases when the particle moves closer to the wall. However, higher drag coefficients are observed for a sedimenting particle in a positive shear ($\gamma^* > 0$), when compared to the negative shear field ($\gamma^* < 0$). This variation decreases as separation distance increases since the effect of $C_{\text{D},1}$ rapidly decays with l^*. A relatively small difference is observed when using Eq. (3.26) compared to Eq. (6.7) to calculate $C_{\text{D},1}$, a result of shear being relatively low in this analysed system.

Next the lift correlations derived for a linear shear flow at $Re_{\text{slip},\infty} \leq \mathcal{O}(10^{-1})$ are used to predict migration velocities. Similar to the previous section, the slip velocity of the sedimenting particle is first calculated using Eq. (7.7). The values are then

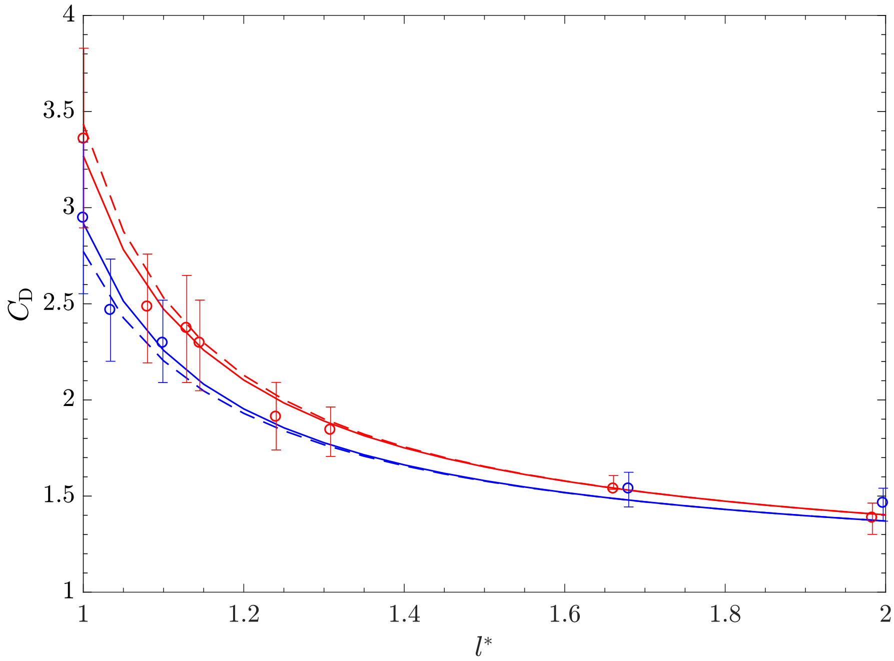

(a) Drag coefficient when $C_{D,1}$ is evaluated by Eq. (6.7) (solid) and Eq. (3.26) (dashed). For all cases $C_{D,2}$ is evaluated by Eqs. (3.19, 3.9). Experiments: $Re_{slip,\infty} = 0.029, \gamma^*_\infty = -0.116$ (○), $Re_{slip}, \infty = 0.029, \gamma^*_\infty = 0.116$ (○).

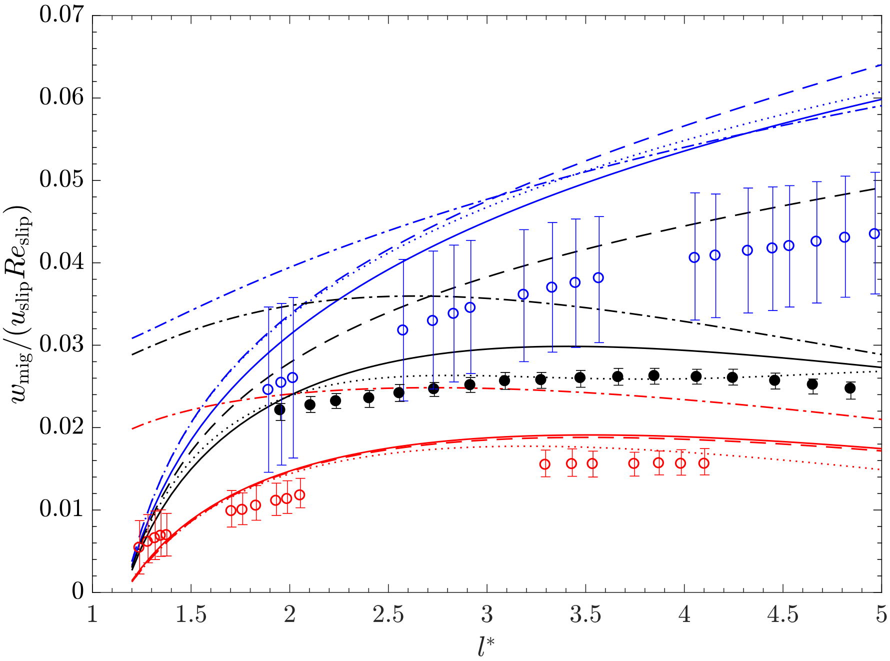

(b) Migration velocity when C_L is evaluated by using proposed lift Eq. (7.4) (solid), inner-region model Eq. (3.47) using Magnaudet et al. [156] coefficients (dashed), outer-region model Eq. (3.45) using Takemura et al. [242] coefficients (dashed dotted) and empirical fit Takemura [239] (dotted). Experiments: $Re_{slip,\infty} = 0.1, \gamma^*_\infty = -0.061$ (○), $Re_{slip,\infty} = 0.17, \gamma^*_\infty = 0.044$ (○), $Re_{slip}, \infty = 0.55, \gamma^*_\infty = -0.033$ (○). Outer-region data are indicated using solid circles, and inner-region data by hollow circles.

FIGURE 7.11: Analysis of a sedimenting particle in a linear single wall-bounded flow

combined with the new lift correlation given for a freely-rotating particle to find the measured dimensionless transverse migration velocity of the particle relative to the fluid $(w_{\mathrm{mig}}/(u_{\mathrm{slip}}Re_{\mathrm{slip}}))$,

$$\frac{w_{\mathrm{mig}}}{u_{\mathrm{slip}}Re_{\mathrm{slip}}} = \frac{C_{\mathrm{L}}}{C_{\mathrm{D}\perp}} \tag{7.10}$$

Here $C_{\mathrm{D}\perp}$ is again evaluated using the Faxen inner-region expression Eq. (7.9) and C_{L} is evaluated using the new correlation given in Eq. (7.4).

Figure 7.11b shows the dimensionless migration velocity as a function of normalised separation distance for three different $Re_{\mathrm{slip},\infty}$. Note that two cases are for negative shear rates and the other for a positive shear rate. All the data reported for the lowest two $Re_{\mathrm{slip},\infty}$ numbers are in the inner-region as the dimensionless Stokes length extends up to $l^* = 10$ for $Re_{\mathrm{slip},\infty} = 0.1$ and $l^* = 5.9$ for $Re_{\mathrm{slip},\infty} = 0.17$. For these two experiments, note that the Saffman length is much larger than the Stokes length since $\epsilon \ll 1$. For $Re_{\mathrm{slip},\infty} = 0.55$, the inner-region shrinks as the non-dimensional Stokes length reduces to $l^* = 1.81$ while the non-dimensional Saffman length spans up to $l^* = 5.5$. Therefore all the experimental data for this case are in the outer-region according to the definition of the region boundary at $l^* = \min(L^*_{\mathrm{S}}, L^*_{\mathrm{G}})$.

Based on experimental results, Takemura et al. [242] suggested an empirical fit for the migration velocity by combining the lift and the wall normal drag coefficients. Although the migration velocity predictions of this fit closely follow the experimental results (i.e., dotted lines in figure 7.11b), this correlation does not provide information about individual forces acting on the particle, and hence this fit cannot be used to predict the particle behaviour when different hydrodynamic forces are acting on a particle simultaneously.

The quantitative agreement of the present model against the experimental data is actually better for the largest two $Re_{\mathrm{slip},\infty}$ values, than for the $Re_{\mathrm{slip},\infty} = 0.1$ case. However, as the migration velocity is very small for $Re_{\mathrm{slip},\infty} = 0.1$, Takemura et al. [242] suggested that the experimental measurements could be less reliable for the entire range of l^* for this case. For $Re_{\mathrm{slip},\infty} = 0.17$ and 0.55, the proposed lift correlation captures both the inner and outer-region behaviour in both negative and positive shear environments reasonably well. Unsurprisingly, Eq. (7.4) follows the inner-region model prediction of Takemura et al. [242] for $Re_{\mathrm{slip},\infty} = 0.17$ as all the experimental measurements are well within the inner-region. Interestingly, the calculated migration velocities for $Re_{\mathrm{slip},\infty} = 0.55$, using the new lift correlation, capture the experimental outer-region behaviour fairly well in the region between the normalised Stokes and Saffman lengths ($1.82 < l^* < 5.5$).

7.4 Closure

The lift and drag forces acting on a spherical particle in a single wall-bounded flow field are examined via numerical computation. The Navier-Stokes equations are solved using a finite-volume solver to find the fluid flow around the particle in large computational flow domains. Forces are obtained under the conditions of finite slip in both quiescent and linear shear flows. The effect of slip velocity, shear rate and wall separation are investigated by varying the slip and shear Reynolds number over the range $Re_{\text{slip}}, Re_{\gamma} = 10^{-3} - 10^{-1}$, and the wall separation distance over $l^* = 1.2 - 9.5$.

Based on the numerical results, we present a new lift force correlation in terms of three force coefficients, valid for any particle-wall separation distance (excluding contact), and $Re_{\text{slip}}, Re_{\gamma} \leq 0.1$. These three lift coefficients, $C_{\text{L},1}$, $C_{\text{L},2}$ and $C_{\text{L},3}$, are defined to be functions of only shear rate, slip velocity and shear rate and only slip velocity, respectively, in addition to wall distance. First a correlation for the slip based lift coefficient ($C_{\text{L},3}$) is proposed based on the lift results obtained for a particle translating in quiescent flow. This coefficient, which is independent of shear, reduces to the unbounded value of zero in the limit $l^* \to \infty$, and asymptotes to the inner-region theoretical value in the limits of $Re \to 0$ and $l^* \to 1$. The shear based lift coefficient, $C_{\text{L},1}$ is adopted from chapter 6. The remaining coefficient, $C_{\text{L},2}$, is calculated by subtracting the force contributions due to pure shear ($C_{\text{L},1}$) and pure slip ($C_{\text{L},3}$) from the numerical lift force results that are computed in a linear flow for both leading and lagging freely-rotating particles. By combining existing inner and outer-region based lift correlations, a new expression is then proposed to capture the $C_{\text{L},2}$ coefficient behaviour. The net lift model obtained by combining all three lift coefficients covers both strong slip and shear flows and is applicable for negative or positive slip and shear rates. To our knowledge, this is the first lift model proposed for a rigid particle that accurately captures the transition in lift force behaviour between the inner and outer regions.

The performance of existing drag models are also compared against the numerical drag results for $Re_{\text{slip}}, Re_{\gamma} \leq 0.1$. The drag force coefficients computed for both non-rotating and freely-rotating particles in quiescent flows agree reasonably well with the inner-region Faxen [80] predictions over the entire wall separation range. For linear shear flows, the most accurate drag predictions are obtained using the chapter 6 and Faxen [80] drag models.

The behaviour of freely translating neutrally-buoyant particles in a linear shear flow and sedimenting particles in both quiescent and linear shear flows are examined using the new lift correlations and examined drag correlations. The results are validated against numerical (chapter 6) [77] and experimental values [239, 241]. The new lift correlation captures the numerical lift coefficient variation of the freely-translating neutrally-buoyant particles reasonably well. The correlation predicts the shear dependency of the lift coefficient and reduces to zero as the separation distance increases. The computed migration values for negatively-buoyant particles, using the new lift correlation also agree well with the experimental measurements in quiescent flows. While the inner-region slip based drag coefficient given by Faxen performs well for small $Re_{\text{slip}} < 0.1$, the inner-outer-region-based correlation by Takemura [239] captures the drag variation when $0.1 < Re_{\text{slip}} < 1$. For negatively-buoyant particles in linear shear flows, the proposed lift model performs better than the other existing theoretical models when predicting the migration velocity for both positive and negative shear rates. However, a significant difference, noted at the lowest slip Reynolds number may be attributed to uncertainties in the measurements as mentioned in the experimental study.

Overall, the proposed new lift correlations, valid for any particle-wall separation distance (excluding contact), will aid in providing accurate constitutive equations for interphase forces to be used in particle-based Lagrangian approaches [152, 167] or interpenetrating continua based Eulerian-Eulerian [171] systems and will provide new opportunities to simulate many critical multiphase biological and industrial problems.

Part III

DILUTE SUSPENSION STUDY

Chapter 8

Two-Fluid Model Development

Particle migration in solid-liquid suspensions is often observed in many industrial applications related to food, petroleum, and mineral processing units [249]. Such migration can occur due to passive hydrodynamic forces leading to different particle distribution patterns. In the particle-separation context, it is beneficial to predict the suspension behaviour to optimise the devices' performance.

On a microscopic scale, the motion of individual particles in suspensions can be examined by solving the Navier-Stokes equations for the flow around each particle. However, such analytical and numerical solution methods are mathematically complicated and computationally expensive and time-consuming. For many applications, the macroscopic level predictions for suspension flows are sufficient, and the details of the flow on the particle scale are not required. To model particle distribution at the macroscopic level, suspensions are often treated as a continuum. Although a significant number of continuum models are developed to examine the multi-particle effects, many of them are used to model suspensions that satisfy the Stokes condition at elevated bulk concentrations.

The main aim of the second part of this thesis is to modify the existing multiphase continuum models to predict the particle migration in dilute suspensions when 'particle scale' inertia is relevant. In this chapter, we present the governing equations developed for a multiphase framework, which accounts for multi-particle effects, inertial lift forces, and other wall-bounded forces. In the subsequent chapters, different force implementation methods and model performance are examined and validated against analytical and experimental results for simple shear flows.

8.1 Solution method

As for the multiphase framework that accounts for the multi-particle effects, Harvie [107]'s two-fluid framework based on Jackson [117]'s volume averaging technique is employed. In this two-fluid approach, both fluid and particle phases are treated as continuum phases with separate continuity and momentum equations.

In the derivation of these equations, the following assumptions are employed [107]:

(a) *Particle Reynolds numbers are small:* The fluid inertia is neglected in the derivation, and the Stokes equations are employed when determining the stress field surrounding each particle. Further, the inertial type Reynolds stress on both solid and fluid phases are neglected. The Reynolds stress terms are related to momentum transport due to fluctuations in particle velocities and fluid velocities surrounding a particle. Neglecting Reynolds stress does not necessarily imply that the inertial lift forces acting on the particles are less significant [107, 117]. However, Harvie's model neglects the inertial lift forces, considering the viscous force magnitudes.

(b) *Wall effects are negligible:* Wall-bounded forces are not included in the derivation. Hence, the model equations are valid only at large distances from system boundaries.

(c) *Suspension is a continuum:* The phase averaged values change over distances that are large compared to the particle size.

(d) *Time derivatives on the local particle scale are negligible:* Added mass effects, basset forces and other memory effects are ignored [116].

Unlike Jackson's model, which is limited to dilute suspensions, Harvie's two-fluid framework can be applied across both dilute and semi-dilute regimes. In Jackson's model, the stress field surrounding each particle is approximated by only accounting for the stress field surrounding a single particle in pure fluid and hence precludes all forms of particle-particle interactions. However, in Harvie's model, the effect of particle collisions due to both short and long range hydrodynamic interactions are also included when solving the stress field disturbances. For this, an additional stress field due to surrounding particles is accounted for. However, when determining the stress due to particle interactions, Harvie has only considered the pair-wise interactions and employed the semi-dilute assumption.

In the subsequent sections, the governing equations and closure expressions of Harvie [107] are presented. However, to account for the small finite inertial and wall effects responsible for cross-stream migration, modifications on the interphase momentum exchange terms are made by integrating the particle-scale force models developed in chapters 6 and 7.

8.2 Momentum and continuity

A mono-disperse suspension of rigid, spherical particles in a Newtonian fluid is considered for this study. Both fluid and solid phases are assumed to be incompressible, and hence the corresponding fluid and solid phase densities, ρ_f and ρ_s, are treated as material constants. The individual mass and momentum conservation equations for fluid and solid phases are [107];

Continuity Equations

Fluid:

$$\frac{\partial \rho_\mathrm{f}\phi_\mathrm{f}}{\partial t} + \boldsymbol{\nabla}\cdot\rho_\mathrm{f}\phi_\mathrm{f}\boldsymbol{u}_\mathrm{f} = \boldsymbol{0} \tag{8.1a}$$

Solid:

$$\frac{\partial \rho_\mathrm{s}\phi_\mathrm{s}}{\partial t} + \boldsymbol{\nabla}\cdot\rho_\mathrm{s}\phi_\mathrm{s}\boldsymbol{u}_\mathrm{s} = \boldsymbol{0} \tag{8.1b}$$

Linear Momentum Equations

Fluid:

$$\frac{\partial \rho_\mathrm{f}\phi_\mathrm{f}\boldsymbol{u}_\mathrm{f}}{\partial t} + \boldsymbol{\nabla}\cdot\rho_\mathrm{f}\phi_\mathrm{f}\boldsymbol{u}_\mathrm{f}\boldsymbol{u}_\mathrm{f} = -\phi_\mathrm{f}\boldsymbol{\nabla}p_\mathrm{f} - \boldsymbol{\nabla}\cdot\boldsymbol{\tau}_\mathrm{f} + \rho_\mathrm{f}\phi_\mathrm{f}\boldsymbol{g} - \boldsymbol{M} \tag{8.2a}$$

Solid:

$$\frac{\partial \rho_\mathrm{s}\phi_\mathrm{s}\boldsymbol{u}_\mathrm{s}}{\partial t} + \boldsymbol{\nabla}\cdot\rho_\mathrm{s}\phi_\mathrm{s}\boldsymbol{u}_\mathrm{s}\boldsymbol{u}_\mathrm{s} = -\phi_\mathrm{s}\boldsymbol{\nabla}(p_\mathrm{f}+\hat{p}_\mathrm{s}) - \boldsymbol{\nabla}p_\mathrm{s} - \boldsymbol{\nabla}\cdot\boldsymbol{\tau}_\mathrm{s} + \rho_\mathrm{s}\phi_\mathrm{s}\boldsymbol{g} + \boldsymbol{M} \tag{8.2b}$$

Here the subscripts 'f' and 's' denote fluid and particle phases respectively. In these expressions, $\boldsymbol{u}$, p_f, p_s, $\hat{p}_\mathrm{s}$, $\boldsymbol{g}$, $\boldsymbol{\tau}$ and $\boldsymbol{M}$ are species velocity, hydrodynamic pressure, solid phase pressure, solid phase specific pressure, mean gravity, viscous stress tensor and interphase force respectively. The sum of all volume fractions needs to be equal to one. Hence, for a monodispersed system the fluid phase and particle phase volume fractions,

ϕ_f and ϕ_s can be written as;

$$\phi_\mathrm{f} + \phi_\mathrm{s} = 1 \tag{8.3}$$

The constitutive equations for p_s, $\hat{p}_\mathrm{s}$, $\boldsymbol{\tau}$ and $\boldsymbol{M}$ close the equation system by considering the structure of the flow field and material properties through numerical and experimental correlations.

8.3 Stress and strains

The viscous stresses for solid and fluid phases are defined under dilute assumptions accounting for the deformation strain rate tensor in each phase [107]. However, the viscous stress partition of a suspension is not definitive in a two-fluid model given that the distinctions between the deformation strain rate variations on each phase are specified using closure assumptions.

8.3.1 Strain rates

The shear stress of each phase is defined based the phase deviatoric stress strain tensor ($\boldsymbol{\gamma}_\mathrm{i}$);

$$\boldsymbol{\gamma}_\mathrm{tot,i} = \boldsymbol{\gamma}_\mathrm{i} + \gamma_\mathrm{sph,i}\boldsymbol{I} \tag{8.4a}$$

where the total strain tensor is defined as:

$$\boldsymbol{\gamma}_\mathrm{tot,i} = (\boldsymbol{\nabla}\boldsymbol{u}_\mathrm{i} + (\boldsymbol{\nabla}\boldsymbol{u}_\mathrm{i})^\mathrm{T}); \tag{8.4b}$$

and the spherical strain rate is defined as:

$$\gamma_\mathrm{sph,i} = \frac{1}{N_\mathrm{dim}}\mathrm{tr}(\boldsymbol{\gamma}_\mathrm{tot,i.}) \tag{8.4c}$$

Here N_dim represents the number of dimensions of the system. Note that when obtaining an equivalent divergence free strain rate tensor ($\boldsymbol{\gamma}_\mathrm{i}$), the symmetric strain rate tensor needs to be deconstructed. Here, the total symmetric strain, is broken into two parts. The first term on the left hand side of Eq. (8.4a) is the trace-less symmetric tensor that represents a gradual shearing deformation with no change in volume, whereas the second term on the left hand side of the equation is the spherical strain rate multiplied by the unit tensor representing a gradual isotropic expansion or contraction. For a three-dimensional flow, the expansion rate tensor ($\gamma_{\text{sph,i}}\boldsymbol{I}$) is 1/3 of the divergence of the velocity field and indicates the rate of increase in the volume of a fixed amount of fluid. For a two-dimensional flow (i.e., thin field), the divergence of velocity field has only two terms and quantifies the change in an area rather than volume. Therefore, the factor 1/3 in the expansion rate term should be replaced by 1/2 in that case. To account for this behaviour N_{dim} is used [107]. However, for non expanding or contracting fluid flow systems used in the present thesis, $\gamma_{\text{sph,i}} = 0$ and hence $\boldsymbol{\gamma}_{\text{i}} = \boldsymbol{\gamma}_{\text{tot,i}}$.

The strain rate magnitude (γ_{i}) and the non-dimensional strain rate tensor ($\hat{\boldsymbol{\gamma}}_{\text{i}}$) are defined as,

$$\gamma_{\text{i}} = \sqrt{\frac{1}{2}\boldsymbol{\gamma}_{\text{i}} : \boldsymbol{\gamma}_{\text{i}}} \tag{8.5a}$$

$$\hat{\boldsymbol{\gamma}}_{\text{i}} = \frac{\boldsymbol{\gamma}_{\text{i}}}{\gamma_{\text{i}}} \tag{8.5b}$$

Further, the total inner product of the normalised strain and deviatoric stress strain tensor is given as,

$$\boldsymbol{\gamma}_{\text{ipn,tot,s}} = \boldsymbol{\gamma}_{\text{i}} \cdot \hat{\boldsymbol{\gamma}}_{\text{i}} \tag{8.6a}$$

Similar to the previous, the deviatoric part of the total inner product tensor can be written as,

$$\boldsymbol{\gamma}_{\text{ipn,s}} = \boldsymbol{\gamma}_{\text{ipn,tot,s}} - \gamma_{\text{ipn,sph,i}}\boldsymbol{I} \tag{8.6b}$$

where the spherical strain tensor of the inner product is,

$$\gamma_{\text{ipn,sph,i}} = \frac{1}{N_{\text{dim}}}\text{tr}(\boldsymbol{\gamma}_{\text{i}} \cdot \hat{\boldsymbol{\gamma}}_{\text{i}}) \tag{8.6c}$$

8.3.2 Shear stress of fluid phase

The fluid phase shear stress tensor, $\boldsymbol{\tau}_{\text{f}}$, is defined by,

$$\boldsymbol{\tau}_{\text{f}} = -\mu_{\text{dilute}}\boldsymbol{\gamma}_{\text{f}} \tag{8.7}$$

where μ_{dilute} is the viscosity of the suspension at the dilute limit. As for the closure expression for μ_{dilute}, the Einstein viscosity model given by,

$$\mu_{\text{dilute}} = \mu_{\text{f}}(1 + 2.5\phi_{\text{s}}) \tag{8.8}$$

is selected [107]. The approach of using the suspension mixture viscosity at dilute condition for the fluid phase is similar to previous studies [267].

8.3.3 Shear stress of solid phase

The solid phase shear stress tensor, $\boldsymbol{\tau}_{\text{s}}$, is defined by,

$$\boldsymbol{\tau}_{\text{s}} = -\mu_{\text{f}}\phi_{\text{s}}^2(\hat{\mu}_{\text{col,s}}\boldsymbol{\gamma}_{\text{s}} - \hat{\mu}_{\text{sid1,s}}\boldsymbol{\gamma}_{\text{ipn,s}}) \tag{8.9}$$

The deviatoric part of the hydrodynamic particle collision tensor is captured by this model. The first term of the right hand side of the equation indicates the shear stress due to particle collision. The additional spherical contribution of the shear induced diffusion contributions (discussed in §8.4.2) that can occur due to the first normal stress are removed from the collision stress tensor. This term is removed from the solid phase stress to avoid double counting the normal components, as the same term is added as a shear induced diffusion pressure term in Eq. 8.24.

The non-dimensional collision viscosity ($\hat{\mu}_{\text{col,s}}$) is related to the effective suspension mixture shear viscosity (μ_{m}) via [107],

$$\mu_{\text{m}} = \mu_{\text{f}}(1 + 2.5\phi_{\text{s}} + \hat{\mu}_{\text{col,s}}\phi_{\text{s}}^2) \tag{8.10}$$

Here, $\hat{\mu}_{\text{col,s}}\phi_{\text{s}}^2$ captures the higher-order effects of solid concentration on the suspension shear viscosity, particularly when the suspension is concentrated. Berry et al. [23] has fitted an empirical function for $\hat{\mu}_{\text{col,s}}$ based on a new parameter introduced as the 'influence length'. The influence length captures the effective range of pairwise interactions and hence depends on the surrounding particle concentration. The function of this parameter is proposed to satisfy both limiting conditions of both dilute ($\phi_{\text{s}} \to 0$) and concentrated conditions ($\phi_{\text{s}} \to \phi_{\text{s,max}}$). Hence, the final form of μ_{m} closely follows other effective suspension viscosity functions available in the literature (see figure C.2). However, at dilute conditions, authors have suggested that the developed correlations for the influence length could be underestimating the real values, which could directly affect the collision viscosity.

8.4 Solid pressure

The solid phase experiences an extra particle pressure due to particle normal contacts. The notion of a particle pressure has been controversial, especially for motion at low Reynolds numbers in suspension studies. Jeffrey et al. [118] was the first to deduce a closure expression for the suspension pressure for a system with hydrodynamic, Brownian, and specific inter-particle forces. This was further modified and applied in recent suspension studies performed using mixture models [38, 85, 182, 189, 249].

In the two-fluid framework, the formulation of the solid pressure in a suspension at very dilute conditions can be presented as,

$$p_{\mathrm{s}} = p_{\mathrm{osm,s}} + p_{\mathrm{sid,s}} \tag{8.11}$$

Eq. (8.11) accounts for two main particle migration mechanisms known as Brownian motion and shear induced migration. Brownian motion or diffusion is the random motion of solid particles due to bombardment by other particles, which is important for small micro and nanoscale particles. The solid pressure due to this Brownian motion can also be denoted as a form of osmotic pressure ($p_{\mathrm{osm,s}}$). Conversely, the shear induced diffusion occurs due to both local shear gradients and concentration gradients in a system. The pressure due to the shear induced diffusion is termed as SID pressure ($p_{\mathrm{sid,s}}$). The significance of these migration mechanisms is usually determined by the Péclet number, Pe ($= 6\pi\mu_m\gamma a^3/k_{\mathrm{B}}T$), representing the ratio of shear-driven motion to Brownian motion at the particle scale [85]. Generally, for high Pe numbers, Brownian diffusion becomes less significant and allows the shear induced migration to dominate in the system. At such occurrences, $p_{\mathrm{sid,s}} \gg p_{\mathrm{osm,s}}$. However, for the particle sizes of interest in this study, $a = 1 - 10\mu$m both Brownian diffusion and shear induced diffusion become relevant, and hence $p_{\mathrm{sid,s}}$ and $p_{\mathrm{osm,s}}$ are both significant.

8.4.1 Osmotic pressure

Osmotic pressure due to Brownian motion at dilute conditions ($\phi_\mathrm{s} < 0.01$) can be approximated by the van't Hoff expression, which considers the linearity of solid pressure with the energy of thermal fluctuations ($nk_\mathrm{B}T$),

$$\begin{aligned} p_{\mathrm{osm,s}} &= nk_\mathrm{B}T \\ &= \frac{\phi_\mathrm{s}}{(4/3)\pi a^3} k_\mathrm{B}T \end{aligned} \tag{8.12}$$

Here n, k_B and T represent particle number density, Boltzmann constant and the absolute temperature of system respectively. The number density, n, is also equal to $N/V = \phi_\mathrm{s}/v$ where N is the total number of solid particles, V is the total volume and v is volume of single particle.

However, with increasing solid concentration the osmotic pressure in a system increases non-linearly. To capture this behaviour, the ideal osmotic pressure given by Eq. (8.12) is modified with a compressibility factor, $Z(\phi_\mathrm{s})$ as below,

$$\begin{aligned} p^{\mathrm{tot}}_{\mathrm{osm,s}} &= p_{\mathrm{osm,s}} Z(\phi_\mathrm{s}) \\ &= nk_\mathrm{B}TZ(\phi_\mathrm{s}) \end{aligned} \tag{8.13}$$

Carnahan and Starling [40] were the first to suggest a statistical model (Eq. 8.14) for $Z(\phi_\mathrm{s})$, which is valid for solid fractions as high as $\phi_\mathrm{s} = 0.5$. The model considered that momentum and energy exchange is through direct contact collisions. Using a similar framework, but assuming that the momentum and energy exchange occurs in a collisionless suspension, Buyevich [37] suggested a new statistical model (Eq. 8.15) for $Z(\phi_\mathrm{s})$. This model assumed that the inter-particle exchange is carried out only through fields of fluid velocity and pressure. Eq. (8.14) and Eq. (8.15), which provides excessive pressure due to collisional and collisionless suspensions, coincide in the low concentration range. However, at high bulk concentrations, Eq. (8.15) is somewhat smaller than Eq. (8.14).

It is required that the $Z(\phi_\mathrm{s})$ diverges at a maximum solid packing fraction (ϕ_max) to describe the jamming behaviour of the suspension. However, previously discussed statistical models fail to capture this behaviour. Correlating the free volume fraction, which indicates the amount of volume available for a new hard-sphere of the same size, several

Study	$Z(\phi_s)$	Eq.
Carnahan and Starling [40]	$\dfrac{1+\phi+\phi^2-\phi^3}{(1-\phi)^3}$	(8.14)
Buyevich [37]	$\dfrac{2\ln(1-\phi_s)}{\phi_s}+\dfrac{3(1-2\phi_s)}{(1-\phi_s)}+\dfrac{\phi_s}{2}\dfrac{(15-8\phi_s-\phi_s^2)}{(1-\phi_s)^2}$	(8.15)
Enskog in Buyevich [37]	$(1-\hat{\phi}_s^{1/3})^{-1}$	(8.16)
Woodcock [256]	$3(1-\hat{\phi}_s)^{-1}$	(8.17)
Kamien and Liu [121]	$\hat{\phi}_s^{1/3}(1-\hat{\phi}_s^{1/3})^{-1}$	(8.18)

TABLE 8.1: Closure relations for compressibility factor.

studies suggested closure expressions for $Z(\phi_s)$ using the reduced solid volume fraction ($\hat{\phi}_s = \phi_s/\phi_{max}$). Enskog first suggested a model for $Z(\phi_s)$ using the free volume fraction that tends to infinity as the solid concentration reaches its maximum packing fraction [38]. Using a similar approach, Woodcock [256] suggested another correlation, which was later used in Frank et al.'s SBM study to model osmotic pressure. In a recent study, Kamien and Liu [121] suggested a new correlation based on the reduced volume fraction, which follows the Carnahan–Starling equation even at high volume fractions ($\phi_s \sim 0.5$). A summary of the equations for these different methods are provided in table 8.1, and the equations are compared in figure 8.1.

Several studies on suspension modelling [233, 249, 252, 253], have expressed the non-ideal (excess) part of the osmotic pressure ($p_{osm,s}^{non\text{-}id} = p_{osm,s}^{tot} - p_{osm,s}$) using the excess chemical potential of a system given by $\mu_{chem,s}^{exc}$. This non-ideal osmotic pressure and the excess chemical potential are related using Helmholtz free energy in the form of [233, 253],

$$\boldsymbol{\nabla} p_{osm,s}^{non-id} = \frac{\phi_s}{v}\boldsymbol{\nabla}\mu_{chem,s}^{exc} \tag{8.19}$$

Accounting for the Carnahan–Starling equation for the compressibility factor in $p_{osm,s}^{tot}$, the excess chemical potential can be simplified as [233],

$$\mu_{chem,s}^{exc} = \frac{\phi_s(8-9\phi_s+3\phi_s^2)}{(1-\phi_s)^3} \tag{8.20}$$

Implementation

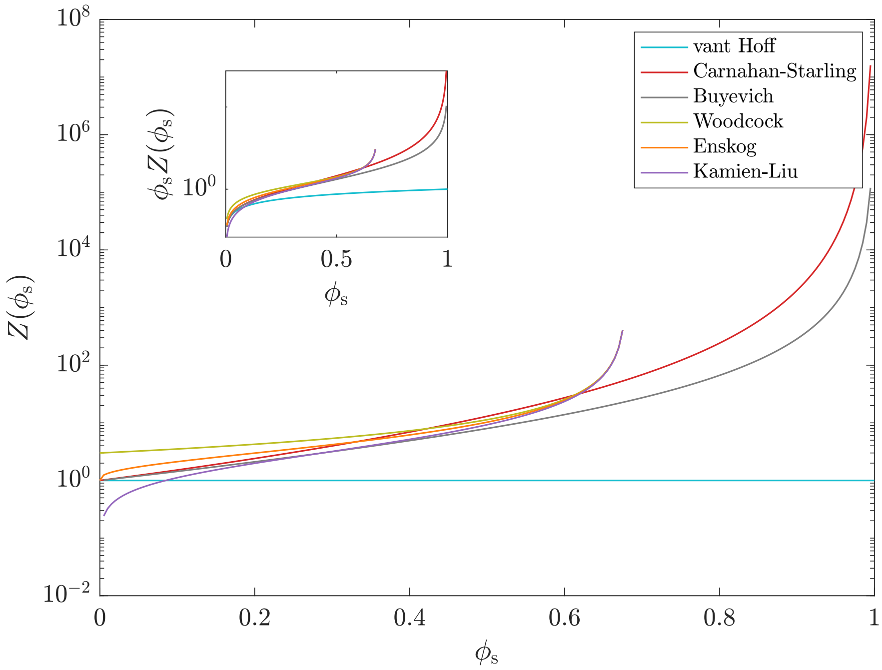

FIGURE 8.1: Compressibility factor variation with solid volume fraction. Here $\phi_{\max} = 0.68$.

The net osmotic pressure is partitioned into ideal and non-ideal osmotic pressure components, allowing other multi-component solid species models to be introduced in the system in future work[a]. With this partitioning the non-ideal pressure is set to the Carnahan–Starling excess pressure as follows,

$$\begin{aligned}\nabla p^{\text{tot}}_{\text{osm,s}} &= \nabla p_{\text{osm,s}} + \nabla p^{\text{non-id}}_{\text{osm,s}} \\ &= \nabla p_{\text{osm,s}} + \frac{\phi_s}{v}\nabla \mu^{\text{exc}}_{\text{chem,s}}\end{aligned} \tag{8.21}$$

Defining the excess solid pressure, $\hat{p}_{\text{exc,s}}$, equal to $\hat{\mu}^{\text{exc}}_{\text{chem,s}}/v$ term in Eq. (8.21), $\hat{p}_{\text{exc,s}}$ can be related to total osmotic pressure via,

$$\nabla p^{\text{tot}}_{\text{osm,s}} = \nabla p_{\text{osm,s}} + \phi_s \nabla \hat{p}_{\text{exc,s}} \tag{8.22}$$

Note that the excess solid pressure which is based on Carnahan–Starling equation does not diverge at the maximum solid volume fraction.

In summary, equating the osmotic pressure and shear induced diffusion pressure to solid phase pressure ($p_s = p_{\text{osm,s}} + p_{\text{sid,s}}$) and excess solid pressure to the solid specific pressure

[a]Mohammad Nouri PhD thesis work

($\hat{p}_{\mathrm{s}} = \hat{p}_{\mathrm{exc,s}}$), the final form of the pressure terms in Eq. 8.2 can be presented as,

$$\phi_{\mathrm{s}} \boldsymbol{\nabla} \hat{p}_{\mathrm{s}} + \boldsymbol{\nabla} p_{\mathrm{s}} = \phi_{\mathrm{s}} \boldsymbol{\nabla} \hat{p}_{\mathrm{exc,s}} + \boldsymbol{\nabla} p_{\mathrm{osm,s}} + \boldsymbol{\nabla} p_{\mathrm{sid,s}} \tag{8.23}$$

It should be noted that the excess pressure that arises in the suspension flows analysed in this thesis is negligible as we operate in the dilute regime, and hence the choice of Carnahan–Starling equation for the excess solid pressure is immaterial.

8.4.2 SID pressure

SID pressure originates from the shear induced diffusive motion of particles. Given that the theoretical background on SID motion has been broadly discussed in §4.2, here we only detail Berry et al.'s formulation of SID pressure in the context of the two-fluid framework.

The concept of capturing the shear induced diffusion as a pressure force, or otherwise as a normal particle stress, was initially suggested by Brady and coworkers [183, 189]. The group suggested the suspension balance model to evaluate the viscously generated normal stresses in the particle phase as an additional suspension pressure. In these studies, the SID pressure scales linearly with the suspension shear rate. However, they also assume that the solid stress is isotropic, and hence these models do not predict the particle migration that is observed in curvilinear flows. Later, Morris and coworkers [182] considered the normal stress differences present in the particle phase stress tensor and suggested a closure expression for a shear induced pressure using an anisotropic flow aligned stress tensor. The suggested model successfully predicts most of the observed particle migrations in simple curvilinear flows. Although this shear induced pressure force has been extensively employed in the mixture model framework, a frame-invariant generalisation for the SID pressure that applies to flows in complex geometries has been studied only in a few studies [175].

Harvie has included the shear induced diffusion pressure force into the two-fluid framework presented for a mono-disperse suspension. In the averaged equations for the solid phase, the SID pressure force is presented as a normal stress force due to hydrodynamic-particle interaction. The scalar p_{sid} function employed in Harvie's two-fluid model is,

$$p_{\text{sid,s}} = \mu_{\text{f}}\phi_{\text{s}}^{2}(\hat{\mu}_{\text{sid1,s}}\gamma_{\text{ipn-sph,s}} + \hat{\mu}_{\text{sid2,s}}\gamma_{\text{s}}) \tag{8.24}$$

Here $\hat{\mu}_{\text{sid1,s}}$ and $\hat{\mu}_{\text{sid2,s}}$ are the non-dimensional viscosity coefficients related to the first and second normal stresses. This formulation also allows us to capture the anisotropic nature of the suspensions. Empirical correlations for $\hat{\mu}_{\text{sid1,s}}$ and $\hat{\mu}_{\text{sid2,s}}$ were suggested by Berry et al. [23], using an anisotropy function that accounts for the particle roughness.

8.5 Interphase momentum transfer

The interphase force $\boldsymbol{M}$, which arises due to interaction between phases, represents the force on the particulate phase due to the fluid phase. Here $\boldsymbol{M}$ presents collectively the drag forces ($\boldsymbol{M}_{\text{D}}$) and the lift forces ($\boldsymbol{M}_{\text{L}}$) acting on the particles.

$$\boldsymbol{M} = \boldsymbol{M}_{\text{D}} + \boldsymbol{M}_{\text{L}} \tag{8.25}$$

Harvie's two-fluid model only includes unbounded drag forces originating from slip velocity ($\boldsymbol{M}^{\text{ub}}_{\text{D,slip}}$) and flow curvature ($\boldsymbol{M}^{\text{ub}}_{\text{D,shear-gradient}}$). The wall effects and inertial effects are neglected in the equation averaging process. However, as discussed in the previous chapters, the inertial lift forces and other wall-bounded forces become equally significant in predicting dilute suspensions particle distributions at finite particle Reynolds numbers.

To our knowledge, no study has attempted to include these particle-scale inertial forces in any multiphase framework, in at least part, due to the lack of generalised closure relations for the wall-bounded lift and drag forces [252]. Given that we have developed these force relationships for single particles in chapters 6 and 7 for finite slip and shear Reynolds numbers, new closure models for wall-bounded interphase momentum exchanging term are suggested in this section. We implement wall-bounded viscous drag forces ($\boldsymbol{M}^{\text{wb}}_{\text{D,slip}}$ and $\boldsymbol{M}^{\text{wb}}_{\text{D,shear}}$) and wall-bounded and unbounded inertial lift forces ($\boldsymbol{M}^{\text{ub}}_{\text{L,shear-gradient}}$, $\boldsymbol{M}^{\text{wb}}_{\text{L,slip}}$, $\boldsymbol{M}^{\text{wb}}_{\text{L,slip-shear}}$ and $\boldsymbol{M}^{\text{wb}}_{\text{L,shear}}$) within Harvie's two-fluid framework as shown in Eq.

(8.26).

$$\boldsymbol{M}_{\mathrm{D}} = \boldsymbol{M}^{\mathrm{ub}}_{\mathrm{D,slip}} + \boldsymbol{M}^{\mathrm{ub}}_{\mathrm{D,shear\text{-}gradient}} + \boldsymbol{M}^{\mathrm{wb}}_{\mathrm{D,slip}} + \boldsymbol{M}^{\mathrm{wb}}_{\mathrm{D,shear}} \tag{8.26a}$$

$$\boldsymbol{M}_{\mathrm{L}} = \boldsymbol{M}^{\mathrm{ub}}_{\mathrm{L,shear\text{-}gradient}} + \boldsymbol{M}^{\mathrm{wb}}_{\mathrm{L,slip}} + \boldsymbol{M}^{\mathrm{wb}}_{\mathrm{L,slip\text{-}shear}} + \boldsymbol{M}^{\mathrm{wb}}_{\mathrm{L,shear}} \tag{8.26b}$$

The following assumptions are made when including these extra forces to the two-fluid model:

(a) *Interphase forces act on both the solid and fluid phases:* The conservation of global momentum at suspension length scales indicates that the total momentum transferred between the phases should be zero. However, near wall regions, the momentum transfer happens between the solid, fluid and walls, and hence the momentum partitioning becomes complex. For this study, all the interphase forces originating from wall interactions are assumed to act on both solid and fluid phases equally but in the opposite direction based on the analysis provided in §9.2.1.

(b) *The presence of other particles does not alter wall-bounded lift forces or drag forces:* Wall-bounded forces are most significant near system boundaries. This assumption is partly justified by experimental observations that suggest that the particle concentration is low near the walls. Hence the effect of the other particles on the particle migration velocity is neglected for wall-bounded forces, and inertial forces based on dilute, isolated particles are applied.

(c) *The combined effect of the flow curvature and the walls on these particle-scale inertial forces are considered by other parts of the model:* Shear gradients (or velocity curvatures) in a flow produce additional drag and lift forces in a suspension system, even in an unbounded flow. Near system boundaries, these shear-gradient induced unbounded lift and drag forces are further modified by the presence of the wall. For dilute suspensions in Couette flows, the fluid flow profiles near walls are relatively linear, and hence wall-bounded shear-gradient effects are neglected in this study.

8.5.1 Drag force

Drag forces in a system can originate from various flow features, including phase slip velocity, fluid shear, fluid flow curvature, and wall effects. In many multiphase studies, wall and shear effects on the drag force are not included due to lack of closure equations. The slip velocity and shear-gradient based drag forces are commonly modelled via the Stokes drag and the Faxen drag in multi-fluid formulations, modelling dilute non-inertial suspensions.

8.5.1.1 Stokes slip drag

The relative motion of the fluid and solid phases results in a drag force acting in the opposite direction in each phase. Like most other two-fluid models [117, 267], in Harvie's study, the drag force acting on a single particle is defined based on unbounded flow at Stokes limit, and thus neglects any wall effects or inertial effects. The interphase momentum term, resulting from unbounded slip based drag force is defined as;

$$\boldsymbol{M}^{\mathrm{ub}}_{\mathrm{D,slip}} = -\beta_1(\boldsymbol{u}_{\mathrm{s}} - \boldsymbol{u}_{\mathrm{f}}) \tag{8.27}$$

where β_1 is the corresponding multi-particle dimensional drag coefficient. This coefficient β_1 can be obtained using the single particle drag coefficient $C^{\mathrm{ub}}_{\mathrm{D},2}\mu_{\mathrm{f}}a$. As shown in chapter 7 results, $C^{\mathrm{ub}}_{\mathrm{D},2}$ can be evaluated via Stokes drag coefficient 6π without inertial modification for the small particles Reynolds numbers considered in this study ($\mathcal{O}(Re_{\mathrm{slip}}) < 1$). The multi-particle drag coefficient, β_1, is obtained by multiplying the solid particle number density, $n(= \phi_{\mathrm{s}}/(\frac{4}{3}\pi a^3))$, representing the drag on the suspension, per total volume of suspension:

$$\beta_1 = nC^{\mathrm{ub}}_{\mathrm{D},2}\mu_{\mathrm{f}}a = \frac{9\mu_{\mathrm{f}}\phi_{\mathrm{s}}}{2a^2} \tag{8.28}$$

Sedimentation experiments performed for moderately dilute suspensions reported that particles settle at speeds significantly slower than in otherwise pure fluid due to particle-particle interaction effects [104, 161]. Hence, many multiphase studies have introduced a hindered drag function $H(\phi_{\mathrm{s}})$ to the multi-particle drag coefficient β_1 to account for this behaviour in suspension flow modelling [120, 182, 249, 252]. This function modifies the drag on particles to account for multi-particle effects. Following Masliyah [161] here, we modify Eq. (8.28) as,

$$\beta_1 = \frac{9\mu_{\mathrm{f}}\phi_{\mathrm{s}}}{2a^2}\frac{1}{H(\phi_{\mathrm{s}})} \tag{8.29}$$

The modification $1/H(\phi_s)$ considers the increase in drag on a particle due to other particles. Here the drag coefficient is correlated with the suspension density. However, the definition and application of the hindered drag function is often unclear in the literature. Based on the mean-field flow theory applied for a sedimentation problem, some studies define a hindered drag function $F(\phi_s)$ as the ratio of a particle's sedimenting velocities in the presence and absence of other particles in the system [104, 207]. Therefore considering both Richardson and Zaki [207]'s and Masliyah [161]'s hindered function definitions and equating the sedimenting velocity, it can be shown that $\phi_f^2/F(\phi_s) = 1/H(\phi_s)$ for a multi-particle system.

In the literature, many theoretical and empirical expressions are available for $H(\phi_s)$. All decrease monotonically with increasing solid volume fraction with most giving $H(0) = 1$. The most commonly used closure expressions for monodisperse rigid spheres are listed in table 8.2 [35, 97] and plotted in figure 8.2.

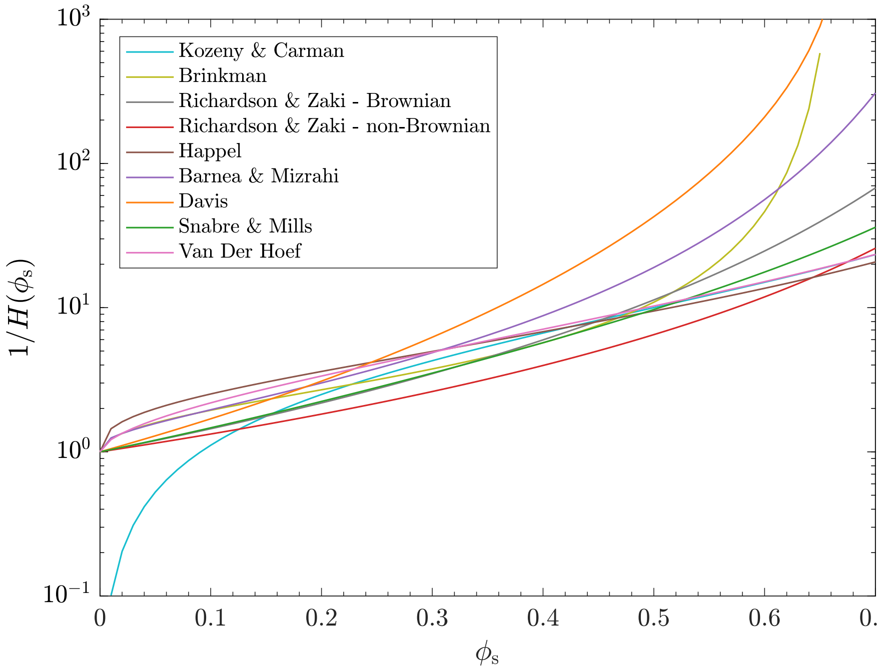

FIGURE 8.2: Hindered drag function variation with solid volume fraction.

Most of the hindered drag functions have a similar form. The Carman-Kozeny semi-theoretical model given in Eq. (8.30) was initially developed for concentrated suspensions, and thus, it overpredicts the hindered drag function as the volume fraction approaches zero [39]. Several attempts have been made to improve upon this behaviour and to find expressions for $H(\phi_s)$ valid over the entire solid fraction range. This was first addressed by Brinkman [34], whose model is valid for dilute conditions (see figure

Study	$H(\phi_s)$	Eq.
Carman [39]	$(1-\phi_s)/10\phi_s$	(8.30)
Brinkman [34]	$[1+3/4\phi_s(1-\sqrt{8/\phi_s-3})](1-\phi_s)^{-2}$	(8.31)
Richardson and Zaki [207]	$(1-\phi_s)^{n-2}$	(8.32)
Happel [104]	$(3-4.5\phi_s^{1/3}+4.5\phi_s^{5/3}-3\phi_s^2)[(3+2\phi_s^{5/3})(1-\phi_s)^2]^{-1}$	(8.33)
Barnea and Mizrahi [15]	$(1-\phi_s)^2[1+\phi_s^{1/3}\exp(5\phi_s/3(1-\phi_s))]^{-1}$	(8.34)
Davis [63]	$(1-\hat{\phi}_s)(1-\phi_s)^{n-3}$	(8.35)
Mills and Snabre [176]	$[1+4.6\phi_s/(1-\phi_s)^3]^{-1}(1-\phi_s)^{-1}$	(8.36)
Van Der Hoef [248]	$[10\phi_s(1-\phi_s)^{-2}+(1-\phi_s)^2(1+1.5\sqrt{\phi_s})]^{-1}(1-\phi_s)^{-1}$	(8.37)

TABLE 8.2: Correlations available for hindered drag functions for monodispersed rigid spheres.

8.2). However, this model diverges at $\phi_s = 0.67$, predicting zero value for hindered drag function (i.e., infinite drag force) and hence is not valid beyond that point. Note that even at the solid packing limit, the drag on each particle by the surrounding fluid should be finite as fluid is still able to move through the gaps between particle. Another widely used empirical correlation in the multiphase framework is Richardson and Zaki [207]'s model. This model predicts the experimental data accurately, and the model uses $n = 5.5$ and $n = 4.65$ coefficients for Brownian ($\mathcal{O}(Pe) < 10$) and non-Brownian particles ($\mathcal{O}(Pe) > 10$), respectively. Several other correlations based on experimental studies [15, 176] and numerical studies [248] also provide monotonically decreasing hindered drag functions. Like the Brinkman model, the Davis model diverges at the random close packing limit predicting zero for the hindered drag function (infinite drag). This is based on the fact that the suspension has no settling velocity. However, we argue that even at this limit, the drag is still finite ($H(\phi_s) \neq 0$), with settling velocities going to zero due to other (e.g., steric forces) effects.

In this study, Richardson and Zaki's model, which is independent of $\phi_{s,max}$, is adopted. Given typical Péclet numbers considered ($Pe \geq \mathcal{O}(10^{10})$), we use a coefficient similar to the non-Brownian coefficient of $n = 4.5$.

8.5.1.2 Faxen drag

Stokes drag expression (Eq. 8.27), originally derived for a single particle, only considers particle translation in a quiescent fluid at low Reynolds number. Hence, this expression does not account for any velocity gradients in the fluid phase. Later Faxen [80] proposed an additional drag term considering a particle moving in an unbounded fluid flow with non-zero and varying shear-gradient. The additional drag due to the varying shear gradients of fluid phase velocity had been included as an interphase momentum force in many multiphase flow models [117, 120, 266]. As the force originates due to the interaction of the particle with the fluid, it acts in opposite directions in each phase. The Faxen interphase force acting on the solid species at dilute condition is given as,

$$\boldsymbol{M}^{\mathrm{ub}}_{\mathrm{D,shear\text{-}gradient}} = \beta_2 \boldsymbol{\nabla}^2 \boldsymbol{u}_{\mathrm{f}} \tag{8.38}$$

The phase average multi-particle dimensional drag coefficient corresponding to Faxen drag, β_2, can be obtained by converting the single particle Faxen drag correlation, $C^{\mathrm{ub}}_{\mathrm{D,faxen}}\mu_{\mathrm{f}}a^3$, where $C^{\mathrm{ub}}_{\mathrm{D,faxen}} = \pi$, into a force acting on a suspension of particles, expressed

$$\beta_2 = nC^{\mathrm{ub}}_{\mathrm{D,shear\text{-}gradient}}\mu_{\mathrm{f}}a^3 = \frac{3\mu_{\mathrm{f}}\phi_{\mathrm{s}}}{4} \tag{8.39}$$

per total volume of suspension.

In the presence of a shear-gradient, the Faxen drag force can cause the solid phase to lag or lead the fluid. For example, in pressure driven flows (i.e., pipe flows), the constant negative shear-gradient produces a constant negative Faxen drag force on the particle phase across the entire radius. This causes the solid phase to lag the fluid in absence of any additional forces. Accounting for the mixture phase momentum equation for fully developed, steady-state flow, Harvie [107] suggests a modified multi-particle coefficient for the Faxen force as,

$$\beta_2 = \frac{7\mu_{\mathrm{f}}\phi_{\mathrm{s}}}{4} \tag{8.40}$$

which produces the single particle Faxen lag velocity when both drag and pressure forces are considered on dilute suspensions.

8.5.1.3 Wall-bounded slip drag

The presence of a wall significantly affects the Stokes unbounded slip-drag force due to the additional disturbance in the velocity field. At the single particle scale, the wall effect on the slip-drag force has been extensively studied by Faxen [104], who proposed new correlations accounting for particles translating parallel and normal to walls. These correlations were further investigated in chapter 7 where the analytical models were verified for $Re_{\mathrm{slip}} < \mathcal{O}(10^{-1})$.

Based on the wall-slip based drag results presented in chapter 7, we propose a wall-bounded interphase momentum force acting on solid-phase resulting from wall-bounded slip as,

$$\boldsymbol{M}^{\mathrm{wb}}_{\mathrm{D,slip}} = -\beta_3(\boldsymbol{I} - \boldsymbol{n}_{\mathrm{w}}\boldsymbol{n}_{\mathrm{w}}) \cdot (\boldsymbol{u}_{\mathrm{s}} - \boldsymbol{u}_{\mathrm{f}}) - \beta_4 \boldsymbol{n}_{\mathrm{w}}\boldsymbol{n}_{\mathrm{w}} \cdot (\boldsymbol{u}_{\mathrm{s}} - \boldsymbol{u}_{\mathrm{f}}) \tag{8.41}$$

The first term in the right hand side of Eq. (8.41) accounts for the wall correction specific to particles that slip tangential to a wall, and the second term accounts for a wall correction specific to particles that slip normal to the wall. Here β_3 and β_4 are the multi-particle dimensional coefficients corresponding to $C^{\mathrm{wb}}_{\mathrm{D,2}}$ and $C^{\mathrm{wb}}_{\mathrm{D,2\perp}}$, respectively. These single particle coefficients can be related to the multi-particle force coefficients as,

$$\beta_3 = nC^{\mathrm{wb}}_{\mathrm{D,2}}\mu_{\mathrm{f}}a = \frac{9\mu_{\mathrm{f}}\phi_{\mathrm{s}}}{2a^2}\left(\left[1 - \frac{9}{16}\left(\frac{a}{l}\right) + \frac{1}{8}\left(\frac{a}{l}\right)^3 - \frac{45}{256}\left(\frac{a}{l}\right)^4 - \frac{1}{16}\left(\frac{a}{l}\right)^5\right]^{-1} - 1\right) \tag{8.42}$$

$$\beta_4 = nC^{\mathrm{wb}}_{\mathrm{D,2\perp}}\mu_{\mathrm{f}}a = \frac{9\mu_{\mathrm{f}}\phi_{\mathrm{s}}}{2a^2}\left(\left[1 - \frac{9}{8}\left(\frac{a}{l}\right) + \frac{1}{2}\left(\frac{a}{l}\right)^3 - \frac{135}{256}\left(\frac{a}{l}\right)^4 + \xi\left(\frac{a}{l}\right)^5\right]^{-1} - 1\right) \tag{8.43}$$

As discussed in §3.2.2, the best estimate for ξ in Eq. (8.43) is 39/256. However, noting that this will predict ∞ for $C^{\mathrm{wb,in}}_{\mathrm{D,2,\perp}}$ when $l/a = 1$, ξ is adjusted to 40/256 to give a finite value for $C^{\mathrm{wb,in}}_{\mathrm{D,2,\perp}}$ at $l/a = 1$ in this study. Issues related to force behaviour at walls are discussed in chapter 9.

As discussed in the previous section, similar to other unbounded models, all wall-bounded force models are applied in both solid and fluid phases with an equal magnitude but opposite direction. This implies that there is no direct interaction between particles and the wall, with all forces acting through the fluid phase. In reality, the partitioning of these forces between the solid, fluid, and wall in this region is complex, with different interpretations at the particle and the suspension length scales. Our assumption of equal magnitude opposing interphase forces represents a pragmatic approach to this multi-scale problem. Further, it is assumed that the presence of other particles does not alter the wall-bounded slip drag force.

Wall-normal and particle-wall separation lengths

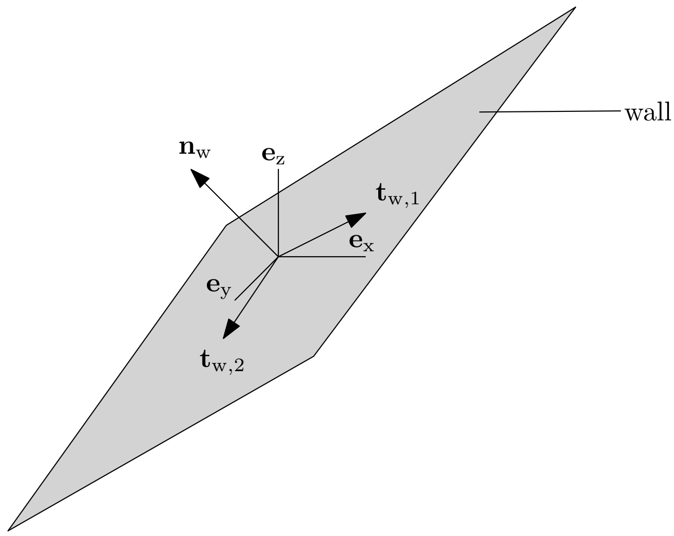

FIGURE 8.3: Illustration of unit normal and unit tangents of an arbitrarily wall oriented in the 3D space.

To obtain the slip velocity components tangent and normal to a wall in 3D space (Figure 8.3), we introduce an outward unit normal wall vector ($\boldsymbol{n}_\mathrm{w}$). The orthogonal wall tangents ($\boldsymbol{t}_{\mathrm{w},1}$ and $\boldsymbol{t}_{\mathrm{w},2}$) are arbitrarily chosen such that $\boldsymbol{I} = \boldsymbol{n}_\mathrm{w}\boldsymbol{n}_\mathrm{w} + \boldsymbol{t}_{\mathrm{w},1}\boldsymbol{t}_{\mathrm{w},1} + \boldsymbol{t}_{\mathrm{w},2}\boldsymbol{t}_{\mathrm{w},2}$ [26].

The wall separation distance for each cell within the computational mesh (l) is defined as the shortest distance from the domain cell centre to the closest boundary (wall) face centre. For the non-dimensional values $l/a < 1$, a minimum cut-off value of $l = a$ is used in simulations where the local mesh cell size is smaller than the particle radius to avoid nonphysical coefficient values. The implications of this choice in the near wall region are discussed in chapter 9.

8.5.1.4 Wall-bounded shear drag

In the wall's presence, the effects of shear rates on the drag force become more significant and result in extra wall shear drag force on particles. The single particle studies in linear shear flows [77, 156] and the results of §6.3 suggest that freely-translating particles lag in the fluid flow in positive shear flows due to this wall shear drag force. The wall shear drag acts in the opposite direction the fluid flow, noting that the fluid velocity at the wall is zero (no-slip velocity boundary condition).

Based on the single particle zero-slip drag results presented in §6.3, the interphase momentum force due to wall-shear can be presented in terms of the fluid shear rates as,

$$\boldsymbol{M}^{\mathrm{wb}}_{\mathrm{D,shear}} = -\beta_5 \boldsymbol{n}_{\mathrm{w}} \cdot \boldsymbol{\gamma}_{\mathrm{f}} \cdot (\boldsymbol{I} - \boldsymbol{n}_{\mathrm{w}}\boldsymbol{n}_{\mathrm{w}}) \tag{8.44}$$

This interphase force is defined to be always parallel to the wall. In the single particle studies, the fluid shear variation normal to the wall and at the wall is considered (chapter 6). However, in the suspension force implementation the local solid phase shear rate is employed. Hence, this assumes that the strain rates of fluid and solid phases are similar at dilute conditions ($\boldsymbol{\gamma}_{\mathrm{f}} \approx \boldsymbol{\gamma}_{\mathrm{s}}$), and that in the wall regions, these forces are significant as there is minimal variation in $\boldsymbol{\gamma}_{\mathrm{s}}$ away from the wall. The multi-particle wall shear dimensional drag coefficient, β_5, is hence defined based on Eq. 6.6 as,

$$\beta_5 = nC^{\mathrm{wb}}_{\mathrm{D},1}\mu_{\mathrm{f}}a^2 = \frac{3\mu_{\mathrm{f}}\phi_{\mathrm{s}}}{4\pi a}\left(\frac{15\pi}{8}\left(\frac{a}{l}\right)^2\left[1 + \frac{9}{16}\left(\frac{a}{l}\right) + 0.5801\left(\frac{a}{l}\right)^2 - 3.34\left(\frac{a}{l}\right)^3 \right.\right.$$
$$\left.\left. +4.15\left(\frac{a}{l}\right)^4\right] + (3.001Re_\gamma^2 - 1.025Re_\gamma)\right) \tag{8.45}$$

In the two-fluid context, the dimensionless shear based particle Reynolds number (Re_γ) is thus defined by considering the solid phase local strain rate magnitude as below,

$$Re_\gamma = \frac{|\gamma_{\mathrm{s}}|a^2\rho_{\mathrm{f}}}{\mu_{\mathrm{f}}} \tag{8.46}$$

Similar to the other wall-bounded slip forces, the wall-shear drag force is also applied in both the solid and fluid phases as equal and opposite and it is assumed that the presence of other particles does not alter the magnitude of these forces.

8.5.2 Lift Force

Lift forces are inertial in origin and hence reduce to zero for rigid particles in the Stokes (zero Reynolds number) limit [33]. However, at finite particle Reynolds numbers, in unbounded shear flows, rigid particles experience lift when moving relative to the undisturbed fluid velocity either when there is finite shear within the fluid, or particle rotation relative to the fluid [210, 211]. In bounded flows (i.e., near a wall), particles experience an additional lift force due to wall, shear and slip effects at finite slip and shear Reynolds numbers.

A few multiphase studies have attempted to include lift forces in the two-fluid framework developed for dilute suspensions [72, 100, 120, 171]. These studies implemented double wall-bounded lift models defined for planar Poiseuille flows [108, 250] and unbounded slip-shear lift forces [211] to predict the 'tubular-pinch effect' observed in dilute suspensions. Although the two-fluid models qualitatively predicted the expected particle distributions, the results have not been quantitatively validated. These two-fluid models also neglect other multi-particle forces such as the shear induced diffusion force.

Our primary interest in this study is to implement single wall-bounded inertial lift models to capture particle migration in linear shear flows. Unlike previous theoretical lift models, the developed lift correlations in chapters 6 and 7 are valid for arbitrary particle wall separation distances, and particle Reynolds numbers up to $Re_{\mathrm{slip}}, Re_{\gamma} < \mathcal{O}(10^{-1})$. These new lift models are implemented as wall-shear, wall-slip, and wall-slip-shear interphase momentum forces.

8.5.2.1 Wall-bounded shear lift

The wall-shear lift is a function of the fluid shear and separation distance (see chapter 6). It always directs particles away from the wall. Hence, the corresponding interphase momentum force acting on the solid phase is defined as a wall normal force pointing into the fluid. Assuming $\boldsymbol{\gamma}_{\mathrm{f}} \approx \boldsymbol{\gamma}_{\mathrm{s}}$;

$$\boldsymbol{M}_{\mathrm{L,shear}}^{\mathrm{wb}} = \alpha_1 |\gamma_{\mathrm{s}}|^2 \boldsymbol{n}_{\mathrm{w}} \tag{8.47}$$

where

$$\alpha_1 = n a^4 \rho_{\mathrm{f}} C_{\mathrm{L},1} = \frac{3a\phi_{\mathrm{s}}\rho_{\mathrm{f}}}{4\pi} C_{\mathrm{L},1} \tag{8.48}$$

Here $C_{\mathrm{L},1}$ for a freely rotating particle (Eq. 6.1);

$$C_{\mathrm{L},1} = f_1(Re_\gamma)C_{\mathrm{L},1}^{\mathrm{wb,out}}(l^*/L_{\mathrm{G}}{}^*) + f_2(Re_\gamma)C_{\mathrm{L},1}^{\mathrm{wb,in}}(1/l^*) \tag{8.49}$$

$$f_1(Re_\gamma) = 0.9250\exp\left(-0.3500Re_\gamma\right) - 0.0135\exp\left(-7000Re_\gamma\right); \tag{8.50}$$

$$C_{\mathrm{L},1}^{\mathrm{wb,out}}(l^*/L_{\mathrm{G}}^*) = 1.982\exp\left[-0.1150\left(l^*/L_{\mathrm{G}}^*\right)^2 - 0.2771\left(l^*/L_{\mathrm{G}}^*\right)\right]; \tag{8.51}$$

$$f_2(Re_\gamma) = 1 + \sqrt{Re_\gamma}; \tag{8.52}$$

$$C_{\mathrm{L},1}^{\mathrm{wb,in}}(1/l^*) = 1.0575(1/l^*) - 2.4007(1/l^*)^2 - 1.9610(1/l^*)^3; \tag{8.53}$$

is used based on the findings of chapter 6. In the two-fluid context, the dimensionless Saffman length is defined by considering the solid phase local strain rate magnitude as below,

$$L_{\mathrm{G}}^* = \frac{L_{\mathrm{G}}}{a} = \frac{\sqrt{\gamma_{\mathrm{s}}/\nu_{\mathrm{f}}}}{a} \tag{8.54}$$

8.5.2.2 Wall-bounded slip lift

The wall-slip lift is a function of the slip velocity parallel to the wall and the separation distance (see chapter 7). Again, this force is always directed away from the wall. Therefore the corresponding interphase momentum force acting on the solid phase is defined as a wall-normal force pointing into the fluid based on the absolute slip velocity magnitude. Additionally, the slip velocities normal to a wall are assumed to be smaller than the slip velocities parallel to a wall. Hence, the net slip velocity magnitude is considered rather than isolating the wall tangential slip component magnitude when defining the wall-bounded slip lift interphase force:

$$\boldsymbol{M}_{\mathrm{L,slip}}^{\mathrm{wb}} = \alpha_3|(\boldsymbol{u}_{\mathrm{s}} - \boldsymbol{u}_{\mathrm{f}})|^2\boldsymbol{n}_{\mathrm{w}} \tag{8.55}$$

where

$$\alpha_3 = na^2\rho_{\mathrm{f}}C_{\mathrm{L},3} = \frac{3\phi_{\mathrm{s}}\rho_{\mathrm{f}}}{4\pi a}C_{\mathrm{L},3} \tag{8.56}$$

Here $C_{\mathrm{L},3}$ of a freely-rotating particle is defined using Eq. (7.2b) as;

$$C_{\mathrm{L},3} = C_{\mathrm{L},3}^{\mathrm{wb,out}}(l^*/L_{\mathrm{S}}{}^*) + C_{\mathrm{L},3}^{\mathrm{wb,in}}(1/l^*) \tag{8.57}$$

$$C_{\mathrm{L},3}^{\mathrm{wb,out}} = 6\pi\left[3/\left(32 + 2\left(l/L_{\mathrm{S}}\right) + 3.8(l/L_{\mathrm{S}})^2 + 0.049(l/L_{\mathrm{S}})^3\right)\right] \tag{8.58}$$

$$C_{\mathrm{L},3}^{\mathrm{wb,in}} = 0.4757(1/l^*) - 1.268(1/l^*)^2 + 0.7427(1/l^*)^3 \tag{8.59}$$

The dimensionless Stokes length (L^*_S) is defined based on the absolute phase slip velocity magnitudes in the system:

$$L^*_\mathrm{S} = \frac{L_\mathrm{S}}{a} = \frac{|(\boldsymbol{u}_\mathrm{s} - \boldsymbol{u}_\mathrm{f})|}{\nu_\mathrm{f} a} \tag{8.60}$$

8.5.2.3 Wall-bounded slip-shear lift

The slip-shear lift is a function of the slip velocity, fluid shear, and the separation distance (see chapter 7). Unlike the above two lift models, the wall slip-shear lift depends on both the slip velocity and the fluid shear rate direction. Assuming $\boldsymbol{\gamma}_\mathrm{f} \approx \boldsymbol{\gamma}_\mathrm{s}$, the interphase momentum force acting on the solid phase based on wall-slip-shear is defined as,

$$\boldsymbol{M}^{\mathrm{wb}}_{\mathrm{L,slip\text{-}shear}} = -\alpha_2 \boldsymbol{\gamma}_\mathrm{s} \cdot (\boldsymbol{u}_\mathrm{s} - \boldsymbol{u}_\mathrm{f}) \tag{8.61a}$$

where

$$\alpha_2 = n a^3 \rho_\mathrm{f} C_{\mathrm{L},2} = \frac{3\phi_\mathrm{s}\rho_\mathrm{f}}{4\pi} C_{\mathrm{L},2} \tag{8.61b}$$

Here $C_{\mathrm{L},2}$ for a freely-rotating particle is defined using Eq. (7.3b) as;

$$C_{\mathrm{L},2} = -C^{\mathrm{wb,out}}_{\mathrm{L},2} \frac{1}{|\gamma^*|} + C^{\mathrm{wb,in}'}_{\mathrm{L},2}(1/l^*) \tag{8.61c}$$

where

$$C^{\mathrm{wb,out}}_{\mathrm{L},2} = f(\epsilon, l/L_\mathrm{G}) C^{\mathrm{ub}}_{\mathrm{L},2} \tag{8.61d}$$

$$C^{\mathrm{ub}}_{\mathrm{L},2} = \frac{9}{\pi} \epsilon J(\epsilon) \tag{8.61e}$$

$$f(\epsilon, l/L_\mathrm{G}) = 1 - \exp\Big[-\frac{11}{96}\pi^2 (l/L_\mathrm{G})/J(\epsilon) \Big] \tag{8.61f}$$

$$J(\epsilon) = 2.255(1 + 0.20\epsilon^{-2})^{-3/2} \tag{8.61g}$$

$$C^{\mathrm{wb,in}'}_{\mathrm{L},2} = -2.6729 - 0.8373(1/l^*) + 0.4683(1/l^*)^2 \tag{8.61h}$$

Ideally, the lift model associated with $C^{\mathrm{wb,in}\prime}_{\mathrm{L},2}$ requires a phase slip velocity tangential to the wall and shear variation only normal to the wall. However, in this implementation, the total shear rate tensor and the phase slip vector is employed, assuming the phase slip components normal to walls and shear variation parallel to walls are insignificant.

The suggested correlation for $C_{\mathrm{L},2}$ captures both wall-bounded and unbounded contributions. For example, in the unbounded limit ($l^* \to \infty$), Eq. (8.61c) reduces to;

$$C_{\mathrm{L},2} = -\frac{9}{\pi}\epsilon J(\epsilon)\frac{1}{|\gamma^*|} - 2.6729 \tag{8.62}$$

The resulting unbounded slip-shear lift interphase force $\boldsymbol{M}^{\mathrm{ub}}_{\mathrm{L,slip\text{-}shear}}$ from Eq. (8.61a) is,

$$\boldsymbol{M}^{\mathrm{ub}}_{\mathrm{L,slip\text{-}shear}} = \frac{3\phi_{\mathrm{s}}\rho_{\mathrm{f}}}{4\pi}\left(-\frac{9}{\pi}\epsilon J(\epsilon)\frac{|(\boldsymbol{u}_{\mathrm{s}}-\boldsymbol{u}_{\mathrm{f}})|}{a|\boldsymbol{\gamma}|} - 2.6729\right)\boldsymbol{\gamma}_{\mathrm{s}}\cdot(\boldsymbol{u}_{\mathrm{s}}-\boldsymbol{u}_{\mathrm{f}}) \tag{8.63}$$

Given that $\epsilon = |\sqrt{\gamma_{\mathrm{s}}\nu}/(\boldsymbol{u}_{\mathrm{s}}-\boldsymbol{u}_{\mathrm{f}})|$, this becomes:

$$\boldsymbol{M}^{\mathrm{ub}}_{\mathrm{L,slip\text{-}shear}} = \frac{3\phi_{\mathrm{s}}\rho_{\mathrm{f}}}{4\pi}\left(-\frac{9}{\pi}\frac{|\gamma_{\mathrm{s}}|^{-1/2}\nu^{1/2}}{a}J(\epsilon) - 2.6729\right)\boldsymbol{\gamma}_{\mathrm{s}}\cdot(\boldsymbol{u}_{\mathrm{s}}-\boldsymbol{u}_{\mathrm{f}}) \tag{8.64}$$

In Saffman's limit $\epsilon \to \infty; J(\epsilon) \to 2.255$, Eq. (8.64) becomes:

$$\boldsymbol{M}^{\mathrm{ub}}_{\mathrm{L,slip\text{-}shear}} = \underbrace{-\frac{3(6.46)\phi_{\mathrm{s}}}{4\pi}\frac{\mu_{\mathrm{f}}^{1/2}\rho_{\mathrm{f}}^{1/2}}{a}|\gamma_{\mathrm{s}}|^{-1/2}\boldsymbol{\gamma}_{\mathrm{s}}\cdot(\boldsymbol{u}_{\mathrm{s}}-\boldsymbol{u}_{\mathrm{f}})}_{\boldsymbol{M}^{\mathrm{ub}}_{\mathrm{L,Saffman}}\text{ - 1st order term}} - \underbrace{\frac{3(2.6729)\phi_{\mathrm{s}}}{4\pi}\rho_{\mathrm{f}}\boldsymbol{\gamma}_{\mathrm{s}}\cdot(\boldsymbol{u}_{\mathrm{s}}-\boldsymbol{u}_{\mathrm{f}})}_{\text{Additional term}} \tag{8.65}$$

The model recovers Saffman's first order term with the correct lift force direction. The additional lift force term, originates from the single particle model based on our numerical results for finite inertial conditions, increases the net lift force, and acts in the same direction as the first order lift force. It is worth noting that Saffman's original second-order term's coefficient, deduced for $Re_{\mathrm{slip}}, Re_{\gamma} \ll 1$, is 1.375 and results in a force opposite to the first-order force direction.

A few two-fluid models have employed Saffman's first order expression for the slip-shear based unbounded lift model [72, 162, 171]. However, the slip-shear unbounded lift model alone cannot predict the experimentally observed neutrally-buoyant particle migration or the 'tubular-pinch effect' in pipe flows, as the inertial induced particle migration is mainly governed by the wall-shear and shear-gradient of the flow (flow curvature induced). Hence, Drew [72] and McTigue et al. [171] used double-wall-bounded models presented for neutrally-buoyant particles, specifically for predicting the 'tubular-pinch effect'.

8.5.2.4 Unbounded shear-gradient lift

Flow curvature, or otherwise a shear-gradient in the fluid flow, can cause an inertial lift force on a finite-size particle. Although many single particle studies have examined double wall-bounded shear gradient lift forces, particularly relevant to 2D Poiseuille flows [11, 108, 217, 250], only a few multiphase flow studies have employed these models to analyse the suspension behaviour [171]. The main limitation associated with these double wall-bounded single particle lift is the geometric dependency.

Asmolov [11] presented a single particle scale unbounded shear gradient lift model accounting for both shear rate, and shear-gradient, existing in a planar Poiseuille flow. The model, derived for outer-region based flow, uses a point particle assumption to obtain the closure equation. The shear-gradient lift direction always points from low shear rate to high shear rate rate regions. For example, in a 2D channel flow, this lift will direct particles towards the channel walls, whereas in Taylor-Couette flows with an inner rotating cylinder, this force will direct particles towards the inner wall.

Asmolov [11] plotted the variation of the shear-gradient lift coefficient, $C_{\mathrm{L,SG}}$, as a variation of a dimensional scalar function, σ (figure 8.4). The author defined σ based on a 2D parabolic flow, giving $\sigma = 4(\gamma H/u_{\mathrm{max}})^{-3/2} Re^{-1/2}$, with the definitions: local shear rate (γ), maximum velocity (u_{max}), channel height (H) and pipe channel Reynolds number (Re). However, in the present study, σ is interpreted in terms of the local shear rate (γ) and local shear-gradient (γ'), approximating that $\sigma = 4u_{\mathrm{max}}H^{-2}(\nu^{1/2}\gamma^{-3/2})$ and $\gamma' = 2u_{\mathrm{max}}H^{-2}$ which results in $\sigma = 2\gamma'\nu^{1/2}\gamma^{-3/2}$.

Using the shear based force scaling, and assuming $\boldsymbol{\gamma}_{\mathrm{f}} \approx \boldsymbol{\gamma}_{\mathrm{s}}$, the interphase momentum force acting on the solid phase based on the unbounded shear-gradient is presented as;

$$\boldsymbol{M}^{\mathrm{ub}}_{\mathrm{L,shear\text{-}gradient}} = \alpha_4 |\gamma_{\mathrm{s}}|^2 \frac{\boldsymbol{\nabla}\gamma_{\mathrm{s}}}{|\boldsymbol{\nabla}\gamma_{\mathrm{s}}|} \tag{8.66a}$$

where

$$\alpha_4 = n a^4 \rho_{\mathrm{f}} C_{\mathrm{L,SG}} = \frac{3a\phi_{\mathrm{s}}\rho_{\mathrm{f}}}{4\pi} C_{\mathrm{L,SG}} \tag{8.66b}$$

Here the unit vector of the gradient in local shear rate magnitude, $\boldsymbol{\nabla}\gamma_{\mathrm{s}}/|\boldsymbol{\nabla}\gamma_{\mathrm{s}}|$, determines the shear gradient lift direction. Given that α_4 is always negative, the shear gradient lift acts from low to high shear regions.

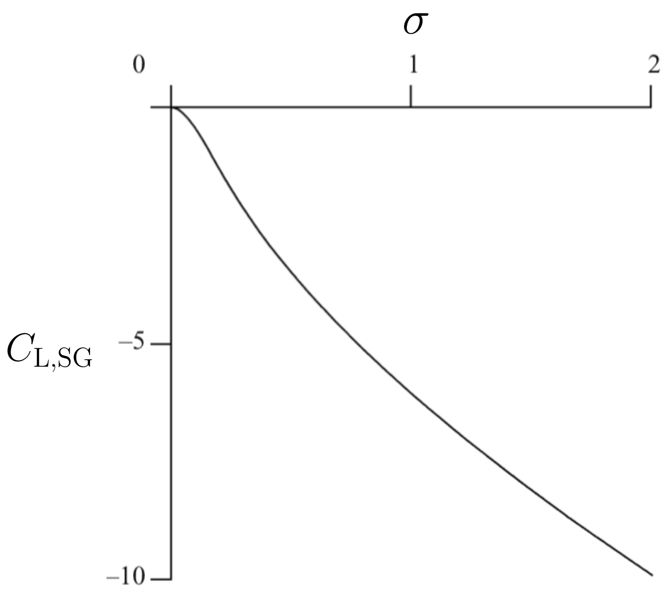

FIGURE 8.4: Shear-gradient lift coefficient for a particle in unbounded parabolic flow. Here $\sigma = 4\gamma^{-3/2}Re^{-1/2}$ Adopted from Asmolov [11] study.

Although the current application of the Two-Fluid Model (TFM) focuses on linear shear flows, we use experimental results from the Taylor-Couette apparatus to validate the TFM in subsequent chapters. Hence the flow curvature induced inertial force, which becomes significant in such flow configurations, is captured by the unbounded shear-gradient lift force.

8.6 Closure

The two-fluid model framework developed by Harvie to predict dilute suspension systems is modified by including inertial and wall-bounded particle-scale lift and drag forces. The modifications in this study include two wall-bounded drag forces that originate from slip and shear, three wall-bounded lift forces that originate from slip, shear, and the combined effect of slip-shear derived in chapters 6 and 7, and one unbounded lift force originating from the shear-gradient. Further, constitutive equations required to close specific components of the momentum equations (i.e., compressibility, hindered settling function) are selected from the literature.

The wall-bounded particle-scale force implementation methods and the accuracy of the model predictions will be examined in subsequent chapters against analytical and experimental results. A few of the parameters in Harvie's model, mainly related to shear induced diffusion (i.e., roughness and collision-based viscosity) that require further validation and tuning, will be calibrated against experimental results.

Chapter 9

Two-Fluid Model Implementation

One of the objectives of this work is to implement wall-bounded forces in the two-fluid model framework to examine the migration of neutrally buoyant particles in 1D and 2D Couette flow geometries. However, the solid phase boundary conditions near walls and the wall-bounded force implementation methods are not fully developed in the literature. This chapter discusses the methodologies used to implement the boundary conditions and wall-bounded forces in a broader context.

9.1 Boundary conditions

Inaccurate boundary conditions in suspension modelling can cause erroneous fluid and particle distributions. In both periodic and developing flows, the boundary conditions at the walls play a critical role in predicting accurate particle concentrations near walls [208]. Inlet and outlet boundary conditions in developing flows (i.e., pressure-driven flows) are also important in capturing accurate solid profile development along the flow direction.

In this section, the wall boundary conditions are tested using a 1D and 2D periodic flow setup. The geometries used for the study are shown in figure 9.1. Figure 9.1a shows a 1D linear Couette flow within two flat walls, whereas figure 9.1b illustrates the bird's eye view of a 2D Taylor-Couette flow domain within two concentric cylinders. Note that the periodic mesh treatment applied along the long side in the 1D domain ensures zero gradients for velocity, pressure, and solid concentrations normal to the computational wall. All the boundary conditions applied to the periodic domains are summarised in table 9.1.

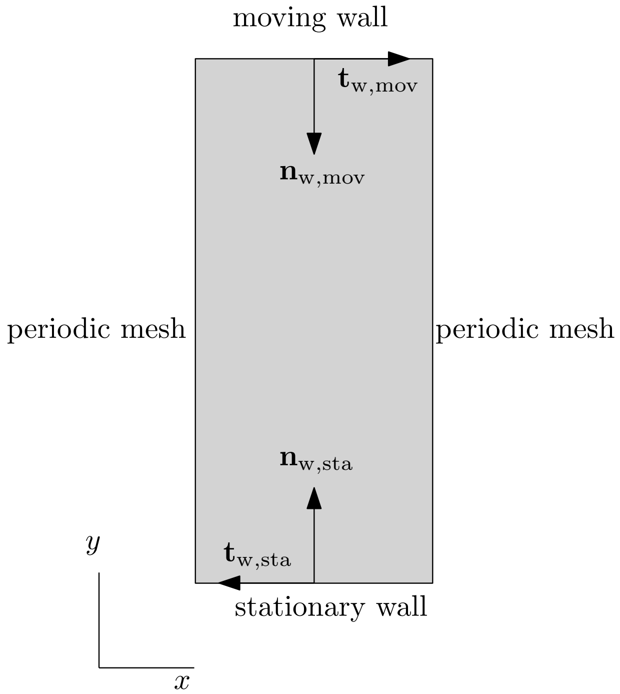

(a) 1D Couette flow

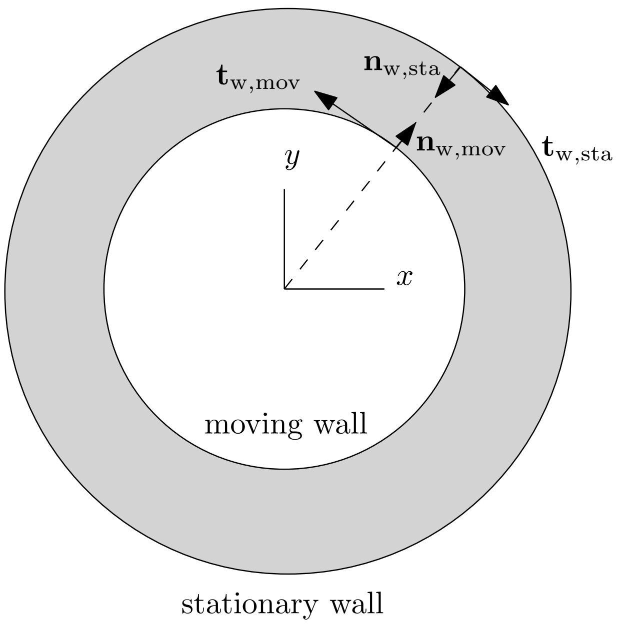

(b) 2D Couette flow

FIGURE 9.1: Graphical representation of the geometry of the periodic domains used for the Taylor-Couette flow setup.

Velocity boundary condition

boundary	momentum - wall normal	momentum - wall tangential	pressure	solid volume fraction
moving wall	$\boldsymbol{u}_\mathrm{f} \cdot \boldsymbol{n}_\mathrm{w,mov} = 0$ $\boldsymbol{u}_\mathrm{s} \cdot \boldsymbol{n}_\mathrm{w,mov} = 0$	$\boldsymbol{u}_\mathrm{f} \cdot \boldsymbol{t}_\mathrm{w,mov} = u_\mathrm{wall}$ $\boldsymbol{u}_\mathrm{s} \cdot \boldsymbol{t}_\mathrm{w,mov} = ?$	$\boldsymbol{d}_\mathrm{f} \cdot \boldsymbol{n}_\mathrm{w,mov} = 0$	$\boldsymbol{\nabla}\phi_\mathrm{s} \cdot \boldsymbol{n}_\mathrm{w,mov} = 0$
stationary wall	$\boldsymbol{u}_\mathrm{f} \cdot \boldsymbol{n}_\mathrm{w,sta} = 0$ $\boldsymbol{u}_\mathrm{s} \cdot \boldsymbol{n}_\mathrm{w,sta} = 0$	$\boldsymbol{u}_\mathrm{f} \cdot \boldsymbol{t}_\mathrm{w,sta} = 0$ $\boldsymbol{u}_\mathrm{s} \cdot \boldsymbol{t}_\mathrm{w,sta} = ?$	$\boldsymbol{d}_\mathrm{f} \cdot \boldsymbol{n}_\mathrm{w,sta} = 0$	$\boldsymbol{\nabla}\phi_\mathrm{s} \cdot \boldsymbol{n}_\mathrm{w,sta} = 0$

TABLE 9.1: Boundary conditions applied in TFM simulations. Solid phase tangential velocity boundary conditions are to be examined.

The fluid and solid phases fluxes normal to the walls are zero due to impermeable walls, and hence, each phase velocity component normal to each wall is set to zero without any further investigation. Given that the Knudsen number is low for the present simulations, the fluid phase velocity at the walls can be set using the no-slip boundary condition. In the two-fluid context, the boundary condition for the solid phase tangential velocity near the wall remains uncertain. Therefore the implementation of this boundary condition is broadly discussed in the next section.

Pressure boundary condition

The fluid pressure gradient across the walls is defined as zero. For this, the fluid phase dynamic force $\boldsymbol{d}_\mathrm{f}(= -\boldsymbol{\nabla} p_\mathrm{f})$ normal to the wall is set to zero. Further, Rhie-Chow interpolation is adopted ensure a strong coupling between the pressure and velocity at the mesh scale and to avoid non-physical pressure oscillations [206, 269]. This interpolation correlates the difference between the pressure gradient $(\Delta \boldsymbol{d}_\mathrm{f} \cdot \boldsymbol{n}_\mathrm{w})$ and velocity difference $(\Delta \boldsymbol{u}_\mathrm{f} \cdot \boldsymbol{n}_\mathrm{w})$ normal to computational cell faces. The delta value refers to the magnitude difference between the face and adjacent cell values.

Solid concentration boundary condition

The solid concentration at the wall is an unknown, and hence we specify the concentration gradients normal to the wall as zero.

9.1.1 Solid phase velocity at wall

Many two-fluid studies use no-slip boundary conditions at the walls for the particle phase. This condition assumes that particles are moving at the walls' velocity for moving walls

($\boldsymbol{u}_\mathrm{s} \cdot \boldsymbol{t}_\mathrm{w,mov} = u_\mathrm{wall}$) or remain immobile near stationary walls ($\boldsymbol{u}_\mathrm{s} \cdot \boldsymbol{t}_\mathrm{w,sta} = 0$). Based on single particle hydrodynamics, this condition is only valid for a force-free particle in a uniform flow (i.e., neutrally buoyant particles in uniform flows) under low slip Reynolds numbers. There is also uncertainty about how the wall particle velocity should be defined, given that no particle centres are lying precisely on the wall.

In the presence of fluid shear, neutrally buoyant particles near walls do not generally obey the familiar 'no-slip' boundary condition. Analytical and numerical models of single particle studies illustrate that particles lag near a wall in the presence of positive shear. This boundary condition can be introduced as a fixed negative slip velocity for the solid phase BC in the two-fluid framework. The lubrication theories for 2D linear shear flows predict the slip velocity for a freely translating and rotating particle at the wall as $u_\mathrm{slip,w} = -a\gamma_\mathrm{f}$ under Stokes conditions [92]. Here γ_f is the fluid shear rate magnitude. However, for finite inertial conditions, an analytical value or a correlation for the slip velocity is unavailable. For inertial flows, the numerical findings of §6.4.1 and (see figure 6.4) suggest a weakly dependent slip velocity for force-free particles. Accounting for the drag correlations developed in §6.3, the extrapolated slip velocity, $u_\mathrm{slip,w}$ can be approximated as $\sim -0.3a\gamma_\mathrm{f}$ at the wall (figure 6.4). Hence, the new boundary condition can be presented as,

$$\boldsymbol{u}_\mathrm{s} \cdot \boldsymbol{t}_\mathrm{w,mov} = u_\mathrm{wall} + \chi(\boldsymbol{\gamma}_\mathrm{f} : \boldsymbol{t}_\mathrm{w,mov}\boldsymbol{n}_\mathrm{w,mov})$$

and

$$\boldsymbol{u}_\mathrm{s} \cdot \boldsymbol{t}_\mathrm{w,sta} = \chi(\boldsymbol{\gamma}_\mathrm{f} : \boldsymbol{t}_\mathrm{w,sta}\boldsymbol{n}_\mathrm{w,sta}),$$

with $\chi = -0.3a$. To account for multi-particle effects, the latter BC is further modified by replacing $\boldsymbol{\gamma}_\mathrm{f}$ with $-\boldsymbol{\tau}_\mathrm{f}/\mu_\mathrm{f}$, noting that $\boldsymbol{\tau}_\mathrm{f} = -\mu_\mathrm{dilute}\boldsymbol{\gamma}_\mathrm{f}$ and $\mu_\mathrm{dilute} = \mu_\mathrm{f}(1 + 2.5\phi_\mathrm{s})$.

Instead of specifying the solid velocity at the wall, another option is to set the solid phase shear stress to zero at the walls. This boundary condition will adjust the particle phase velocity near the wall to ensure zero stress on the particle phase at the wall.

The effects of 'slip', 'no-slip' and 'zero-stress' boundary conditions on the phase slip and the particle distribution near the walls are examined using a 1D simple shear flow simulation. All three BCs are summarised in table 9.2. The geometry used in the simulations is a thin, one-dimensional rectangular channel with a uniform mesh across

BC	moving wall	stationary wall
no-slip	$\boldsymbol{u}_\mathrm{s} \cdot \boldsymbol{t}_\mathrm{w,mov} = u_\mathrm{wall}$	$\boldsymbol{u}_\mathrm{s} \cdot \boldsymbol{t}_\mathrm{w,sta} = 0$
zero-stress	$\boldsymbol{\tau}_\mathrm{s} : \boldsymbol{t}_\mathrm{w,mov}\boldsymbol{n}_\mathrm{w,mov} = 0$	$\boldsymbol{\tau}_\mathrm{s} : \boldsymbol{t}_\mathrm{w,sta}\boldsymbol{n}_\mathrm{w,sta} = 0$
slip	$\boldsymbol{u}_\mathrm{s} \cdot \boldsymbol{t}_\mathrm{w,mov} = u_\mathrm{wall} - \chi/\mu_\mathrm{f}(\boldsymbol{\tau}_\mathrm{f} : \boldsymbol{t}_\mathrm{w,mov}\boldsymbol{n}_\mathrm{w,mov})$	$\boldsymbol{u}_\mathrm{s} \cdot \boldsymbol{t}_\mathrm{w,sta} = -\chi/\mu_\mathrm{f}(\boldsymbol{\tau}_\mathrm{f} : \boldsymbol{t}_\mathrm{w,sta}\boldsymbol{n}_\mathrm{w,sta})$

TABLE 9.2: Wall boundary conditions for solid-phase velocity. The solid phase slip length, $\chi = -0.3a$, is based on the findings in chapter 6 (figure 6.4).

the domain (figure 9.2). The element height is 0.16% of the domain height and 0.067 times the particle radius. Note that a detailed mesh sensitivity analysis is provided in the next chapter. Parameters used for the present simulation are summarised in table 9.3.

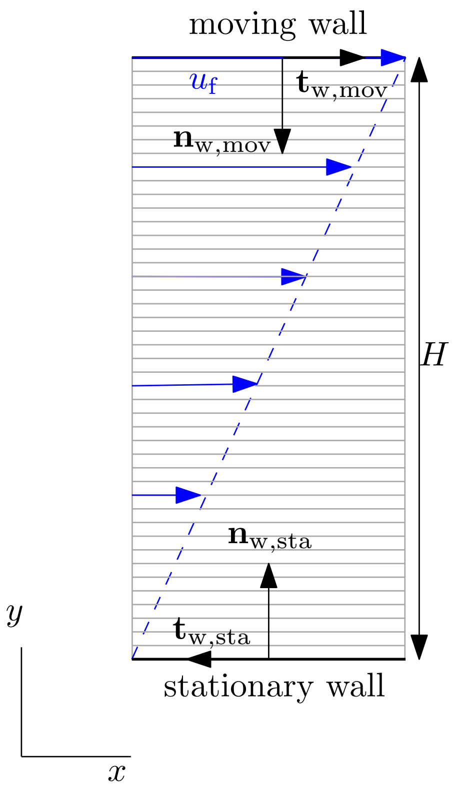

FIGURE 9.2: Graphical representation of the geometry and mesh used for the 1D linear shear flow (not to scale).

Figure 9.3 shows the slip velocity variation within the two-flat walls geometry as a function of particle separation distance. The choice of solid-phase velocity boundary condition has affected the velocity distribution, resulting in notable phase slip velocities parallel to the walls (within the highlighted region). Note that the highlighted regions' thickness represents the particle radius, and that much of the slip velocity's variation between different BCs occurs in this region. The simulation results are also compared with the

Parameter	Symbol	Value
Bulk concentration	ϕ_{b}	0.001
Fluid kinetic viscosity	μ_{f}	0.0175 Pa s
Fluid density	ρ_{f}	$1050\,\mathrm{kg\,m^{-3}}$
Solid density	ρ_{s}	$1050\,\mathrm{kg\,m^{-3}}$
Particle radius	a	175 µm
Domain height	H	7 mm
Wall velocity	u_{wall}	$0.1976\,\mathrm{m\,s^{-1}}$

TABLE 9.3: Simulation parameters.

single particle analytical slip results from chapter 6, Eq. 6.8. The single particle analytical correlation, evaluated at distances greater than one particle radius from the wall is also shown in figure 9.3.

The slip velocities, outside of the one particle radius grey zone, generally indicate that particles lag (lead) the flow near the stationary (moving) wall. This result, observed for all boundary conditions, is mainly due to the wall-shear drag force ($\boldsymbol{M}^{\mathrm{wb}}_{\mathrm{D,shear}}$), which acts in the opposite direction to the fluid flow for a positive shear, and the same direction as the fluid flow for a negative shear (for an upward facing wall). However, there are small slip velocity peaks occurring for all of the simulation results close to the centreline of the channel. The reasons for these two slip velocity peaks observed near the channel centerline are broadly discussed in the next chapter. In the following we focus on the slip velocities occurring closer to the simulation walls.

Overall, the results illustrate a strong slip velocity dependence on the solid phase velocity BC, particularly near the wall (around the highlighted regions). Given that the slip velocity near a wall directly affects the particle lift force, the correct solid phase velocity boundary condition is critical in predicting accurate particle migration in dilute suspensions. The slip velocity for the no-slip BC changes near the wall within the highlighted region, as the slip velocity approaches zero at walls. A rapid change of the slip velocity can also be seen for the zero-stress BC. The zero-stress BC in a TFM predicts that particles lead and lag near the stationary and moving walls, respectively. Conversely, the slip BC predicts the opposite consistent with the predictions of analytical slip velocity direction. However, for all BCs, the slip velocities predicted by TFM largely match the single particle analytical results shortly after one particle radius separation from each wall.

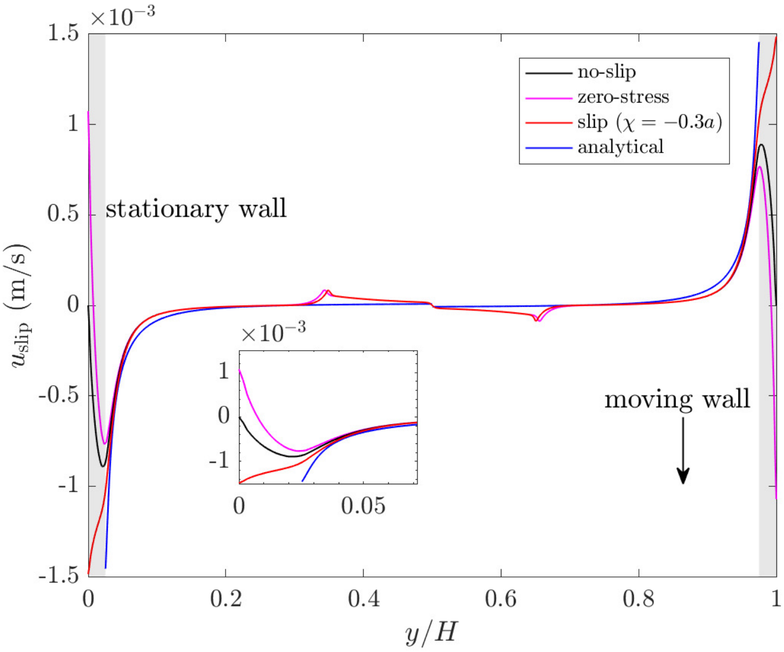

FIGURE 9.3: Slip velocity variation across a 1D linear shear flow for different solid phase wall boundary conditions at dilute condition ($\phi_{\mathrm{b}} = 0.001$). TFM simulations with slip-length BC (—); no-slip BC (—); zero-stress BC (—) and single particle analytical prediction based on Eq. (6.8) (—). Highlighted region thickness represents particle radius.

In continuum models, the particle phase velocity is ill-defined when the particle-wall separation distance is less than the particle radius (highlighted regions), yet computationally still solved for this region (The fluid velocity is defined in this region). This represents an inconsistency in the method. However, as the particle radius decreases, the relative size of these regions decreases, and the difference between the analytical and simulation results can be expected to reduce. Hence, to examine the effect of particle size on the slip BC, TFM simulations are performed for different a/H ratios, and the results are shown in figure 9.4. Numerical slip results for the smallest particle size ($a/H = 0.0125$) closely follow the analytical slip velocity predictions for most of the domain width, showing that the single particle based slip BC becomes more accurate as a/H is decreased. Note that as an alternative modelling choice, the proposed slip BC could possibly be modified to match the single particle analytical slip results at a distance of one radius away from the wall by choosing a suitable function for χ. This has not been attempted, noting that the slip velocity at distances only slightly larger than the particle radius are adequately predicted by the presented slip model.

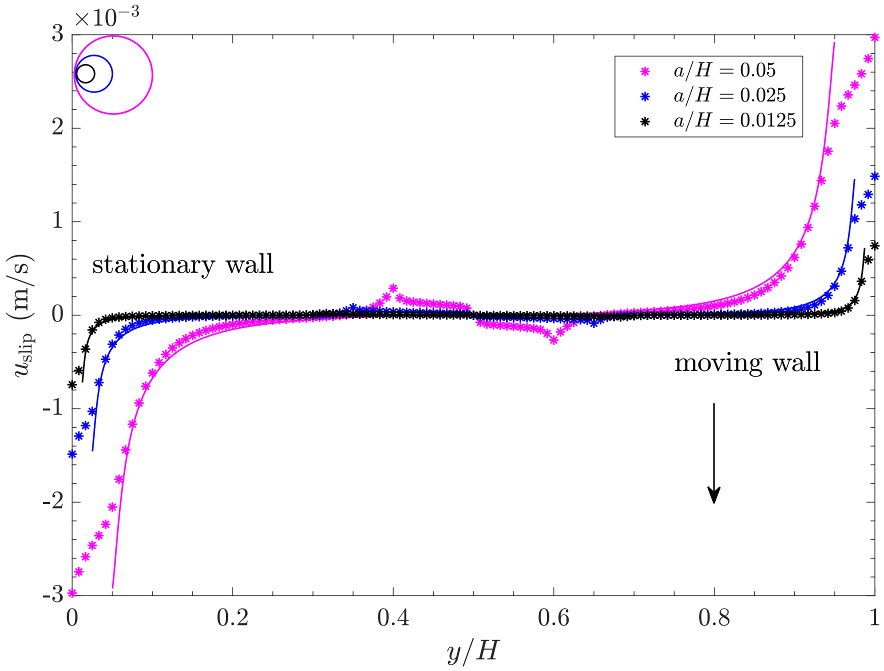

FIGURE 9.4: Slip velocity variation across a 1D linear shear flow for different particle sizes with slip BC at $\phi_{\mathrm{b}} = 0.001$. TFM simulations with slip-length BC ($*$) and single particle analytical prediction (——) based on Eq. (6.8).

Figure 9.5 shows how early-state ($t = 10\,\mathrm{s}$) and steady-state ($t = 9000\,\mathrm{s}$) solid distributions vary across along the gap width for different solid-phase velocity BCs. There is no significance difference between the solid distributions at early-state for the tested BCs. At steady-state, the boundary condition only affects the particle distribution near the wall. Although no significant difference is observed between the no-slip and slip boundary conditions for both time intervals, at steady-state, the zero-stress BC causes particles to remain near walls. At early-state, similar particle retention ($\phi = \phi_{\mathrm{b}}$) at the walls is also observed for all three BCs.

For the purpose of investigating the reasons for particle trapping near walls, the net force variation in the y-direction for the slip and zero-stress BCs at steady-state ($t = 9000\,\mathrm{s}$) are shown in figure 9.6. Large force variations within one radius distance of both the stationary and moving walls between the two BCs are observed. Note from chapter 8, that within these one radius zones lift and drag coefficients are evaluated using $l/a = 1$ (i.e., touching wall values). The negative force peak near the stationary wall and the positive force peak near the moving wall trap particles in the highlighted regions. A force contribution analysis (Figure 9.7), confirms that this behaviour is mainly due to the wall-normal slip drag ($\boldsymbol{M}^{\mathrm{wb}}_{\mathrm{D,slip},\perp}$). However, there is a sudden increase (decrease) of net lift force at the stationary (moving) wall only for the slip BC, and this force variation causes

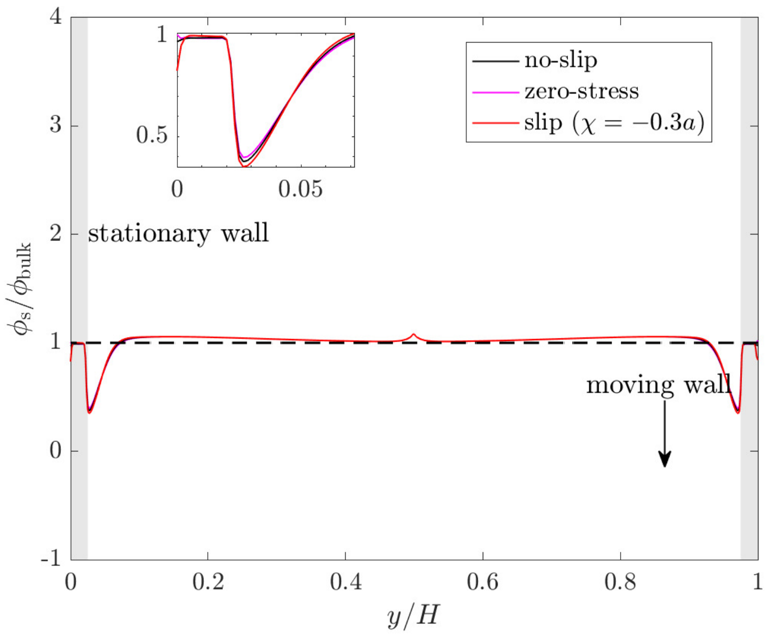

(a) t =10 s (early-state)

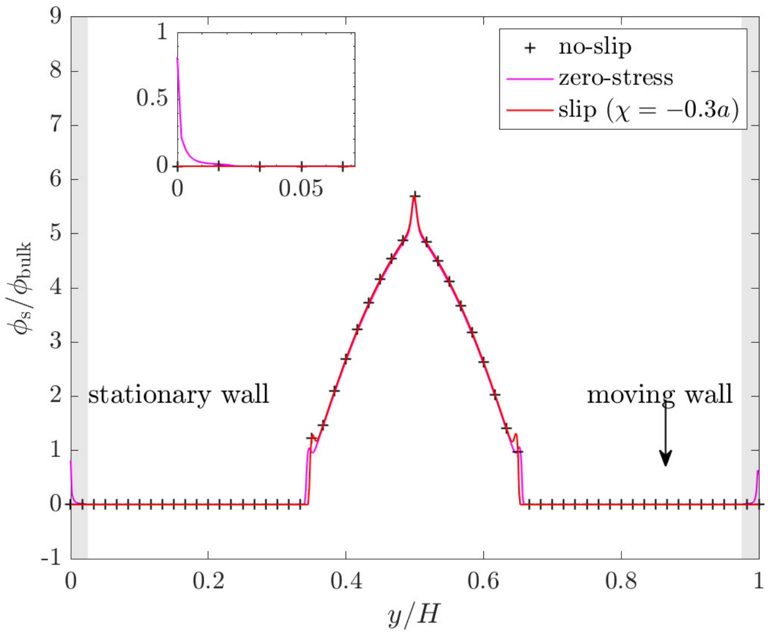

(b) t =9000 s (steady-state)

FIGURE 9.5: Non-dimensional solid concentration variation across a 1D linear shear flow for different solid phase wall boundary conditions in a dilute suspension.

the particles to migrate away from the wall. According to the single particle double wall-bounded theories [108, 250] and available experimental evidence (see next chapter) [157], particles migrate towards the centre of the channel in a linear shear flow, without any particles being trapped by the hydrodynamic forces at wall. Hence, when considering

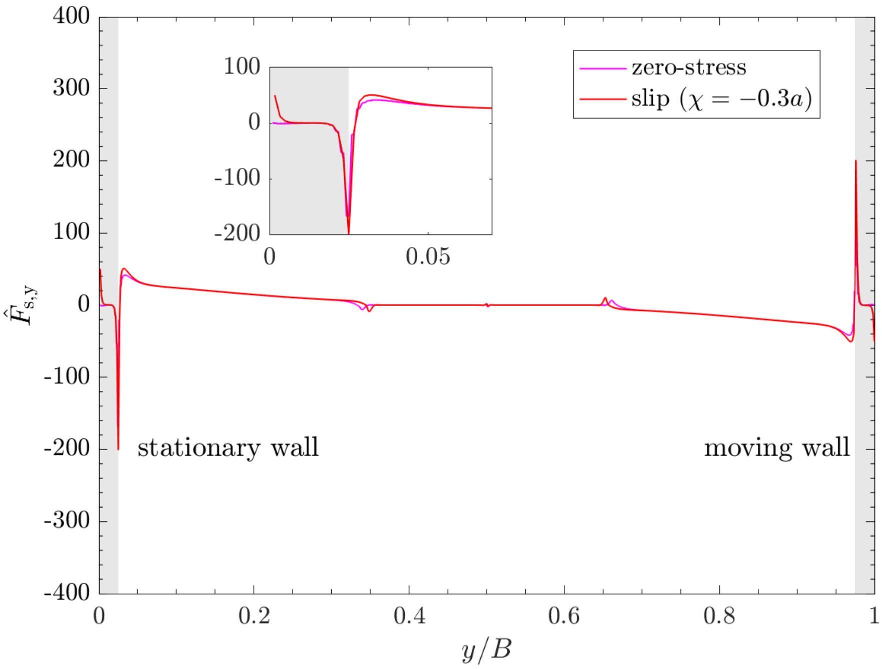

FIGURE 9.6: Normalised net lateral force distribution for zero-stress and slip BCs at t =9000 s (steady-state).

both the slip velocity behaviour and particle distributions, the 'slip' BC most accurately captures both behaviours and is used in this study.

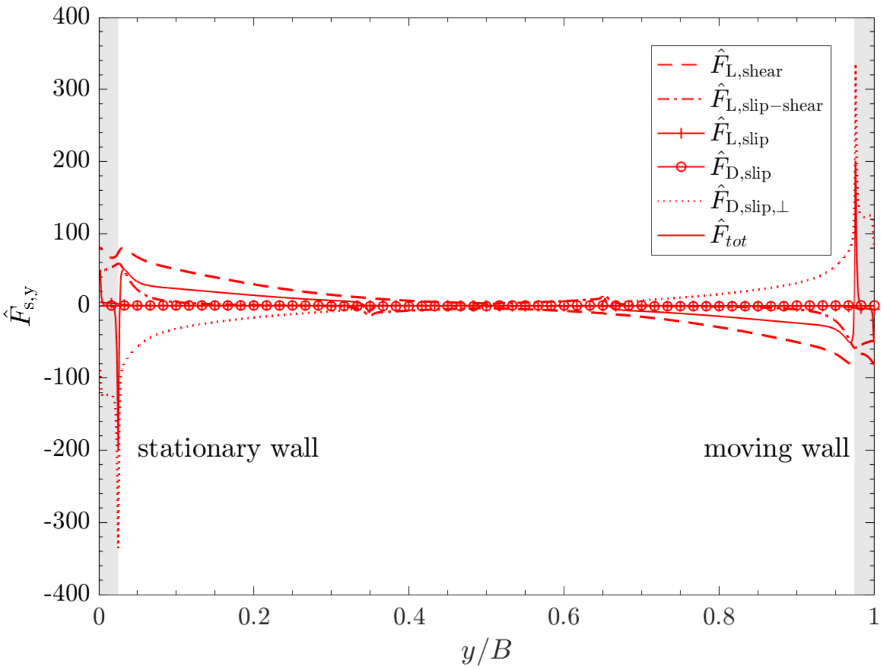

FIGURE 9.7: Normalised lateral force components for slip BCs at t =9000 s (steady-state).

9.2 Force implementation

This section discusses different implementation methods for wall-bounded forces in a TFM framework and examines:

(a) the effect of application phase

(b) the effect of secondary walls (i.e., in flow bounded by two walls) on particle-scale inertial forces

on the solid distributions of neutrally buoyant particles.

9.2.1 Application phase of wall-bounded force

Two modelling choices are examined here to implement wall-bounded forces in the TFM framework. In the first method, the wall-bounded forces are applied only to the solid phase (Eq. 9.1), assuming that the wall induced forces act directly between particles and the walls only. In the second method, wall-bounded forces are applied to both phases with equal and opposite contributions (Eq. 8.2), with the consequence that the wall induced forces act via the fluid phase.

Modified Linear Momentum Equations (solid-only application phase)

Fluid:

$$\frac{\partial \rho_\mathrm{f}\phi_\mathrm{f}\boldsymbol{u}_\mathrm{f}}{\partial t} + \boldsymbol{\nabla}\cdot\rho_\mathrm{f}\phi_\mathrm{f}\boldsymbol{u}_\mathrm{f}\boldsymbol{u}_\mathrm{f} = -\phi_\mathrm{f}\boldsymbol{\nabla}p_\mathrm{f} - \boldsymbol{\nabla}\cdot\boldsymbol{\tau}_\mathrm{f} + \rho_\mathrm{f}\phi_\mathrm{f}\boldsymbol{g} - \boldsymbol{M}^{\mathrm{ub}}_{\mathrm{D,slip}} - \boldsymbol{M}^{\mathrm{ub}}_{\mathrm{D,shear\text{-}gradient}} \tag{9.1a}$$

Solid:

$$\begin{aligned}\frac{\partial \rho_\mathrm{s}\phi_\mathrm{s}\boldsymbol{u}_\mathrm{s}}{\partial t} + \boldsymbol{\nabla}\cdot\rho_\mathrm{s}\phi_\mathrm{s}\boldsymbol{u}_\mathrm{s}\boldsymbol{u}_\mathrm{s} = -\phi_\mathrm{s}\boldsymbol{\nabla}(p_\mathrm{f}+\hat{p}_\mathrm{s}) - \boldsymbol{\nabla}p_\mathrm{s} - \boldsymbol{\nabla}\cdot\boldsymbol{\tau}_\mathrm{s} + \rho_\mathrm{s}\phi_\mathrm{s}\boldsymbol{g} +\\ \boldsymbol{M}^{\mathrm{ub}}_{\mathrm{D,slip}} + \boldsymbol{M}^{\mathrm{ub}}_{\mathrm{D,shear\text{-}gradient}} + \boldsymbol{M}^{\mathrm{wb}}_{\mathrm{D,slip}} + \boldsymbol{M}^{\mathrm{wb}}_{\mathrm{D,shear}}\\ \boldsymbol{M}^{\mathrm{ub}}_{\mathrm{L,shear\text{-}gradient}} + \boldsymbol{M}^{\mathrm{wb}}_{\mathrm{L,slip}} + \boldsymbol{M}^{\mathrm{wb}}_{\mathrm{L,slip\text{-}shear}} + \boldsymbol{M}^{\mathrm{wb}}_{\mathrm{L,shear}}\end{aligned} \tag{9.1b}$$

In many previous studies, the unbounded drag [117, 267] and unbounded lift [171] forces that result from the phase relative motion have been applied in both solid and fluid phases, following the second method. This method ensures that the net momentum contributions from these forces within the system are zero. In this study, consistent with other TFM in the literature, all interphase forces are generally defined to act in the opposite direction in each phase with equal magnitudes (Eq. 8.2). Conversely, the wall induced forces can be applied to act only on the solid phase, similar to solid pressure. Hence, it is required to understand the effect of the active phases of wall-bounded forces.

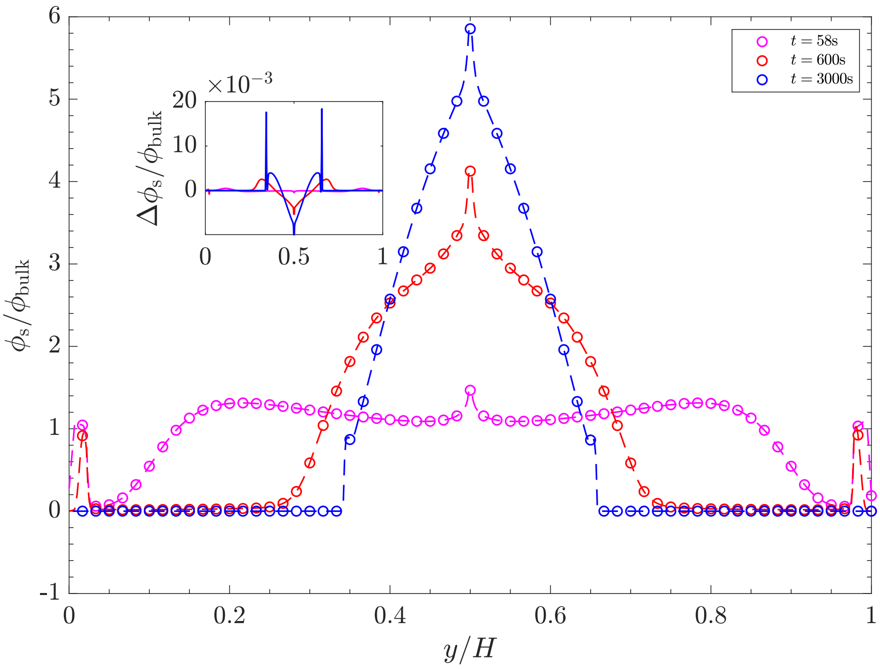

FIGURE 9.8: Development of particle distribution when wall-bounded forces act only on the solid phase (Eq. 9.1, ○) or act on both solid and fluid phases (Eq. 8.2, - - -). Inset illustrates the difference between these two methods in terms of solid distribution.

Figure 9.8 shows the transient particle distribution profiles for the two implementation methods, and the inset shows the difference between these two methods in terms of particle concentration. As indicated, there are only small differences between the results produced using these two implementation methods. The maximum deviation is about 0.1% and occurs near the particle clustering zone. A plausible explanation for the results not showing a significant change depending on whether the forces are applied to the solid phase or both phases could be the dilute conditions used in this study. Given that the wall-bounded particle-scale forces are proportional to the solid volume fraction, the particle-scale forces acting on the fluid phase become less significant in both implementation methods at dilute conditions. However, with increasing initial bulk concentration, a difference between the particle distribution for the two different application methods can be expected. Hence care is needed when implementing wall-bounded forces in solid and fluid phases for concentrated suspensions. Since the dilute condition analysis shows that the active phase effect is less significant, we continue using Eq. 8.2, in which wall-bounded forces are applied in both phases, in the remainder of the study.

9.2.2 Secondary wall effects

Three different methods to account for the effect of secondary walls when implementing the wall-bounded forces are examined in this section. For this, a simple geometry with flow bounded by two flat walls is considered.

Single-wall method

In this method, the effect of the secondary wall on the particle-scale inertial forces is neglected, which is justified when the separation distance between the two walls is large. Here, the particles only experience the particle-scale wall-bounded forces due to the closest flat wall. For this method, wall-normals directing from the closest wall to each computational cell (or a particle) are considered (Figure 9.9a). This wall-normal framework can easily be employed in complex geometries (i.e., bifurcation, expansions).

When the separation distance between walls becomes comparable with the disturbed flow regions caused by the particle, the effect of the secondary wall on the single wall-bounded particle-scale forces becomes more significant. For such cases, it is necessary to account for all other adjacent walls to calculate the net particle-scale force. Further, in symmetric flow domains, the net particle-scale wall forces with respect to forces normal to that axis should be zero at the symmetric axis (i.e., the centerline of the channel), and the particle-scale wall forces should be continuous across the channel centerline. However, the single-wall-bounded force implementation method cannot ensure a continuous force reduction to zero at the symmetric axis. Two new methods, namely, the 'extended-wall method' and the 'multiplier method', are introduced to address these two issues, respectively.

Extended-wall method

Under this method, particle-scale wall-forces acting on particles due to both walls are considered. To account for the effect of any secondary walls, additional wall-normals directing from the remaining wall to the computational cells (or particles) are defined (Figure 9.9b). Although this wall-normal framework can be easily adopted for simple

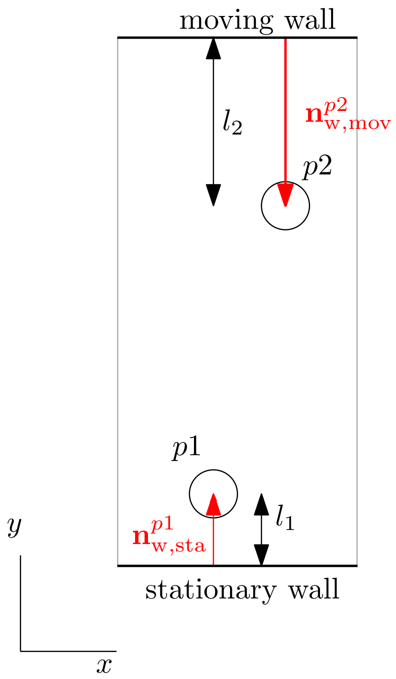

(a) Single wall-normal method

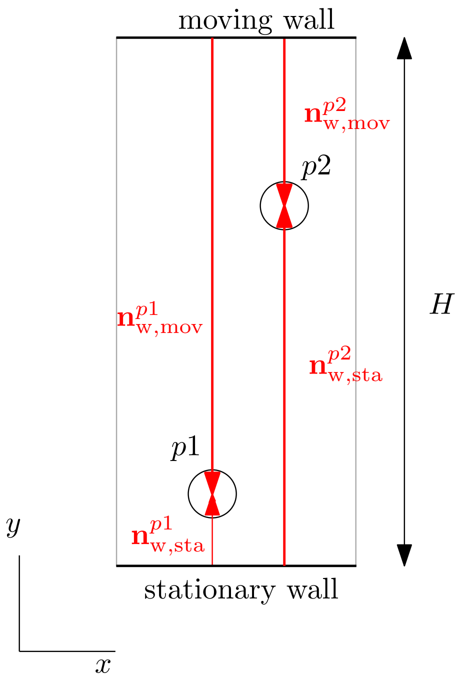

(b) Extended wall-normal method

FIGURE 9.9: Graphical representation of the wall-normal vector definitions for different wall-normal methods in 1D flow domains.

geometries (i.e., pipe and channel flows), it is not easily generalised to more complex geometries with varying cross-sectional areas or bifurcations/junctions.

Multiplier method

To ensure a continuous force reduction to zero at the symmetric axis, all the wall-bounded force coefficients ($\beta_3, \beta_4, \beta_5$, α_1, α_2 and α_3) are multiplied by a simple linear polynomial function forcing the forces to smoothly reduce zero at the channel centreline. This method uses the wall-normals defined for the single-wall bounded framework (Figure 9.9a). The polynomial function, $f_{\text{multiplier}}$, used as the multiplier is,

$$f_{\text{multiplier}} = 1 - \frac{l}{H/2} \tag{9.2}$$

However, such multiplication will change the exact single particle based force coefficients. Further, using a multiplier on wall-bounded forces is only applicable for symmetric flow domains, and again not easy to generalise to more complex geometries.

Simulations in 1D geometries are performed to examine the effect of these different force implementation methods on the steady-solid distribution. A neutrally-buoyant particle

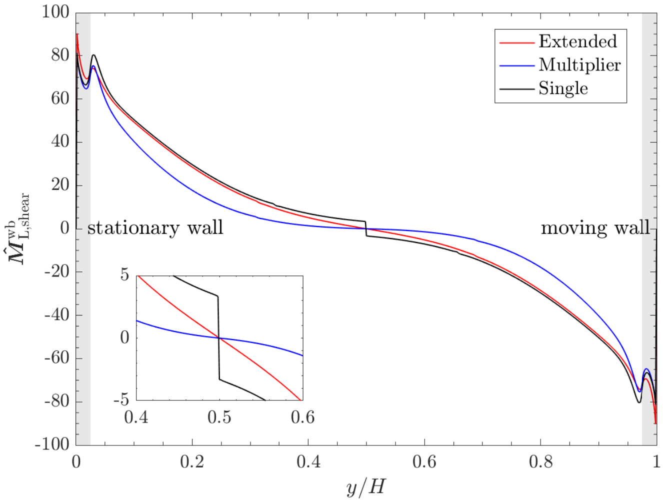

(a) Wall-bounded shear lift

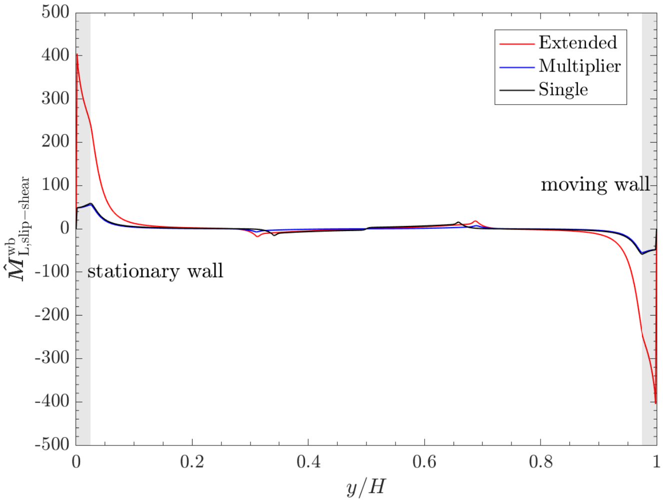

(b) Wall-bounded slip-shear lift

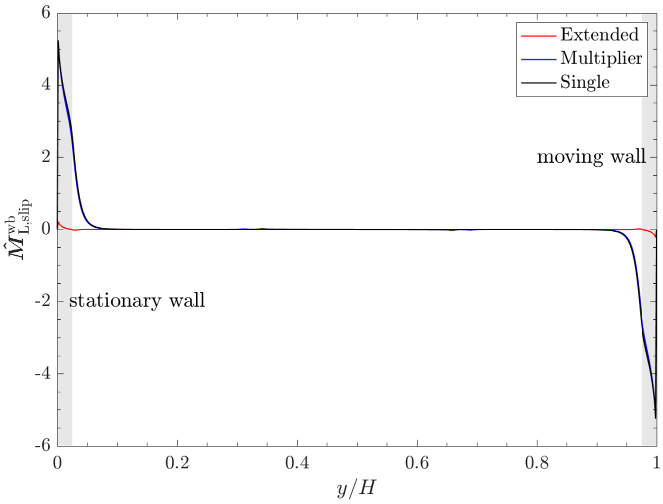

(c) Wall-bounded slip lift

FIGURE 9.10: Lift force variation for different wall-bounded force implementation methods.

suspension sheared at a rate of $\gamma = 24\mathrm{s}^{-1}$ is considered. The particle and the channel size considered for this study are $a = 350\mu$m and $H = 7$mm respectively.

The wall-bounded lift force variation obtained from the model for the three different implementation methods are shown in figure 9.10. All three net lift force magnitudes per unit solid volume fraction, $\hat{\boldsymbol{M}}(= \boldsymbol{M}/\phi_\mathrm{s})$, reduce significantly with increasing distance from either wall. The wall-shear lift is the highest lift contribution in the system for the single-wall and multiplier method, whereas the wall-slip lift is the lowest ($\hat{\boldsymbol{M}}^{\mathrm{wb}}_{\mathrm{L,shear}} \gg \hat{\boldsymbol{M}}^{\mathrm{wb}}_{\mathrm{L,slip\text{-}shear}} \gg \hat{\boldsymbol{M}}^{\mathrm{wb}}_{\mathrm{L,slip}}$). Only for the extended-wall method, the slip-shear lift magnitude dominates the wall-shear lift magnitude near walls. Interestingly, the slip-shear lift, $\hat{\boldsymbol{M}}^{\mathrm{wb}}_{\mathrm{L,slip\text{-}shear}}$ shows a sudden increase at $y/H \approx 0.28$ and ≈ 0.62 - the reasons for this behaviour will be investigated in §10.3.3. Except for this abnormality, all three lift forces direct particles away from the walls towards the centreline of the channel.

The secondary wall has a significant effect on the force magnitudes for the selected test case. The single wall-bounded forces rapidly reduce to near-zero values with increasing wall separation distance but are still large enough at the centreline such that indicate discontinues at $y/H = 0.5$ are present. Here both the multiplier method and the extended wall implementation methods predict continuous lift force variation across the domain with zero lift forces at the channel centre. However, while the wall-shear lift force ($\hat{\boldsymbol{M}}^{\mathrm{wb}}_{\mathrm{L,shear}}$) closely follows the single-wall implementation method, the wall-slip force ($\hat{\boldsymbol{M}}^{\mathrm{wb}}_{\mathrm{L,slip}}$) and slip-shear lift force ($\hat{\boldsymbol{M}}^{\mathrm{wb}}_{\mathrm{L,slip}}$) results deviate significantly from the single wall-bounded method. Unlike the shear rate, which is constant throughout the domain, slip velocities varies with the separation distance and are the largest near the walls. Although the the wall-slip and slip-shear lift forces decrease with the separation distance, large slip velocities near the secondary wall alter the force variations (Figure figure 9.10c). The wall-slip lift near the walls reduce and slip-shear lift near walls increase when the secondary wall effects are included. Although the slip-lift force contribution is relatively small, slip-shear contribution is significant, and hence could have a considerable effect on the particle migration velocities.

The steady-state particle distributions for different wall-bounded force implementation methods are shown in figure 9.11. The maximum volume fraction obtained at the channel centre is strongly dependent on the force implementation method. For the single-wall-bounded method, an intense peak for concentration is observed. This behaviour

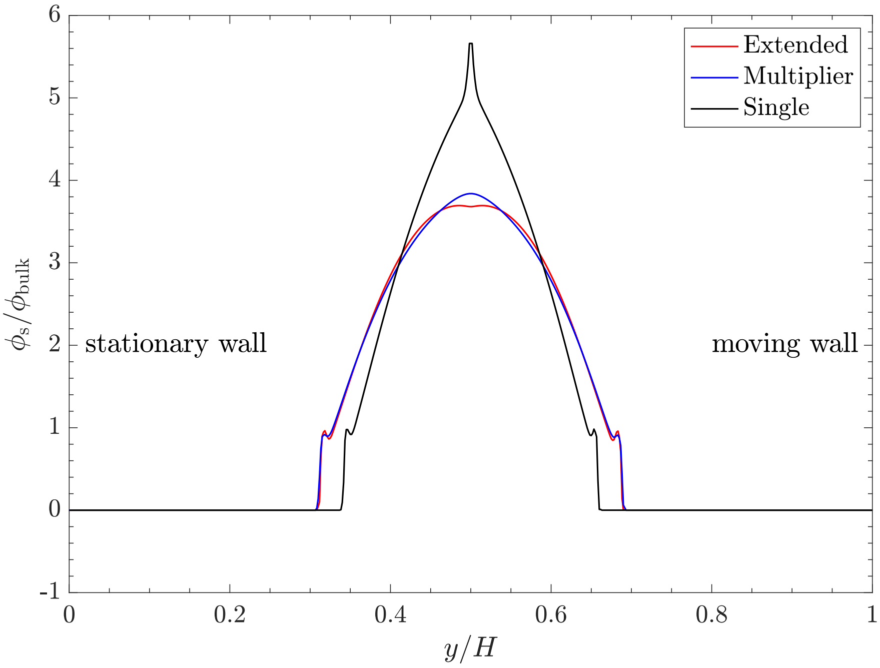

FIGURE 9.11: Particle distributions for different wall-bounded force implementation methods.

is mainly due to the discontinuity of the net wall-bounded particle-scale forces at the centre, as shown in figure 9.10. However, for the other two implementation methods, the reported maximum concentrations are low and more consistent with each other. Although there remains a considerable effect from the secondary wall on particle-scale wall-bounded forces, the steady-state particle distributions do not vary significantly for both the extended-wall and multiplier methods.

Due to the lack of correlations for bounded walls across the range of parameters that we are interested in this study, and as the extended-wall method cannot be generalized in complex geometries, the single-wall implementation method has to be chosen for this study. Note that Vasseur and Cox [250] and Ho and Leal [108] presented double-wall-bounded models for linear shear flow. However, these correlations are applicable when both the walls are located in the particle's disturbed flow's inner region. For the domain size, particle size, and shear Reynolds numbers of interest in this study, both the walls are located in the outer region for most particle-wall separation distances and hence, require outer region-based inertia dependent correlations.

9.3 Closure

Appropriate solid phase velocity boundary conditions and wall-bounded face implementation methods have been chosen based on sensitivity studies and convenience in implementation. Also, an assessment of differences in the final solid distributions introduced by our assumptions is analysed in this chapter. Although A new solid phase velocity boundary condition is introduced to match the analytical particle slip velocity. The application phase of wall-bounded forces has no significant effect on the particle distribution, particularly for the dilute condition. Hence all wall-bounded particle-scale inertial forces are implemented in a way to act on both phases with equal magnitude and opposite direction, similar to unbounded drag forces. The presence of secondary walls and the implementation method significantly affect the final particle distribution, mainly due to the sudden change of lift force direction at the channel centre. However, the single-wall method is chosen over the other two methods, as neither the extended-wall nor multiplier method can be generalised to complex geometries.

Chapter 10

Two-Fluid Model for Couette Flows

The two-fluid model framework developed in the previous two chapters is employed to model neutrally buoyant particle migration under dilute conditions in a thin-gap Taylor Couette flow. The developed TFM accounts for interphase momentum transfer forces that include wall-bounded and unbounded lift and drag forces, in addition to the diffusive forces such as osmotic and shear induced diffusion forces. Experimental data obtained from previous work by Majji and Morris [157] are used for model validation.

In §10.1, experimental results presented in Majji and Morris [157]'s study are extracted via image processing for quantitative comparison to simulations results. In §10.2, 1D simulations are conducted for linear shear flows to examine the particle distribution. In this section, Berry et al. [23]'s SID diffusion model parameters such as collision viscosity and particle roughness are adjusted by comparing the simulation results with Majji and Morris's experimental data, assuming the flow curvature of Taylor-Couette flow is negligible. Following 1D simulations, in §10.3, 2D simulations are performed for Taylor-Couette flows, and the effects of shear induced diffusive forces and shear gradient lift force on particle equilibrium locations are analysed.

10.1 The Majji and Morris experiments

Majji and Morris [157] used a Taylor-Couette apparatus consisting of two vertical coaxial cylinders to observe neutrally-buoyant particle migration (figure 10.1). In the experiment, the outer cylinder was held fixed while the inner cylinder was rotated. The stable

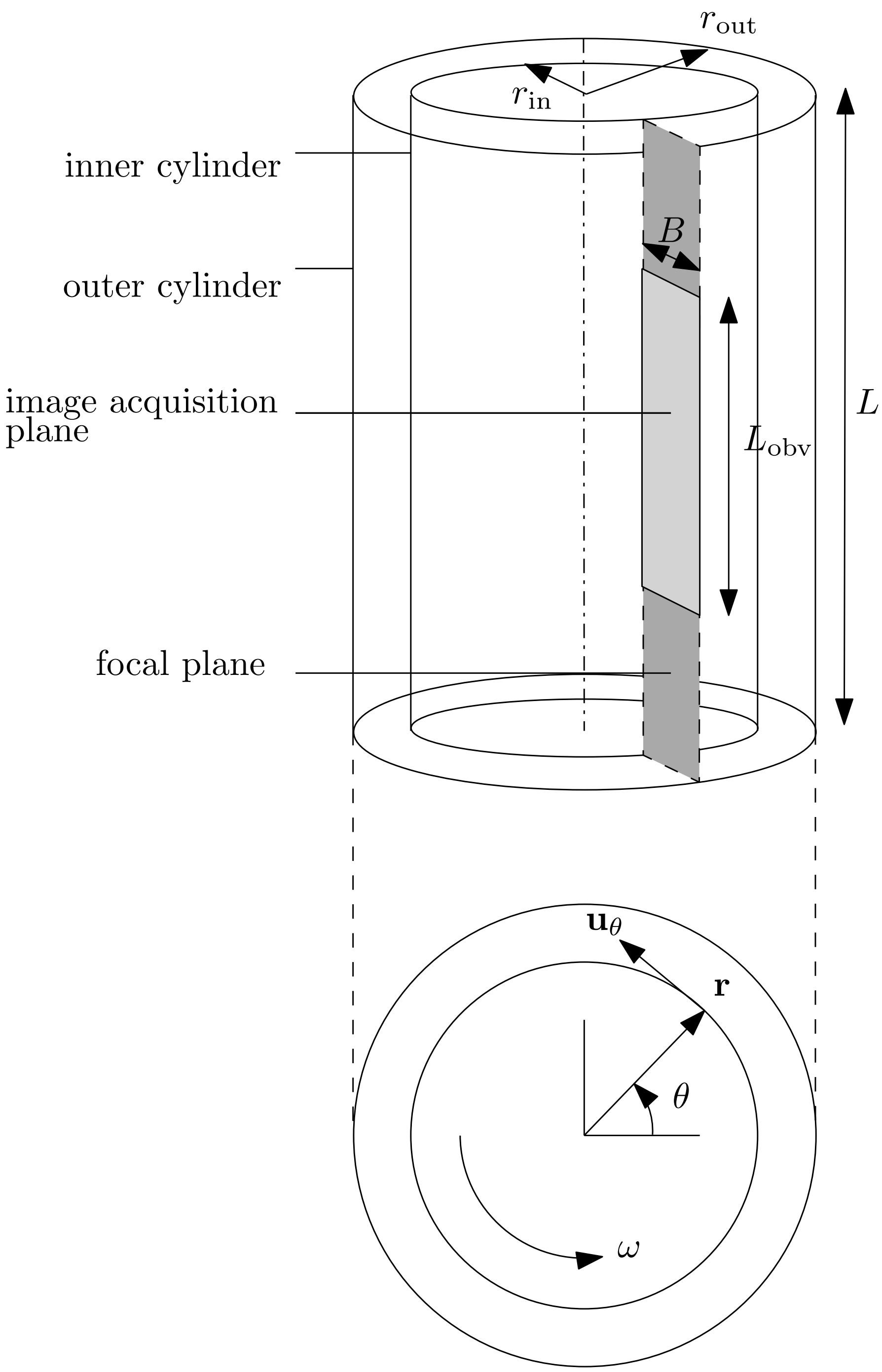

FIGURE 10.1: Schematic of the experimental apparatus with two concentric cylinders Majji and Morris [157].

flow for this geometry, typically known as circular Couette flow (CCF), was obtained at low angular speeds. Translational flow regimes such as Taylor vortex flow (TVF) and wavy vortex flow (WVF) were also obtained by increasing the inner cylinder's rotational speed. However, for the present study, we only use the results related to CCF, particularly relevant for low Reynolds number hydrodynamics.

The apparatus and suspension details of Majji and Morris's experiments are outlined here. The inner cylinder radius r_{in} and outer cylinder radius r_{out} were 50.15 mm and 57.15 mm, respectively. The resulting annular gap size B was 7 mm. The inner cylinder height L was 144 mm. A dilute suspension of polystyrene particles with a bulk solid volume fraction ϕ_{b} of 0.001 (0.1% in volume basis) has been used, where the particle density ρ_{s} and diameter $d(=2a)$ were $1050\,\text{kg}\,\text{m}^{-3}$ and 350 ± 50 µm, respectively. The suspending fluid density ρ_{f} has been matched to the particle density. The fluid viscosity, μ_{f}, was measured as 0.0175 Pa s, at the operating temperature.

After filling the annular gap volume with the dilute suspension, the submerged inner cylinder was rotated with an angular speed of ω. The behaviour of the flow confined was characterised by the Taylor-Couette flow (rotational) Reynolds number (Re_{TC}) [157],

$$Re_{\text{TC}} = \frac{\rho_{\text{f}}(r_{\text{out}} - r_{\text{in}})r_{\text{in}}\omega}{\mu_{\text{f}}} \tag{10.1}$$

The experimental results presented for the lowest Reynolds number, $Re_{\text{TC}} = 83$, are only considered for this study. This Reynolds number corresponds to $\omega = 3.94\,\text{rad}\,\text{s}^{-1}$, wall velocity $u_{\text{wall}} = 0.1976\,\text{m}\,\text{s}^{-1}$, and particle based shear Reynolds number, $Re_{\gamma} = 0.052$.

In the experimental apparatus, the ratio between the height and the annular gap, L/B, was equal to 20.5. Since the cylinder lengths are adequately long enough to neglect the bottom and top surface effects and the re-circulations are negligible for $Re_{\text{TC}} = 83$, the flow can be essentially considered unidirectional (i.e., variation happens only in radial direction) and, the simulation domain can be simplified to 2D flow between concentric circles. Under these circumstance, when the viscosity is assumed to be uniform (consistent with dilute assumption), the undisturbed azimuthal velocity, u_θ, in $\boldsymbol{e}_\theta$ direction is:

$$u_\theta = A_1 r + A_2 \frac{1}{r} \tag{10.2}$$

where,

$$A_1 = \omega \frac{-\eta^2}{1-\eta^2};$$
$$A_2 = \omega r_{\text{in}}^2 \frac{1}{1-\eta^2};$$

Here $\eta(= r_{\text{in}}/r_{\text{out}})$ is the inner to outer radius ratio. The velocity components u_{r} in the radial direction $\boldsymbol{e}_{\text{r}}$ and u_{z} in the longitudinal direction $\boldsymbol{e}_{\text{z}}$ are considered to be zero.

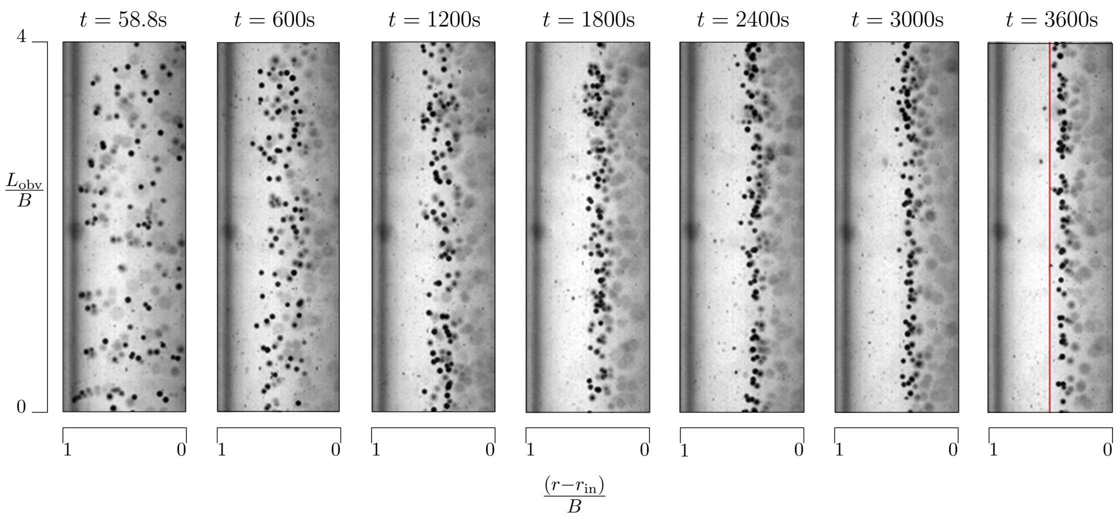

FIGURE 10.2: Gray scale images in Majji and Morris [157]'s experimental study. Adopted from Majji and Morris [157].

10.1.1 Data extraction

The imaging method described in Majji and Morris [157] is as follows. Particle distributions in the $B \times L_{\text{obv}}$ plane were recorded using a high-speed camera. The camera lens was placed so that particles that are sufficiently close to the focal plane appeared sharp in the images. As mentioned in Majji and Morris [157], the lens has focused particles in the depth of approximately 1 cm near the focal length. However, this 1 cm focus depth appears to be too large, particularly to describe the focused image plane depth with sharp particle images. This issue is further discussed in the next section. Particle distribution profiles obtained for different time intervals extracted from Majji and Morris [157] are shown in figure 10.2. Each image includes particle images taken for multiple time points to enhance the visualisation of the particle's equilibrium locations.

In this section, the method used to obtain the particle volume fractions from the Majji and Morris [157] images is described. First, individual image planes for each time interval obtained from Majji and Morris [157]'s paper are resized to an image size of 184×530 pixels. All the resized images are converted to 8-bit Gray-scale images and then converted to binary images using ImageJ programme [216]. This process requires thresholding limits to do the conversion, in which the minimum and maximum threshold values determine whether a pixel needs to be replaced with a black pixel or a white pixel. The resulting images are presented in figure 10.3. Note that the minimum and maximum threshold limits common for all the images are carefully selected so that it was possible to identify only clear particles (sufficiently in focus) in all images. This process equilibrates uneven illumination via background homogenisation. The source code used for this post processing is available in Appendix D.

10.1.2 Intensity based quantification

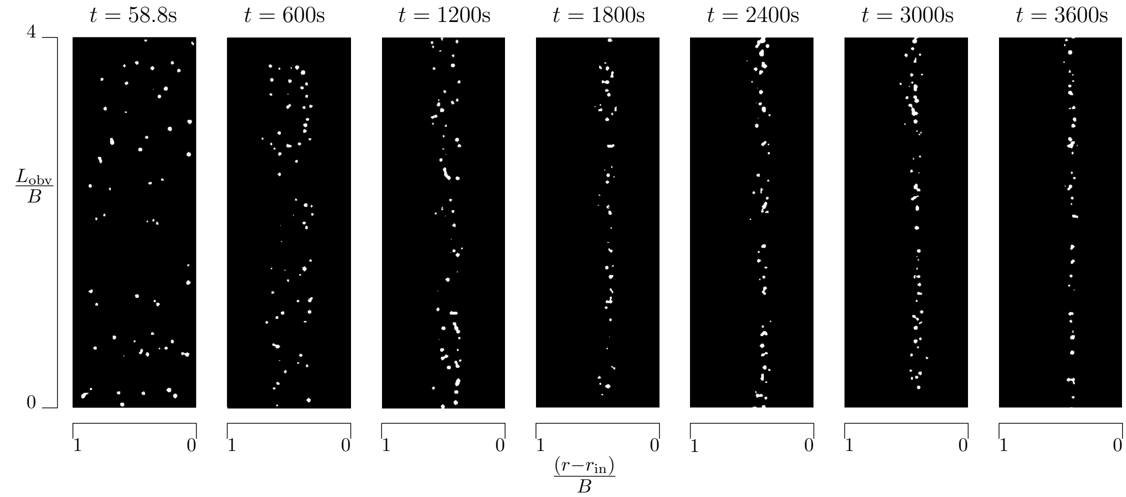

FIGURE 10.3: Post-processed 2D binary images of Majji and Morris [157]'s experimental study.

The area fraction distribution of the particles in each of the 2D image planes, analogous to concentration distribution, is quantified via image intensity. For this, surface histogram plots of the binary images are obtained, as shown in figure 10.4. The histograms show the binary equivalent pixel values, which vary between 0 and 255. The 2D intensity values along the longitudinal direction ($\boldsymbol{e}_{\mathrm{z}}$) are first projected (summed) to the radial axis to obtain the 1D particle distribution variation in the radial direction ($\boldsymbol{e}_{\mathrm{r}}$). The resulting net intensity, I, is divided by the average intensity across the gap to obtain the normalised intensity, I^*, values across the gap width as:

$$I^*(r) = \frac{I(r)}{\dfrac{1}{B}\displaystyle\int_{r_{\mathrm{in}}}^{r_{\mathrm{out}}} I(r)dr} \tag{10.3}$$

The normalised intensity variation, which also represents normalised area fraction variation along r direction, is shown in figure 10.5. These values can be assumed to represent the normalised volume basis concentration variation along the radial direction, under the conditions of the image plane thickness being infinitesimally small ($I^*(r) = \phi_{\mathrm{s}}(r)/\phi_{\mathrm{bulk}}$). If the focal depth is not insignificant (i.e., 1 cm as mentioned in Majji and Morris [157]),

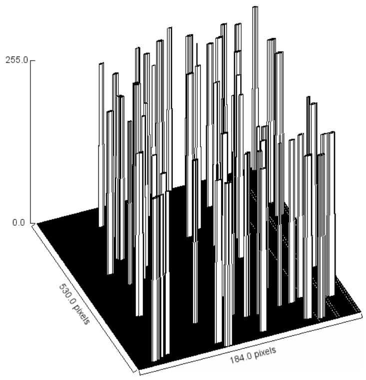

(a) 58.8 s

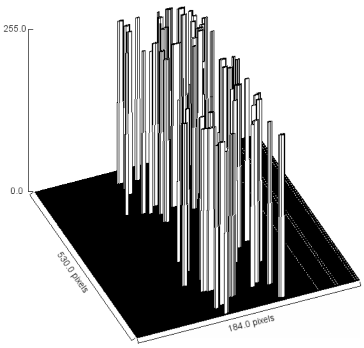

(b) 600 s

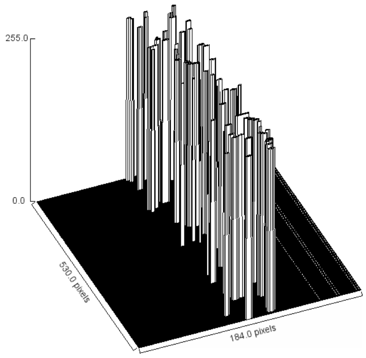

(c) 1200 s

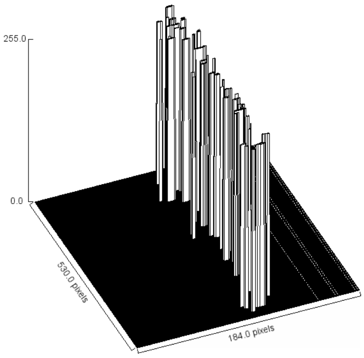

(d) 1800 s

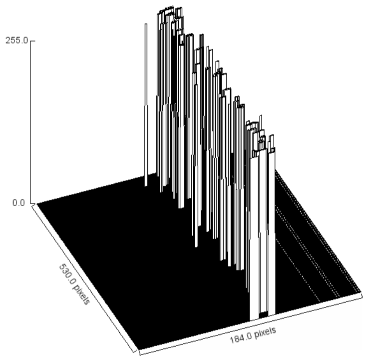

(e) 2400 s

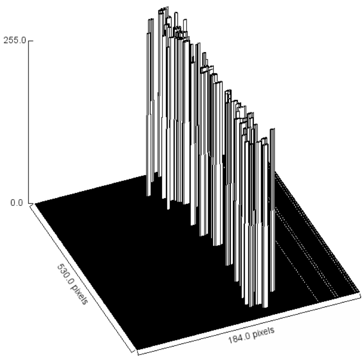

(f) 3000 s

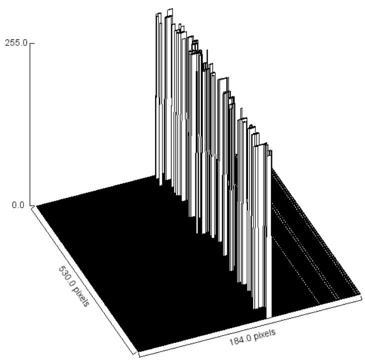

(g) 3600 s

FIGURE 10.4: Surface intensity plots of binary images at different time intervals.

particles will appear to be closer to the inner cylinder, but also spread over the finite region. However, the current distribution cannot be explained by a large focal length effect as peaks in the results are thin. Hence, the peak particle distributions suggests that the focal length effects are not substantial for the given focal length and according to the employed consistent thresholding techniques.

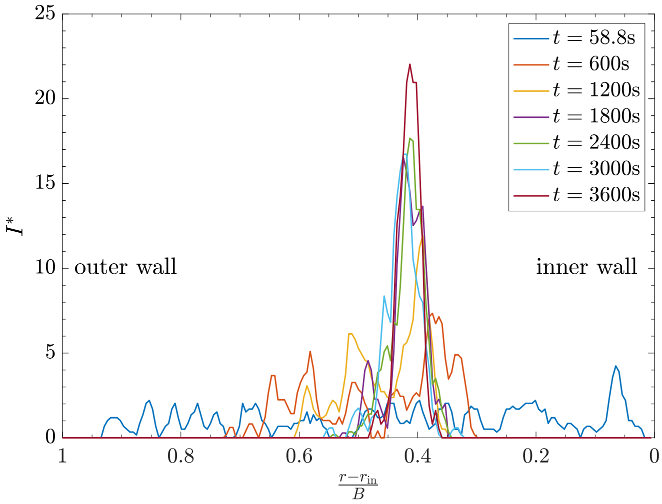

FIGURE 10.5: Non-dimensional intensity variation across the gap width for different time intervals.

10.2 Simple shear flow

The ratio between the inner and outer cylinder radius, η $(= r_{\text{in}}/r_{\text{out}})$, is equal to 0.877 for the thin gap Couette flow device used in Majji and Morris [157]'s study. As mentioned in Majji and Morris [157]'s work, when the azimuthal velocity is scaled by the inner cylinder velocity ($r_{\text{in}}\omega$) and the radial coordinate scaled by the outer radius of Couette cell (r_{out}), it can be shown that Eq. (10.2) can be written as;

$$\frac{u_\theta}{r_{\text{in}}\omega} = \frac{-\eta}{1-\eta^2}\left(r/r_{\text{out}} - \frac{1}{r/r_{\text{out}}}\right) \tag{10.4}$$

When η approaches one, the second term in Eq. (10.4), which is due to curvature, becomes negligible compared to the first term, and therefore the velocity becomes as a simple linear shear flow between two flat plates. With this assumption, the geometry used in the simulation is simplified to an infinitesimally thin, one-dimensional section of the actual annular gap width $B = 7\,\text{mm}$ (figure 10.6a).

Transient simulations are conducted to study the time-dependent particle distributions. The two-fluid model developed in chapter 8 is implemented in *arb* multiphysics finite volume code [106]. The boundary conditions discussed in the §9.1 and the single-wall force implementation method discussed in the §9.2.2 are applied for the simulation. The moving inner wall velocity u_{wall} is defined to be equal to Majji and Morris [157]'s experimental value of $0.1976\,\text{m}\,\text{s}^{-1}$.

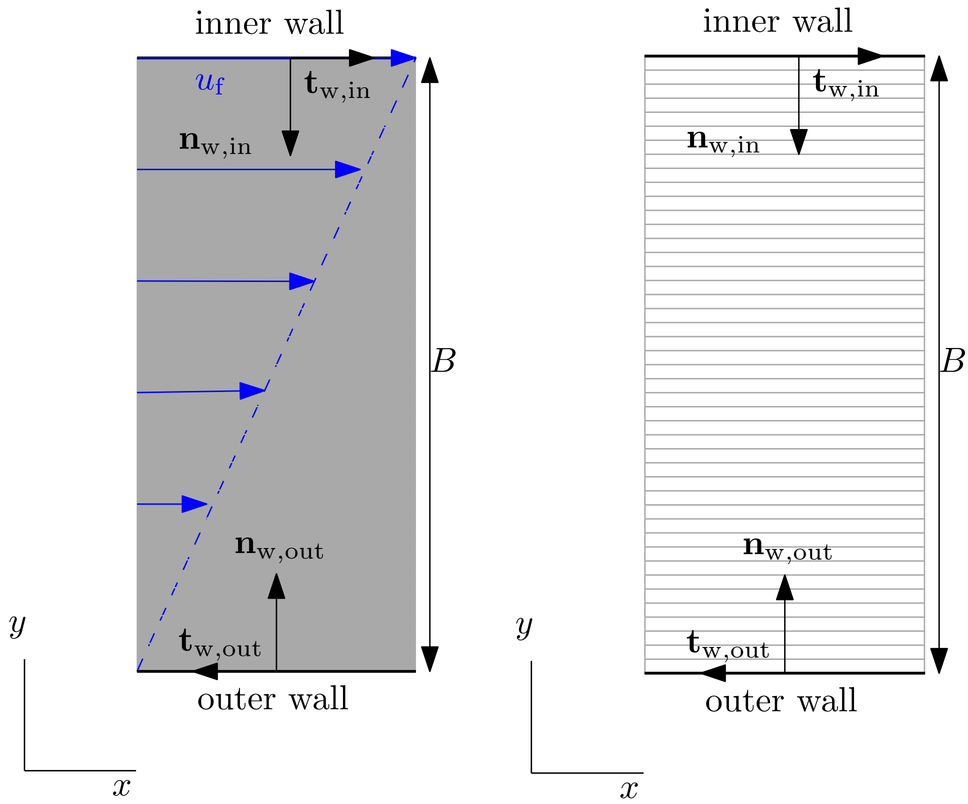

(a) Geometry (b) Mesh

FIGURE 10.6: Graphical representation of the geometry and mesh used for the 1D linear flow simulations (not to scale).

Boundary	Momentum - Wall normal	Momentum - Wall tangential	Pressure	Solid volume fraction
inner wall	$\boldsymbol{u}_{\text{f}} \cdot \boldsymbol{n}_{\text{w,in}} = 0$ $\boldsymbol{u}_{\text{s}} \cdot \boldsymbol{n}_{\text{w,in}} = 0$	$\boldsymbol{u}_{\text{f}} \cdot \boldsymbol{t}_{\text{w,in}} = u_{\text{wall}}$ $\boldsymbol{u}_{\text{s}} \cdot \boldsymbol{t}_{\text{w,in}} = u_{\text{wall}} - \chi/\mu_{\text{f}}(\boldsymbol{\tau}_{\text{f}} : \boldsymbol{t}_{\text{w,in}}\boldsymbol{n}_{\text{w,in}})$	$\boldsymbol{d}_{\text{f}} \cdot \boldsymbol{n}_{\text{w,in}} = 0$	$\boldsymbol{\nabla}\phi_{\text{s}} \cdot \boldsymbol{n}_{\text{w,in}} = 0$
outer wall	$\boldsymbol{u}_{\text{f}} \cdot \boldsymbol{n}_{\text{w,out}} = 0$ $\boldsymbol{u}_{\text{s}} \cdot \boldsymbol{n}_{\text{w,out}} = 0$	$\boldsymbol{u}_{\text{f}} \cdot \boldsymbol{t}_{\text{w,out}} = 0$ $\boldsymbol{u}_{\text{s}} \cdot \boldsymbol{t}_{\text{w,out}} = -\chi/\mu_{\text{f}}(\boldsymbol{\tau}_{\text{f}} : \boldsymbol{t}_{\text{w,out}}\boldsymbol{n}_{\text{w,out}})$	$\boldsymbol{d}_{\text{f}} \cdot \boldsymbol{n}_{\text{w,out}} = 0$	$\boldsymbol{\nabla}\phi_{\text{s}} \cdot \boldsymbol{n}_{\text{w,out}} = 0$

TABLE 10.1: Boundary conditions applied in 1D linear flow simulations. Here, the solid phase slip length, $\chi = -0.3a$ (see §9.1 for details).

10.2.1 Time discretization

A dynamic time-stepping method is employed to reduce simulation wall-time. A small initial time step of $\Delta t_0 \approx 0.9\,$s is chosen based on a predefined Courant–Friedrichs–Lewy (CFL) number (100) to provide adequate temporal resolution at beginning of the simulation when the particle migration happens most rapidly. Next, Δt is increased until either a maximum time-step value or a maximum CFL number is met. Conversely, when the simulation rapidly changes due to physical or numerical conditions, the time step value is decreased. Dynamic time-step regulation occurs in response to the number of Newton iterations performed per time step. The simulations are run for a longer time than the experimental time duration to ensure steady-state particle distributions. The simulation's steady-state condition is assured when the maximum (peak) particle concentration value becomes constant.

Case	$\Delta t_{\text{inc}}\%$	Wall time (s)
A	10	404
B	20	315
C	40	244
D	80	97.7

TABLE 10.2: Effect of time step increment on simulation wall time.

The percentage increase between two consecutive time steps (i.e., $\Delta t_{\mathrm{i}-1}$ and Δt_{i}), $\Delta t_{\text{inc}}\%$ is given as;

$$\Delta t_{\text{inc}}\% = \frac{\Delta t_i - \Delta t_{i-1}}{\Delta t_{i-1}} \times 100$$

The effect of $\Delta t_{\text{inc}}\%$ on the wall time and the transient peak particle concentration as a function of time is examined. As shown in table 10.2, the wall time decreases from 404 to 97.7 seconds when increasing $\Delta t_{\text{inc}}\%$. However, the time-differencing error increased for high $\Delta t_{\text{inc}}\%$, as shown in figure 10.7, which shows the transient peak particle concentration variation. Initial peak concentration variation is the same for all $\Delta t_{\text{inc}}\%$ values as the simulation starts with a small initial time step. However, at $1000\text{s} < t < 3000\text{s}$, peak concentration varies significantly, and large $\Delta t_{\text{inc}}\%$ cannot capture this behaviour. Accounting for both wall-time and simulation accuracy, $\Delta t_{\text{inc}}\%$ is maintained at 20% for the remaining simulations.

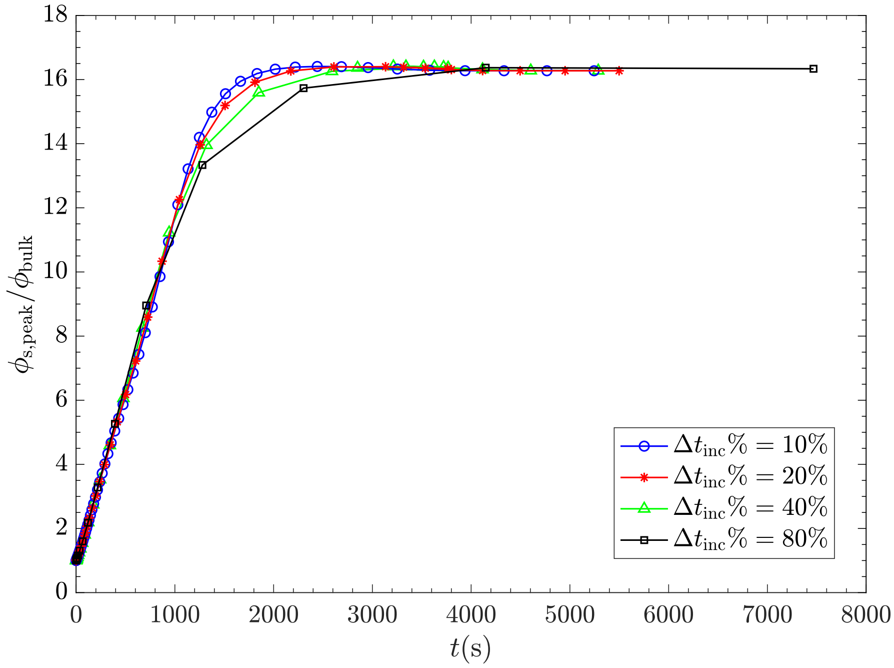

FIGURE 10.7: Comparison of maximum solid peak concentration ($\phi_{\mathrm{s,peak}}$) variation for cases with different time step increments.

10.2.2 Mesh sensitivity

Mesh	N_{y}	$\Delta y/B$	$a/\Delta y$
A	40	0.0250	1
B	300	0.0033	7.5
C	600	0.0016	15
D	1000	0.0010	25
E	5000	0.0002	125

TABLE 10.3: 1D mesh parameters for different meshes.

In 1D Couette-flow, the bulk flow occurs parallel to the wall, and particle flow (migration) occurs normal to the walls. Experimental results show a large concentration occurs near the centre between the two flat walls. However, wall-bounded forces and slip velocities are expected to vary significantly near the walls. A well-refined uniform mesh, with N_{y} mesh points in y-direction and a constant aspect ratio of cells throughout the domain, is constructed to capture both the concentration and velocity gradients (figure 10.6b).

A mesh sensitivity study is conducted to quantify the effect of cell height (Δy) on the resulting particle distributions. The various meshes are detailed in table 10.3. Figure 10.8 shows the effect of Δy on the steady-state particle distribution. The steady-state particle distribution is less sensitive to the mesh quality as Meshes B, C, D and E produce nearly

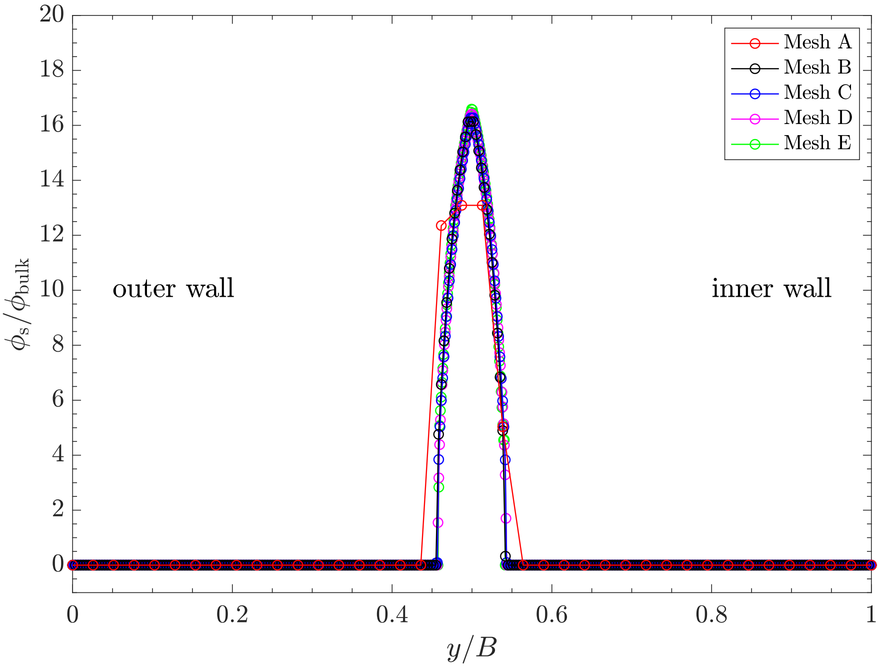

FIGURE 10.8: Comparison of steady-state solid distribution for different meshes. Simulation parameters: $\epsilon = 10^{-6}$ and $\hat{\mu}_{col,s} \times 0.01$

identical results. However, the lowest mesh resolution (Mesh A) exhibits a significant difference in the peak particle concentration. Accounting for both simulation wall-time and the 'best compromise' accuracy, Mesh C is employed in the remainder of the study.

10.2.3 Particle migration results

The simulated transient particle distributions across the 1D domain obtained at the same time intervals of Majji and Morris [157]'s experiments are shown in figure 10.9. The 1D model predictions, which assume the azimuthal velocity is linear with the radius, are also compared against Majji and Morris [157]'s experimental results. Simulation results show that the particle distribution reaches its steady-state conditions at approximately $t = 2000\,\mathrm{s}$. Overall, the model only predicts the transient particle distribution reasonably well up to $t = 600\,\mathrm{s}$. The poorest comparison with experiments is obtained for the larger time intervals of $t \geq 1200\,\mathrm{s}$. 1D model predictions do not capture the experimentally observed shift of the peak concentration location towards the moving inner wall (inner cylinder). As previously discussed in §10.1.2, this shift is not an artefact of the imaging technique. Generally, the shear gradient lift is the main force that favours particles to migrate towards the high shear rate regions, accounting for the asymmetry of the shear field [99, 157]. However, as a purely linear shear flow is considered in these simulations, shear rate gradient-based hydrodynamic forces are not relevant. The discrepancies highlight the significance of the curvature effect (shear gradient effects) on particle migration, further investigated in §10.3. The other difference between the model predictions and experimental results is the maximum concentration (peak concentration) value. Overall, at steady-state, the model predicts a lower peak concentration of $\phi_{\mathrm{s}}/\phi_{\mathrm{bulk}} \approx 6$ and a blunt shape particle distribution profile. Conversely, for $t \geq 1200\,\mathrm{s}$, the experimental results exhibit sharp peaks of $\phi_{\mathrm{s}}/\phi_{\mathrm{bulk}} \approx 12 - 20$, suggesting that the inward migration of particles is being limited in the model.

For this case, the inward particle migration can be limited by either the viscous diffusive forces acting down the concentration gradient, or the particle-scale inertial lift forces acting towards the wall. Hence, the behaviour of shear induced diffusive force and lift force components, specifically in the y-direction, are examined to understand the forces responsible for this model behaviour. Figure 10.10 shows the three main wall-bounded lift force and shear induced diffusion pressure force variations across the gap width under steady-state conditions. While most these forces act towards the channel centre for most of the domain region ($\hat{F}_{\mathrm{s,y}} > 0$ for $0 < y/B < 0.5$ and $\hat{F}_{\mathrm{s,y}} < 0$ for $0.5 < y/B < 1$), the slip-shear lift force and the shear induced diffusive pressure force reverse direction at $y/B \approx 0.35$ and 0.65 and start to act towards the wall. Here $\hat{F}_{\mathrm{s,y}}$ indicates the y component of each of the forces, acting on the solid phase and divided by the local solid concentration. The slip-shear lift force, which depends only on the slip velocity direction in a uniform shear flow, is the strongest force acting to resist the particle clustering, as shown in figure 10.10. The change in slip-shear force direction results from the change in the slip velocity direction, which itself results from the increased influence of particle interaction forces in regions where the particle concentration is non-dilute. Particle interaction forces include viscous strain forces, dependent on the collision viscosity, and shear induced diffusion forces, dependent on the normal stress viscosity and particle roughness. The effect of both these forces is examined in the next two sections, with specific reference to the particle distributions and slip velocities observed near the centre of the Couette flow.

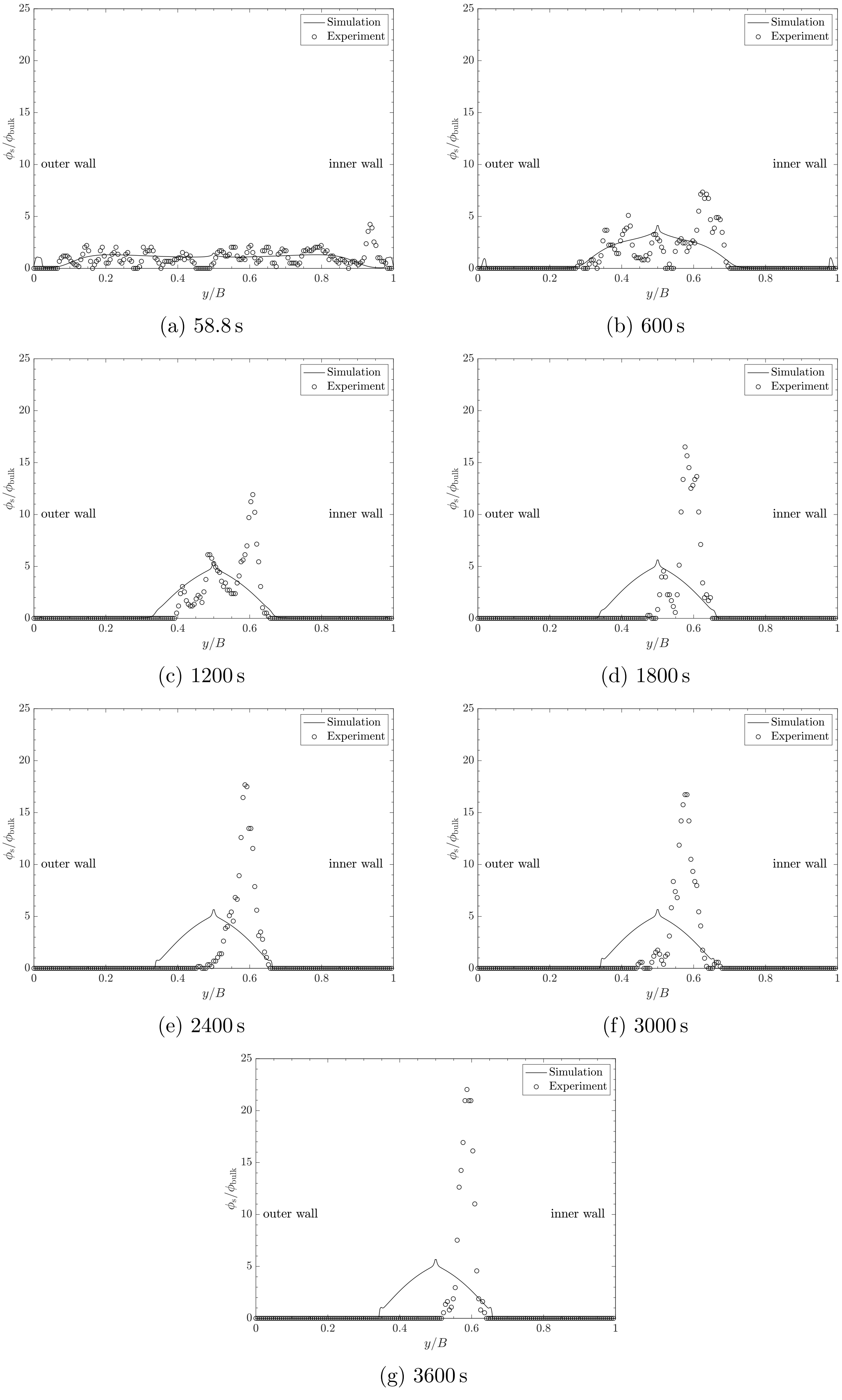

(a) 58.8 s (b) 600 s (c) 1200 s (d) 1800 s (e) 2400 s (f) 3000 s (g) 3600 s

FIGURE 10.9: Transient solid distribution of dilute suspension.

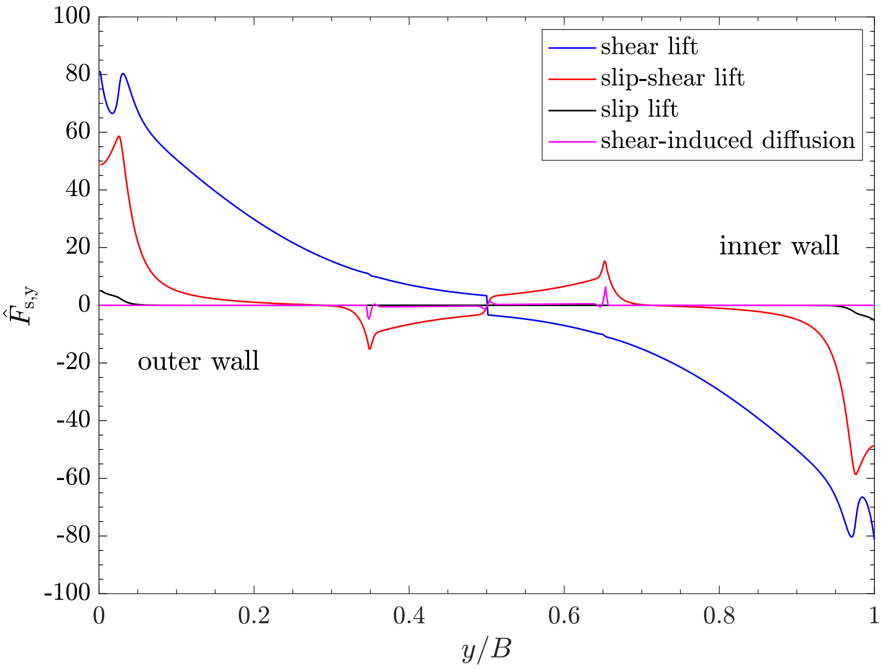

FIGURE 10.10: Normalised force variation between two flat walls in linear shear flows at steady-state condition (t =9000 s).

10.2.4 Effect of collision viscosity

Multi-body interactions in particle-enriched zones can increase the collision viscosity $\hat{\mu}_{\text{col,s}}$. Such an increase can affect the solid-phase stress, as shown in Eq. 8.9, resulting in changes in the system's slip velocities. To quantify the effect of $\hat{\mu}_{\text{col,s}}$ on both the slip velocity and the particle distribution, different multipliers on $\hat{\mu}_{\text{col,s}}$ $(\times 0.5, 0.1$ and $0.01)$ are used in a sensitivity study, and the model predictions are compared against the experimental Majji and Morris's results.

Note that, here we employ Berry et al. [23]'s preliminary dilute closure expressions for $\hat{\mu}_{\text{col,s}}$, which account for the influence length of a second particle and the particle roughness in modelling the viscosity via,

$$\hat{\mu}_{\text{col,s}} = \hat{B}_1(\hat{r}_\infty) + \hat{B}_2(\hat{r}_\infty) + f_2[\hat{B}_1(\hat{r}_{\text{sid}}) + \hat{B}_2(\hat{r}_{\text{sid}})] \tag{10.5}$$

where,

$$\begin{aligned} \hat{r}_\infty(\phi_s) &= \hat{r}_{\text{col},1}(\phi_s) + \hat{r}_{\text{col},2}(\phi_s) + 2 \\ \hat{r}_{\text{sid}} &= \min(\hat{r}_{\text{sid},3}(\phi_s) + 2\hat{\varepsilon}, \hat{r}_\infty - 2) + 2 \end{aligned} \tag{10.6}$$

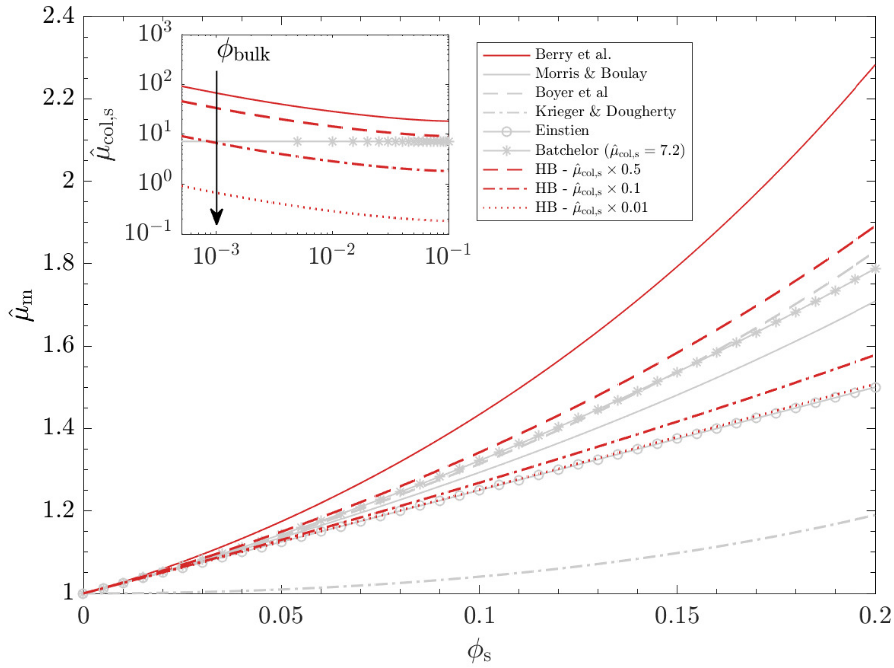

FIGURE 10.11: Mixture and collision viscosity as a function of particle concentration for different multipliers.

Here $\hat{r}_\infty(\phi_\mathrm{s})$ and $\hat{r}_\mathrm{sid}(\phi_\mathrm{s})$ are the non-dimensional influence length and SID length scale. $\hat{\varepsilon}$ is the non-dimensional roughness. Overall, $\hat{r}_\infty(\phi_\mathrm{s})$ and $\hat{r}_\mathrm{sid}(\phi_\mathrm{s})$ functions are developed so that $r_{\mathrm{col},1}(\phi_\mathrm{s})$ and the roughness $\hat{\varepsilon}$ capture the low volume fraction behaviour, whereas $r_{\mathrm{col},2}$ and $\hat{r}_\mathrm{sid}$ capture the high volume fraction variation [23]. Hence, the fitting functions proposed for $r_{\mathrm{col},1}$,$r_{\mathrm{col},2}$, $r_{\mathrm{sid},3}$ and f_2, account for the shear viscosity behaviour in both the dilute $\phi_\mathrm{s} \to 0$ and concentrated $\phi_\mathrm{s} \to \phi_\mathrm{max}$ limits. The $\hat{B}_1$ and $\hat{B}_2$ functions are calculated by integrating particle-particle interaction forces over the modelled particle distribution around each reference particle [23]. All expressions given in Berry et al. [23] to obtain $\hat{\mu}_{\mathrm{col,s}}$ are provided in Appendix C.

Based on Harvie's TFM framework, the shear viscosity of the suspension can also be written as (Eq. 8.10):

$$\hat{\mu}_\mathrm{m} = \frac{\mu_\mathrm{m}}{\mu_\mathrm{f}} = 1 + 2.5\phi_\mathrm{s} + \hat{\mu}_{\mathrm{col,s}}\phi_\mathrm{s}^2$$

Hence, the final form of suspension shear viscosity, which is employed in this study, can be obtained by substituting the Berry et al.'s collision viscosity correlation (Eq. 10.6) for to Eq. 8.10.

Figure 10.11 shows the effect of different suspension shear viscosity multipliers for $\hat{\mu}_{\mathrm{col,s}}$

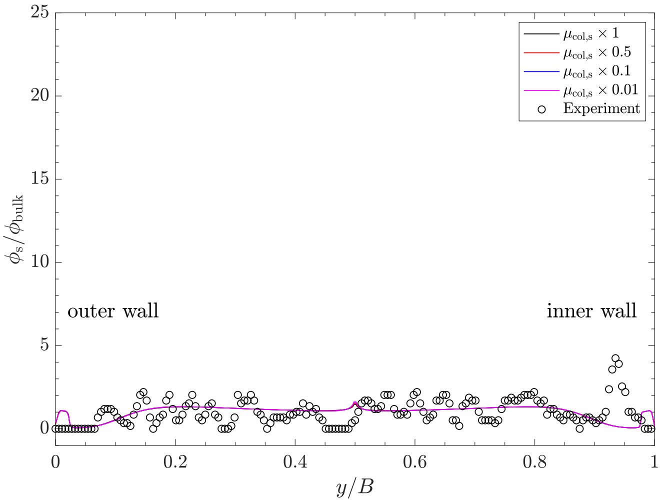

(a) 58.8 s

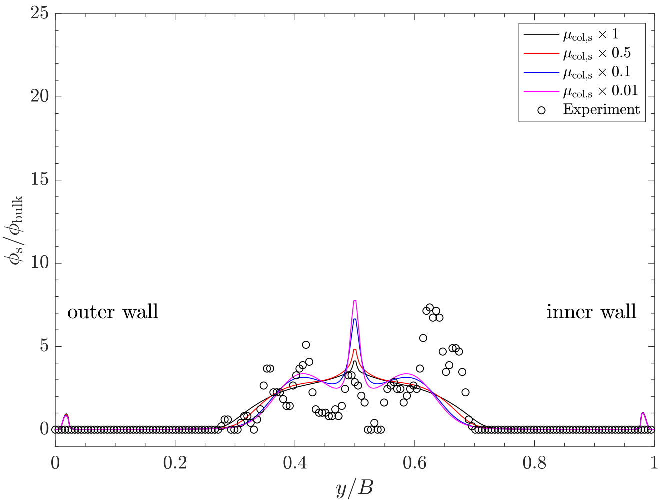

(b) 600 s

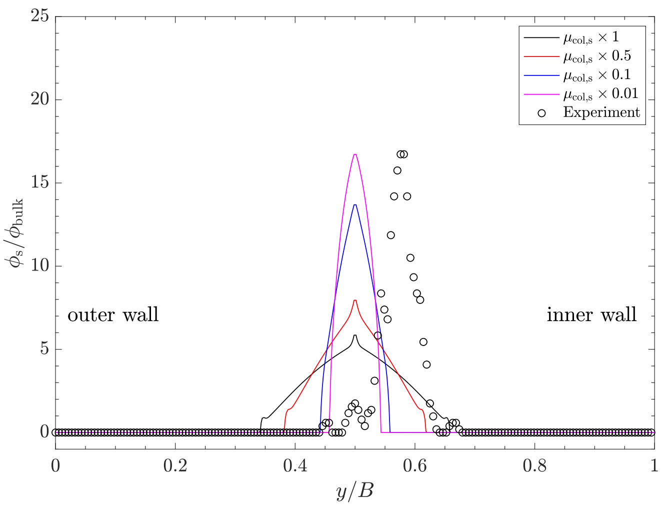

(c) 3000 s

FIGURE 10.12: Comparison of concentration profiles for different $\hat{\mu}_{\mathrm{col,s}}$ multipliers at different time intervals. Here $\phi_{\mathrm{bulk}} = 0.001$.

have on the mixture viscosity, for the low particle volume fractions most relevant for this study. The values are also compared against other available models listed in table 4.3. The inset of figure 10.11 illustrates the isolated $\hat{\mu}_{\mathrm{col,s}}$ variation with the particle volume fraction for the same multipliers. The collision viscosity values are compared against the higher-order term of Batchelor's shear viscosity model (given in table 4.3) at the dilute limit.

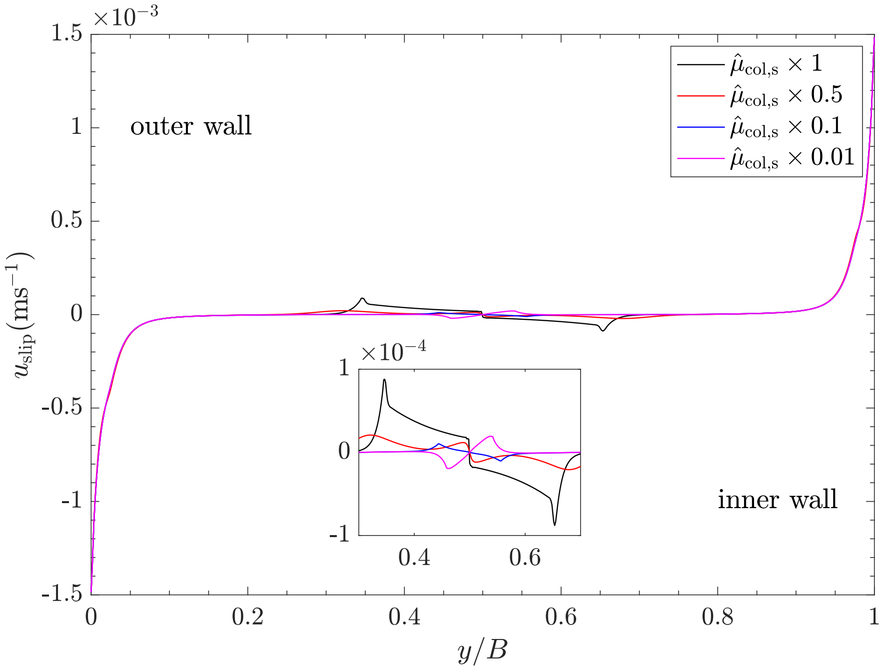

FIGURE 10.13: Effect of collision viscosity on the slip velocity at steady state (t =9000 s).

The particle distributions resulting from the four different shear viscosity multipliers at three different times (58.8, 600, and 3000 seconds) are given in figure 10.12. Owing to the low collision viscosity in the case with $\hat{\mu}_{\mathrm{col,s}} \times 0.01$, the number of particles that migrate to the centre is the largest compared to the three other cases, and this behaviour is most significant for the highest time considered. The original viscosity model, which is the case with $\hat{\mu}_{\mathrm{col,s}} \times 1$, does not accurately capture the experimental solid distribution as time increases. These results suggest that the preliminary dilute collision viscosity model of Berry et al. [23] needs further development. Notably, when a viscosity multiplier is chosen that produces a mixture viscosity closer to established dilute regime models (i.e., $\hat{\mu}_{\mathrm{col,s}} \times 0.01$) which effectively recovers Einstein's results), the predicted particle distributions are more consistent with the experimental results.

Given that shear induced diffusion is low for a dilute system ($\propto \phi^2$), lift forces should be responsible for limiting the particle migration in these experiments. With the prior knowledge of the slip-lift significance discussed in the previous section (figure 10.10), the effect of the collision viscosity on the slip velocity is further examined to understand the particle distribution. The slip velocity variation at $t = 3000\,\mathrm{s}$ across the 1D geometry for the same collision viscosity multipliers are shown in figure 10.13. For all four multipliers, small 'surges' in slip velocities occur where particle concentrations change, near the particle clustering zones ($0.4 < y/B < 0.6$). However, by decreasing the strength of collision viscosity, local slip velocity variations reduce, and the remaining small surges of slip shift towards the centre of the channel, consistent with the particle clustering zones.

Overall, these results illustrate an interesting phenomenon. Namely, the particle collision induced viscosity of a suspension influences the slip of particles, which in turns effects particle distributions via the particle-scale lift forces. Notably this occurs in our modelling even when the particle collision viscosity is lower than the more established theories (see inset 10.11). Hence even under dilute conditions with $\phi_{\mathrm{bulk}} = 0.001$, particle interactions influence particle behaviour.

10.2.5 Effect of roughness

Non-dimensional particle roughness, a parameter that affects short-range particle interactions, has been included in Berry et al. [23]'s preliminary SID-based viscosity and collision viscosity models. Under dilute conditions in particular, particle roughness influences the shear induced diffusion and the particle phase stress tensor and plays a critical role in modelling the subsequent particle hydrodynamics and distribution. Although the shear induced diffusion force is relatively small under dilute conditions, as shown in figure 10.10, in regions where shear or concentration changes abruptly, shear induced diffusion can become nearly as significant as the other lift forces. Given that the collision viscosity model has been presented in Eq. (10.5), the Berry et al. [23]'s SID-based viscosity model employed in this study is presented in Eq. (10.6).

$$\hat{\mu}_{\mathrm{sid},1} = 2f_1\left[\frac{2}{7}\hat{B}_1(\hat{r}_{\mathrm{sid}}) + \frac{1}{5}\hat{B}_2(\hat{r}_{\mathrm{sid}})\right] \tag{10.7}$$

$$\hat{\mu}_{\mathrm{sid},2} = 2f_1\frac{1}{7}\hat{B}_1(\hat{r}_{\mathrm{sid}})$$

and

$$\hat{\mu}_{\rm sid} = \hat{\mu}_{\rm sid,1} + \hat{\mu}_{\rm sid,2}$$

Here, the the screening length due to shear induced diffusion, $\hat{r}_{\rm sid}$ is given by Eq. (10.6). Functional forms of the non-dimensional shear induced viscosities, (i.e., $\hat{\mu}_{\rm sid,1}$ and $\hat{\mu}_{\rm sid,2}$) given in the Berry et al. [23] study are detailed in Appendix C.

The effect of non-dimensional particle roughness, $\hat{\varepsilon}$, on model predictions is studied by comparing the particle distribution profiles for different particle roughness values available in the literature [56, 68, 89, 180]. Often, the values for dimensional roughness, ε, particularly for PMMA and polystyrene particles, varies between 0.1-100 nm and are independent of the particle size [89, 180]. Since Majji and Morris has used $a = 175\,\mu$m size polystyrene particles, the practically relevant range of non-dimensional particle roughness can be estimated to be $\mathcal{O}(10^{-7}) < \hat{\varepsilon} < \mathcal{O}(10^{-2})$. However, $\hat{\varepsilon}$'s lower-bound value can be much less than $\mathcal{O}(10^{-7})$ for relatively smooth particles. Hence, the tests are performed for $10^{-40} \leq \hat{\varepsilon} \leq 10^{-2}$ in this study.

The concentration profiles for cases with different particle roughness are shown in figure 10.14. The figure shows the solids distribution at different times of 58, 600, and 3600 seconds. For the given low collision viscosity ($\hat{\mu}_{\rm col,s} \times 0.01$), it is observed that as the $\hat{\varepsilon}$ increases, the inward particle migration in the domain decreases along with its peak concentration. Also, with decreasing particle roughness, steady-state particle distributions are attained much later than with the larger particle roughness value, of $\hat{\varepsilon} = 10^{-2}$, as shown in figure 10.15. Although the peak concentration values are slightly between the two roughnesses of $\hat{\varepsilon} = 10^{-6}$ and $\hat{\varepsilon} = 10^{-40}$, it can be seen that the difference between the particle distribution profiles for these two $\hat{\varepsilon}$ values is relatively insignificant for all the time intervals (Figure 10.14).

In summary, the preliminary SID model of Berry et al. [23] suggests that for particle roughnesses typical of the experimental particles, the significance of SID could range from minor to insignificant. The comparison of the experimental and simulation results shows that the best correspondence is achieved when SID effects are insignificant under these dilute conditions.

Future work is required to determine whether the Berry et al. [23]'s roughness model correctly relates SID to particle roughness, and to quantify particle roughness more

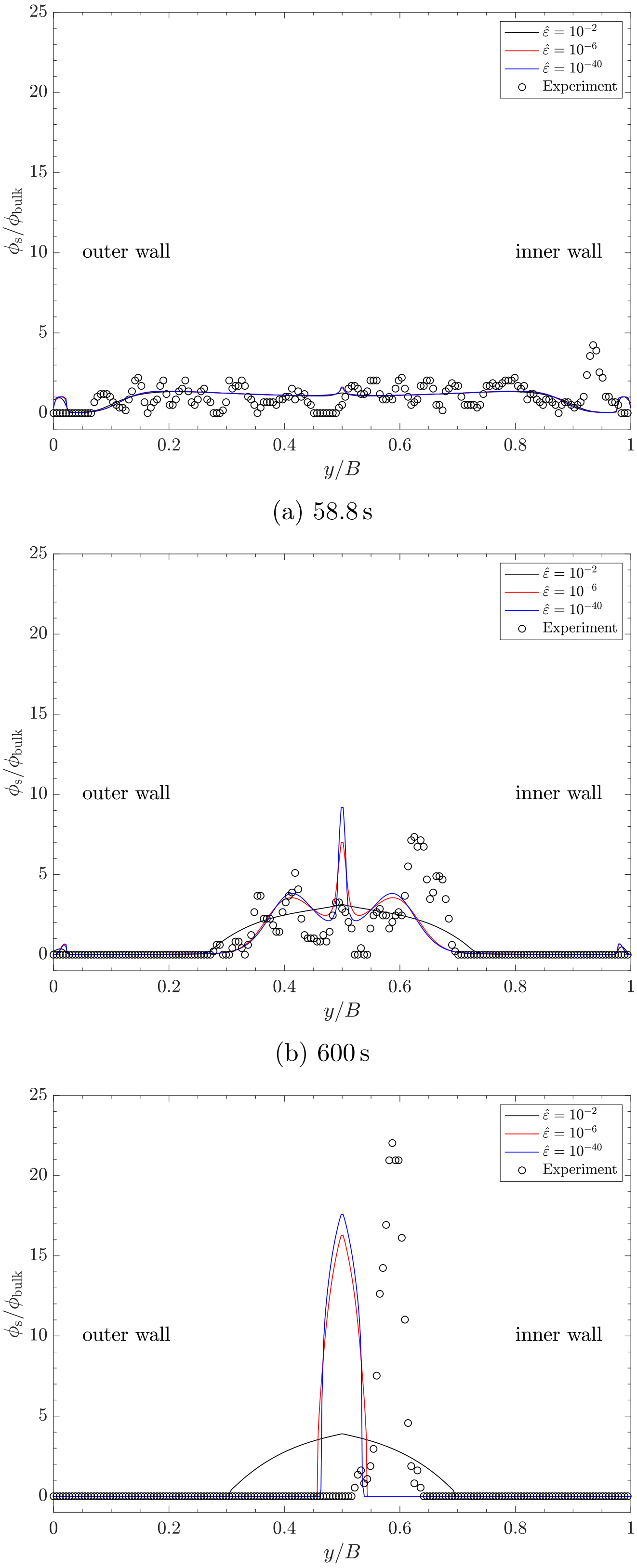

(a) 58.8 s

(b) 600 s

(c) 3600 s

FIGURE 10.14: Concentration profiles for different $\hat{\varepsilon}$ at different times. Here $\phi_{\text{bulk}} = 0.001$.

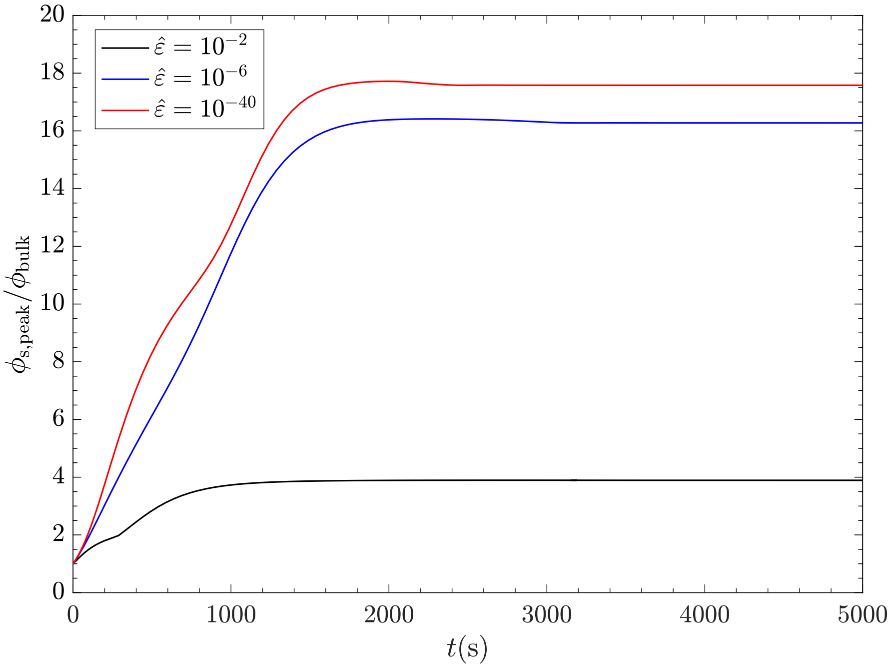

FIGURE 10.15: Transient variation of the peak particle concentration for different non-dimensional particle roughness values.

accurately in particle migration experiments.

10.2.6 Effect of extra lift and drag forces

In this section, the significance of the extra interface forces developed in this thesis in the two-fluid model (e.g., drag force; $\boldsymbol{M}^{\mathrm{wb}}_{\mathrm{D,slip}}$, $\boldsymbol{M}^{\mathrm{wb}}_{\mathrm{D,shear}}$, and lift forces; $\boldsymbol{M}^{\mathrm{wb}}_{\mathrm{L,slip}}$, $\boldsymbol{M}^{\mathrm{wb}}_{\mathrm{L,slip\text{-}shear}}$, $\boldsymbol{M}^{\mathrm{wb}}_{\mathrm{L,shear}}$) is analysed by performing simulations with and without these new force terms. Figure 10.16 shows steady-state particle distribution profiles for two cases. In the first case ('with extra forces'), simulations are performed with all the interphase momentum forces given in Eq. (8.26). Whereas in the second case ('without extra forces'), only the default unbounded drag force correlations (e.g., $\boldsymbol{M}^{\mathrm{ub}}_{\mathrm{D,slip}}$ and $\boldsymbol{M}^{\mathrm{ub}}_{\mathrm{D,shear\text{-}gradient}}$), are used as presented in Harvie [107]'s two-fluid model.

his figure shows that the extra forces introduced in this thesis govern the particle migration in linear shear flows. In the absence of these forces, particles do not migrate as there is no driving mechanism.

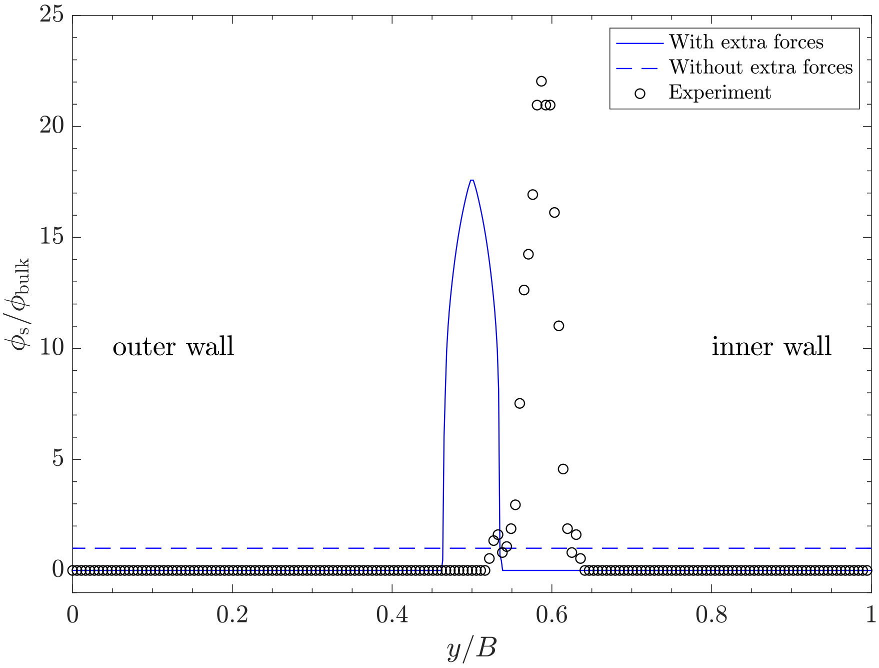

FIGURE 10.16: Steady state solid distribution profiles in the presence and absence of the extra forces developed in this thesis.

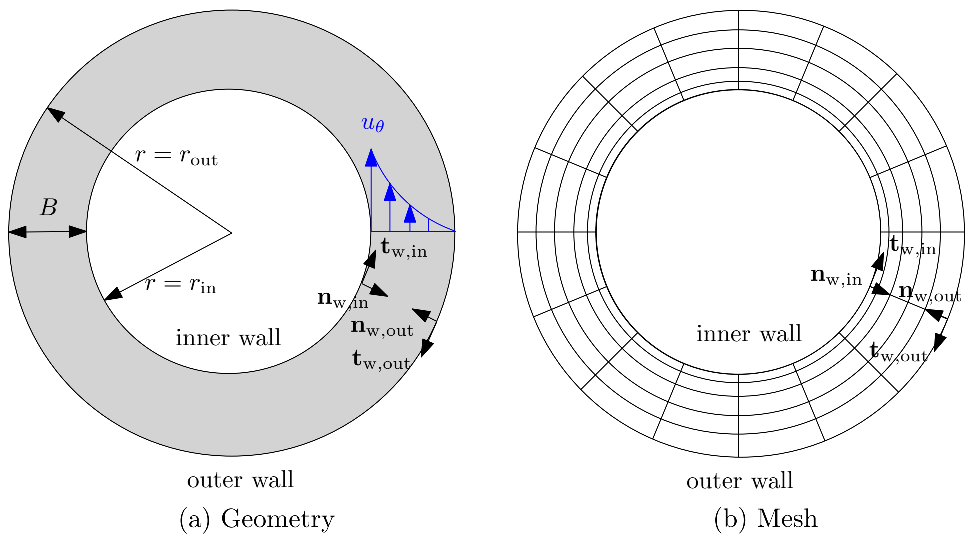

FIGURE 10.17: Graphical representation of the geometry and mesh used for the 2D Taylor-Couette flow simulations (not to scale).

10.3 2D Taylor-Couette flow

In this section, 2D Taylor-Couette flow simulations are performed to examine the Majji and Morris [157] experimental study's particle migration. Unlike the 1D simulations considered in the previous section, no simplifications for the azimuthal velocity profiles are made. Hence the azimuthal velocity in this 2D flow varies non-linearly in the radial direction (Eq. 10.2).

The computational domain is considered to be the fluid-filled annular gap between the two cylinders. Since the bulk fluid flow occurs only in the azimuthal direction, and flow variation in the axial direction is negligible, a 2D flow between two concentric circles is considered. The 2D geometry used is shown in figure 10.17. Following the experimental work of Majji and Morris [157], the radii for cylinders are set for $r_{\mathrm{in}} = 50.15\,\mathrm{mm}$ and $r_{\mathrm{out}} = 57.15\,\mathrm{mm}$, respectively.

The boundary conditions applied are similar to the conditions applied in the previous 1D simulations but here without the periodic mesh construct. The BCs are summarised in table 10.4. The azimuthal velocity of inner cylinder is set as $u_{\mathrm{wall}} = 0.1976\,\mathrm{m\,s^{-1}}$ which corresponds to $Re_{\mathrm{TC}} = 83$.

Boundary	Momentum - Wall normal	Momentum - Wall tangential	Pressure	Solid volume fraction
inner wall	$\boldsymbol{u}_{\mathrm{f}} \cdot \boldsymbol{n}_{\mathrm{w,in}} = 0$ $\boldsymbol{u}_{\mathrm{s}} \cdot \boldsymbol{n}_{\mathrm{w,in}} = 0$	$\boldsymbol{u}_{\mathrm{f}} \cdot \boldsymbol{t}_{\mathrm{w,in}} = u_{\mathrm{wall}}$ $\boldsymbol{u}_{\mathrm{s}} \cdot \boldsymbol{t}_{\mathrm{w,in}} = u_{\mathrm{wall}} - \chi/\mu_{\mathrm{f}}(\boldsymbol{\tau}_{\mathrm{f}} : \boldsymbol{t}_{\mathrm{w,in}}\boldsymbol{n}_{\mathrm{w,in}})$	$\boldsymbol{d}_{\mathrm{f}} \cdot \boldsymbol{n}_{\mathrm{w,in}} = 0$	$\boldsymbol{\nabla}\phi_{\mathrm{s}} \cdot \boldsymbol{n}_{\mathrm{w,in}} = 0$
outer wall	$\boldsymbol{u}_{\mathrm{f}} \cdot \boldsymbol{n}_{\mathrm{w,out}} = 0$ $\boldsymbol{u}_{\mathrm{s}} \cdot \boldsymbol{n}_{\mathrm{w,out}} = 0$	$\boldsymbol{u}_{\mathrm{f}} \cdot \boldsymbol{t}_{\mathrm{w,out}} = 0$ $\boldsymbol{u}_{\mathrm{s}} \cdot \boldsymbol{t}_{\mathrm{w,out}} = -\chi/\mu_{\mathrm{f}}(\boldsymbol{\tau}_{\mathrm{f}} : \boldsymbol{t}_{\mathrm{w,out}}\boldsymbol{n}_{\mathrm{w,out}})$	$\boldsymbol{d}_{\mathrm{f}} \cdot \boldsymbol{n}_{\mathrm{w,out}} = 0$	$\boldsymbol{\nabla}\phi_{\mathrm{s}} \cdot \boldsymbol{n}_{\mathrm{w,out}} = 0$

TABLE 10.4: Boundary conditions applied in 2D Taylor-Couette flow simulations. Here the solid phase slip length $\chi = -0.3a$ (see §9.1 for details).

10.3.1 Mesh sensitivity

A non-uniform structured mesh is employed to discretize the 2D computational domain. Small mesh elements are used near the moving inner wall with a geometric progression growth factor of 0.01, producing larger elements near the stationary outer wall. This ensures adequate resolution at the inner cylinder where relatively large velocity gradients are expected.

A mesh sensitivity study is conducted to examine the effect of the minimum cell height in the radial direction, Δr_{min}, on the resulting particle distributions. For this, the number of mesh points in the radial direction, N_{r}, is gradually increased while maintaining a constant cell growth factor of 1.01. The number of mesh points on around the circumferential azimuthal direction, N_{θ}, is also increased to ensure small aspect ratio cells, as shown in table 10.5. Here, $\mathrm{AR}_{\mathrm{min}}$ represents the aspect ratio of the thinnest cell (near inner wall) of a given mesh.

Mesh	N_{r}	N_{θ}	$\Delta r_{\mathrm{min}}/B$	$a/\Delta r_{\mathrm{min}}$	$\mathrm{AR}_{\mathrm{min}}$	Total Cells
A	20	80	0.0454	0.4	24.8	722
B	50	200	0.0155	1.2	29.0	4802
C	100	400	0.0059	3.3	38.4	19602
D	200	800	0.0016	12.2	71.1	79202

TABLE 10.5: 2D mesh parameters for different meshes.

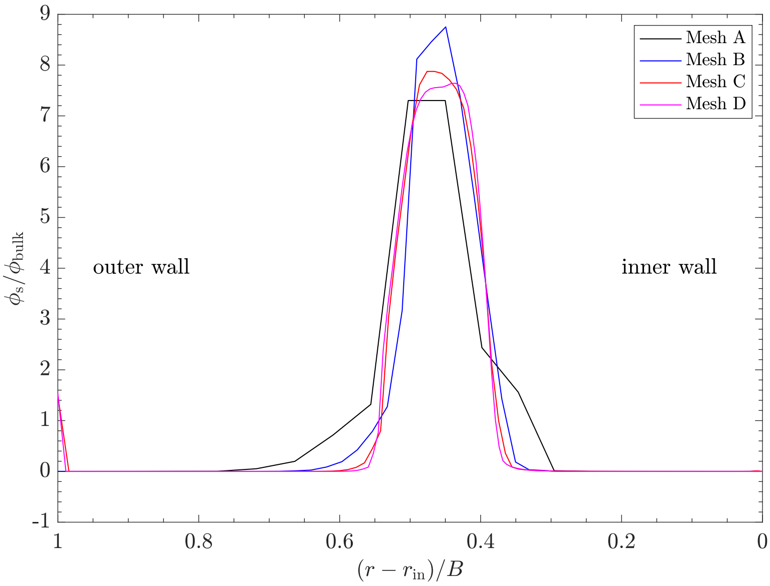

FIGURE 10.18: Particle distribution at t =1200 s for different 2D meshes.

Figure 10.18 shows the particle distribution profiles at t =1200 s for four different meshes. As Δr_{min} is reduced, the relative difference between the particle distributions decreases, causing the solid profiles to nearly overlap for the two most refined meshes (Mesh C and Mesh D). However, Mesh D's total cell count is almost five times larger than the Mesh C, while the cell count in the radial direction, which is most critical for the simulations, only doubles. Hence Mesh C is employed in the remainder of the present study.

10.3.2 Particle migration results

Transient particle distribution profiles in the 2D Couette flow are examined in this section. Similar to the 1D simulations, Berry et al. [23]'s preliminary normalised collision viscosity, $\hat{\mu}_{\mathrm{s,col}}$, is decreased by a factor of 100 to be consistent with more established literature. The non-dimensional roughness, $\hat{\varepsilon}$, is selected as 10^{-6}, largely removing the influence of SID on the results.

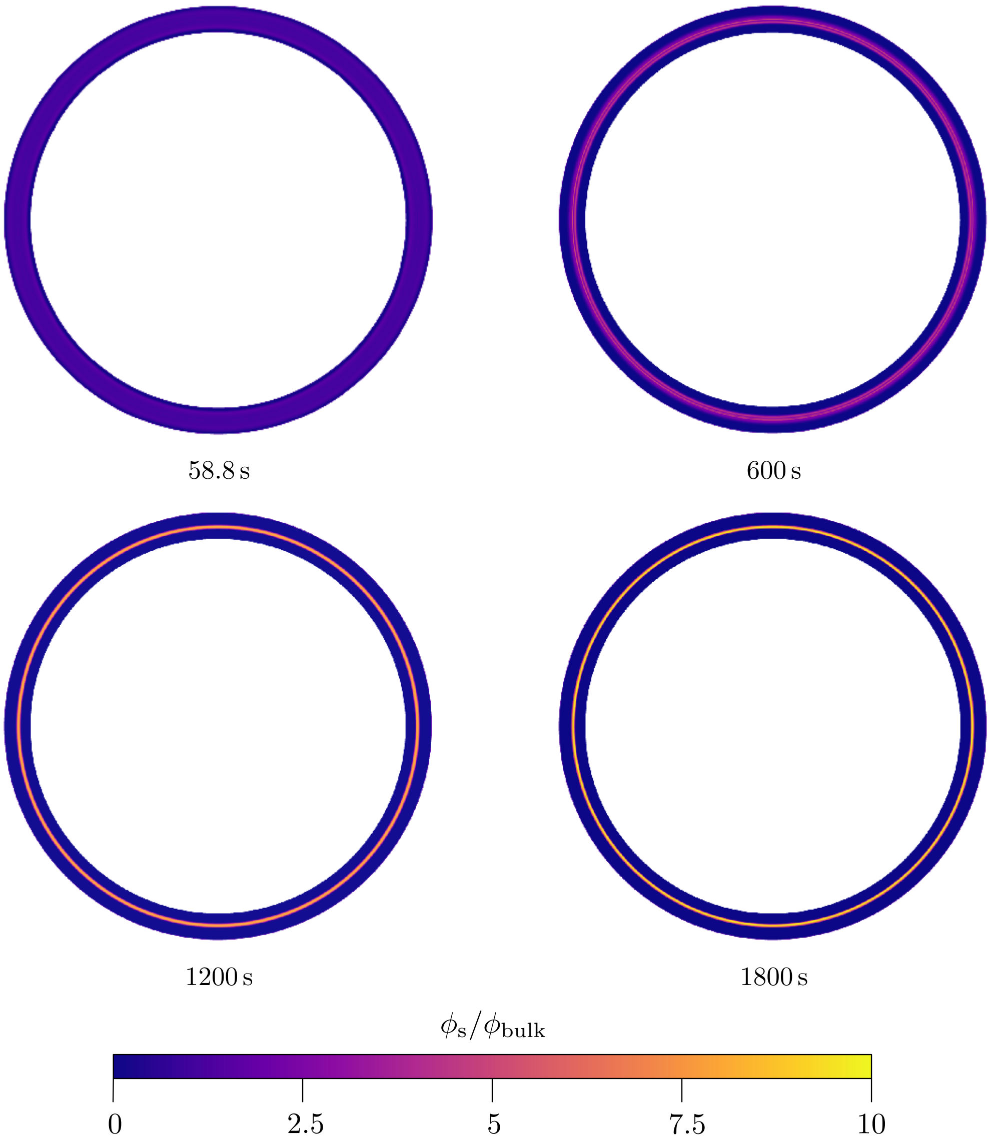

FIGURE 10.19: Simulated results of the normalised particle distributions in a Taylor-Couette flow (top-view).

In this 2D flow, unlike in the previously considered 1D linear flow, shear gradient lift forces make a significant contribution to particle migration velocities. The single-particle shear gradient lift force coefficient, $C_{\mathrm{L,SG}}$, required to model this force, has to be determined based on a parameter σ, which depends on the local shear-rate (γ) and shear rate gradient (γ') magnitudes. Here, $\sigma(= 2\gamma'\nu^{1/2}\gamma^{-3/2})$ [11] is calculated based on the undisturbed analytical velocity profile given in Eq. (10.2). For Taylor Couette flow (TCF), $\gamma = 2A_2r^{-2}$ and $\gamma' = 4A_2r^{-3}$ results in a constant σ value of $2.828{A_2}^{-1/2}\nu^{1/2}$. Detailed calculations for the shear rate and shear rate gradients in cylindrical coordinates are provided in Appendix D. Based on the inner and outer cylinder radii, suspension's kinematic viscosity, and the selected lowest rotational speed, A_2 and σ are evaluated as 0.0429 and 0.0556. For the calculated σ value, $C_{\mathrm{L,SG}}$ is determined as 0.1041 using figure 8.4 and employed in the TFM.

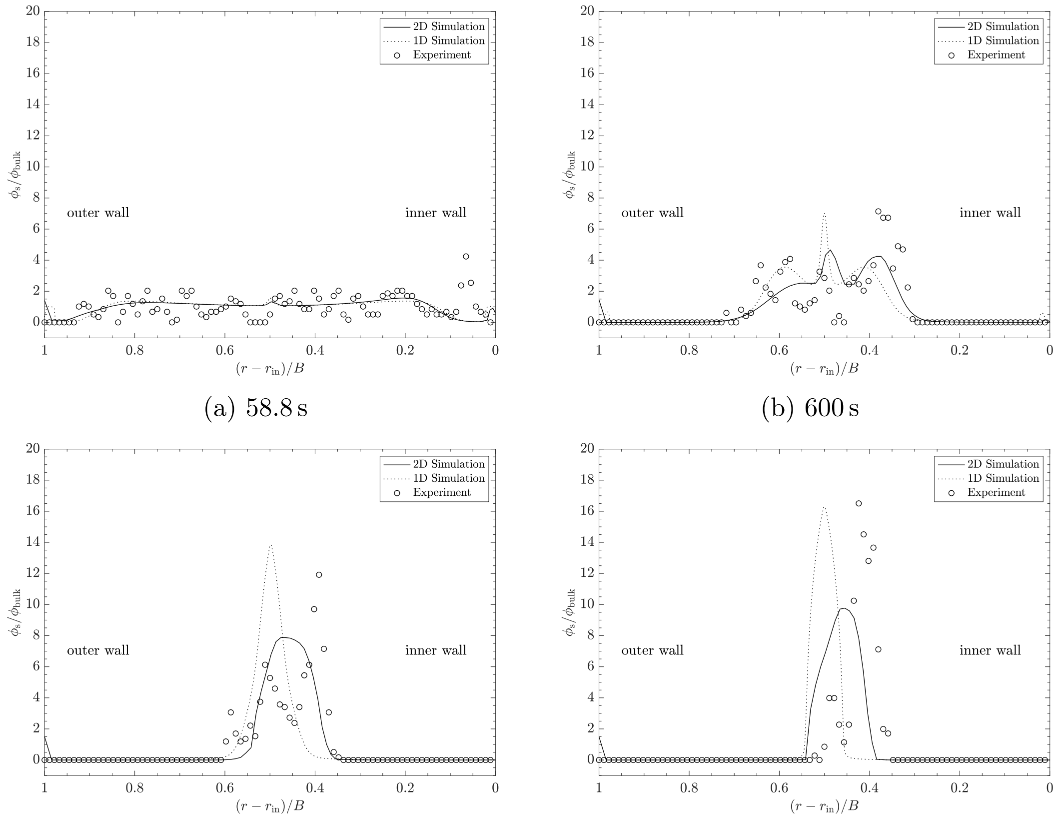

(a) 58.8 s

(b) 600 s

(c) 1200 s

(d) 1800 s

FIGURE 10.20: Transient particle distribution in a 2D Taylor-Couette flow and the comparable particle distribution in 1D linear flow profile that uses the same $\hat{\mu}_{\mathrm{s,col}}$ and $\hat{\varepsilon}$.

2D simulation results of the particle distribution in a Taylor-Couette flow obtained at the same time intervals as the experiments are shown in figure 10.19. Due to numerical issues, possibly related to the implementation of the postulated shear gradient lift force, most 2D flow simulations are performed only up to $t = 1800$ s. After $t \approx$1000 s, the 2D flow simulations required a large number of smaller time steps to produce converged results, resulting in a large wall-time. Nevertheless, all presented results have a non-dimensional convergence residual of $< 10^{-12}$ [106], and satisfy the model equations.

The radial particle volume fractions, extracted from the 2D profiles, are compared against Majji and Morris [157]'s experimental results in figure 10.20. Model predictions agree reasonably with experimental results up to $t = 1200$ s. Overall, the particle equilibrium location has shifted towards the inner rotating cylinder ($(r - r_{\mathrm{in}})/B \approx 0.42$), similar to experimental observations. However, the peak particle concentration value and the cusp shape are not as well predicted, particularly for $t = 1800\,\mathrm{s}$. Also, weaker particle migration away from the outer wall is predicted by the model (figure 10.20 at $t = 1800\,\mathrm{s}$), and this could be a potential cause of the predicted peaks not being as sharp peaks as observed in the experiments.

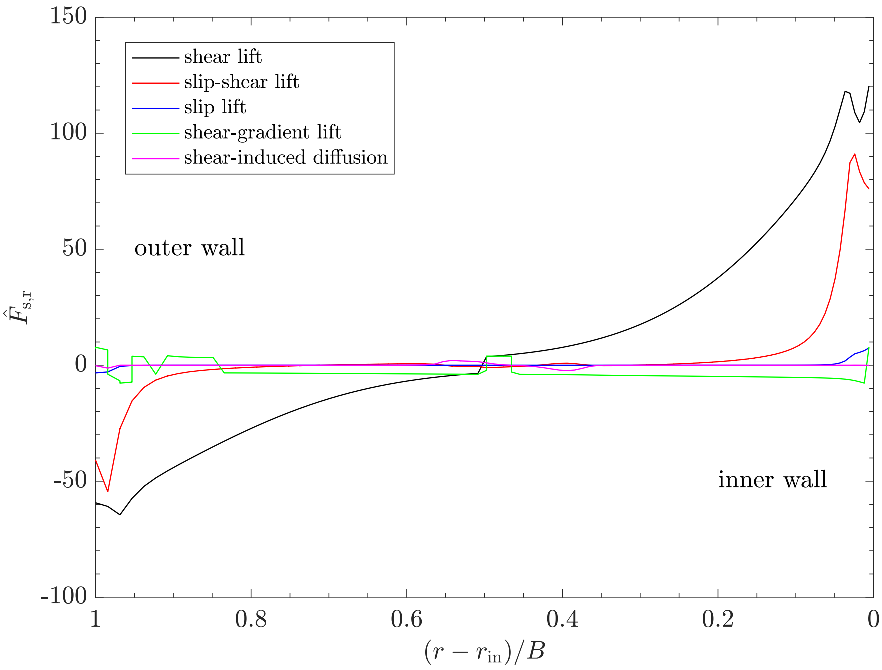

FIGURE 10.21: Normalised force variations between two walls in Taylor-Couette flows at $t = 1200\,\mathrm{s}$.

Unlike in 1D simple shear flows, the hydrodynamic forces due to flow curvature (i.e., SID pressure diffusive force and shear gradient lift force) can become more significant in 2D Taylor-Couette flow. Note that these are modelled using the frame-invariant stress tensor of Harvie [107]. Further, the non-linear azimuthal velocities in the radial direction cause a varying shear rate field within the annular gap. To examine the significance of these forces, different lift forces and shear induced diffusion forces acting in the radial direction are compared in figure 10.21. As expected, asymmetric wall-bounded lift forces are observed. The shear dependent wall forces, which are more significant in driving neutrally buoyant particles, become larger near the rotating inner wall compared to the stationary outer wall. Hence particles near the outer wall migrate more slowly towards the centre of the gap width, compared to the particles near the rotating inner wall. This behaviour explains the lack of particle migration away from the stationary outer wall, and the reduced peak particle concentration values observed for $t \geq 1200\,\mathrm{s}$.

10.3.3 Effect of shear gradient force

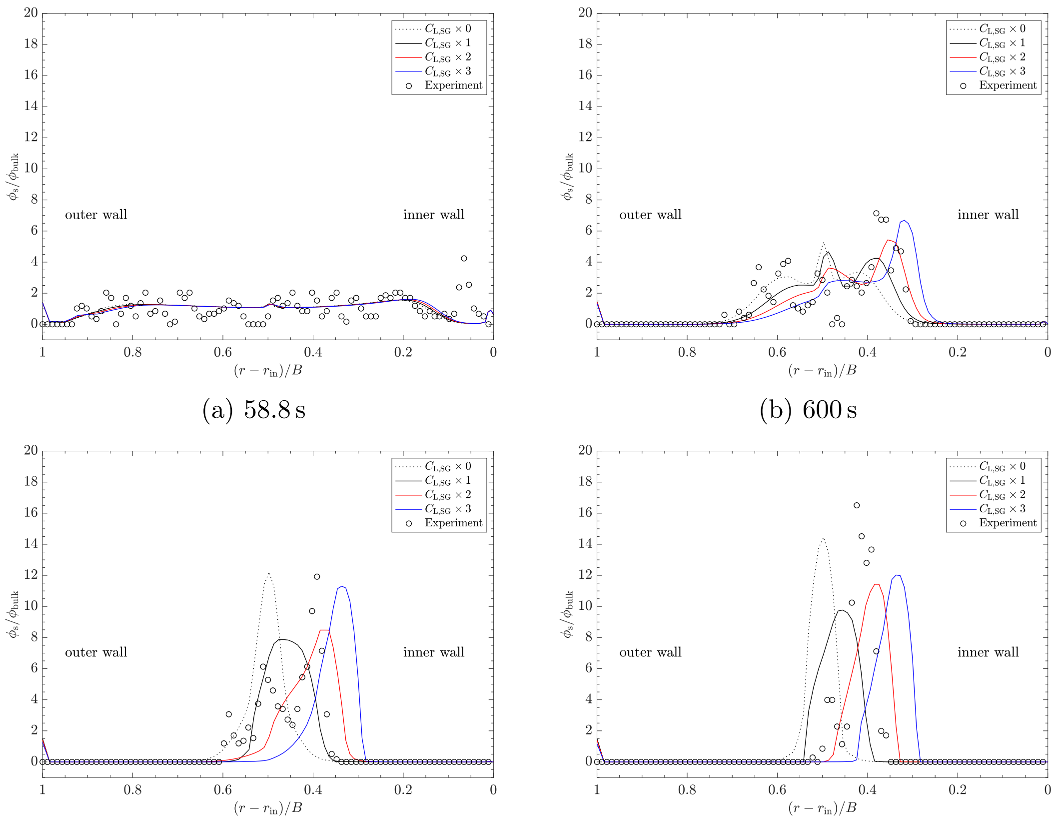

(a) 58.8 s (b) 600 s

(c) 1200 s (d) 1800 s

FIGURE 10.22: Effect of shear gradient lift force on the particle distributions in 2D Taylor-Coutte flows.

In this section, the effect of shear gradient lift force on the particle distribution is investigated using different multipliers for $C_{L,SG}$. Simulation results of the radial particle distribution for three different multipliers on $C_{L,SG}$ are shown in figure 10.22. The shear gradient lift force acts from the low shear rate region (stationary outer wall) to the high shear rate region (rotating inner wall) throughout the domain, favouring the particle migration towards the inner wall region. With increasing shear gradient lift, the particles' equilibrium position shifted towards the inner rotating wall, and the peak particle concentration has been increased. The best correspondence between simulations and experiments occurs for a shear gradient multiplier of 2. Considering the approximations used to model this shear gradient lift force, the correspondence is encouraging.

10.4 Closure

The two-fluid model, which includes wall-bounded lift and drag forces, is applied to predict neutrally buoyant particle migration in linear shear flows, and Taylor-Couette flows at finite inertia under dilute conditions. The lift forces that act perpendicular to the wall become non-negligible in finite-inertia flows and govern particle migration. The shear induced diffusion based on particle roughness, local particle concentration and local shear rate becomes less significant than particle-scale inertial lift forces for dilute suspensions. Even at dilute conditions ($\phi_{\text{bulk}} < 0.001$), the higher-order terms of the suspension shear viscosity (collision viscosity) indirectly influence the particle migration. They modify the solid phase's slip velocity in particle clustering regions, thereby influencing slip-shear lift forces.

The model performance is evaluated by comparing the predicted particle distribution profiles to experimental data obtained from Majji and Morris [157]'s thin-gap Taylor-Couette flow system. The model predictions are found to qualitatively agree with the experimental data, confirming that the shear gradient lift force is responsible for shifting the particle's equilibrium location towards the inner rotating cylinder. Despite the quantitative agreement for initial times intervals, peak particle concentrations are under-predicted by the model at large time intervals. However, when considering the approximations used to model this unbounded shear gradient lift force, the simulations' results are encouraging, and the results point towards further work necessary to quantify the isolated shear gradient lift.

Part IV

STUDY CONCLUSIONS

Chapter 11

Conclusions and Suggested Future Work

The central point of the thesis is that particle-scale inertial lift forces are crucial for modelling the hydrodynamic behaviour of dilute suspension.

Direct numerical simulations of a single particle translating at low but finite slip and shear Reynolds number were undertaken (Chapters 5, 6 and 7) to address the limitations identified in the single wall-bounded models (Chapter 3). Based on these numerical results, generalised wall-bounded lift and drag force models, valid for any particle-wall separation distances (except contact) and slip and shear Reynolds numbers up to $\mathcal{O}(10^{-1})$, were developed. The developed models were then used to predict slip and migration velocities of neutrally buoyant and buoyant particles translating near walls. The predictions were validated against available numerical and experimental results.

Evidence was presented that shows that existing suspension modelling frameworks fail to correctly predict particle distributions in dilute suspensions under finite inertial conditions (Chapter 4). Hence, the developed particle-scale wall-bounded force models and other existing wall-bounded force models were implemented within Harvie [107]'s preliminary two-fluid framework to predict averaged particle migration in dilute suspensions (Chapter 8). A new solid phase velocity boundary condition was introduced to the two-fluid model based on the single-particle slip velocity study, and this boundary condition was validated against analytical slip velocity solutions under dilute conditions. Different methods were examined for the wall-bounded force implementation (Chapter 9). The developed two-fluid model, which accounts for three different particle-scale inertial lift forces as well as a shear-induced diffusive force, was applied to predict the migration of neutrally buoyant particles in simple shear and thin-gap Taylor-Couette flows (Chapter 10). The results were qualitatively compared against a previously reported experimental study.

In summary the lift models were able to predict the observed particle migration in the thin gap Taylor-Couette flow, however, it was found necessary to

(a) account for shear gradients resulting from the cylindrical geometry,
(b) introduce a shear gradient lift force, and
(c) model the interactions between the lift forces from the two opposing walls

to correctly predict the steady-state particle distributions in the device. The two effects captured by points (b) and (c) in the above require more theoretical analysis and validation.

In this chapter, specific conclusions from this study are discussed relating to the two main research objectives outlined in §1.2. Based on the current outcomes, suggestions for future studies in dilute particle migration modelling are also outlined.

11.1 Conclusions

Specific conclusions related to the single-particle study (Chapters 5-7 in Part II):

- **A numerical framework that can accurately calculate the very small magnitude wall induced forces acting on single particles was developed.**

  The numerical framework developed in this thesis allows measuring small magnitude forces that act on a single particle in the low slip and shear Reynolds number regimes where theories and experiments cannot easily be attained.

- **A new lift force correlation was developed for a particle translating with a finite slip in a linear shear flow. This model is expressed in terms of three force coefficients, and is valid for any non-contact particle-wall separation distance, and $\boldsymbol{Re}_{\mathbf{slip}}, \boldsymbol{Re}_{\gamma} \leq 0.1$.**

A new lift model was proposed for a rigid particle that accurately captures the transition in the lift force behaviour between the inner and outer regions. The three lift coefficients, $C_{\mathrm{L},1}$, $C_{\mathrm{L},2}$ and $C_{\mathrm{L},3}$, were defined to be functions of only shear rate, slip velocity and shear rate, and only slip velocity, respectively, in addition to wall distance. The net lift model obtained by combining all three lift coefficients is able to cover both strong slip and shear flows, and are applicable for negative or positive slip and shear rates.

- **The shear-based lift coefficient of a particle translating near a wall under a zero-slip condition was found to decrease as shear rate was increased.**

  The lift forces acting on a spherical particle in a single wall-bounded linear shear flow field under a zero-slip condition were examined (apparently for the first time at low Re) via numerical computation for different particle-wall separation distances. The effect of shear rate was investigated by varying the shear Reynolds number across practically relevant ranges. A significant decrease in the lift coefficient was observed as the shear rate was increased. This effect was more pronounced at larger separation distances.

- **A shear-based drag force, independent of slip velocity, was developed for particles translating in the linear shear flow near walls under a zero-slip condition.**

  A new drag force model, with higher order terms in separation distance, was proposed for particles translating at zero-slip in linear shear flows, following a previous analytical model [156]. The shear-based drag rapidly decreased to zero away from the wall for all examined shear rates. A shear based inertial correction was also provided for the drag coefficient. For particles translating at finite slip velocity in linear shear flows, the most accurate drag predictions were obtained by combining the new shear-based drag and Faxen [80] slip-based drag models. The shear based drag model proposed in this study was found to be critical in predicting the velocities of neutrally buoyant particles.

- **Negative slip velocities were founded for force-free particles translating in linear shear flows.**

  The slip velocities of force-free (neutrally buoyant) particles predicted using the developed shear based drag model and existing slip based drag model were validated against new numerical results obtained at finite shear Reynolds numbers. The predicted slip velocities were negative and almost independent of inertia, confirming that force-free particles lag the fluid flow near a wall in positive shear fields.

- **The inertial dependency on the lift force was found to be significant for force-free particles translating in a linear shear flows.**

  The lift force acting on force-free particles calculated utilising all the three lift coefficients was also validated against numerical results for practically relevant shear rates. The net lift coefficients of force free-particles was dependent on inertia and rapidly reduced to zero as the wall-separation distance increased, very similar to zero-slip particles.

- **The wall-bounded lift and drag force models were successfully validated against experimental results for buoyant particles.**

  Sedimenting particles in both quiescent and linear shear flows were examined using the new lift correlations and examined drag correlations. Particle slip and migration velocities, calculated using the proposed models, agreed reasonably well with the available experimental results.

Specific conclusions related to the dilute suspension (two-fluid model) study (Chapters 8-10 in Part III):

- **Particle-scale wall-bounded inertial lift and viscous drag force models were implemented within a two-fluid framework which accounts for shear-induced diffusion.**

  At lower volume fractions, the predictions of the existing shear-induced diffusion-based models do not capture the rate of migration and near-wall concentrations observed experimentally, although the same models produce reasonable predictions at larger volume fractions. Neglecting wall-bounded forces and inertial lift forces were identified as possible reasons for the discrepancies. In this present thesis, wall-bounded forces relevant for simple shear flows were implemented in Harvie [107]'s preliminary two-fluid framework. The average motion of particles at practically relevant intermediate inertial conditions was examined under dilute conditions.

- **A new solid phase velocity boundary condition, which recovers the single-particle analytical slip velocity, was introduced to the two-fluid framework.**

  Many two-fluid studies employ no-slip boundary conditions for the solid phase velocity, assuming that the particles are moving at the same velocity as the wall. Alternatively, some studies use a zero-stress boundary condition on the solid phase. However, our single-particle study showed that freely-rotating, force-free particles lag the fluid flow for a positive shear rate near a stationary wall, which is not predicted by either of the above boundary conditions. Instead, a new slip velocity boundary condition, which is a function of solid phase stress and fluid velocity, was introduced in this work. This new boundary condition was capable of recovering the analytical slip velocity under dilute conditions. Further, these slip velocities near walls were used when calculating particle-scale slip-based lift forces to quantify cross-stream particle migration. However, it is worth mentioning that only one boundary condition was extensively tested in the present thesis (e.g., the solid velocity at the wall), and therefore some uncertainties remain about other inlet and outlet boundary conditions for non-periodic flows.

- **The modified TFM, which includes particle-scale inertial forces, predicted particle distributions in qualitative agreement with experimental results in Couette flow for dilute suspensions.**

  The two-fluid model with particle-scale inertial forces was used to predict the transient particle distributions in linear and cylindrical Couette flows. The results agreed well qualitatively with the analytical and experimental results, predicting that the particles migrate to the centre of Couette flow.

- **The increased slip velocities limited particle accumulation in the Couette flow centre due to high collision viscosity predicted by the Berry et al. [23]'s preliminary model.**

  The solid phase slip velocities were significantly affected by a high collision viscosity employed in the preliminary two-fluid model, even under the examined dilute conditions. This resulted in sharp spikes in the solid phase slip velocity at various locations with the thin Couette gap. Due to this effect, increased slip-shear lift forces near particle clustering zones far away from walls were reported. Hence, particles were pushed towards the walls in simple shear flows by the slip-shear lift reducing the peak particle concentration. The study suggests that the preliminary model of Berry et al. [23], which is used to predict collision viscosity, requires modifications at the dilute limit to accurately capture multi-body effects.

- **No significant difference in the steady-state particle distribution was observed when the particle-scale wall-bounded forces are applied to the solid phase or both phases in the two-fluid model framework under dilute conditions.**

  Within the TFM framework, it is unclear whether the wall induced forces should act directly between the particles and walls or act on the walls via the fluid phase. This is a conceptually difficult multi-scale question to resolve, noting that generally, the wall induced particle-scale forces are not included in TFMs. Importantly, however, for this application, the particle distributions obtained by applying wall-bounded particle-scale only on the solid phase or on both phases were the same for dilute conditions.

  For more concentrated systems this modelling choice will require more analysis.

- **The unbounded shear gradient lift force model employed in the TFM was responsible for shifting the particle equilibrium position towards the inner cylinder of the Taylor-Couette flow device.**

  The experimentally observed shift of the particle's equilibrium location towards the inner rotating cylinder in Taylor-Coutte flow was predicted by the model when using a simplified form of Asmolov [11]'s unbounded shear gradient lift force. The simulation results were encouraging when considering the approximations used to model this force.

11.2 Future work

The migration of particles relevant in industrial or biological flows is a complex phenomenon that depends on various parameters such as size, rigidity, and shape that have not been systematically explored. Even for hard-spherical particles, fundamental studies concerning particle-wall and particle-particle interactions for a range of bulk concentrations in different shear flows require further investigations to model hard sphere suspension behaviour.

In the single-particle context, future work should examine:

- **How the wall-bounded shear-gradient lift force varies as a function of wall-separation distance.**

  The present study employs an unbounded shear-gradient lift force to capture the velocity curvature induced lift, together with a wall-bounded shear lift. However, similar to the shear lift, the shear-gradient lift could also be a function of the wall separation distance. The net lift force on a sphere moving near a single wall in a parabolic flow has been studied theoretically for extremely low particle Reynolds numbers [257] and numerically for finite particle Reynolds numbers in the parabolic flow bounded between two flat walls [12, 110]. However, many lift models derived for parabolic flows are geometric-specific and hence, only present the net lift force that combines the shear and shear-gradient effect. Hence, these models cannot be applied for arbitrary flow configurations where shear and shear gradients are not directly linked to wall separation distance. Thus, the development of more generalised shear-gradient lift models, applicable for any flow geometry, is desirable.

- **Effects of double walls and curved walls on the lift force acting on a particle translating with zero-slip velocity.**

  When developing the wall-bounded lift and drag models, the present thesis accounts for a particle translating near a single flat wall. Generally there is a lack of bounded flow lift correlations valid for the finite particle Reynolds numbers and wall spacing relevant to this study. Hence, quantifying the secondary wall effect on a particle translating with a zero-slip velocity in bounded flows is also desirable to examine via DNS. The developed correlations could then be applied in two-fluid models, thereby establishing the validity of using existing single wall-bounded lift models in more complex wall-bounded geometries.

In the dilute suspension and two-fluid framework context, future work should examine:

- **The use of mixture strain rates instead of solid phase strain rates to characterise lift, drag and hydrodynamic forces.**

  Harvie [107]'s preliminary two-fluid framework uses solid phase strain rates to calculate hydrodynamic forces under the dilute assumption. Following this, the newly implemented particle-scale forces also use solid-phase flow fields to calculate shear based lift and drag forces. However, significant differences between the solid and fluid phase velocity fields were observed near the walls and particle clustering regions. The mixture flow field information, such as mixture strain rates based on the mixture velocity, or fluid phase phase strain rates should be further tested to examine the effect of this choice on model performance.

- **Hindered settling effects on the lift force.**

  'Hindered settling' functions capture the increase in local particle strain rates from the fluid phase as the solid volume fraction increases. In the present study, theses functions are applied to the unbounded drag only, and not to any wall induced drag or lift forces. While hindered settling effects are not significant for the dilute concentrations considered in this study, more generally, the effect of particle concentration on particle migration velocities should also be tested more extensively to ascertain whether or not to include any function based on particle concentration for the studied particle-scale forces.

- **Experimental measurements of particle distributions for a series of dilute and semi-dilute suspensions for finite inertial conditions.**

  When particle sizes become larger, inertial effects become more significant, and the rheological constitutive laws need to be modified accordingly. Nevertheless, as shown in figure 2.6, the experiments in this field are confined to either concentrated - low particle Reynolds numbers, or dilute - intermediate particle Reynolds numbers. Hence, experimental measurements are not available that allow both inertia and diffusive forces to be explored together. Systematic experiments to measure particle roughness, rheology, and particle distribution in dilute and semi-dilute suspensions will provide valuable insight into developing constitutive models.

- **Migration of complex mixtures of particles and fluid**

  Collisions between different types of particles (deformable, non-spherical) and inertial lift forces of non-spherical, deformable particles remain relatively unexplored.

However, the shape and rigidity of a particle and the non-Newtonian behaviour of fluid play a substantial role in determining particle migration dynamics, especially for targeted applications such as cell migration in micro-vessels or microfluidics. Therefore more studies are needed to better understand the mechanisms controlling distributions in complex suspensions.

Appendix A

Clarification on Takemura's 2004 experimental results

In §7.3.2, slip and migration velocities of a negatively-buoyant particle in a quiescent fluid are studied by comparing the analytical predictions against Takemura [239]'s experimental results. For slip velocity analysis, data are extracted from figure 2 of the Takemura [239] study. In the original study, experimental results corresponding to three $Re_{\text{slip},\infty} \times 2 (= 0.18, 0.51, 1)$ numbers are reported together with analytical predictions. As a verification step, an attempt is made here to reproduce these plots using the same analytical correlations given in the Takemura [239] study. For this, the digitised analytical results presented in the original figure are compared against the analytical predictions of Takemura [239]'s by using Eq. 3.18 correlation for $C_{\text{D},2}$.

$$u_{\text{slip}} = -6\pi \frac{\nu}{a} \left(\frac{Re_{\text{slip},\infty}}{-C_{\text{D},2}} \right) \tag{A.1}$$

where,

$$C_{\text{D},2} = C_{\text{D},2}^{\text{ub}} + C_{\text{D},2}^{\text{wb}}$$

$$C_{\text{D},2}^{\text{ub}} = 6\pi$$

$$\frac{C_{\text{D},2}^{\text{wb}}}{6\pi} = \left[1 - \left(\frac{C_{\text{D},2}^{\text{wb,out}}}{6\pi} \frac{l}{a} \right) \left(\frac{a}{l} \right) + \frac{1}{8} \left(\frac{a}{l} \right)^3 - \frac{45}{256} \left(\frac{a}{l} \right)^4 - \frac{1}{16} \left(\frac{a}{l} \right)^5 \right]^{-1} - 1$$

In order to predict the analytical slip using Eq. A.1, both ν and $Re_{\text{slip},\infty}$ values are required. In the original study, experimental parameters which correspond to these $Re_{\text{slip},\infty}$ are not directly provided. Instead, the kinematic viscosity (ν) and density

(ρ_f) values of four different oils were reported with solid density (ρ_s) values for two different particles (say Type 1 and Type 2). However, the exact type of oil and particle combinations used for the experiment is also not stated. All possible oil and particle combinations are therefore analysed in table A.1 to workout which combinations give the closest reported three $Re_{\mathrm{slip},\infty}(= au_{\mathrm{slip},\infty}/\nu)$:

Particle	ρ_s ($\mathrm{kg\,m^{-3}}$)	ν ($\mathrm{mm\,s^{-2}}$)	ρ_f ($\mathrm{kg\,m^{-3}}$)	$Re_{\mathrm{slip},\infty}$ ($au_{\mathrm{slip},\infty}/\nu$)	$Re_{\mathrm{slip},\infty,\mathrm{tak}}$ ($2au_{\mathrm{slip},\infty}/\nu$)
Type 1	3200	10.5	931	3.084	6.168
		19.8	951	0.842	1.683
		28.6	954	0.402	0.803
		47.1	959	0.147	0.294
Type 2	2500	10.5	931	2.133	4.265
		19.8	**951**	**0.580**	**1.159**
		28.6	**954**	**0.276**	**0.553**
		47.1	**959**	**0.101**	**0.201**

TABLE A.1: Parameters related to negatively-buoyant particle in a quiescent fluid experimental study of Takemura [239].

Surprisingly, none of the combinations could produce the $Re_{\mathrm{slip},\infty}$ that were originally stated in the study. Hence, the highlighted combinations in table A.1, that closely matches the reported $Re_{\mathrm{slip},\infty,\mathrm{tak}}$ in Takemura [239] (i.e., 0.18, 0.51 and 1.0) are considered for the rest of the calculations. Therefore, by substituting $\nu = 19.8, 28.6$ and $0.202\,\mathrm{mm\,s^{-2}}$ for $Re_{\mathrm{slip},\infty,,\mathrm{tak}} = 0.18, 0.51$ and 1.0, u_slip values are obtained by Eq. A.1 for comparison. Figure A.1 shows the calculated slip velocity results and the digitised slip velocity results of Takemura [239]'s study. The use of $Re_{\mathrm{slip},\infty} \times 2 = 0.51$ and 1 together with $\nu = 28.6$ and $19.8\,\mathrm{mm\,s^{-2}}$ could reproduce the digitised plot behaviour reasonably well compared to $Re_{\mathrm{slip},\infty} \times 2 = 0.18$ together with ν and $47.1\,\mathrm{mm\,s^{-2}}$. The results for the lowest slip Reynolds number show a considerable deviation from the digitised results. Ideally, these pairs of curves should overlap, noting that the same analytical expressions given in Takemura [239] are used in the present study to calculate the slip velocity.

Discrepancies could occur due to either measurement errors or reporting errors. Instead of using the reported $Re_{\mathrm{slip},\infty}$, the actual $Re_{\mathrm{slip},\infty}$ that corresponds to fluid properties, as given in table A.1, are also used to calculate slip velocity. Figure A.2 shows the variation

Note that Takemura [239]'s definition for Reynolds number is $Re_{\mathrm{slip},\infty,,\mathrm{tak}} = 2au_{\mathrm{slip},\infty}/\nu$

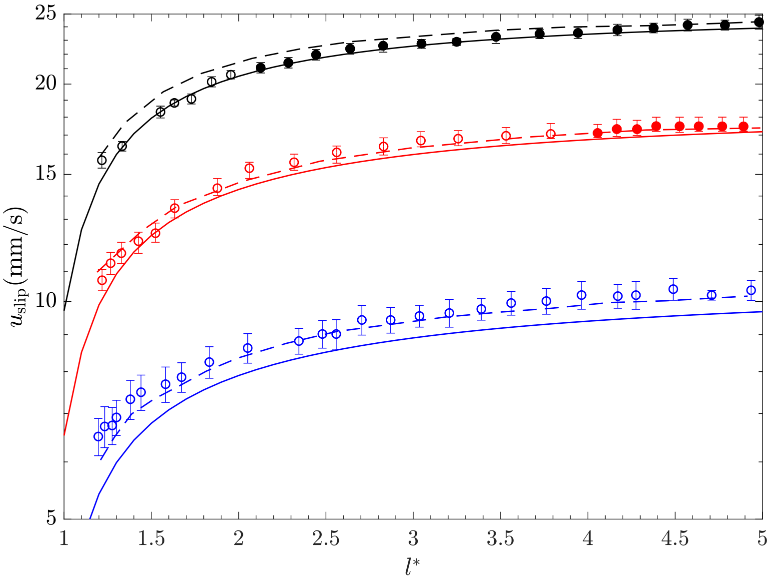

FIGURE A.1: Slip velocity calculated using Eq. A.1 in present study (solid) and in Takemura [239]'s study (dashed line). Takemura [239]'s study results are obtained by digitising the figure 2 in the original work. The combinations used here are $Re_{\text{slip},\infty} \times 2 = 0.18$ and $\nu = 47.1\,\text{mm}\,\text{s}^{-2}$ (○), $Re_{\text{slip},\infty} \times 2 = 0.51$ and $\nu = 28.6\,\text{mm}\,\text{s}^{-2}$ (○), $Re_{\text{slip},\infty} \times 2 = 0.1$ and $\nu = 19.8\,\text{mm}\,\text{s}^{-2}$ (○)

in slip velocities when real $Re_{\text{slip},\infty}$ is used instead of reported $Re_{\text{slip},\infty}$. These results are compared with the same digitised data.

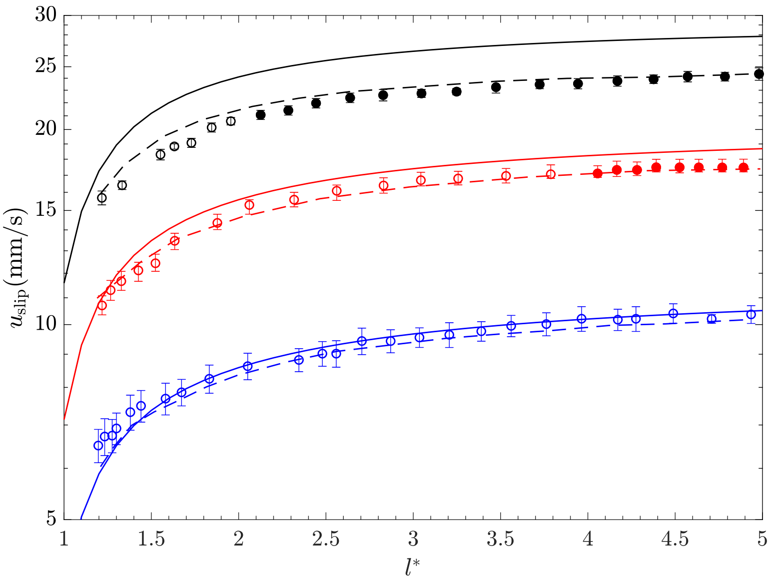

FIGURE A.2: Slip velocity calculated using Eq. A.1 in present study (solid) and in Takemura [239]'s study (dashed line). Takemura [239]'s study results are obtained by digitising the figure 2 in the original work. The combinations used here are $Re_{\text{slip},\infty} \times 2 = 0.201$ and $\nu = 47.1\,\text{mm}\,\text{s}^{-2}$ (○), $Re_{\text{slip},\infty} \times 2 = 0.553$ and $\nu = 28.6\,\text{mm}\,\text{s}^{-2}$ (○), $Re_{\text{slip}} \times 2 = 1.159$ and $\nu = 19.8\,\text{mm}\,\text{s}^{-2}$ (○)

Interestingly, figure A.2 shows that using real $Re_{\text{slip},\infty}$ based on fluid parameters agrees well with the digitised data for the lowest $Re_{\mathrm{slip},\infty}$ used. However, no good correspondence is visible for the other two Reynolds numbers.

Therefore, assuming there is a reporting error in the lowest Reynolds number, $Re_{\mathrm{slip},\infty} \times 2 = 0.201$ is used instead of $Re_{\mathrm{slip},\infty} \times 2 = 0.18$ in present study.

Appendix B

Summary - Lift and Drag Models

Summary sheet of the recommended equations for lift and drag forces for a freely-rotating particle based on the analysis in this study.

B.1 Lift force

$$F_{\mathrm{L}}^{*} = C_{\mathrm{L},1} Re_{\gamma}^{2} + \mathrm{sgn}(\gamma^{*}) C_{\mathrm{L},2} Re_{\mathrm{slip}} Re_{\gamma} + C_{\mathrm{L},3} Re_{\mathrm{slip}}^{2} \tag{5.1}$$

$$F_{\mathrm{L}}^{*} = F_{\mathrm{L}} \rho / \mu^{2}$$

$$\gamma^{*} = \gamma a / u_{\mathrm{slip}}$$

$$Re_{\mathrm{slip}} = |a \rho u_{\mathrm{slip}} / \mu|$$

$$Re_{\gamma} = |\gamma a^{2} \rho / \mu|$$

$$\epsilon = \sqrt{Re_{\gamma}} / Re_{\mathrm{slip}}$$

$$C_{\mathrm{L},1} = f_1(Re_\gamma)C_{\mathrm{L},1}^{\mathrm{wb,out}}(l^*/L_{\mathrm{G}}{}^*) + f_2(Re_\gamma)C_{\mathrm{L},1}^{\mathrm{wb,in}'}(1/l^*) \tag{6.1}$$

$$f_1(Re_\gamma) = 0.9250\exp\left(-0.3500Re_\gamma\right) - 0.0135\exp\left(-7000Re_\gamma\right) \tag{6.2}$$

$$C_{\mathrm{L},1}^{\mathrm{wb,out}}(l^*/L_{\mathrm{G}}^*) = 1.982\exp\left[-0.1150\left(l^*/L_{\mathrm{G}}^*\right)^2 - 0.2771\left(l^*/L_{\mathrm{G}}^*\right)\right] \tag{6.3}$$

$$f_2(Re_\gamma) = 1 + \sqrt{Re_\gamma} \tag{6.4}$$

$$C_{\mathrm{L},1}^{\mathrm{wb,in}'}(1/l^*) = 1.0575(1/l^*) - 2.4007(1/l^*)^2 - 1.9610(1/l^*)^3\dagger \tag{6.5}$$

$$C_{\mathrm{L},3} = C_{\mathrm{L},3}^{\mathrm{wb,out}}(l^*/L_{\mathrm{S}}{}^*) + C_{\mathrm{L},3}^{\mathrm{wb,in}'}(1/l^*) \tag{7.2b}$$

$$C_{\mathrm{L},3}^{\mathrm{wb,out}} = 6\pi\left[3/\left(32 + 2\left(l/L_{\mathrm{S}}\right) + 3.8(l/L_{\mathrm{S}})^2 + 0.049(l/L_{\mathrm{S}})^3\right)\right] \tag{3.37}$$

$$C_{\mathrm{L},3}^{\mathrm{wb,in}'} = 0.4757(1/l^*) - 1.268(1/l^*)^2 + 0.7427(1/l^*)^{3\dagger} \tag{7.1b}$$

$$C_{\mathrm{L},2} = -C_{\mathrm{L},2}^{\mathrm{wb,out}}\frac{1}{|\gamma^*|} + C_{\mathrm{L},2}^{\mathrm{wb,in}'}(1/l^*) \tag{7.3b}$$

$$C_{\mathrm{L},2}^{\mathrm{wb,out}} = f(\epsilon, l/L_{\mathrm{G}})C_{\mathrm{L},2}^{\mathrm{ub}} \tag{3.40}$$

$$C_{\mathrm{L},2}^{\mathrm{ub}} = \frac{9}{\pi}\epsilon J(\epsilon) \tag{3.29}$$

$$f(\epsilon, l/L_{\mathrm{G}}) = 1 - \exp\left[-\frac{11}{96}\pi^2(l/L_{\mathrm{G}})/J(\epsilon)\right] \tag{3.43}$$

$$J(\epsilon) = 2.255(1 + 0.20\epsilon^{-2})^{-3/2} \tag{3.32}$$

$$C_{\mathrm{L},2}^{\mathrm{wb,in}'} = -2.6729 - 0.8373(1/l^*) + 0.4683(1/l^*)^{2\dagger} \tag{3.58}$$

---

† Corresponding to referred equation, but without the highest order term of with respect to $(1/l^*)$

B.2 Drag force

$$F_{\mathrm{D}}^{*} = -\mathrm{sgn}(\gamma) C_{\mathrm{D},1} Re_{\gamma} - \mathrm{sgn}(u_{\mathrm{slip}}) C_{\mathrm{D},2} Re_{\mathrm{slip}} \tag{5.2}$$

$$C_{\mathrm{D},2} = C_{\mathrm{D},2}^{\mathrm{ub}} + C_{\mathrm{D},2}^{\mathrm{wb,in}} \tag{3.18}$$

$$C_{\mathrm{D},2}^{\mathrm{ub}} = 6\pi \tag{3.13}$$

$$\begin{aligned} C_{\mathrm{D},2}^{\mathrm{wb,in}} = 6\pi \Big(\Big[& 1 - 9/16(1/l^{*}) + 1/8(1/l^{*})^{3} - 45/256(1/l^{*})^{4} \\ & -1/16(1/l^{*})^{5} \Big]^{-1} - 1 \Big) \end{aligned} \tag{3.19}$$

$$\begin{aligned} C_{\mathrm{D},1} = (15\pi/8)(1/l^{*})^{2} \Big[& 1 + 9/16(1/l^{*}) + 0.5801(1/l^{*})^{2} - 3.34(1/l^{*})^{3} \\ & +4.15(1/l^{*})^{4} \Big] + (3.001 Re_{\gamma}^{2} - 1.025 Re_{\gamma}) \end{aligned} \tag{6.7}$$

Appendix C

Viscosity correlations proposed in Berry et al. 2021 for TFM

Closure expression for non-dimensional mixture viscosity:

$$\hat{\mu}_{\mathrm{m}} = \frac{\mu_{\mathrm{m}}}{\mu_{\mathrm{f}}} = 1 + 2.5\phi_{\mathrm{s}} + \hat{\mu}_{\mathrm{col,s}}\phi_{\mathrm{s}}^2$$

Closure expression for non-dimensional collision viscosity:

$$\hat{\mu}_{\mathrm{col,s}} = \hat{B}_1(\hat{r}_\infty) + \hat{B}_2(\hat{r}_\infty) + f_2[\hat{B}_1(\hat{r}_{\mathrm{sid}}) + \hat{B}_2(\hat{r}_{\mathrm{sid}})]$$

where,

$$\hat{B}_1(\hat{r}_\infty) = \hat{B}_{1,\hat{r}_\infty,b} \times (\hat{r}_\infty - 2) + \hat{B}_{1,\hat{r}_\infty,c} \times (\hat{r}_\infty - 2)^2 + \hat{B}_{1,\hat{r}_\infty,d} \times (\hat{r}_\infty - 2).^{\hat{B}_{1,\hat{r}_\infty,n}}$$

$$\hat{B}_2(\hat{r}_\infty) = 0.5\hat{B}_{2,\hat{r}_\infty,a} \times (\hat{r}_\infty - 2)^{\hat{B}_{2,\hat{r}_\infty,n}}$$

$$\hat{B}_1(\hat{r}_{\mathrm{sid}}) = \hat{B}_{\hat{r}_{\mathrm{sid1}},b} \times (\hat{r}_{\mathrm{sid}} - 2) + \hat{B}_{\hat{r}_{\mathrm{sid1}},c} \times (\hat{r}_{\mathrm{sid}} - 2)^2 + \hat{B}_{\hat{r}_{\mathrm{sid1}},d} \times (\hat{r}_{\mathrm{sid}} - 2)^{\hat{B}_{\hat{r}_{\mathrm{sid1}},n}}$$

$$\hat{B}_2(\hat{r}_{\mathrm{sid}}) = 0.5\hat{B}_{\hat{r}_{\mathrm{sid2}},a} \times (\hat{r}_{\mathrm{sid}} - 2)^{\hat{B}_{\hat{r}_{\mathrm{sid2}},n}}$$

and

$$\hat{r}_{\infty}(\phi_{\mathrm{s}}) = \hat{r}_{\mathrm{col},1}(\phi_{\mathrm{s}}) + \hat{r}_{\mathrm{col},2}(\phi_{\mathrm{s}}) + 2$$
$$\hat{r}_{\mathrm{sid}} = \min(\hat{r}_{\mathrm{sid},3}(\phi_{\mathrm{s}}) + 2\hat{\varepsilon}, \hat{r}_{\infty} - 2) + 2$$
$$\hat{r}_{\mathrm{col},1}(\phi_{\mathrm{s}}) = \hat{r}_{\infty,\mathrm{c1}}\left(\frac{1}{\max(\phi, \phi_{\mathrm{tol}})}\right)^{\hat{r}_{\infty,\mathrm{n1}}}$$
$$\hat{r}_{\mathrm{col},2}(\phi_{\mathrm{s}}) = \hat{r}_{\infty,\mathrm{c2}}\left(\frac{1}{\max(\phi_{\max} - \phi, \phi_{\mathrm{tol}})}\right)^{\hat{r}_{\infty,\mathrm{n2}}} - \left(\frac{1}{\phi_{\max}}\right)^{\hat{r}_{\infty,\mathrm{n2}}}$$
$$\hat{r}_{\mathrm{sid},3}(\phi_{\mathrm{s}}) = \hat{r}_{\mathrm{col},2}\hat{r}_{\infty,\mathrm{c3}}\left(\frac{\phi}{\phi_{\max}}\right)^{\hat{r}_{\infty,\mathrm{n3}}}$$

$$f_1 = \frac{f_{\mathrm{c}} - f_{\mathrm{e}}}{2g}$$
$$f_2 = -f_1 g + f_{\mathrm{c}} - 1$$

Closure expressions for non-dimensional shear induced diffusion viscosities:

$$\hat{\mu}_{\mathrm{sid},1} = 2f_1\left[\frac{2}{7}\hat{B}_1(\hat{r}_{\mathrm{sid}}) + \frac{1}{5}\hat{B}_2(\hat{r}_{\mathrm{sid}})\right]$$
$$\hat{\mu}_{\mathrm{sid},2} = 2f_1\frac{1}{7}\hat{B}_1(\hat{r}_{\mathrm{sid}})$$

and

$$\hat{\mu}_{\mathrm{sid}} = \hat{\mu}_{\mathrm{sid},1} + \hat{\mu}_{\mathrm{sid},2}$$

Parameters used in present work:

$$\phi_{\mathrm{tol}} = 10^{-9}$$
$$\phi_{\mathrm{max}} = 0.58$$

$$\hat{B}_{1,\hat{r}_\infty,b} = 2.3456652$$
$$\hat{B}_{1,\hat{r}_\infty,c} = 1.2265859$$
$$\hat{B}_{1,\hat{r}_\infty,d} = 3.8539574$$
$$\hat{B}_{1,\hat{r}_\infty,n} = 0.37$$

$$\hat{B}_{2,\hat{r}_\infty,a} = 14.419448$$
$$\hat{B}_{2,\hat{r}_\infty,n} = 0.3560000$$
$$\hat{B}_{\hat{r}_{\mathrm{sid1}},b} = 2.3456652$$
$$\hat{B}_{\hat{r}_{\mathrm{sid1}},c} = 1.2265859$$
$$\hat{B}_{\hat{r}_{\mathrm{sid1}},d} = 3.8539574$$
$$\hat{B}_{\hat{r}_{\mathrm{sid1}},n} = 0.37$$
$$\hat{B}_{\hat{r}_{\mathrm{sid2}},a} = 14.419448$$
$$\hat{B}_{\hat{r}_{\mathrm{sid2}},n} = 0.35600000$$

$$\hat{r}_{\infty,\mathrm{c1}} = 0.53$$
$$\hat{r}_{\infty,\mathrm{c2}} = 2.2$$
$$\hat{r}_{\infty,\mathrm{c3}} = 1$$
$$\hat{r}_{\infty,\mathrm{n1}} = 0.33333334$$
$$\hat{r}_{\infty,\mathrm{n2}} = 0.72500000$$
$$\hat{r}_{\infty,\mathrm{n3}} = 2.5$$

$$g = 4/(3\pi)$$
$$f_{\mathrm{c}} = 1 + 1/3.6$$
$$f_{\mathrm{e}} = -1/3.6$$
$$\hat{\epsilon} = 11 \times 10^{-6}$$

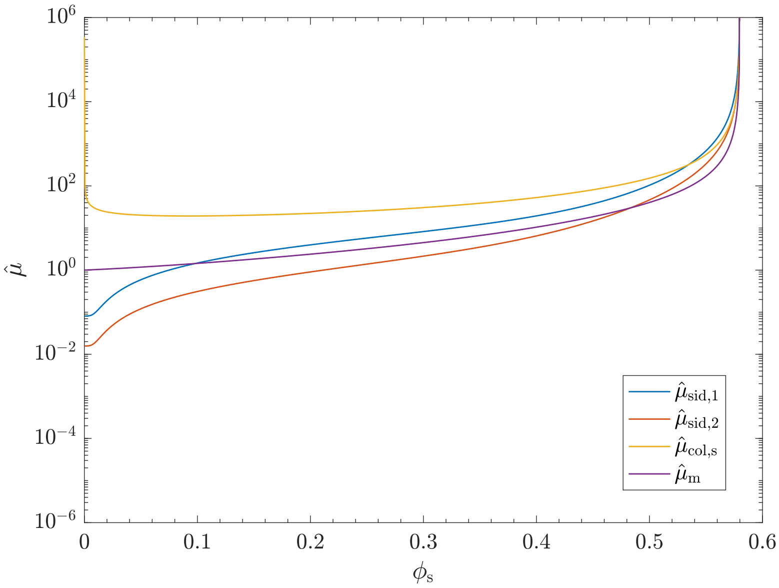

FIGURE C.1: Magnitudes of the viscosity coefficients proposed by Berry et al. [23].

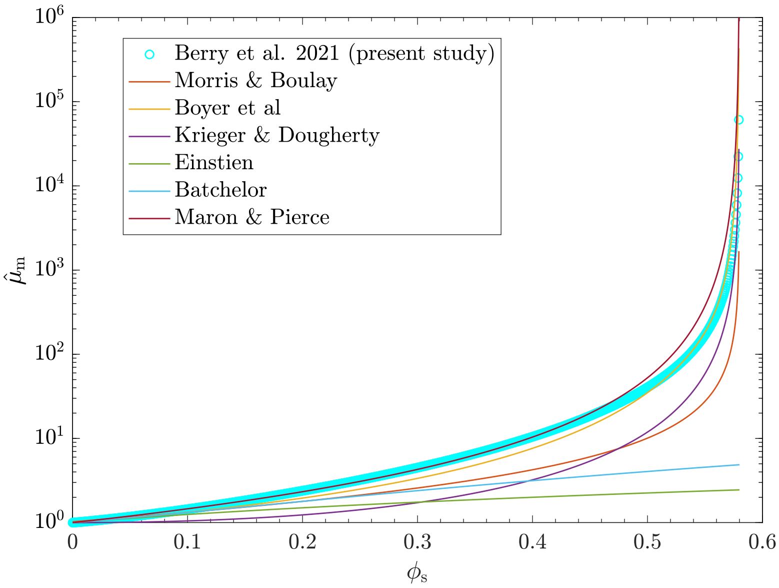

FIGURE C.2: Non-dimensional mixture viscosity

Appendix D

Taylor-Couette Flow Field

Analytical expressions for the velocities, shear-rates and shear rate gradients related to Taylor-Couette flow is presented using a cylindrical coordinate system.

D.1 Velocity

The velocity vector in cylindrical coordinate,

$$\mathbf{u} = u_{\mathrm{r}}\mathbf{e}_{\mathrm{r}} + u_{\theta}\mathbf{e}_{\theta} + u_{\mathrm{z}}\mathbf{e}_{\mathrm{z}} \tag{D.1}$$

Here,

$$u_{\mathrm{r}} = 0; \tag{D.2}$$

$$u_{\theta} = A_1 r + A_2 \frac{1}{r} \tag{D.3}$$

$$u_{\mathrm{z}} = 0; \tag{D.4}$$

where $A_1 = \omega \frac{-\eta^2}{1-\eta^2}$; and $A_2 = \omega r_{\mathrm{in}}^2 \frac{1}{1-\eta^2}$.

D.2 Gradient of velocity

∇ operator on $\mathbf{u}$ in cylindrical coordinates,

$$\boldsymbol{\nabla}\mathbf{u} = \begin{bmatrix} [\boldsymbol{\nabla}\mathbf{u}]_{\mathrm{rr}} & [\boldsymbol{\nabla}\mathbf{u}]_{\mathrm{r}\theta} & [\boldsymbol{\nabla}\mathbf{u}]_{\mathrm{rz}} \\ [\boldsymbol{\nabla}\mathbf{u}]_{\theta\mathrm{r}} & [\boldsymbol{\nabla}\mathbf{u}]_{\theta\theta} & [\boldsymbol{\nabla}\mathbf{u}]_{\theta\mathrm{z}} \\ [\boldsymbol{\nabla}\mathbf{u}]_{\mathrm{zr}} & [\boldsymbol{\nabla}\mathbf{u}]_{\mathrm{z}\theta} & [\boldsymbol{\nabla}\mathbf{u}]_{\mathrm{zz}} \end{bmatrix} \tag{D.5}$$

$$= \begin{bmatrix} \dfrac{\partial u_{\mathrm{r}}}{\partial r} & \dfrac{\partial u_\theta}{\partial r} & \dfrac{\partial u_{\mathrm{z}}}{\partial r} \\ \dfrac{1}{r}\dfrac{\partial u_{\mathrm{r}}}{\partial \theta} - \dfrac{u_\theta}{r} & \dfrac{1}{r}\dfrac{\partial u_\theta}{\partial \theta} + \dfrac{u_{\mathrm{r}}}{r} & \dfrac{1}{r}\dfrac{\partial u_{\mathrm{z}}}{\partial \theta} \\ \dfrac{\partial u_{\mathrm{r}}}{\partial z} & \dfrac{\partial u_\theta}{\partial z} & \dfrac{\partial u_{\mathrm{z}}}{\partial z} \end{bmatrix} \tag{D.6}$$

When $u_{\mathrm{r}} = 0$, $u_\theta = f(r)$, and $u_{\mathrm{z}} = 0$, Eq. (D.6) reduces to,

$$= \begin{bmatrix} 0 & \dfrac{\partial u_\theta}{\partial r} & 0 \\ -\dfrac{u_\theta}{r} & 0 & 0 \\ 0 & 0 & 0 \end{bmatrix} \tag{D.7}$$

D.3 Deformation tensor

Strain rate defined using velocity gradients Eq. (D.7),

$$\boldsymbol{\gamma} = \boldsymbol{\nabla}\mathbf{u} + \boldsymbol{\nabla}\mathbf{u}^{\mathrm{T}} \tag{D.8}$$

$$= \begin{bmatrix} 0 & \dfrac{\partial u_\theta}{\partial r} - \dfrac{u_\theta}{r} & 0 \\ \dfrac{\partial u_\theta}{\partial r} - \dfrac{u_\theta}{r} & 0 & 0 \\ 0 & 0 & 0 \end{bmatrix}$$

Strain rate magnitude is obtained as,

$$\gamma = \sqrt{\frac{1}{2}\boldsymbol{\gamma} : \boldsymbol{\gamma}} \tag{D.9}$$

$$= \left| \frac{\partial u_\theta}{\partial r} - \frac{u_\theta}{r} \right| \tag{D.10}$$

By substituting Eq. (D.3) to u_θ Eq. (D.10) reduced to,

$$\begin{aligned} &= \left|\left(A_1 - A_2\frac{1}{r^2}\right) - \left(A_1 + A_2\frac{1}{r^2}\right)\right| \\ &= \left|-2A_2\frac{1}{r^2}\right| \\ &= 2A_2\frac{1}{r^2} \end{aligned} \tag{D.11}$$

D.4 Gradient of a shear-rate

The gradient of shear rate magnitude, γ, is obtained using Eq. (D.10) as,

$$\boldsymbol{\nabla}\gamma = \begin{bmatrix} [\boldsymbol{\nabla}\gamma]_{\mathrm{r}} \\ [\boldsymbol{\nabla}\gamma]_{\theta} \\ [\boldsymbol{\nabla}\gamma]_{\mathrm{z}} \end{bmatrix} \tag{D.12}$$

$$= \begin{bmatrix} \dfrac{\partial\gamma}{\partial r} \\ \dfrac{1}{r}\dfrac{\partial\gamma}{\partial\theta} \\ \dfrac{\partial\gamma}{\partial z} \end{bmatrix} \tag{D.13}$$

Since $\gamma = f(r)$, Eq. (D.13) reduces to,

$$= \begin{bmatrix} \dfrac{\partial\gamma}{\partial r} \\ 0 \\ 0 \end{bmatrix} \tag{D.14}$$

Magnitude of $\boldsymbol{\nabla}\gamma$, is obtained by using,

$$\gamma' = \sqrt{\boldsymbol{\nabla}\gamma \cdot \boldsymbol{\nabla}\gamma} \tag{D.15}$$

$$\begin{aligned} &= \left|\frac{\partial\gamma}{\partial r}\right| \\ &= \left|\frac{\partial(-2A_2\frac{1}{r^2})}{\partial r}\right| \\ &= \left|4A_2\frac{1}{r^3}\right| \\ &= 4A_2\frac{1}{r^3} \end{aligned} \tag{D.16}$$

D.5 σ parameter

σ parameter is used to determine the shear-gradient lift coefficient using figure 8.4. The definition for σ is provided in Asmolov [11] as,

$$\sigma = 2\gamma' \nu^{1/2} \gamma^{-3/2}$$

By substituting Eqs. D.11 and D.16 to the previous expression,

$$= 2.828 {A_2}^{-1/2} \nu^{1/2} \tag{D.17}$$

D.6 Laplacian of a velocity vector

∇^2 operator in $\mathbf{u}$ in cylindrical coordinates,

$$\nabla^2 \mathbf{u} = \begin{bmatrix} [\nabla^2 \mathbf{u}]_{\mathrm{r}} \\ [\nabla^2 \mathbf{u}]_{\theta} \\ [\nabla^2 \mathbf{u}]_{\mathrm{z}} \end{bmatrix} \tag{D.18}$$

$$= \begin{bmatrix} \dfrac{\partial}{\partial r}\left(\dfrac{1}{r}\dfrac{\partial}{\partial r}(r u_{\mathrm{r}})\right) + \dfrac{1}{r^2}\dfrac{\partial^2 u_{\mathrm{r}}}{\partial \theta^2} + \dfrac{\partial^2 u_{\mathrm{r}}}{\partial \mathrm{z}^2} - \dfrac{2}{r^2}\dfrac{\partial u_\theta}{\partial \theta} \\ \dfrac{\partial}{\partial r}\left(\dfrac{1}{r}\dfrac{\partial}{\partial r}(r u_{\theta})\right) + \dfrac{1}{r^2}\dfrac{\partial^2 u_{\theta}}{\partial \theta^2} + \dfrac{\partial^2 u_{\theta}}{\partial \mathrm{z}^2} + \dfrac{2}{r^2}\dfrac{\partial u_{\mathrm{r}}}{\partial \theta} \\ \dfrac{1}{r}\dfrac{\partial}{\partial r}\left(r\dfrac{\partial (r u_{\mathrm{z}})}{\partial r}\right) + \dfrac{1}{r^2}\dfrac{\partial^2 u_{\mathrm{z}}}{\partial \theta^2} + \dfrac{\partial^2 u_{\mathrm{z}}}{\partial \mathrm{z}^2} \end{bmatrix} \tag{D.19}$$

When $u_{\mathrm{r}} = 0$, $u_\theta = f(r)$, and $u_{\mathrm{z}} = 0$, Eq. (D.19) reduces to,

$$= \begin{bmatrix} 0 \\ \dfrac{\partial}{\partial r}\left(\dfrac{1}{r}\dfrac{\partial}{\partial r}(r u_{\theta})\right) \\ 0 \end{bmatrix} \tag{D.20}$$

$$= \begin{bmatrix} 0 \\ \dfrac{\partial^2 u_\theta}{\partial r^2} + \dfrac{1}{r}\dfrac{\partial u_\theta}{\partial r} - \dfrac{u_\theta}{r^2} \\ 0 \end{bmatrix} \tag{D.21}$$

Substituting the values for the θ in the matrix using the following values $\dfrac{u_\theta}{r^2} = A_1/r + A_2/r^3; \dfrac{\partial u_\theta}{\partial r} = A_1 - A_2/r^2; \dfrac{\partial^2 u_\theta}{\partial r^2} = 2A_2/r^3$,

$$= \begin{bmatrix} 0 \\ 0 \\ 0 \end{bmatrix} \tag{D.22}$$

Therefore the Laplacian magnitude is obtained by using,

$$\mathrm{mag}(\boldsymbol{\nabla}^2\mathbf{u}) = \sqrt{\boldsymbol{\nabla}^2\mathbf{u} \cdot \boldsymbol{\nabla}^2\mathbf{u}} \tag{D.23}$$

$$= 0 \tag{D.24}$$

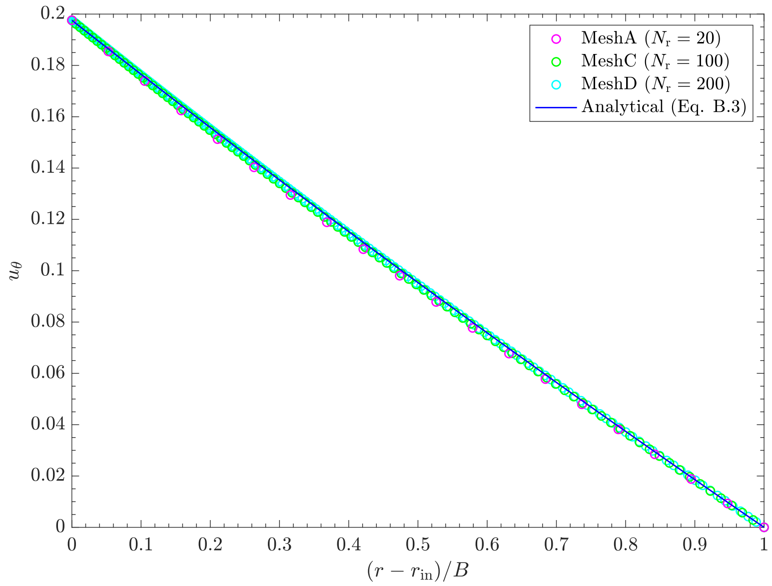

FIGURE D.1: Azimuthal velocity variation in radial direction in Taylor-Coutte flow.

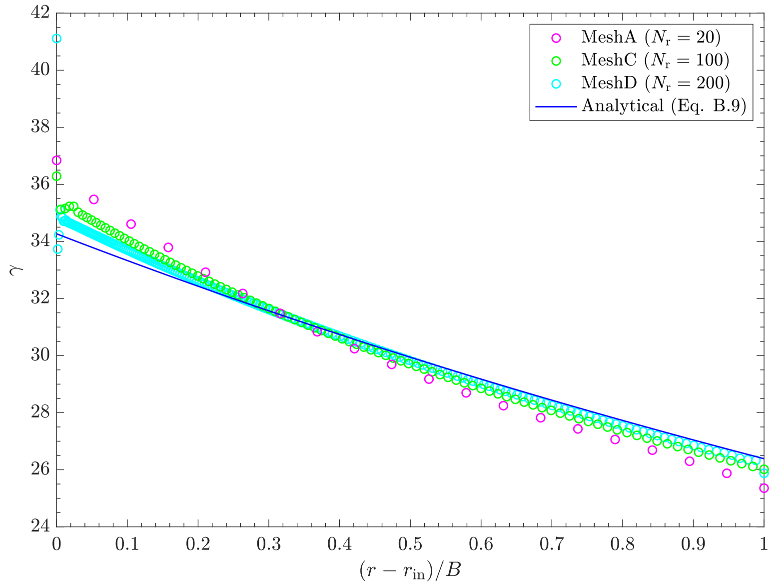

FIGURE D.2: Shear rate variation in radial direction in Taylor-Coutte flow.

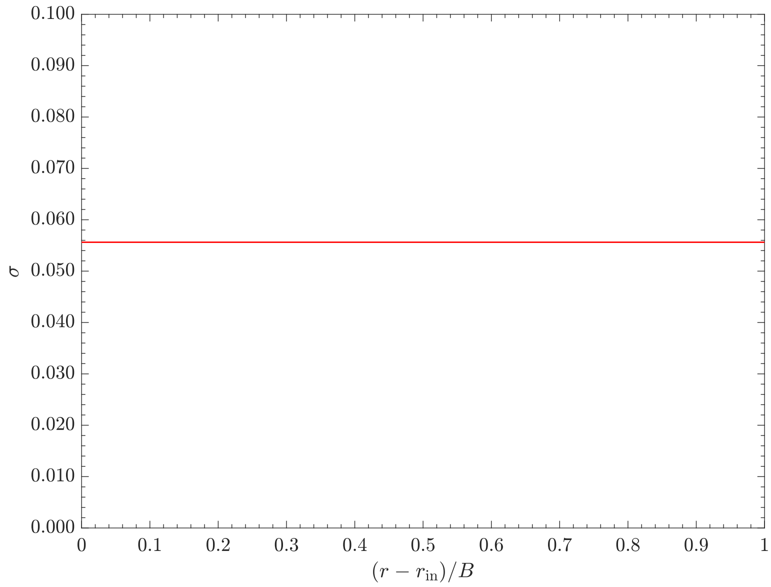

FIGURE D.3: σ parameter variation in radial direction in Taylor-Coutte flow.

D.7 Source code - Image J

```
open("C:/Users/Desktop/plot/1a.png");
run("8-bit");
setAutoThreshold("Default");
run("Threshold...");
setThreshold(0, 32);
setOption("BlackBackground", true);
```

```
run("Convert to Mask");
run("Surface Plot...", "polygon=100 shade draw axis smooth");
selectWindow("1a.png");
run("Select All");
run("Plot Profile");
selectWindow("Plot of 1a");
saveAs("PNG", "C:/Users/Desktop/plot/1b.png");
selectWindow("Surface Plot");
saveAs("PNG", "C:/Users/Desktop/plot/1c.png");
selectWindow("1a.png");
saveAs("PNG", "C:/Users/Desktop/plot/1d.png");
```

Bibliography

[1] M. Abbas, P. Magaud, Y. Gao, and S. Geoffroy. Migration of finite sized particles in a laminar square channel flow from low to high Reynolds numbers. *Physics of Fluids*, 26(12):123301, 2014.

[2] J. R. Abbott, N. Tetlow, A. L. Graham, S. A. Altobelli, E. Fukushima, L. A. Mondy, and T. S. Stephens. Experimental observations of particle migration in concentrated suspensions: Couette flow. *Journal of Rheology*, 35(5):773–795, 1991.

[3] A. Acrivos, R. Mauri, and X. Fan. Shear-induced resuspension in a Couette device. *International Journal of Multiphase Flow*, 19(5):797–802, 1993.

[4] F. W. Altena and G. Belfort. Lateral migration of spherical particles in porous flow channels: application to membrane filtration. *Chemical Engineering Science*, 39(2):343–355, 1984.

[5] S. A. Altobelli, R. C. Givler, and E. Fukushima. Velocity and concentration measurements of suspensions by nuclear magnetic resonance imaging. *Journal of Rheology*, 35(5):721–734, 1991.

[6] A. Ambari, M. B. Gauthier, and E. A. Guyon. Wall effects on a sphere translating at constant velocity. *Journal of Fluid Mechanics*, 149(1):235–253, 1984.

[7] H. Aoki, Y. Kurosaki, and H. Anzai. Study on the tubular pinch effect in a pipe flow : 1^{st} Report, motion of a single particle. *Transactions of the Japan Society of Mechanical Engineers*, 44(382):2026–2033, 1978.

[8] P. A. Arp and S. G. Mason. The kinetics of flowing dispersions: IX. Doublets of rigid spheres (experimental). *Journal of Colloid and Interface Science*, 61(1): 44–61, 1977.

[9] E. S. Asmolov. Lift force exerted on a spherical particle in a laminar boundary layer. *Fluid Dynamics*, 24(5):710–714, 1989.

[10] E. S. Asmolov. Dynamics of a spherical particle in a laminar boundary layer. *Fluid Dynamics*, 25(6):886–890, 1990.

[11] E. S. Asmolov. The inertial lift on a spherical particle in a plane Poiseuille flow at large channel Reynolds number. *Journal of Fluid Mechanics*, 381:63–87, 1999.

[12] E. S. Asmolov, A. L. Dubov, T. V. Nizkaya, J. Harting, and O. I. Vinogradova. Inertial focusing of finite-size particles in microchannels. *Journal of Fluid Mechanics*, 840:613–630, 2018.

[13] T. R. Auton. The lift force on a spherical body in a rotational flow. *Journal of Fluid Mechanics*, 183:199–218, 1987.

[14] P. Bagchi and S. Balachandar. Effect of free rotation on the motion of a solid sphere in linear shear flow at moderate Re. *Physics of Fluids*, 14(8):2719–2737, 2002.

[15] E. Barnea and J. Mizrahi. A generalized approach to the fluid dynamics of particulate systems: Part 1. General correlation for fluidization and sedimentation in solid multiparticle systems. *The Chemical Engineering Journal*, 5(2):171–189, 1973.

[16] W. Bartok and S. G. Mason. Particle motions in sheared suspensions: V. Rigid rods and collision doublets of spheres. *Journal of Colloid Science*, 12(3):243–262, 1957.

[17] G. K. Batchelor. *An Introduction to Fluid Dynamics*. Cambridge University Press, Cambridge, 1967.

[18] G. K. Batchelor. The stress system in a suspension of force-free particles. *Journal of Fluid Mechanics*, 41(3):545–570, 1970.

[19] G. K. Batchelor. The effect of brownian motion on the bulk stress in a suspension of spherical particles. *Journal of Fluid Mechanics*, 83(1):801, 2008.

[20] G. K. Batchelor and J. T. Green. The hydrodynamic interaction of two small freely-moving spheres in a linear flow field. *Journal of Fluid Mechanics*, 56(2):375–400, 1972.

[21] G. K. Batchelor and J. T. Green. The determination of the bulk stress in a suspension of spherical particles to order c^2. *Journal of Fluid Mechanics*, 56(3):401–427, 1972.

[22] L. E. Becker, G. H. McKinley, and H. A. Stone. Sedimentation of a sphere near a plane wall: weak non-newtonian and inertial effects. *Journal of Non-Newtonian Fluid Mechanics*, 63(2):201–233, 1996.

[23] J. D. Berry, N. I. K. Ekanayake, Nouri M., and D. J. E. Harvie. Multifluid modelling of suspension flows. *In preparation*, 2020.

[24] A. A. S. Bhagat, S. S. Kuntaegowdanahalli, and I. Papautsky. Enhanced particle filtration in straight microchannels using shear-modulated inertial migration. *Physics of Fluids*, 20(10):101702, 2008.

[25] P. M. Biesheuvel, Henk V., and Victor B. Microdivers to study sedimentation in polydisperse, concentrated colloidal suspensions. *AIChE Journal*, 47(9):1969, 2001.

[26] R. B. Bird, W. E. Stewart, and E. N. Lightfoot. *Transport Phenomena.* John Wiley & Sons, Inc., second edition edition, 2002.

[27] G. Bossis and J. F. Brady. Self-diffusion of Brownian particles in concentrated suspensions under shear. *The Journal of Chemical Physics*, 87(9):5437–5448, 1987.

[28] F. Boyer, É. Guazzelli, and O. Pouliquen. Unifying suspension and granular rheology. *Physical Review Letters*, 107(18):188301, 2011.

[29] J. F. Brady and G. Bossis. Stokesian dynamics. *Annual Review of Fluid Mechanics*, 20(1):111–157, 1988.

[30] J. F. Brady and J. F. Morris. Microstructure of strongly sheared suspensions and its impact on rheology and diffusion. *Journal of Fluid Mechanics*, 348:103–139, 1997.

[31] G. Brans, C. G. P. H. Schroën, R. G. M. van der Sman, and R. M. Boom. Membrane fractionation of milk: state of the art and challenges. *Journal of Membrane Science*, 243(1):263–272, 2004.

[32] V. Breedveld, D. Van Den Ende, A. Tripathi, and A. Acrivos. The measurement of the shear-induced particle and fluid tracer diffusivities in concentrated suspensions by a novel method. *Journal of Fluid Mechanics*, 375:297–318, 1998.

[33] F. P. Bretherton. The motion of rigid particles in a shear flow at low Reynolds number. *Journal of Fluid Mechanics*, 14(2):284–304, 1962.

[34] H. C. Brinkman. A calculation of the viscous force exerted by a flowing fluid on a dense swarm of particles. *Flow, Turbulence and Combustion*, 1(1):27, 1949.

[35] T. A. Brzinski. Observation of two branches in the hindered settling function at low Reynolds number. *Physical Review Fluids*, 3(12), 2018.

[36] J. E. Butler and R. T. Bonnecaze. Imaging of particle shear migration with electrical impedance tomography. *Physics of Fluids*, 11(8):1982–1994, 1999.

[37] Y. A. Buyevich. Hydrodynamics of dispersions including diffusional effects. *Archives of Mechanics*, 42(4-5):429–442, 1990.

[38] Y. A. Buyevich. Particle distribution in suspension shear flow. *Chemical Engineering Science*, 51(4):635–647, 1996.

[39] P. C. Carman. Permeability of saturated sands, soils and clays. *The Journal of Agricultural Science*, 29(2):262–273, 1938.

[40] N. F. Carnahan and K. E. Starling. Equation of state for nonattracting rigid spheres. *The Journal of Chemical Physics*, 51(2):635–636, 1969.

[41] D. Chan and R. L. Powell. Rheology of suspensions of spherical particles in a Newtonian and a non-Newtonian fluid. *Journal of Non-Newtonian Fluid Mechanics*, 15 (2):165–179, 1984.

[42] B. K Chapman. *Shear-induced migration phenomena in concentrated suspensions.* Thesis, 1990.

[43] B. K. Chapman and D. T. Leighton. Dynamic viscous resuspension. *International Journal of Multiphase Flow*, 17(4):469–483, 1991.

[44] Y. L. Chen. Inertia and deformation driven migration of a soft particle in confined shear and Poiseuille flow. *RSC Advances*, 4(34):17908–17916, 2014.

[45] P. Cherukat and J. B. McLaughlin. The inertial lift on a rigid sphere in a linear shear flow field near a flat wall. *Journal of Fluid Mechanics*, 263(1):1–18, 1994.

[46] P. Cherukat and J. B. McLaughlin. The inertial lift on a rigid sphere in a linear shear flow field near a flat wall. *Journal of Fluid Mechanics*, 285:407, 1995.

[47] P. Cherukat, J. B. McLaughlin, and A. L. Graham. The inertial lift on a rigid sphere translating in a linear shear flow field. *International Journal of Multiphase Flow*, 20(2):339–353, 1994.

[48] P. Cherukat, J. B. McLaughlin, and D. S. Dandy. A computational study of the inertial lift on a sphere in a linear shear flow field. *International Journal of Multiphase Flow*, 25(1):15–33, 1999.

[49] W. Chester, D. R. Breach, and I. Proudman. On the flow past a sphere at low Reynolds number. *Journal of Fluid Mechanics*, 37(4):751–760, 1969.

[50] Y. Choi, K. W. Seo, and S. J. Lee. Lateral and cross-lateral focusing of spherical particles in a square microchannel. *Lab on a Chip*, 11(3):460–465, 2011.

[51] Y. S. Choi and S. J. Lee. Holographic analysis of three-dimensional inertial migration of spherical particles in micro-scale pipe flow. *Microfluidics and Nanofluidics*, 9(4):819–829, 2010.

[52] A. W. Chow, S. W. Sinton, J. H. Iwamiya, and T. S. Stephens. Shear-induced particle migration in Couette and parallel-plate viscometers: NMR imaging and stress measurements. *Physics of Fluids*, 6(8):2561–2576, 1994.

[53] B. Chun and A. J. C Ladd. Inertial migration of neutrally buoyant particles in a square duct: An investigation of multiple equilibrium positions. *Physics of Fluids*, 18(3):031704, 2006.

[54] B. Chun, J. S. Park, H. W. Jung, and Y. Y. Won. Shear-induced particle migration and segregation in non-Brownian bidisperse suspensions under planar Poiseuille flow. *Journal of Rheology*, 63(3):437–453, 2019.

[55] R. Clift, J. R. Grace, and M. E. Weber. *Bubbles, drops, and particles.* Academic Press, New York, 1978.

[56] É. Couturier, F. Boyer, O. Pouliquen, and É. Guazzelli. Suspensions in a tilted trough: second normal stress difference. *Journal of Fluid Mechanics*, 686:26–39, 2011.

[57] R. G. Cox and H. Brenner. The lateral migration of solid particles in poiseuille flow — I theory. *Chemical Engineering Science*, 23(2):147–173, 1968.

[58] R. G. Cox and S. K. Hsu. The lateral migration of solid particles in a laminar flow near a plane. *International Journal of Multiphase Flow*, 3(3):201–222, 1977.

[59] L. Crowl and A. L. Fogelson. Analysis of mechanisms for platelet near-wall excess under arterial blood flow conditions. *Journal of Fluid Mechanics*, 676:348–375, 2011.

[60] L. M. Crowl and A. L. Fogelson. Computational model of whole blood exhibiting lateral platelet motion induced by red blood cells. *International Journal for Numerical Methods in Biomedical Engineering*, 26(3/4):471–487, 2010.

[61] F. R. Da Cunha and E. J. Hinch. Shear-induced dispersion in a dilute suspension of rough spheres. *Journal of Fluid Mechanics*, 309:211–223, 1996.

[62] D. S. Dandy and H. A. Dwyer. A sphere in shear flow at finite Reynolds number: effect of shear on particle lift, drag, and heat transfer. *Journal of Fluid Mechanics*, 216:381–410, 1990.

[63] R. H. Davis. Sedimentation of noncolloidal particles at low Reynolds numbers. *Annual Review of Fluid Mechanics*, 17:91, 1985.

[64] R. H. Davis and K. H. Birdsell. Hindered settling of semidilute monodisperse and polydisperse suspensions. *AIChE Journal*, 34(1):123, 1988.

[65] R. H. Davis and D. T. Leighton. Shear-induced transport of a particle layer along a porous wall. *Chemical Engineering Science*, 42(2):275–281, 1987.

[66] T. Dbouk, E. Lemaire, L. Lobry, and F. Moukalled. Shear-induced particle migration: Predictions from experimental evaluation of the particle stress tensor. *Journal of Non-Newtonian Fluid Mechanics*, 198:78–95, 2013.

[67] T. Dbouk, L. Lobry, and E. Lemaire. Normal stresses in concentrated non-Brownian suspensions. *Journal of Fluid Mechanics*, 715:239–272, 2013.

[68] A. Deboeuf, G. Gauthier, J. Martin, Y. Yurkovetsky, and J. F. Morris. Particle pressure in a sheared suspension: A bridge from osmosis to granular dilatancy. *Physical Review Letters*, 102(10):108301, 2009.

[69] D. Di Carlo, J. F. Edd, K. J. Humphry, H. A. Stone, and M. Toner. Particle segregation and dynamics in confined flows. *Physical Review Letters*, 102(9):094503, 2009.

[70] A. M. C. Dinther, Schro A., A. Imhof, H. M. Vollebregt, and R. M. Boom. Flow-induced particle migration in microchannels for improved microfiltration processes. *Microfluidics and Nanofluidics*, 15(4):451–465, 2013.

[71] G. Drazer, J. Koplik, B. Khusid, and A. Acrivos. Deterministic and stochastic behaviour of non-Brownian spheres in sheared suspensions. *Journal of Fluid Mechanics*, 460:307–335, 2002.

[72] D. A. Drew. Two-phase flows: Constitutive equations for lift and Brownian motion and some basic flows. *Archive for Rational Mechanics and Analysis*, 62(2):149–163, 1976.

[73] D. A. Drew. The lift force on a small sphere in the presence of a wall. *Chemical Engineering Science*, 43(4):769–773, 1988.

[74] E. C. Eckstein, D. G. Bailey, and A. H. Shapiro. Self-diffusion of particles in shear flow of a suspension. *Journal of Fluid Mechanics*, 79(1):191–208, 1977.

[75] A. Einstein. Über die von der molekularkinetischen Theorie der Wärme geforderte Bewegung von in ruhenden Flüssigkeiten suspendierten Teilchen. *Annalen der Physik*, 322(8):549–560, 1905.

[76] N. I. K. Ekanayake, J. D. Berry, A. D. Stickland, I. L. Muir, S. K. Dower, and D. J. E. Harvie. Lift and drag forces on a particle near a wall at low Reynolds numbers. *21st Australasian Fluid Mechanics Conference; Adelaide, Australia*, 2018.

[77] N. I. K. Ekanayake, J. D. Berry, A. D. Stickland, D. E. Dunstan, I. L. Muir, S. K. Dower, and D. J. E. Harvie. Lift and drag forces acting on a particle moving with zero slip in a linear shear flow near a wall. *Journal of Fluid Mechanics*, 904:A6, 2020.

[78] N. I. K. Ekanayake, J. D. Berry, and D. J. E. Harvie. Lift and drag forces acting on a particle moving in the presence of slip and shear near a wall. *Journal of Fluid Mechanics*, 915:A103, 2021.

[79] Z. Fang, A. Mammoli, J. Brady, M. Ingber, L. Mondy, and A. Graham. Flow-aligned tensor models for suspension flows. *International journal of multiphase flow*, 28(1):137–166, 2002.

[80] H. Faxen. Der Widerstand gegen die Bewegung einer starren Kugel in einer zähen Flüssigkeit, die zwischen zwei parallelen ebenen Wänden eingeschlossen ist. *Annalen der Physik*, 373(10):89–119, 1922.

[81] F. Feuillebois. Perturbation problems at low Reynolds number, 2004. Lecture Notes-AMAS.

[82] T. M. Fischer and R. Rosenberger. A boundary integral method for the numerical computation of the forces exerted on a sphere in viscous incompressible flows near a plane wall. *Zeitschrift für angewandte Mathematik und Physik ZAMP*, 38(3): 339–365, 1987.

[83] D. R. Foss and J. F. Brady. Structure, diffusion and rheology of Brownian suspensions by Stokesian dynamics simulation. *Journal of Fluid Mechanics*, 407:167–200, 2000.

[84] David R. Foss and John F. Brady. Self-diffusion in sheared suspensions by dynamic simulation. *Journal of Fluid Mechanics*, 401:243–274, 1999.

[85] M. Frank, D. Anderson, E. R. Weeks, and J. F. Morris. Particle migration in pressure-driven flow of a Brownian suspension. *Journal of Fluid Mechanics*, 493: 363–378, 2003.

[86] Y. O. Fuentes, S. Kim, and D. J. Jeffrey. Mobility functions for two unequal viscous drops in stokes flow. I. Axisymmetric motions. *The Physics of Fluids*, 31 (9):2445–2455, 1988.

[87] F. Gadala-Maria and A. Acrivos. Shear-induced structure in a concentrated suspension of solid spheres.

[88] Y. Gao, P. Magaud, C. Lafforgue, S. Colin, and L. Baldas. Inertial lateral migration and self-assembly of particles in bidisperse suspensions in microchannel flows. *Microfluidics and Nanofluidics*, 23(7):93, 2019.

[89] S. Garland, G. Gauthier, J. Martin, and J. F. Morris. Normal stress measurements in sheared non-Brownian suspensions. *Journal of Rheology*, 57(1):71–88, 2013.

[90] C. Geuzaine and J. Remacle. Gmsh: A 3-D finite element mesh generator with built-in pre-and post-processing facilities. *International Journal for Numerical Methods in Engineering*, 79(11):1309–1331, 2009.

[91] M. Gholami, A. Rashedi, N. Lenoir, D. Hautemayou, G. Ovarlez, and S. Hormozi. Time-resolved 2D concentration maps in flowing suspensions using X-ray. *Journal of Rheology*, 62(4):955–974, 2018.

[92] A. J. Goldman, R. G. Cox, and H. Brenner. Slow viscous motion of a sphere parallel to a plane wall—I Motion through a quiescent fluid. *Chemical Engineering Science*, 22(4):637–651, 1967.

[93] A. J. Goldman, R. G. Cox, and H. Brenner. Slow viscous motion of a sphere parallel to a plane wall—II Couette flow. *Chemical Engineering Science*, 22(4): 653–660, 1967.

[94] S. Goldstein. The steady flow of viscous fluid past a fixed spherical obstacle at small Reynolds numbers. *Proceedings of the Royal Society of London. Series A, Containing Papers of a Mathematical and Physical Character*, 123(791):225–235, 1929.

[95] A. L. Graham, S. A. Altobelli, Eiichi Fukushima, L. A. Mondy, and T. S. Stephens. Note: NMR imaging of shear-induced diffusion and structure in concentrated suspensions undergoing couette flow. *Journal of Rheology*, 35(1):191–201, 1991.

[96] E. Guazzelli. Evolution of particle-velocity correlations in sedimentation. *Physics of Fluids*, 13(6):1537, 2001.

[97] Élisabeth Guazzelli, Jeffrey F. Morris, and Sylvie Pic. *A Physical Introduction to Suspension Dynamics*. Cambridge University Press, Cambridge, United Kingdom, 2011.

[98] Hamed Haddadi and Jeffrey F. Morris. Topology of pair-sphere trajectories in finite inertia suspension shear flow and its effects on microstructure and rheology. *Physics of Fluids*, 27(4):043302, 2015.

[99] J. S. Halow and G. B. Wills. Experimental observations of sphere migration in couette systems. *Industrial & Engineering Chemistry Fundamentals*, 9(4):603–607, 1970.

[100] A. Hamed. Solid particle demixing in a suspension flow of viscous gas. *Journal of Fluids Engineering*, 97(1):106, 1975.

[101] R. E. Hampton, A. A. Mammoli, A. L. Graham, N. Tetlow, and S. A. Altobelli. Migration of particles undergoing pressure-driven flow in a circular conduit. *Journal of Rheology*, 41(3):621, 1997.

[102] M. Han. Particle migration in tube flow of suspensions. *Journal of Rheology*, 43 (5):1157, 1999.

[103] J. Happel and H. Brenner. *Low Reynolds number hydrodynamics*. Springer Netherlands, 1981.

[104] John Happel. Viscous flow in multiparticle systems: Slow motion of fluids relative to beds of spherical particles. *AIChE Journal*, 4(2):197, 1958.

[105] E. Y. Harper and I. Dee Chang. Maximum dissipation resulting from lift in a slow viscous shear flow. *Journal of Fluid Mechanics*, 33(2):209–225, 1968.

[106] D. J. E. Harvie. An implicit finite volume method for arbitrary transport equations. *ANZIAM Journal. Electronic Supplement*, 52:C1126, 2010.

[107] D. J. E. Harvie. Tensorial constitutive equations for the flow of a semi-dilute monodisperse suspension of spheres. *In preparation*, 2020.

[108] B. P. Ho and L. G. Leal. Inertial migration of rigid spheres in two-dimensional unidirectional flows. *Journal of Fluid Mechanics*, 65(02):365, 1974.

[109] A. J. Hogg. The inertial migration of non-neutrally buoyant spherical particles in two-dimensional shear flows. *Journal of Fluid Mechanics*, 272:285–318, 1994.

[110] K. Hood, S. Lee, and M. Roper. Inertial migration of a rigid sphere in three-dimensional Poiseuille flow. *Journal of Fluid Mechanics*, 765:452–479, 2015.

[111] P. A. Hookham. *Concentration and Velocity Measurements in Suspensions Flowing through a Rectangular Channel.* Thesis, California Institute of Technology, 1986.

[112] H. W. Hou, A. A. S. Bhagat, Alvin G. Lin C., P. Mao, Kevin S. Wei T., J. Han, and C. T. Lim. Deformability based cell margination—A simple microfluidic design for malaria-infected erythrocyte separation. *Lab on a Chip*, 10(19):2605–2613, 2010.

[113] A. A. Howard, M. R. Maxey, and K. Yeo. Settling of heavy particles in concentrated suspensions of neutrally buoyant particles under uniform shear. *Fluid Dynamics Research*, 50(4):041401, 2018.

[114] D. M. Husband, L. A. Mondy, E. Ganani, and A. L. Graham. Direct measurements of shear-induced particle migration in suspensions of bimodal spheres. *Rheologica Acta*, 33(3):185–192, 1994.

[115] M. S. Ingber, A. L. Graham, L. A. Mondy, and Z. Fang. An improved constitutive model for concentrated suspensions accounting for shear-induced particle migration rate dependence on particle radius. *International Journal of Multiphase Flow*, 35 (3):270–276, 2009.

[116] M. Ishii and K. Mishima. Two-fluid model and hydrodynamic constitutive relations. *Nuclear Engineering and Design*, 82(2):107, 1984.

[117] R. Jackson. Locally averaged equations of motion for a mixture of identical spherical particles and a Newtonian fluid. *Chemical Engineering Science*, 52(15):2457, 1997.

[118] D. J. Jeffrey, J. F. Morris, and J. F. Brady. The pressure moments for two rigid spheres in low-Reynolds-number flow. *Physics of Fluids. A, Fluid dynamics*, 5(10): 2317, 1993.

[119] R. C. Jeffrey and J. R. A. Pearson. Particle motion in laminar vertical tube flow. *Journal of Fluid Mechanics*, 22(4):721–735, 1964.

[120] G. Johnson, K. R. Rajagopal, and M. Massoudi. A review of interaction mechanisms in fluid-solid flows. Report, USDOE Pittsburgh Energy Technology Center, PA (USA), 1990.

[121] R. D. Kamien and A. J. Liu. Why is random close packing reproducible? *Physical Review Letters*, 99(15):155501, 2007.

[122] H. U. Kang, W. G. Kim, and S. H. Kim. Effect of particle migration on the heat transfer of nanofluid. *Korea-Australia Rheology Journal*, 19(3):99–107, 2007.

[123] A. Karnis, H. L. Goldsmith, and S. G. Mason. The kinetics of flowing dispersions: I. Concentrated suspensions of rigid particles. *Journal of Colloid and Interface Science*, 22(6):531–553, 1966.

[124] A. Karnis, H. L. Goldsmith, and S. G. Mason. The flow of suspensions through tubes: V. Inertial effects. *Canadian Journal of Chemical Engineering*, 44(4):181, 1966.

[125] D Kauzlaric, A Greiner, and J. G. Korvink. A non-local extension of the Phillips model for shear induced particle migration. *Microsystem Technologies*, 17(2):265–272, 2011.

[126] J. M. Kim, S. G. Lee, and C. Kim. Numerical simulations of particle migration in suspension flows: Frame-invariant formulation of curvature-induced migration. *Journal of Non-Newtonian Fluid Mechanics*, 150(2–3):162–176, 2008.

[127] Y. W. Kim and J. Y. Yoo. The lateral migration of neutrally-buoyant spheres transported through square microchannels. *Journal of micromechanics and microengineering*, 18(6), 2008.

[128] C. J. Koh, P. Hookham, and L. G. Leal. An experimental investigation of concentrated suspension flows in a rectangular channel. *Journal of Fluid Mechanics*, 266: 1–32, 1994.

[129] I. Krieger. Rheology of monodisperse latices. *Advances in colloid and interface science*, 3(2):111–136, 1972.

[130] I. Krieger and T. J. Dougherty. A mechanism for non-Newtonian flow in suspensions of rigid spheres. *Transactions of The Society of Rheology*, 3(1):137–152, 1959.

[131] G. Krishnan and D. Leighton. Inertial lift on a moving sphere in contact with a plane wall in a shear flow. *Physics of Fluids*, 7(11):2538–2545, 1995.

[132] G. P. Krishnan and D. T. Leighton. Dynamic viscous resuspension of bidisperse suspensions—I. Effective diffusivity. *International Journal of Multiphase Flow*, 21 (5):721–732, 1995.

[133] G. P Krishnan, S. Beimfohr, and D. T Leighton. Shear-induced radial segregation in bidisperse suspensions. *Journal of Fluid Mechanics*, 321:371–393, 1996.

[134] J. Kromkamp, M. van Domselaar, K. Schroën, R. van der Sman, and R. Boom. Shear-induced diffusion model for microfiltration of polydisperse suspensions. *Desalination*, 146(1):63–68, 2002.

[135] J. Kromkamp, D. T. M. Van Den Ende, D. Kandhai, R. G. M. Van Der Sman, and R. M. Boom. Shear-induced self-diffusion and microstructure in non-Brownian suspensions at non-zero Reynolds numbers. *Journal of Fluid Mechanics*, 529:253–278, 2005.

[136] P. M. Kulkarni. *Suspension mechanics at finite inertia.* Thesis, 2009.

[137] P. M. Kulkarni and J. F. Morris. Suspension properties at finite Reynolds number from simulated shear flow. *Physics of Fluids*, 20(4):040602, 2008.

[138] P. M. Kulkarni and J. F. Morris. Pair-sphere trajectories in finite-Reynolds-number shear flow. *Journal of Fluid Mechanics*, 596:413–435, 2008.

[139] R. Kurose and S. Komori. Drag and lift forces on a rotating sphere in a linear shear flow. *Journal of Fluid Mechanics*, 384:183–206, 1999.

[140] L. G. Leal. Particle motions in a viscous fluid. *Annual Review of Fluid Mechanics*, 12(1):435–476, 1980.

[141] H. Lee and S. Balachandar. Drag and lift forces on a spherical particle moving on a wall in a shear flow at finite Re. *Journal of Fluid Mechanics*, 657:89–125, 2010.

[142] D. Legendre and J. Magnaudet. A note on the lift force on a spherical bubble or drop in a low-Reynolds-number shear flow. *Physics of Fluids*, 9(11):3572–3574, 1997.

[143] D. Legendre and J. Magnaudet. The lift force on a spherical bubble in a viscous linear shear flow. *Journal of Fluid Mechanics*, 368:81–126, 1998.

[144] K. Leiderman and A. L. Fogelson. Grow with the flow: a spatial-temporal model of platelet deposition and blood coagulation under flow. *Mathematical Medicine and Biology : A Journal of the IMA*, 28(1):47–84, 2011.

[145] D. Leighton and A. Acrivos. The lift on a small sphere touching a plane in the presence of a simple shear flow. *Zeitschrift für angewandte Mathematik und Physik*, 36(1):174–178, 1985.

[146] D. Leighton and A. Acrivos. Viscous resuspension. *Chemical engineering science*, 41(6):1377–1384, 1986.

[147] D. Leighton and A. Acrivos. The shear-induced migration of particles in concentrated suspensions. *Journal of Fluid Mechanics*, 181:415–439, 1987.

[148] D. Leighton and A. Acrivos. Measurement of shear-induced self-diffusion in concentrated suspensions of spheres. *Journal of Fluid Mechanics*, 177:109–131, 1987.

[149] Daniel Lhuillier. Migration of rigid particles in non-Brownian viscous suspensions. *Physics of Fluids*, 21(2):023302, 2009.

[150] C. Lin, J. H. Peery, and W. R. Schowalter. Simple shear flow round a rigid sphere: Inertial effects and suspension rheology. *Journal of Fluid Mechanics*, 44(1):1–17, 1970.

[151] E. Loth. Lift of a spherical particle subject to vorticity and/or spin. *AIAA Journal*, 46(4):801–809, 2008.

[152] E. Loth and A. J. Dorgan. An equation of motion for particles of finite Reynolds number and size. *Environmental Fluid Mechanics*, 9(2):187–206, 2009.

[153] M. K. Lyon and L. G. Leal. An experimental study of the motion of concentrated suspensions in two-dimensional channel flow. Part 1. Monodisperse systems. *Journal of Fluid Mechanics*, 363:25–56, 1998.

[154] M. K. Lyon and L. G. Leal. An experimental study of the motion of concentrated suspensions in two-dimensional channel flow. Part 2. Bidisperse systems. *Journal of Fluid Mechanics*, 363:57–77, 1998.

[155] Manninen M., Taivassalo V., and Kallio S. R. On the mixture model for multiphase flow. Technical report, Technical Research Centre of Finland, 1996.

[156] J. Magnaudet, S. H. U. Takagi, and D. Legendre. Drag, deformation and lateral migration of a buoyant drop moving near a wall. *Journal of Fluid Mechanics*, 476: 115 – 154, 2003.

[157] M. Majji and J. F. Morris. Inertial migration of particles in Taylor-Couette flows. *Physics of Fluids*, 30(3):033303, 2018.

[158] R. St J. Manley and S. G. Mason. Particle motions in sheared suspensions. II. Collisions of uniform spheres. *Journal of Colloid Science*, 7:354–369, 1952.

[159] S. H. Maron and P. E. Pierce. Application of ree-eyring generalized flow theory to suspensions of spherical particles. *Journal of Colloid Science*, 11(1):80–95, 1956.

[160] J. M. Martel and M. Toner. Inertial focusing in microfluidics. *Annual Review of Biomedical Engineering*, 16(1):371–396, 2014.

[161] Jacob Masliyah. Hindered settling in a multi-species particle system. *Chemical engineering science*, 34(9):1166, 1979.

[162] M. Massoudi. On the importance of material frame-indifference and lift forces in multiphase flows. *Chemical Engineering Science*, 57(17):3687–3701, 2002.

[163] J. P. Matas, J. Morris, and E. Guazzelli. Inertial migration of rigid spherical particles in Poiseuille flow. *Journal of fluid mechanics*, 515:171–195, 2004.

[164] J. P. Matas, J. F. Morris, and E. Guazzelli. Lateral forces on a sphere. *Oil & gas science and technology*, 59(1):59–70, 2004.

[165] J. P. Matas, J. F. Morris, and E. Guazzelli. Lateral force on a rigid sphere in large-inertia laminar pipe flow. *Journal of Fluid Mechanics*, 621:59–67, 2009.

[166] M. Maxey. Simulation methods for particulate flows and concentrated suspensions. *Annual Review of Fluid Mechanics*, 49(1):171–193, 2017.

[167] M. R. Maxey and J. J. Riley. Equation of motion for a small rigid sphere in a nonuniform flow. *The Physics of Fluids*, 26(4):883–889, 1983.

[168] T. Maxworthy. Accurate measurements of sphere drag at low Reynolds numbers. *Journal of Fluid Mechanics*, 23(2):369–372, 1965.

[169] J. B McLaughlin. Inertial migration of a small sphere in linear shear flows. *Journal of Fluid Mechanics*, 224:261–274, 1991.

[170] J. B. McLaughlin. The lift on a small sphere in wall-bounded linear shear flows. *Journal of Fluid Mechanics*, 246:249–265, 1993.

[171] D. F. McTigue, R. C. Givler, and J. W. Nunziato. Rheological effects of nonuniform particle distributions in dilute suspensions. *Journal of Rheology*, 30(5):1053–1076, 1986.

[172] R. Mei. An approximate expression for the shear lift force on a spherical particle at finite Reynolds number. *International Journal of Multiphase Flow*, 18(1):145–147, 1992.

[173] D. Merhi, E. Lemaire, G. Bossis, and F. Moukalled. Particle migration in a concentrated suspension flowing between rotating parallel plates: Investigation of diffusion flux coefficients. *Journal of Rheology*, 49(6):1429–1448, 2005.

[174] R. M. Miller and J. F. Morris. Normal stress-driven migration and axial development in pressure-driven flow of concentrated suspensions. *Journal of Non-Newtonian Fluid Mechanics*, 135(2):149–165, 2006.

[175] R. M. Miller, J. P. Singh, and J. F. Morris. Suspension flow modeling for general geometries. *Chemical Engineering Science*, 64(22):4597–4610, 2009.

[176] P. Mills and P. Snabre. Settling of a suspension of hard spheres. *Europhysics Letters (EPL)*, 25(9):651–656, 1994.

[177] P. Mills and P. Snabre. Rheology and structure of concentrated suspensions of hard spheres. shear induced particle migration. *Journal de Physique II*, 5(10):1597–1608, 1995.

[178] K. Miura, T. Itano, and M. Sugihara-Seki. Inertial migration of neutrally buoyant spheres in a pressure-driven flow through square channels. *Journal of fluid mechanics*, 749:320, 2014.

[179] K. Miyazaki, D. Bedeaux, and J. B. Avalos. Drag on a sphere in slow shear flow. *Journal of Fluid Mechanics*, 296:373–390, 1995.

[180] J. Y. Moon, S. Dai, L. Chang, J. S. Lee, and R. I. Tanner. The effect of sphere roughness on the rheology of concentrated suspensions. *Journal of Non-Newtonian Fluid Mechanics*, 223:233–239, 2015.

[181] Y. Morita, T. Itano, and M. Sugihara-Seki. Equilibrium radial positions of neutrally buoyant spherical particles over the circular cross-section in Poiseuille flow. *Journal of Fluid Mechanics*, 813:750–767, 2017.

[182] J. F. Morris and F. Boulay. Curvilinear flows of noncolloidal suspensions: The role of normal stresses. *Journal of Rheology*, 43(5):1213–1237, 1999.

[183] J. F. Morris and J. F. Brady. Pressure-driven flow of a suspension: Buoyancy effects. *International Journal of Multiphase Flow*, 24(1):105–130, 1998.

[184] J. F. Morris and B. Katyal. Microstructure from simulated Brownian suspension flows at large shear rate. *Physics of Fluids*, 14(6):1920–1937, 2002.

[185] K. Müller, D. A. Fedosov, and G. Gompper. Margination of micro- and nano-particles in blood flow and its effect on drug delivery. *Scientific Reports*, 4:4871–4871, 2014.

[186] H. Nicolai and E. Guazzelli. Effect of the vessel size on the hydrodynamic diffusion of sedimenting spheres. *Physics of Fluids*, 7(1):3–5, 1995.

[187] H. Nicolai, B. Herzhaft, E. J. Hinch, L. Oger, and E. Guazzelli. Particle velocity fluctuations and hydrodynamic self-diffusion of sedimenting non-Brownian spheres. *Physics of Fluids*, 7(1):12, 1995.

[188] J. T. Norman, H. V. Nayak, and R. T. Bonnecaze. Migration of buoyant particles in low-Reynolds-number pressure-driven flows. *Journal of Fluid Mechanics*, 523: 1–35, 2005.

[189] P. R. Nott and J. F. Brady. Pressure-driven flow of suspensions: simulation and theory. *Journal of Fluid Mechanics*, 275:157–199, 1994.

[190] P. R. Nott, E. Guazzelli, and O. Pouliquen. The suspension balance model revisited. *Physics of Fluids*, 23(4):043304, 2011.

[191] S. Oh, Y. Song, D. I. Garagash, B. Lecampion, and J. Desroches. Pressure-Driven Suspension Flow near Jamming. *Physical Review Letters*, 114(8):088301, 2015.

[192] D. R. Oliver. Influence of particle rotation on radial migration in the Poiseuille flow of suspensions. *Nature*, 194:1269, 1962.

[193] C. W. Oseen. Uber die Stokes' sche Formel und Uber eine verwandte Aufgabe in der Hydrodynamik. *Arkiv Mat., Astron. och Fysik*, 6:1, 1910.

[194] G. Ovarlez, F. Bertrand, and S. Rodts. Local determination of the constitutive law of a dense suspension of noncolloidal particles through magnetic resonance imaging. *Journal of Rheology*, 50(3):259–292, 2006.

[195] N. Phan-Thien and A. L. Graham. Rayleigh similarity solutions and boundary layer flow for concentrated suspensions. *Journal of Non-Newtonian Fluid Mechanics*, 64 (2):157–171, 1996.

[196] N. Phan-Thien, Z. Fang, and A. Graham. Stability of some shear flows for concentrated suspensions. *Rheologica Acta*, 35(1):69–75, 1996.

[197] R. J. Phillips, R. C. Armstrong, R. A. Brown, A. L. Graham, and J. R. Abbott. A constitutive equation for concentrated suspensions that accounts for shear-induced particle migration. *Physics of Fluids A*, 4(1):30, 1992.

[198] T. N. Phung, J. F. Brady, and G. Bossis. Stokesian dynamics simulation of Brownian suspensions. *Journal of Fluid Mechanics*, 313:181–207, 1996.

[199] I. Proudman and J. R. A. Pearson. Expansions at small Reynolds numbers for the flow past a sphere and a circular cylinder. *Journal of Fluid Mechanics*, 2(3): 237–262, 1957.

[200] P. Raiskinmäki, J. A. Åström, M. Kataja, M. Latva-Kokko, A. Koponen, A. Jäsberg, A. Shakib-Manesh, and J. Timonen. Clustering and viscosity in a shear flow of a particulate suspension. *Physical Review E*, 68(6):061403, 2003.

[201] A. Ramachandran and D. T. Leighton. Viscous resuspension in a tube: The impact of secondary flows resulting from second normal stress differences. *Physics of Fluids*, 19(5):053301, 2007.

[202] I. Rampall, J. R. Smart, and D. T. Leighton. The influence of surface roughness on the particle-pair distribution function of dilute suspensions of non-colloidal spheres in simple shear flow. *Journal of Fluid Mechanics*, 339:1–24, 1997.

[203] R. Rao, L. Mondy, A. Sun, and S. Altobelli. A numerical and experimental study of batch sedimentation and viscous resuspension. *International Journal for Numerical Methods in Fluids*, 39(6):465–483, 2002.

[204] R. R. Rao, L. A. Mondy, T. A. Baer, S. A. Altobelli, and T. S. Stephens. NMR Measurements and simulations of particle migration in non-Newtonian fluids. *Chemical Engineering Communications*, 189(1):1, 2002.

[205] R. V. Repetti and E. F. Leonard. Segré-Silberberg annulus formation : A possible explanation. *Nature*, 203(4952):1346–1348, 1964.

[206] C. M. Rhie and W. L. Chow. Numerical study of the turbulent flow past an airfoil with trailing edge separation. *AIAA journal*, 21(11):1525–1532, 1983.

[207] J. F. Richardson and J. F. Zaki. The sedimentation of a suspension of uniform spheres under conditions of viscous flow. *Chemical Engineering Science*, 3(2):65, 1954.

[208] P. J. Roache. Quantification of uncertainty in computational fluid dynamics. *Annual Review of Fluid Mechanics*, 29(1):123–160, 1997.

[209] R. Roscoe. The viscosity of suspensions of rigid spheres. *British journal of applied physics*, 3(8):267–269, 1952.

[210] S. I. Rubinow and J. B. Keller. The transverse force on a spinning sphere moving in a viscous fluid. *Journal of Fluid Mechanics*, 11(3):447–459, 1961.

[211] P. G. T. Saffman. The lift on a small sphere in a slow shear flow. *Journal of Fluid Mechanics*, 22(02):385–400, 1965.

[212] B. Saint-Michel, S. Manneville, S. Meeker, G. Ovarlez, and H. Bodiguel. X-ray radiography of viscous resuspension. *Physics of Fluids*, 31(10), 2019.

[213] M. Sarabian, M. Firouznia, B. Metzger, and S. Hormozi. Fully developed and transient concentration profiles of particulate suspensions sheared in a cylindrical Couette cell. *Journal of Fluid Mechanics*, 862:659–671, 2019.

[214] U. Schaflinger, A. Acrivos, and H. Stibi. An experimental study of viscous resuspension in a pressure-driven plane channel flow. *International Journal of Multiphase Flow*, 21(4):693–704, 1995. ISSN 0301-9322.

[215] L. Schiller. Über die grundlegenden Berechnungen bei der Schwerkraftaufbereitung. *Z. Vereines Deutscher Inge.*, 77:318–321, 1933.

[216] C. A. Schneider, W. S. Rasband, and K. W Eliceiri. NIH Image to ImageJ: 25 years of image analysis. *Nature methods*, 9(7):671–675, 2012.

[217] J. A. Schonberg and E. J. Hinch. Inertial migration of a sphere in Poiseuille flow. *Journal of Fluid Mechanics*, 203:517–524, 1989.

[218] G. Segre and A. Silberberg. Radial particle displacements in Poiseuille flow of suspensions. *Nature*, 189:209–210, 1961.

[219] G. Segre and A. Silberberg. Behaviour of macroscopic rigid spheres in Poiseuille flow Part 2. Experimental results and interpretation. *Journal of Fluid Mechanics*, 14(1):136–157, 1962.

[220] D. Semwogerere and E. Weeks. Shear-induced particle migration in binary colloidal suspensions. *Physics of Fluids*, 20(4):043306, 2008.

[221] D. Semwogerere, J. F. Morris, and E. R. Weeks. Development of particle migration in pressure-driven flow of a Brownian suspension. *Journal of Fluid Mechanics*, 581: 437–451, 2007.

[222] A. Shakib-Manesh, P. Raiskinmäki, A. Koponen, M. Kataja, and J. Timonen. Shear stress in a Couette flow of liquid-particle suspensions. *Journal of Statistical Physics*, 107(1):67–84, 2002.

[223] N. C. Shapley, R. C. Armstrong, and R. A. Brown. Laser Doppler velocimetry measurements of particle velocity fluctuations in a concentrated suspension. *Journal of Rheology*, 46(1):241–272, 2002.

[224] N. C. Shapley, R. A. Brown, and R. C. Armstrong. Evaluation of particle migration models based on laser Doppler velocimetry measurements in concentrated suspensions. *Journal of Rheology*, 48(2):255–279, 2004.

[225] A. Shauly, A. Wachs, and A. Nir. Shear-induced particle migration in a polydisperse concentrated suspension. *Journal of Rheology*, 42(6):1329–1348, 1998.

[226] P. Shi and R. Rzehak. Lift forces on solid spherical particles in unbounded flows. *Chemical Engineering Science*, 208:115145, 2019.

[227] P. Shi and R. Rzehak. Lift forces on solid spherical particles in wall-bounded flows. *Chemical Engineering Science*, 211:115264, 2020.

[228] H. Shichi, H. Yamashita, J. Seki, T. Itano, and M. Sugihara-Seki. Inertial migration regimes of spherical particles suspended in square tube flows. *Physical Review Fluids*, 2(4):044201, 2017.

[229] A. Sierou and J. F. Brady. Rheology and microstructure in concentrated noncolloidal suspensions. *Journal of Rheology*, 46(5):1031–1056, 2002.

[230] A. Sierou and J. F. Brady. Shear-induced self-diffusion in non-colloidal suspensions. *Journal of Fluid Mechanics*, 506:285–314, 2004.

[231] S. W. Sinton and A. W. Chow. NMR flow imaging of fluids and solid suspensions in poiseuille flow. *Journal of Rheology*, 35(5):735–772, 1991.

[232] J. R. Smart and D. T. Leighton. Measurement of the hydrodynamic surface roughness of noncolloidal spheres. *Physics of Fluids A: Fluid Dynamics*, 1(1):52–60, 1989.

[233] E. Spruijt. Sedimentation dynamics and equilibrium profiles in multicomponent mixtures of colloidal particles. *Journal of physics. Condensed matter*, 26(7), 2014.

[234] K. Stewartson. XXXII. On the steady flow past a sphere at high Reynolds number using Oseen's approximation. *Philosophical Magazine*, 1(4):345–354, 1956.

[235] G. G. Stokes. *On the effect of the internal friction of fluids on the motion of pendulums*, volume 9. Pitt Press Cambridge, 1851.

[236] S. R. Subia, M. S. Ingber, L. A. Mondy, S. A. Altobelli, and A. L. Graham. Modelling of concentrated suspensions using a continuum constitutive equation. *Journal of Fluid Mechanics*, 373:193–219, 1998.

[237] J. W. Swan and J. F. Brady. The hydrodynamics of confined dispersions. *Journal of Fluid Mechanics*, 687:254–299, 2011.

[238] M. Tachibana. On the behaviour of a sphere in the laminar tube flows. *Rheologica Acta*, 12(1):58–69, 1973.

[239] F. Takemura. Migration velocities of spherical solid particles near a vertical wall for Reynolds number from 0.1 to 5. *Physics of Fluids*, 16(1):204–207, 2004.

[240] F. Takemura and J. Magnaudet. The transverse force on clean and contaminated bubbles rising near a vertical wall at moderate Reynolds number. *Journal of Fluid Mechanics*, 495:235–253, 2003.

[241] F. Takemura and J. Magnaudet. Lateral migration of a small spherical buoyant particle in a wall-bounded linear shear flow. *Physics of Fluids*, 21(8):083303, 2009.

[242] F. Takemura, J. Magnaudet, and P. Dimitrakopoulos. Migration and deformation of bubbles rising in a wall-bounded shear flow at finite Reynolds number. *Journal of Fluid Mechanics*, 634:463–486, 2009.

[243] T. Tohme, Y. Gao, P. Magaud, L. Baldas, C. Lafforgue, and S. Colin. Inertial migration of spherical particles in bidisperse suspensions flowing in microchannels. In *5th European Conference on Microfluidics*, 2018.

[244] S. Tomotika and T. Aoi. The steady flow of viscous fluid past a sphere and circular cylinder at small Reynolds numbers. *The Quarterly Journal of Mechanics and Applied Mathematics*, 3(2):141–161, 1950.

[245] R. Toy, E. Hayden, C. Shoup, H. Baskaran, and E. Karathanasis. The effects of particle size, density and shape on margination of nanoparticles in microcirculation. *Nanotechnology*, 22(11):115101, 2011.

[246] R. Toy, P. M. Peiris, K. B Ghaghada, and E. Karathanasis. Shaping cancer nanomedicine: the effect of particle shape on the in vivo journey of nanoparticles. *Nanomedicine*, 9(1):121–134, 2014.

[247] A. Tripathi and A. Acrivos. Viscous resuspension in a bidensity suspension. *International Journal of Multiphase Flow*, 25(1):1–14, 1999.

[248] M. A. Van Der Hoef. Lattice-boltzmann simulations of low-Reynolds-number flow past mono- and bidisperse arrays of spheres: results for the permeability and drag force. *Journal of Fluid Mechanics*, 528(1):233, 2005.

[249] R. G. M. van der Sman and H. M. Vollebregt. Effective temperature for sheared suspensions: A route towards closures for migration in bidisperse suspension. *Advances in Colloid and Interface Science*, 185–186:1–13, 2012.

[250] P. Vasseur and R. G. Cox. The lateral migration of a spherical particle in two-dimensional shear flows. *Journal of Fluid Mechanics*, 78(02):385, 1976.

[251] P. Vasseur and R. G. Cox. The lateral migration of spherical particles sedimenting in a stagnant bounded fluid. *Journal of Fluid Mechanics*, 80(3):561–591, 1977.

[252] H. M. Vollebregt. Suspension flow modelling in particle migration and microfiltration. *Soft matter*, 6(24):6052, 2010.

[253] H. M. Vollebregt, R. G. M. van der Sman, and R. M. Boom. Model for particle migration in bidisperse suspensions by use of effective temperature. *Faraday Discussions*, 158:89–103, 2012.

[254] Y. Wang, Y. Gao, P. Magaud, L. Baldas, C. Lafforgue, and S. Colin. Inertial migration of neutrally buoyant particles in square channels at high Reynolds numbers. *arXiv preprint arXiv:1903.07975*, 2019.

[255] A. N. Whitehead. Second approximations to viscous fluid motion. *Quart. J. Math*, 23(1):143–152, 1889.

[256] L. Woodcock. Glass transition in the hard-sphere model and Kauzmann's paradox. *Annals of the New York Academy of Sciences*, 371(1 Structure and):274–298, 1981.

[257] S. Yahiaoui and F. Feuillebois. Lift on a sphere moving near a wall in a parabolic flow. *Journal of Fluid Mechanics*, 662:447–474, 2010.

[258] Y. Yan, J. F. Morris, and J. Koplik. Hydrodynamic interaction of two particles in confined linear shear flow at finite Reynolds number. *Physics of Fluids*, 19(11): 113305, 2007.

[259] K. Yeo and M. R. Maxey. Simulation of concentrated suspensions using the force-coupling method. *Journal of Computational Physics*, 229(6):2401–2421, 2010.

[260] K. Yeo and M. R. Maxey. Dynamics of concentrated suspensions of non-colloidal particles in Couette flow. *Journal of Fluid Mechanics*, 649:205–231, 2010.

[261] G. M. Yezaz Ahmed and A. Singh. Numerical simulation of particle migration in asymmetric bifurcation channel. *Journal of Non-Newtonian Fluid Mechanics*, 166 (1):42–51, 2011.

[262] I. E. Zarraga and D. T. Leighton. Measurement of an unexpectedly large shear-induced self-diffusivity in a dilute suspension of spheres. *Physics of Fluids*, 14(7): 2194–2201, 2002.

[263] I. E. Zarraga, Davide A. Hill, and D. T. Leighton. The characterization of the total stress of concentrated suspensions of noncolloidal spheres in newtonian fluids. *Journal of Rheology*, 44(2):185–220, 2000.

[264] L. Zeng, S. Balachandar, and P. Fischer. Wall-induced forces on a rigid sphere at finite Reynolds number. *Journal of Fluid Mechanics*, 536(1):1, 2005.

[265] L. Zeng, N. Fady, S. Balachandar, and P. Fischer. Forces on a finite-sized particle located close to a wall in a linear shear flow. *Physics of Fluids*, 21(3):033302, 2009.

[266] D. Z. Zhang and Prosperetti A. Averaged equations for inviscid disperse two-phase flow. *Journal of Fluid Mechanics*, 267:185, 1994.

[267] D. Z. Zhang and A. Prosperetti. Momentum and energy equations for disperse two-phase flows and their closure for dilute suspensions. *International Journal of Multiphase Flow*, 23(3):425–453, 1997.

[268] J. Zhang, P. C. Johnson, and A. S. Popel. Effects of erythrocyte deformability and aggregation on the cell free layer and apparent viscosity of microscopic blood flows. *Microvascular Research*, 77(3):265–272, 2009.

[269] S. Zhang, X. Zhao, and S. Bayyuk. Generalized formulations for the rhie–chow interpolation. *Journal of Computational Physics*, 258:880–914, 2014.

[270] H. Zhao, E. S. G. Shaqfeh, and V. Narsimhan. Shear-induced particle migration and margination in a cellular suspension. *Physics of Fluids*, 24(1):011902, 2012.

[271] A. L. Zydney, J. D. Oliver, and C. K. Colton. A constitutive equation for the viscosity of stored red cell suspensions: Effect of hematocrit, shear rate, and suspending phase. *Journal of Rheology*, 35(8):1639–1680, 1991.